Faculty of Science

Department of Imaging and Applied Physics

X-Ray Scattering Study of Cellulosic Arrangements in Plant Cell Wall Materials

Kevin J Jarrett

This thesis is presented for the Degree of
Doctor of Philosophy
of
Curtin University

December 2011

Declaration

To the best of my knowledge and belief this thesis contains no material previously published by any other person except where due acknowledgement has been made.

This thesis contains no material which has been accepted for the award of any other degree or diploma in any university.

Signature: …….

Date: …….

Acknowledgements

It would not have been possible to complete this thesis without the support and love of my family. My Mum, Dad and Nanna have been a constant source of support and encouragement throughout the years I have spent working on this and I can't thank them enough. I can't think of a better little brother to have than William who always been there for me, thanks for everything bro. I'm also very grateful for the support of my extended family; Aunty Carol and Craig, Aunty Jen and Dave and my little cousins Daniel and Alex. I love you all and thank you for everything you've done.

I wouldn't have come this far if not for my supervisors, Professor Craig Buckley and Dr Chris Garvey. Both have been amazing supervisors showing great patience while I was finishing. Thank you both for your support, encouragement and inspiration. I'd also like to thank my thesis chairperson Dr Robert Loss for his support and Prof Brian O'Connor who acted as my interim supervisor for a period. So many staff helped while I was here and I'd like to thank them all, in particular Glen Lawson, Dr Rob Hart and the admin staff. Also it would not have been possible for this project to have started if not for the support of Curtin University, The Australian Nuclear Science and Technology Organisation and The Australian Institute of Nuclear Science and Engineering.

I've made some fantastic friends in both my undergraduate course and during my PhD here at Curtin. They have made it a pleasure to be here and helped immensely in getting me through my studies. In particular Dr Grant Pusey has been a great mate for as long as I've known him. Also Dr Dan Veen, Dr Iain Parnum, Dr Miles Parsons, Dr Andrew Princep and Dr Mark Paskevicous all were in varying stages of study when I started and all have been great mates during my time here. Congratulations to all of them on their success. Last but certainly not least thanks to everyone I've had the privilege to meet through the common room and PHYSSED for all the good times while I've been here.

Table of Contents

Table of Figures

Table of Tables

Abstract

Plant cell walls are the most important source of the polymer cellulose. The cell wall contains crystalline cellulose microfibrils embedded in a matrix of amorphous polymers. The most important of these amorphous polymers are the lignins (polyphenolic compounds) and the hemi-celluloses (a range of polysaccharides). In this thesis we concentrate on the use of wide angle x-ray scattering as a tool to understand the important arrangements of cellulose in cell walls. Other experimental tools are used to supplement this information.

The structure and arrangement of cellulose into microfibrils have been investigated in different plant cell wall materials using x-ray scattering techniques and solid state NMR spectroscopy. The materials have been selected because although all contain a cell wall there are differences in the structure and arrangement of the polymers present, cellulose in particular. The aspects of the cellulose microfibril that been have been investigated are the lateral dimensions of the microfibril and the angle that the microfibril makes with the cell axis; the microfibril angle (MFA). The cell wall of plants is a tough layered structure that is located outside the cell membrane. The cell wall can be flexible or rigid depending on the structural support required by the cell.

Wide angle x-ray scattering (WAXS) and x-ray diffraction (XRD) are closely related techniques that measure the scattering of incident x-rays from a repeating crystal lattice. In general the use of WAXS will refer to the transmission mode and XRD will refer to the reflection mode. The transmission mode provides two dimensional data that is sensitive to the preferred orientation of cellulose microfibrils in the cell wall.

Small angle x-ray scattering is similar to WAXS and XRD. The difference comes from the incident x-ray beam scattering from regions of electron density difference rather than repeat lattice structures. These scattering regions need to be in the range of 1 – 100 nm to be detectable and result in scattering angles of no greater than 5°. In the cell wall the biggest electron density difference is between the voids in the sample (which is normally filled with water in a living or well preserved sample) and

the polymers that make up the cell wall. The chemistry of the polymers in the cell wall is so similar that they have approximately the same electron density.

Cross-polarised magic angle spinning nuclear magnetic resonance (CP-MAS NMR) spectroscopy is a technique used to investigate the local chemical environments of the carbon nuclei in cell wall materials. This method is highly sensitive to changes in chemistry of the sample. Chemical treatments to remove specific components of the cell wall can be investigated with NMR spectra.

The first sample presented here is the palm fibre; which was investigated with WAXS, SAXS and NMR. This sample was selected as the palm is a major crop for the production of bio-diesel and produces large amounts of palm fibre as a by-product. WAXS measurements showed little variation in the lateral dimensions of the microfibril or the MFA along the length of the fibre. SAXS measurements agree with the WAXS measurements of the MFA in showing little variation along the fibre length. Solid state NMR measurements were made to give an indication of the chemistry of these materials and changes during a simple chemical treatment.

The second sample presented in this study is from the maturing stems of native Australian timbers. These samples were studied with wide and small angle x-ray scattering using synchrotron radiation. Multiple WAXS measurements have been made on each sample producing a grid of measurements. The lateral dimensions of the microfibril were consistent both within a sample and between different species. The MFA measured for these samples showed some variation across the grain of the stem. In some cases a layered structure appears to be present, a feature of maturing stems that has not previously been reported in the literature. SAXS measurements of the MFA are in agreement with those from WAXS despite only a single SAXS measurement being made per sample.

The third sample from this study is a piece of acacia wood. This sample was studied as a matured piece of wood in contrast to the maturing stems studied previously. The sample contained annual rings and reaction wood, features not observed in the maturing tree stems. WAXS measurements from a lab based instrument were used to

study the sample. The measurements determined that there was no significant variation in the lateral dimensions of the microfibrils or the MFA

The fourth sample studied for this thesis was a collection of commercial native timbers. XRD measurements were obtained on a lab based diffractometer. Measurements were made with the incident beam parallel to the grain and perpendicular to the grain. The lateral dimensions of the microfibril showed good agreement between the parallel and perpendicular measurements. Any differences in the diffraction patterns of the two sample orientations were not able to be quantified.

The complexity of cell wall materials represents a challenging system for experimental investigation. The different measurements made on a variety of samples indicate that x-ray scattering methods are well suited to such investigations. In general it was found that the orientation of microfibrils in the cell wall was a measureable parameter of a sample that could be obtained rapidly and varied between samples. In contrast the lateral dimensions of the microfibril were not as varied in the samples selected for this work; although it is known that some cell wall materials can contain very large microfibrils.

WAXS is sensitive to both the orientation and size of cellulose microfibrils. While this makes it an excellent technique for cellulose investigation it is not a direct method and requires extensive deconvolution of the data. XRD being similar to WAXS is a good method for the measurement of lateral dimensions, but does not reveal orientational information about the sample. SAXS can be used to determine some information about the cell wall structures. However these must be inferred from the data as it does not measure anything in the cell wall directly, just the scattering from voids in the sample. NMR is a powerful method for distinguishing between cell wall components however this is often not quantifiable in native samples due to the complexities of the obtained spectra. The use of WAXS has consistently revealed cellulosic arrangement in the cell wall with other techniques used providing complementary data.

Chapter 1 Introduction

The focus of this thesis will be on the nanoscale arrangements of polymers in a range of plant cell wall materials. The major functions of the cell wall are to impose restrictions on the dimensions and geometry of the cell, but also to fulfil the mechanical demands of the plant. In this way the cell wall can protect the cell from bursting due to the rapid influx of water by osmosis; flow slowly under conditions of growth, and provide a range of mechanical functioning depending where the cell is in the plant (Preston, 1975). Cellulose makes up most of the cell wall by mass so as the largest component of the cell wall cellulose will be the focus of this study. Cellulose is a polycrystalline material composed of many thin crystallites termed microfibrils.

In contrast with cellulose the other major components (Table 1-1) of the cell wall (the lignins and the hemi-celluloses) are amorphous polymers (Fengel and Wegener, 1989). This thesis will present results largely from x-ray scattering methods and evaluate their suitability with respect to the investigation of orientation and lateral dimensions of the microfibril in the cell wall. In this chapter the basic chemistry and nanoscale arrangements of the cell wall polymers are discussed.

Polymer	Abundance in Wood
Cellulose	35 - 50%
Hemicelluloses	20 - 35%
Lignin	10 - 25%
Structural Protein	1 - 5%

Table 1-1 – The abundance of typical polymers found in wood (Knox *et al.*, 2001).

Cellulose is considered to be the most abundant polymer on Earth (Preston, 1975). Due to this abundance x-ray studies on cell wall materials have been performed for over a century (Hon (1994) reports that S. Nishikawa and S. Ono published results as early as 1913). In this time much information has been obtained on the structure and arrangement of cellulose, including the solution of its crystal structure (Nishiyama *et al.*, 2002; Nishiyama *et al.*, 2003). The crystallographic details of cellulose will be discussed in Chapter Two. X-ray scattering studies continue to be used in the study of cell wall materials due to the power of these techniques to investigate the crystalline phases in an amorphous matrix.

The cell wall is a natural composite material made up of; crystalline cellulose microfibrils embedded in an amorphous polymer matrix. From a chemical perspective cellulose is a homopolymer of two β-1,4 linked glucose residues, cellobiose (Figure 1-1) (Knox *et al.*, 2001). The abundance of hydroxyl groups in the cellobiose unit results in an extensive intra- and inter- polymer chain hydrogen bonding network in the plane of the glucose rings that produces a rigid straight chain molecule (Figure 1-2) (Gardner and Blackwell, 1974a). The degree of polymerisation of the chains vary greatly depending on the species with woody tissue typically containing 300 – 1700 units while cotton and bacteria can range from 800 to 10 000 units (Klemm *et al.*, 2005).

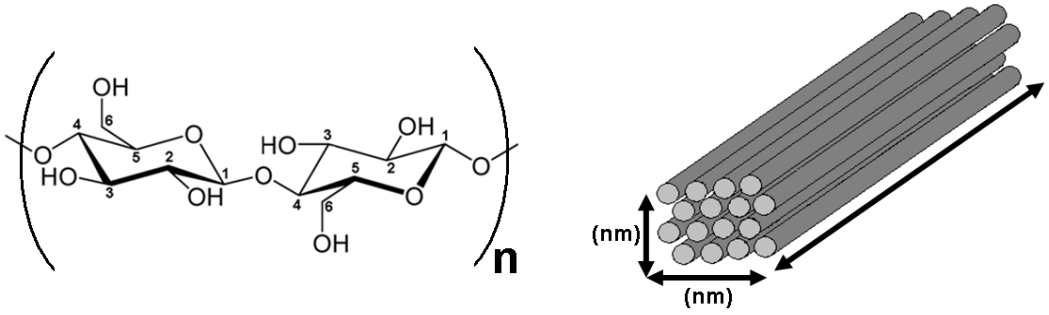

Figure 1-1 – The molecular structure of cellulose (left) and a microfibril made up of sixteen individual cellulose chains (right)

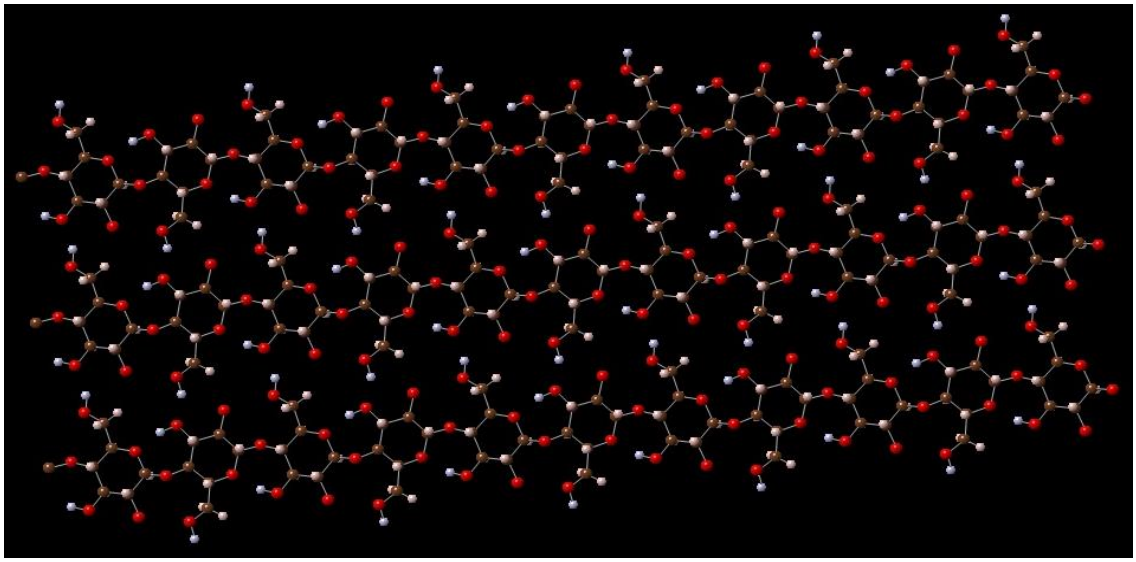

Figure 1-2 – Three cellulose chains arranged adjacent to each other as in a microfibril showing extensive intra- and inter-molecular hydrogen bonding. These sheets stack together to form the microfibril.

As a semi-crystalline polymer it was assumed that cellulose was composed of alternating regions of highly ordered material and disordered material (Garvey *et al.*, 2005b). Experimental evidence from a range of techniques, including NMR (Newman, 1999), x-ray scattering (Muller *et al.*, 2000a) and neutron scattering (Muller *et al.*, 2000b), suggested the semi-crystalline polymer model of cellulose was in need of revision. A composite material was proposed for cellulose instead. In the new model the cellulose microfibril exists as a discrete nano-crystallite. These crystallites aggregate in the cell wall and are linked by hemicelluloses and structural proteins (Knox *et al.*, 2001). This view is also consistent with the modern view of cellulose biosynthesis.

A better understanding of the structure of cellulose can be obtained when considering the biosynthesis of the material. At the most basic level cellulose biosynthesis is a polymerisation of an abundant pool (Ross *et al.*, 1991) of UDP-glucose substrate into a long cellulose chain (Delmer and Amor, 1995). However the process is exceedingly complex with many higher levels of organisation required to effectively produce and deposit cellulose into the cell wall. The enzyme that drives the synthesis, cellulose synthase (*Ces*A1), is a membrane bound protein. These proteins do not occur individually on the membrane and instead form complexes (the so called terminal complex due to the terminal end of the cellulose chains). As a result cellulose is never synthesised as an individual chain, but always as a group of chains (Delmer, 1987). In bacterial cells this complex is linear, but in vascular plants a hexameric rosette complex is formed (Mueller and Brown, 1980). There is a good correlation between the size the microfibril and the size of the rosette complex (Hotchkis and Brown, 1987).

Naturally occurring cellulose (termed cellulose I) is the focus of this thesis. Cellulose I contains two distinct crystalline forms of cellulose that are present in the material in varying ratios (Atalla and Van der Hart, 1984). The two forms are termed cellulose I_α and I_β. The I_α form is often associated with more primitive members of the plant kingdom. For example algal cell walls and bacterial cellulose are almost entirely the α form. The I_β form of cellulose is usually found in more complex vascular plants although there is still an appreciable amount of the I_α form (Van der Hart and Atalla, 1987).

The two crystalline forms of cellulose present contain differing hydrogen bonding networks. The cellulose microfibril can be imagined on three size scales; as an individual cellulose chain, as a plane of cellulose chains side by side and the whole microfibril containing planes stacked on top of each other. The single chain of cellulose shows a large amount of intra-molecular hydrogen bonding. When cellulose chains are located next to each other to form plane hydrogen bonding can take place between chains. These planes of cellulose chains are stacked on top of each other and held together by van der Waals forces, Figure 1-2 (Cousins and Brown, 1995).

The arrangement of the cellulose microfibrils varies depending on which cell wall layer it is deposited into (Figure 1-3). The cell wall consists of a primary wall that is formed during the development of the cell and a secondary wall that is formed after the cell has matured and finished expanding (Preston, 1975).

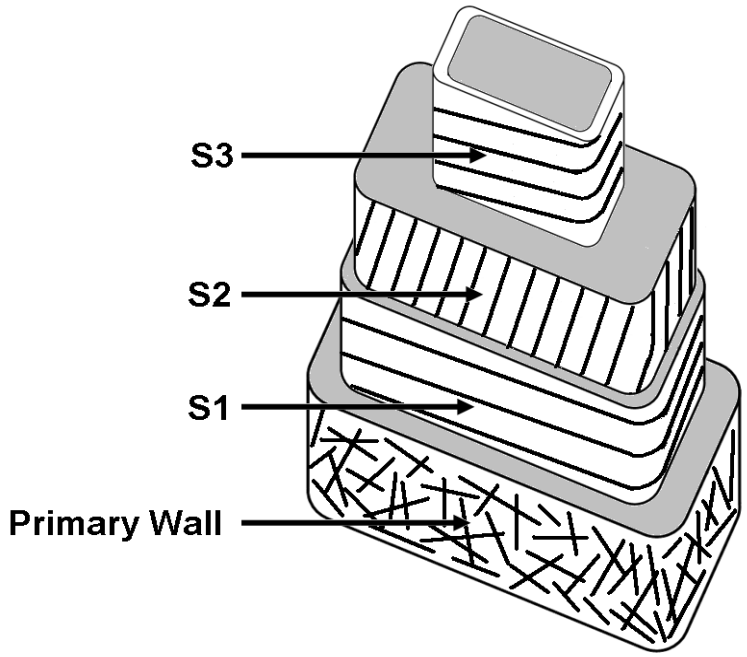

Figure 1-3 – The cell wall layers in a wood cell showing the alignment of embedded crystalline microfibrils in different layers. Figure adapted from (Fengel and Wegener, 1989).

The secondary cell wall is split into three layers. The S2 layer is the thickest in the cell wall and contains highly orientated microfibrils that are defined by the microfibril angle (MFA). The MFA is given by the angle that the S2 cellulose microfibril makes with the cell axis (Meylan, 1967). The S1 and S3 layers also

contain orientated cellulose and in general these microfibrils are approximately perpendicular to the S2 microfibrils (Wardrop and Preston, 1947).

The amorphous matrix of the cell wall is made up of mostly lignin and hemi-cellulose with some other polymers and minerals present in small quantities along with water (Knox *et al.*, 2001). Lignin is the name given to a group of polyphenolic compounds. There are three main monomers being *p*-coumaryl alcohol, coniferyl alcohol and sinapyl alcohol (Figure 1-4). When incorporated into the lignin polymer these monomeric units produce p-hydroxyphenyl (**H**), guaiacyl (**G**) and syringyl (**S**) phenylpropanoids respectively (Boerjan *et al.*, 2003). The composition of lignins varies amongst species, cell types and even cell wall layers. These variations are influenced by genetic cues and environmental conditions (Campbell and Sederoff, 1996). In general angiosperms will incorporate mostly **G** and **S** units with only trace **H** unit present. Gymnosperms on the other hand are composed mostly of **G** units and low levels of **H** units (Baucher *et al.*, 1998).

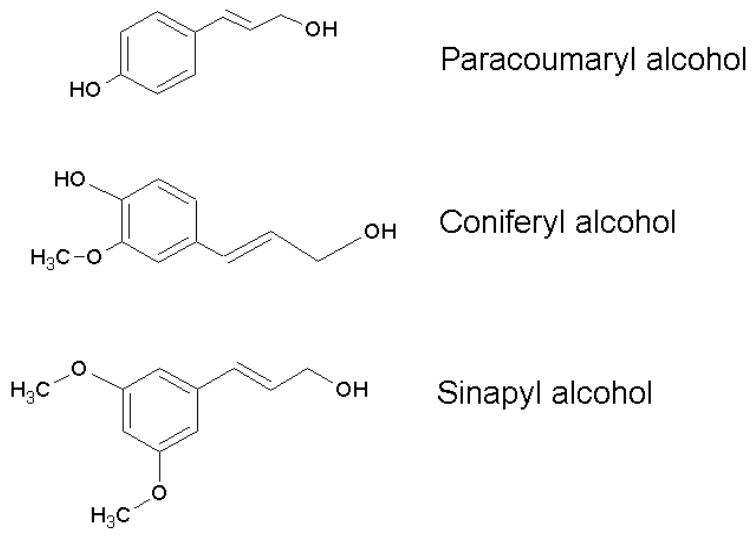

Figure 1-4 – The molecular structure of the three main lignin monomers.

The hemicelluloses are a group of cell wall polymers composed of pentoses (xylose, arabinose), hexoses (mannose, glucose and galactose) and sugar acids (Saha, 2003). Hemicellulose from angiosperms are mostly made up of xylans while gymnosperms are mostly glucomannans (McMillan, 1994) While cellulose is a tough material and resistant to hydrolysis, hemi-cellulose is an amorphous material with very little

mechanical strength that is hydrolysed by dilute acid or base, Figure 1-5 (Sjöström, 1993).

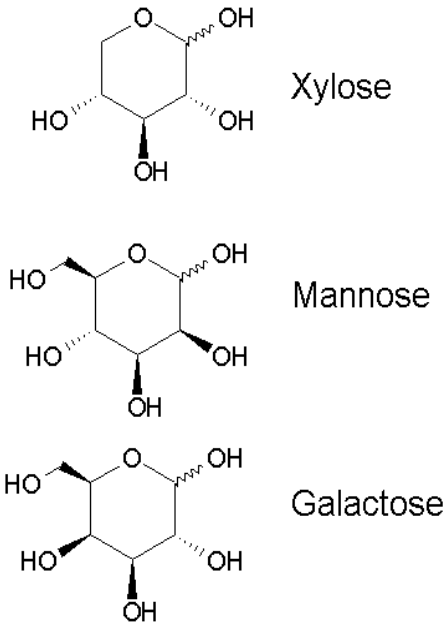

Figure 1-5 – Some of the common sugar monomers for the hemi-celluloses.

Chapter 2 Literature Review and Theoretical Overview

Cellulose has been utilised by man for as long as plant materials have been burnt for warmth. As humans have evolved so too have the methods by which cell wall materials have been utilised by society. Plant fibres were used for making ropes as long ago as 4500 B.C. and soon to follow was the use of fibres in the manufacture of garments. In addition to being pressed into ropes and cloths, cellulosic materials were instrumental in the development of writing materials with sheets of papyrus found in Egypt dating back to 3000 B.C. Later Hindu societies reported ways of cultivating cotton crops, which were then weaved and spun into clothing. Thousands of years later the papermaking industry was founded in China as bast fibres were pulped and pressed into sheets for writing on (Hon, 1994). The historical review of Hon gives a good contextual framework for how the understanding of cellulose structure and arrangement has advanced. Some of the key points from this review are summarised in Chapter 2.1.

Even at this early stage of society the value of cell wall materials can be seen in its variety of uses. The myriad of uses for these materials are tied to the many mechanical properties of cell wall materials, ranging from flexible and lightweight to rigid and dense as well as anything in between. The varied mechanical properties of cell wall materials are particularly impressive given the somewhat limited set of components (polymers) from which to draw (Chapter 1). It is the arrangement of components in the cell wall (cellulose in particular) which largely dictates the mechanical properties of the material (Chapter 2.2). As this varies, so too do the mechanical properties and hence the possible uses of cellulose by humans expands.

2.1 A History of Cellulose Investigation

The cultivation and application of cell wall materials has continued to grow throughout human history although scientific study on cellulose was not reported until the 19th century. According to Hon (1994) nitrocellulose, a cellulose derivative obtained from the dissolution of plant materials in nitric acid, was first reported in 1833 by French chemist Henri Braconnot. The material represented the first manmade fibre and the beginning of cellulose utilisation in the industrial age. The study of cellulose began in 1837 when French chemist Anselme Payen showed that various plant materials (including seeds, root tips, leaves and mosses) could produce a tough, white, fibrous material (Hon, 1994). This marked the first instance of cellulose being purposefully isolated and was achieved by repeatedly dissolving the plant materials in acid and ammonia after extracting the solution with water, alcohol and ether. The term cellulose was first coined after a meeting of the French Academy of Sciences to discuss Payen's work in 1839 (French, 2000).

Hon (1994) reported that Payen's investigation of cellulose drew heavily on the early work of French carbohydrate chemists Joseph Louis Gay-Lussac and Louis Jacques Thenard. This body of work determined the elemental composition of compounds such as sugar and starch but found wood to have a slightly different composition. Payen was able to show that beechwood extractions had a very similar elemental composition to starch. This was the first evidence of cellulose being composed of carbohydrate units, specifically those that make up starch (Hon, 1994). At this stage in the study of cellulose chemistry the concept of long chain molecules was still contentious and numerous groups suggested that cellulose was made up of discrete molecules composed of glucose while others proposed a single molecule.

At the same time the molecular nature of cellulose was being investigated, the morphology of plant fibres was being studied. This analysis was pioneered by Karl Wilhelm von Nägeli, a Swiss botanist better known for his work on chromosomes. Although being closely related to starch chemically, cellulose behaved quite differently physically. According to Hon (1994) Nägeli used polarised light

microscopy in 1858 was used to show that cellulose was birefringent, which was taken as evidence of crystallinity shortly after the chemical isolation.

Cellulose was amongst the first materials studied by XRD. This was the beginning of investigations into the crystal structure of cellulose. The first reported patterns were obtained by Nishikawa and Ono in Japan in 1913 from collected bamboo and hemp fibres (Hon, 1994). This early study was difficult to interpret as the idea of powder x-ray diffraction was not yet fully developed. Despite the difficulties in interpreting the data it was shown that crystallites within the cell wall had a preferred orientation. Hon suggested that Nishikawa would later propose that the crystallinity of cellulose was discontinuous, that is, a polycrystalline material rather than a single crystal. The work of Nishikawa and Ono was instrumental in the work of later investigators who used similar experimental to develop the crystal structures of cellulose (such as Sponsler in 1928).

The early diffraction studies on cellulose are all the more impressive when it is considered that they occurred 10 years before the full chemical structure of cellulose was determined (Haworth, 1929). The additional chemical information assisted greatly in the interpretation of diffraction data. Despite being the first analysis of cellulosics by x-ray diffraction, the work of Nishikawa and Ono was not widely noticed due mostly to the limited availability of the journal. In the early 1920's there was a revival of interest in x-ray investigation of cell wall materials, particularly in Europe. These studies showed that a variety of different materials, cotton, ramie, wood, flax and so on, all had the same reflections, suggesting the same lattice spacings. According to Hon (1994) it was at this time that evidence of a single crystalline structure for cellulose was obtained by German physicist Herzog and Jancke, which became known as native cellulose, or natural cellulose.

Hon (1994) reported that K.H. Meyer and H. Mark developed a unit cell based on x-ray diffraction data that incorporated a monoclinic unit cell in 1929. This report of the monoclinic model suggested a later refinement by Meyer and L. Misch in 1937. Hon (1994) indicates that this work retained all the important modelling aspects done previously by the likes of O.L. Sponsler while maintaining the monoclinic unit cell. This revised model of cellulose was a straight chained polymer composed of 1→4

bonded β glucose molecules. The two glucose molecules correspond to the repeat unit of cellulose, termed cellobiose and was shown to be equal in length to the lattice parameter in the direction of the fibre. This model was later confirmed by Gross and Clark and widely accepted as the structure for native cellulose for many years (Gross and Clark, 1938).

Structural investigation of cellulose in the 1940's was focused on the arrangement of cellulose chains in the unit cell. It was widely accepted that the unit cell contained two basis chains with the corners of the monoclinic cell being equivalent and one through the centre. The question of whether adjacent chains in a single microfibril were arranged parallel or anti-parallel was difficult to answer based on the quality of diffraction patterns of the day. Hon's paper in 1994 indicated that initially Meyer and Mark proposed a parallel arrangement, i.e. the chains in the unit cell all point in the same direction. However it was noted in the review that after the refinement by Meyer and Misch an anti-parallel arrangement was favoured by the authors, arguing that newly synthesised chains should run in both directions. The actual arrangement would not be agreed on for many years. In addition to the arrangement of the cellulose chains, the conformation of molecules was the subject of debate during this period with Meyer and Misch using a straight chained molecule. Space filling models and hydrogen bonds were used by P.H. Hermans & J.D. Booys in 1943 to show that a bent conformation was optimal (Hon, 1994).

This era of cellulose research was dominated by physical investigations. Although significant chemical and biological breakthroughs were made in the period, these were related to the physical aspects of the structure with some interest in chemical modification (the development of derivatives). However towards the end of this time, work was beginning on the process by which plants synthesise their molecular components in the newly developing field of biochemistry. The beginnings of cellulose biosynthesis research grew from the investigation of saccharide synthesis, specifically those related to nucleotides such as uridine diphosphate (UDP) glucose (Leloir, 1972). This lead on to the development of the idea that cells that synthesise cellulose require a source of glucose molecules to fuel the synthetic process (Glaser, 1957a).

Observations of cellulose morphology revealed long microfibrils with varying cross sectional dimensions. This was found to be dependent on the source of the specimen. It was proposed that there was an elementary filament (crystallites), some 700 by 300 nm, which forms a paracrystalline phase (Mukherjee and Woods, 1953). Using this elementary filament it was suggested that the size of the microfibril was 2000 by 1000 nm in its cross section. Later work using higher resolution microscopes and negative staining showed regular fibrils with a width of 35 nm in all celluloses. These were termed elementary fibrils by A. Frey-Wyssling & K. Muhlethaler once the idea of large elementary filaments was abandoned (Hon, 1994). However Muhlethaler would later suggest an elementary fibril 3.5 nm in diameter. These were observed as crystalline along their length however were shown to be mismatched at the surface. This was assumed to be the "amorphous" signal observed in their diffraction patterns (Muhlethaler, 1969). This revised model was thought to contain about 36 individual cellulose chains and the number of chains contained in a cellulose crystallite is intrinsically linked to the synthetic pathway.

In the first half of the 20th century there were a number of breakthroughs in the experimental methodologies of diffraction. For electron diffraction this meant more intense radiation sources and better resolution detection systems. This became evident in 1958 when it was found that an electron diffraction pattern of algal celluloses produced more complex diffraction patterns than x-ray data (Honjo and Watanabe, 1958). The existing model from Meyer and Misch was unsuitable for indexing and interpreting this new data, again opening up discussion as to the nature of the cellulose crystal structure. At first, the existence of additional reflections suggested a unit cell roughly twice as large in two of the crystallographic directions as that of Meyer-Misch. Such a large unit cell was attributed to some sort of superstructure with the repeat unit spanning multiple crystallites. Similar measurements were made and a triclinic unit cell was proposed to compete with the monoclinic unit cell of Meyer and Misch (Fischer and Mann, 1960) (Beg *et al.*, 1974). During this period, the diffraction patterns obtained could be modelled successfully with either unit cell but it was generally agreed upon that the crystal structure of the microfibril was source dependent.

The issue of chain packing was difficult to resolve because of limitations of the samples at the time. Despite the uncertainty over the chain packing it was generally agreed upon that the cellulose chains crystallise almost immediately after synthesis. As a result the orientation of cellulose chains would most likely be driven by the biosynthetic pathway. Industrial uses of cellulose typically involve dissolving the fibres in a swelling agent and recrystallisation. This process was found to give an anti-parallel chain organisation (Viswanathan and Shenouda, 1970). Soon after this, diffraction data from x-ray (Gardner and Blackwell, 1974b; Preston, 1975; Sarko and Muggli, 1974), neutron (Beg *et al.*, 1974) and electron (Claffey and Blackwell, 1976) sources showed that the molecules in a microfibril are most likely to be parallel. The calculation of the packing energy was found to be lower in the parallel arrangement than in the anti-parallel (Sarko, 1976).

The cellulose chain arrangement in the elementary fibrils cannot be separated from the biological processes that produce them. In 1964 it was proposed that cellulose synthases were multisubunit complexes in the so called "ordered granule hypothesis" (Preston, 1964). In this model the enzymatic complexes would self assemble after some form of signalling cascade. The formation of a complex would then allow for the synthesis of glucan chains and the assembly of the cellulose crystal structure. This model was supported by the discovery of linear terminal complexes in algal celluloses (Brown and Montezinos, 1976). The observation of the complexes at the ends of the microfibrils resulted in them being called terminal complexes. Later these complexes were again observed at the ends of microfibrils in plant cells. However these complexes were arranged as hexagonal units, the so called rosette terminal complexes (Mueller and Brown, 1980). Although observed directly these synthase complexes could not be isolated and purified in any significant quantities.

In the early part of the 1980's a significant breakthrough in the structure of the cellulose was made using solid state Nuclear Magnetic Resonance spectroscopy (NMR). The spectra were measured using cross polarisation and magic angle spinning techniques (CP-MAS) (Atalla *et al.*, 1980; Earl and Van der Hart, 1981). These techniques improved the quality of solid ^{13}C NMR spectra. The use of CP increases the intensity of the signal from the naturally deficient ^{13}C nucleus. Anisotropies in the chemical shift of solid state samples results in broadening of the

signals to such an extent that it is difficult to identify important overlapping signals (Schaefer and Stejskal, 1976; Schaefer *et al.*, 1977). Magic angle spinning improves the resolution of the signal by averaging out this anistropy. These measurements showed the presence of two allomorphs in native cellulose via two separate peaks. Varieties of natural samples were measured in this way and were found to be composed of varying amounts of the two allomorphs. The I_α allomorph was found to be predominant in bacterial and algal celluloses while the I_β was found to be the more abundant form in higher plants.

The identification of the two distinct crystalline forms in native cellulosic materials put an end to twenty years of debate regarding the structural nature of the material. Previous diffraction studies were being re-examined in the light of multiple crystalline phases being present. The spectra could be interpreted as linear combinations of the pure I_α and I_β phases (Atalla and Van der Hart, 1984). From the identification of the two phases the two competing models from diffraction studies were implemented together. The two chain monoclinic unit cell is associated with the I_β phase and the one chain triclinic cell is associated with the I_α phase. The evidence for the existence of the triclinic unit cell was particularly useful as it was strong support for the parallel arrangement of cellulose chains in the crystallite.

The early CP-MAS ^{13}C NMR experiments and subsequent interpretation was instrumental in developing the current understanding of cellulosic structure. Although it answered a number of outstanding questions, it left many unanswered in its place. In particular those questions relating to the synthesis of cellulose in living cells was still in need of answering. The presence of two different crystalline forms complicated this problem as it could require a much more complex synthetic pathway to be able to produce the right crystal type for the given circumstances. One of the problems posed was the existence of anti-parallel structures in native sources when the crystallographic information suggests that a parallel structure should be obtained (based on symmetry operations) (Sugiyama *et al.*, 1991b). Such a problem was quickly identified to be a result of defects in the synthetic mechanism although it was suggested that in some algal cell walls two synthetic complexes could be adjacent and facing opposite directions producing microfibrils arranged anti-parallel (Quader, 1991).

For much of the history of cellulosic investigation there has been an inescapable link between the structure of the material and the biological processes that produce it. In particular aspects of the structure such as chain length and crystallinity are better understood in the context of the synthesis of cellulose. *A. xylinum* has been used as a model system for the investigation of cellulose synthesis since Hestrin's group developed the methodology in the 50's. It would be thirty years before membrane preparations attained rates of synthesis comparable to those observed in cell based A. xylinum systems (Aloni *et al.*, 1982). This study identified a soluble enzyme that converts guanosine triphosphate to a signalling compound for the cellulose synthase complex (Ross *et al.*, 1987).

Atalla and Van der Hart developed the NMR analysis of cellulosic materials in the early 80's and while it showed there were two distinct crystal phases in the native material, it did not end the structural investigation of the material. While simple systems, such as *Valonia* and tunicate sources, are composed of mostly one allomorph of cellulose (I_α and I_β respectively) most samples contain approximately equal amounts of both crystal structures. The establishment of two crystal structures in the material left many wondering how these structures interact together in the material. Electron diffraction measurements were made on particularly large microfibrils from algal species. This study found that along the length of the fibril there were regions of almost pure alpha and pure beta crystal structures (Sugiyama *et al.*, 1991a).

In addition to the interaction between these crystal structures, the conversion between the two became the target of investigation. Early work focused on the solid state conversion, usually involving the annealing of a purified sample in an inert atmosphere, and hydrothermal treatments, saturating the sample with steam (Horii *et al.*, 1987). The ease with which CP-MAS NMR can distinguish between the two phases allowed for the rapid confirmation of such conversions (Hirai *et al.*, 1987). The I_β phase is considered to be the more stable of the two as I_α is irreversibly converted to the beta phase by the above techniques (Wada *et al.*, 2008). Later conversion methods included annealing in acidic and alkaline solution (Yamamoto *et al.*, 1989) although a novel new conversion was observed in 2000. This new

conversion mechanism involved bending the individual fibres through a critical angle and is observed to be reversible (Jarvis, 2000).

One of the biggest problems that confronts cellulose research is how the material can contain two distinct crystal phases when produced by a single synthetic complex. The conversion mechanism proposed by Jarvis has gone some way to answering this question. The model proposed is that the cellulose crystallite is polymerised on the plasma membrane towards the cell wall and the lack of space and likely interaction of additional proteins forces the fibre to bend in a particular direction.

2.2 The Arrangement of Cellulose and the Cell Wall Structure

Cellulose makes up the majority of the plant cell wall by mass. In addition to plant cells cellulose is also present in abundant quantities in the cell walls of bacteria, algae and fungal species. The chemical structure of cellulose underpins formation of cellulose crystallites (microfibrils). The microfibril is a single nano-crystal of cellulose chains that forms as long thin fibres with high tensile strength (Wada *et. al.*, 2008). The structure of the cell wall is influenced largely by how these long strands of cellulose are arranged in the amorphous matrix (predominately lignin and hemi-cellulose) of the cell wall.

The chemistry of cellulose has previously been described (Figure 1-1) as a homopolymer of two glucose units linked by a β-1,4 bond (O'Sullivan, 1997). In a review of the structure of cellulose O'Sullivan (1997) reports that a single cellulose chain can be composed of up to 10,000 units in higher plants and up to 15,000 units in cotton species. The unbranched polymer chain forms from the β-1,4 glycosidic bond orientating adjacent glucose rings 180° to each other (Brett, 2000). The two glucose rings is called cellobiose and forms the repeat unit of cellulose. This repeat unit contains multiple sites for inter- and intra-molecular hydrogen bonding (Figure 1-2). As a result extensive hydrogen bonding networks are formed in cellulose molecules and between cellulose molecules (Nishiyama *et. al.*, 2002; Nishiyama *et. al.*, 2003). These x-ray and neutron studies by Nishiyama in 2002 and 2003 also show that not only do adjacent cellulose chains interact through hydrogen bonding but also that sheets of parallel cellulose stack through hydrophobic interactions (Wada *et. al.*, 2008).

All of these interactions related to the chemical structure of cellulose leads to the formation of the cellulose nano-crystallite, or microfibril. The microfibril was proposed as early as 1954 although it was quite a different model to that now currently accepted (Frey-Wyssling, 1954). In the current model the crystallite (only a few nanometres wide but many micrometres long) is formed at the same time as glucose precursors are polymerised into cellulose outside the plasma membrane (Mueller & Brown, 1980). The synthetic machinery for this process is by necessity

complex in nature with many interactions required for initiation of the synthesis (Mutwil *et. al.*, 2008). In general the cellulose that is synthesised by living cells is termed Cellulose I or natural cellulose. This is differentiated from other forms of cellulose that have been altered (O'Sullivan, 1997). These polymorphs of cellulose are;

- Cellulose II – cellulose that has undergone regeneration and/or mercerisation. This process is not reversible.
- Cellulose $III_{(I)}/III_{(II)}$ – cellulose (I or II) that has been treated with liquid ammonia. This process is reversible with the evaporation of ammonia.
- Ceulluose $IV_{(I)}/IV_{(II)}$ – Cellulose III (I or II) that has been heated. This process is not reversible.

The focus here shall remain on Cellulose I as the natural form of cellulose. The crystal structure of Cellulose I has been shown to be made up of a combination of two distinct forms Cellulose I_α (generally associated with more primitive plant species) and/or Cellulose I_β (generally associated with vascular plants) (Atalla & Van der Hart, 1984). It has also been observed that a single microfibril can contain regions of both the I_α and I_β the form of cellulose (Sugiyama *et. al.*, 1991b).

These two forms have distinct crystal structures. Cellulose I_α is comprised of a single chain triclinic unit cell with $P1$ symmetry ($a = 6.717$ Å, $b = 5.962$ Å, $c = 10.400$ Å, $\alpha = 118.08°$, $\beta = 114.80°$, $\gamma = 80.37°$). Cellulose I_β is comprised of the two chain monoclinic unit cell with $P2_1$ symmetry ($a = 7.784$ Å, $b = 8.201$ Å, $c = 10.38$ Å, $\alpha = 90°$, $\beta = 90°$, $\gamma = 96.5°$) (Wada *et. al.*, 2008). In addition to the two structures having different unit cells they also have different hydrogen bonding networks due to the slight differences in interaction between adjacent chains (Nishiyama *et. al.*, 2002; Nishiyama *et. al.*, 2003). It is generally accepted that the I_β form of native cellulose is the most energetically favourable due to the irreversible conversion of the I_α form into I_β (Horii *et. al.*, 1997).

The ratio of cellulose I_α to cellulose I_β produced varies from species to species with very few examples producing a pure form of one or the other. Although there are two

crystal structures present all native cellulose shares an important feature, the parallel arrangement of the polymer chains in the microfibril (Hieta *et. al.*, 1984). The observation of parallel chains in the cellulose microfibril helped to further develop the model of cellulose biosynthesis. Specifically that all cellulose chains are synthesised in the same direction with the terminal rosette complexes located on the outer plasma membrane surface (Brown *et. al.*, 1996). The location of cellulose synthesis becomes important when considering the deposition of microfibrils into the cell wall.

The cell wall has previously been introduced as a layered structure that provides mostly structural support to the cell (Figure 1-3). The arrangement of cellulose varies between layers with the varying needs of particular layer. For the purposes of this thesis the focus will be on the different arrangement between the primary cell wall and the secondary cell wall. The model for three distinct layers of the secondary cell wall was proposed as early as 1935 by I.W. Bailey and T. Kerr based on polarised microscopy observations (Barnett and Bonham, 2004).

The formation of the primary cell wall is associated with the growing cell rather than the mature cell (McNeil *et. al.*, 1984). It is important to note that this is the stage that the primary wall is formed it remains a part of the cell wall throughout the rest of the cell's life. To cope with this period of rapid expansion the primary cell wall needs to be viscous in nature while retaining the desired strength (Cosgrove 2000). In order to achieve this flexibility the cellulose in primary cell walls is not orientated; microfibrils run in all directions within the plane of the cell wall (O'Sullivan, 1997).

There are variances in the degree of polymerisation observed with the primary cell wall typically being lower than the secondary cell wall (Spencer and Maclachlan, 1972). The microfibrils in the primary cell wall are also generally considered to be thinner and contain a lower degree of crystallinity than in the secondary wall (McNeil *et. al.*, 1984).

The secondary cell wall is formed after the initial period of rapid expansion and is required to provide more strength than flexibility. As a result the cellulose microfibrils are packed in tighter and parallel to each other (O'Sullivan, 1997). The

parallel packing of microfibrils in the secondary layer is important for providing compressive strength to the cell wall. Hence the orientation of these parallel microfibrils have an impact on the observed mechanical properties (Burgert *et. al.*, 2004). Because it is the thickest layer and contains the most cellulose the S2 layer is considered to have the greatest contribution to the mechanical properties of the cell wall.

In this S2 layer the orientation of the microfibrils is so important it is routinely measured as the angle relative to the fibre axis (termed the microfibril angle, or MFA). The microfibril angle has been linked to the direction of the microtubule network (Kobayashi *et. al.*, 1988).The MFA of the S2 layer will be discussed in more detail in Chapter 2.3.5 Measurement of the Microfibril Angle. For now it is sufficient to say that the microfibrils are highly orientated in the S2 layer and this orientation is correlated to the mechanical properties of the cell wall (Cave and Walker, 1994).

The MFA is a highly variable parameter with differences being observed not only between species, but also between samples of a particular species and even within a sample (Lichteneggar *et. al.*, 1999). This variation in MFA is often considered in terms of a variation in the mechanical properties and Lichteneggar *et. al.* based their model on three common loading conditions to do with the external factors influencing tree development.

The variation in MFA within a sample is acknowledged in x-ray measurements of the parameter by reporting the value as the mean of all values from the cell walls illuminated in the incident beam (Cave, 1969). As there is a mean value obtained from x-ray measurements there must be a variance within this value. This aspect was explored in greater detail by Evans and it was shown that the variance is made up of a number of experimental factors that contribute to the value of the MFA if it were to be zero (Evans, 1999).

While X-ray diffraction methods consider the interaction between the crystalline cellulose microfibrils and the amorphous matrix of the cell wall, small angle scattering studies are based on the difference between scattering length densities. The system is dominated by the greatest difference observed and in the case of woody

tissue this is between the ordered cellulose microfibrils and the voids present used for the transportation of water and minerals (Jakob *et. al.*, 1994). In neutron scattering experiments the scattering length difference with these voids becomes more prominent (Garvey *et. al.*, 2006).

Although the focus here has been on cellulose it is important to remember that the cell wall is a complex mix of polysaccharides and proteins. The fact cellulose is a crystalline material and the majority of the rest of the cell wall is not makes it an ideal system for various diffraction and scattering experiments (specifically using x-rays). However any observations or results from these physical methods as they pertain to the crystalline microfibril must always be placed into the broader biological context of the cell wall.

2.3 The Theory of X-Ray Diffraction

Diffraction can refer to any number of phenomena observed when a wave interacts with an obstacle. In order for diffraction to be observed the wavelength of the incoming wave must be on the same order of magnitude as the size of the obstacle. For a crystal lattice the lattice planes act as a diffraction grating so incident waves with a wavelength on the order of the atomic spacing are required for diffraction. X-ray wavelengths can vary greatly, however for x-ray diffraction (XRD) experiments only those between 0.5 Å and 2.5 Å are typically considered. In lab based instruments, the generation of x-rays is typically achieved with an x-ray tube. This evacuated tube contains an anode which is bombarded with high energy electrons generating x-rays. Different types of anodes are used to produce different properties in the emitted radiation. Typically a copper anode is used in crystallographic studies; however cobalt and molybdenum are also used.

XRD experiments typically measure the intensity of coherently scattered x-rays from the crystal lattice. The repeating lattice results in a very specific geometry for the interaction of incident and diffracted waves. This geometry (Figure 2-1) can be described by the Bragg condition for diffraction as described in equation (2.1)

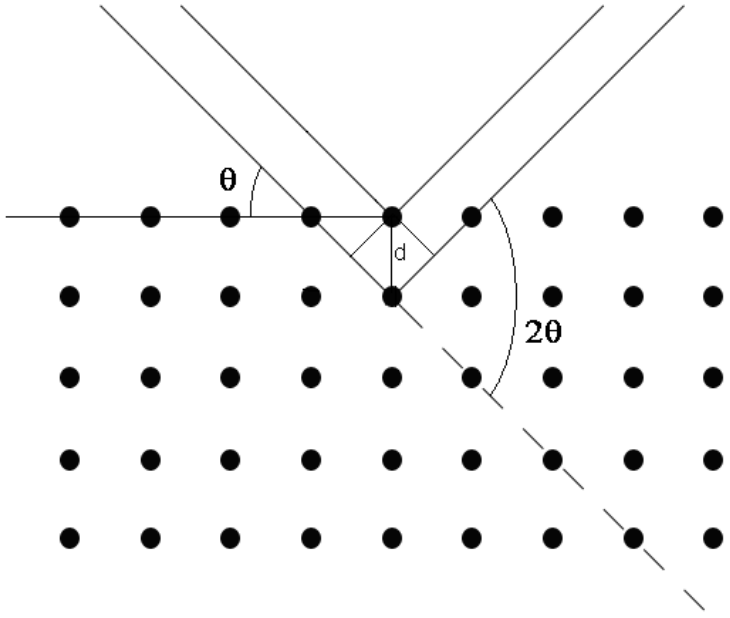

Figure 2-1 - The geometry of incident x-rays at an angle θ being diffracted from a crystal lattice with a lattice spacing d.

A wave incident at an angle θ will interact with a crystal lattice with atomic spacings, *d*, to diffract coherent x-rays at an angle 2θ. The condition for this interaction was developed by W.L. Bragg and W.H. Bragg in 1913 (Guinier, 1963).

$$\lambda = 2d_{hkl} \sin\theta \qquad (2.1)$$

Where λ is the wavelength of the incident radiation and *hkl* refer to the specific crystal plane. This has proven to be a particularly powerful equation for the investigation of crystal structures and is routinely used to determine the spacing's between planes. There are many crystallographic planes in a cellulose microfibril. However typical diffraction experiments show five prominent Bragg peaks attributed to cellulose Figure 2-2. These correspond to the five major crystallographic planes often discussed when investigating the crystal structure of cellulose Figure 2-3.

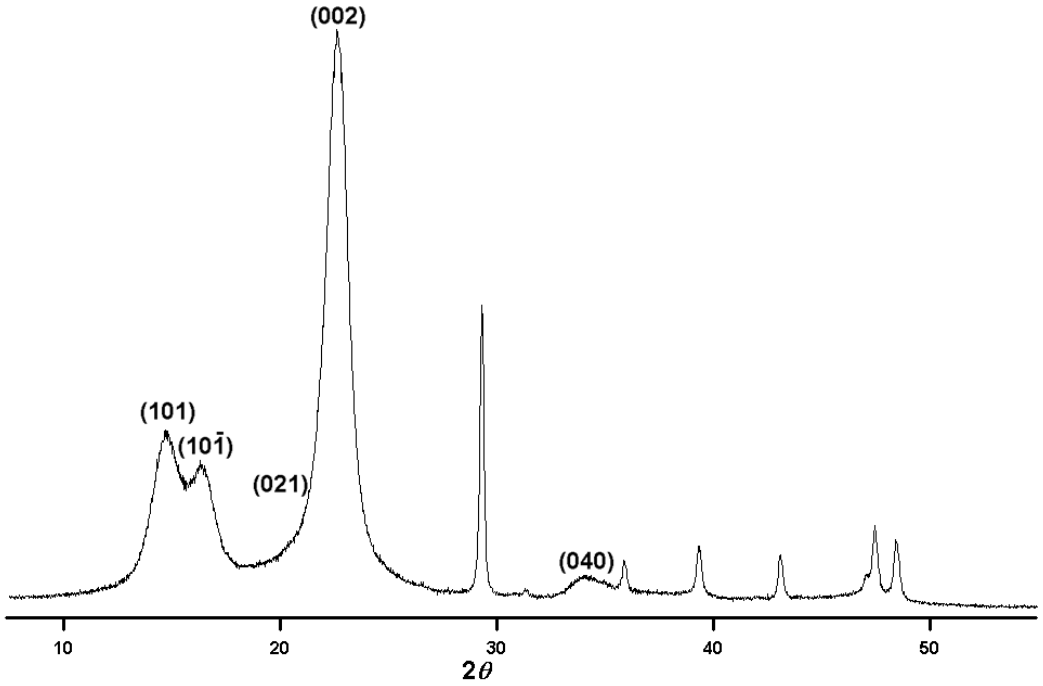

Figure 2-2 - A typical diffraction pattern collected from a cellulosic material (filter paper). Cellulose peaks (2θ = 14.75°, 16.40°, ~20°, 22.67° and 34.08°) have been labelled.

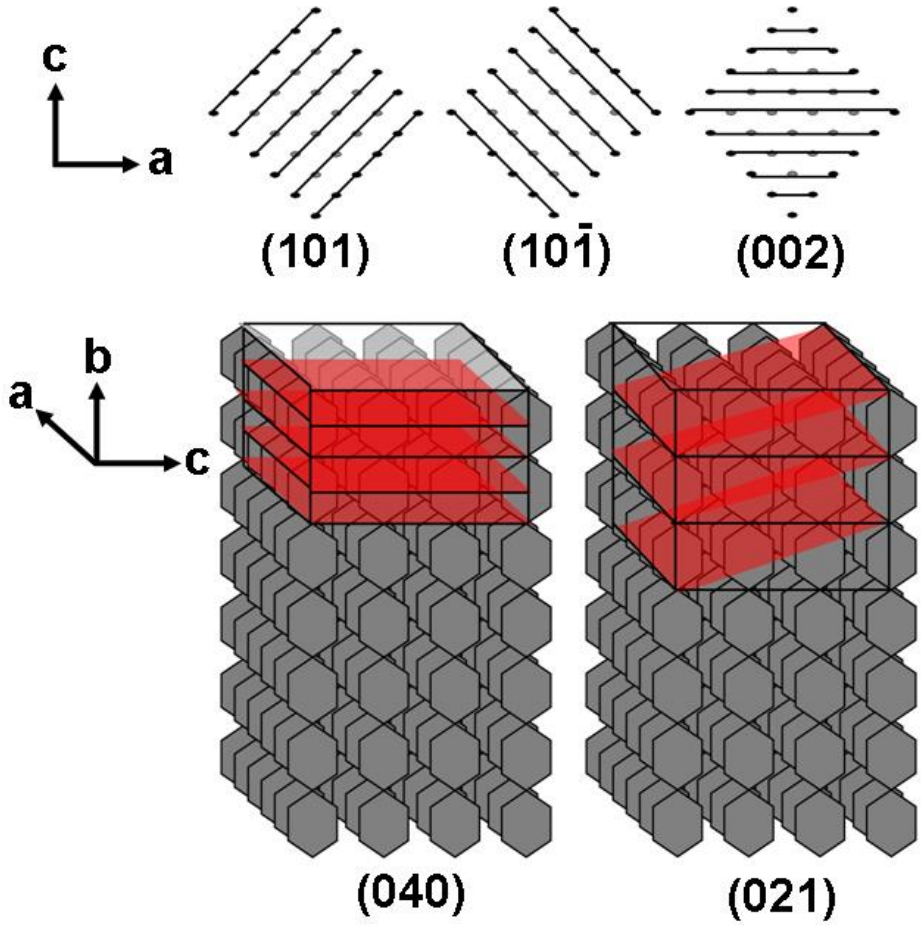

Figure 2-3 – The five major reflections observed in a cellulose microfibril (Newman, 1999).

In Figure 2-2 the cellulose peaks are noticeably broader than those belonging to the binder in filter paper, calcium carbonate (calcite). The peaks are so broad that the (021) reflection cannot be distinguished in this pattern due to the size of the (002) peak. Deconvoluting the diffraction pattern into component peaks is one of the major challenges encountered in the analysis of XRD data from cell wall materials.

XRD experiments measure the intensity of scattered x-rays as a function of the angle. An XRD experiment is usually set up in one of two geometries, reflection (Bragg-Brentano) and transmission (Debye-Scherrer). The Bragg-Brentano geometry is typically used for powder samples and provides the user with one dimensional data of intensity as a function of the scattering angle, $I(2\theta)$. An example of a typical experimental set up is shown in Figure 2-4.

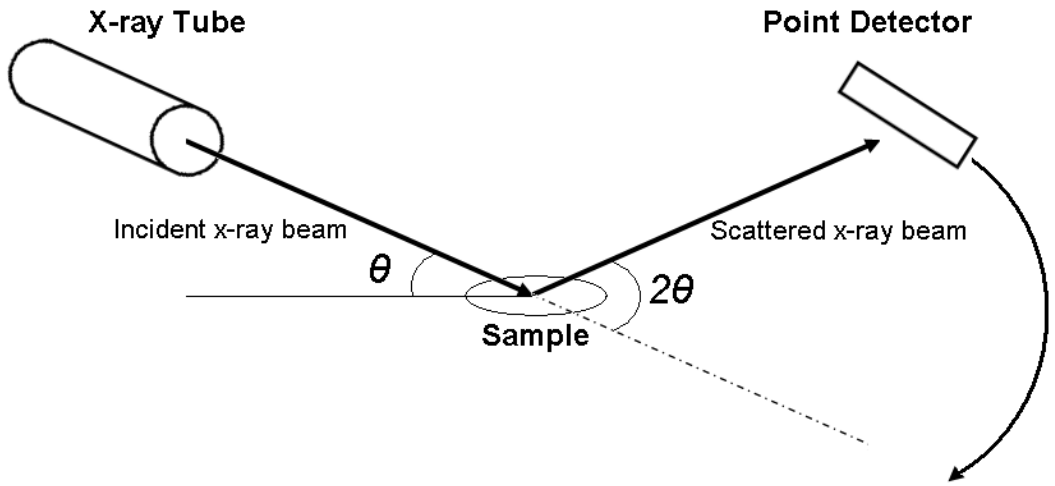

Figure 2-4 – A schematic diagram of the Bragg-Brentano experimental geometry used for powder diffraction experiments. The point detector sweeps out an angle to measure intensity as a function of 2θ over a pre-determined angular range.

The Debye-Scherrer experimental set up (Figure 2-5) uses an incident x-ray beam to pass through the sample and measure the position and intensity of diffracted x-rays on a two dimensional detector behind the sample.

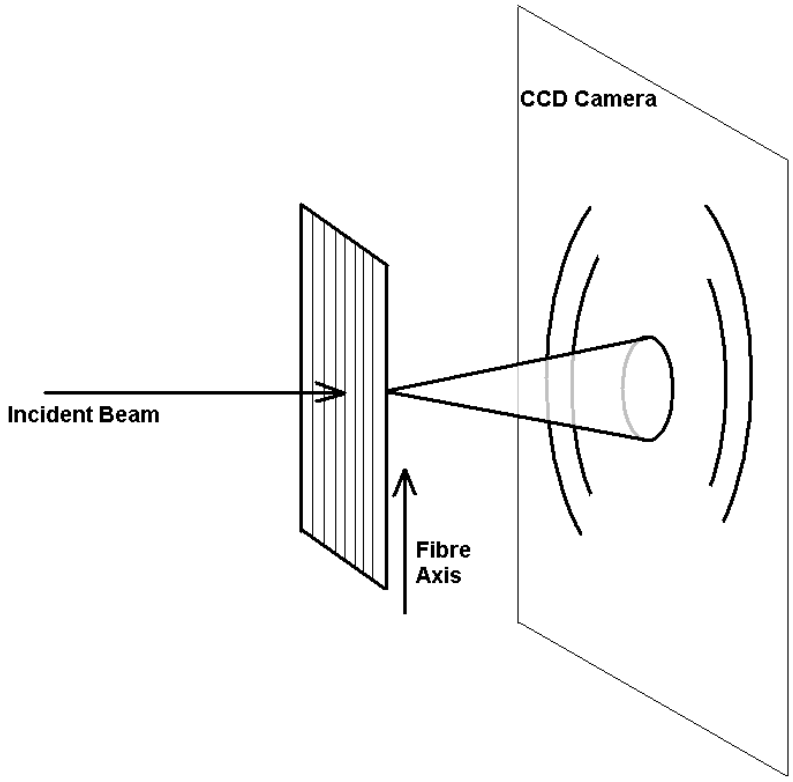

Figure 2-5 – A schematic diagram of the Debye-Scherrer experimental geometry. If the sample is isotropic then symmetric diffraction rings will be observed on the two dimensional detector. However typical cellulosic materials tend to be anisotropic resulting in partial diffraction rings as indicated (Liss *et al.*, 2003).

The two dimensional data typical of cellulosic materials can be reduced to one dimensional data in 2θ by averaging in the radial direction. The result is Intensity as a function of 2θ. However the reduced data needs to be considered carefully if there is any texture in the sample as this can influence the one dimensional pattern. This allows the data to be more easily analysed in terms of the lateral dimensions of the microfibril. For an anisotropic piece of data averaging can be performed around a particular 2θ value (or 2θ range) to obtain the azimuthal average. This average is used to quantify the degree of orientation in the sample and in the case of cell wall materials to determine the MFA.

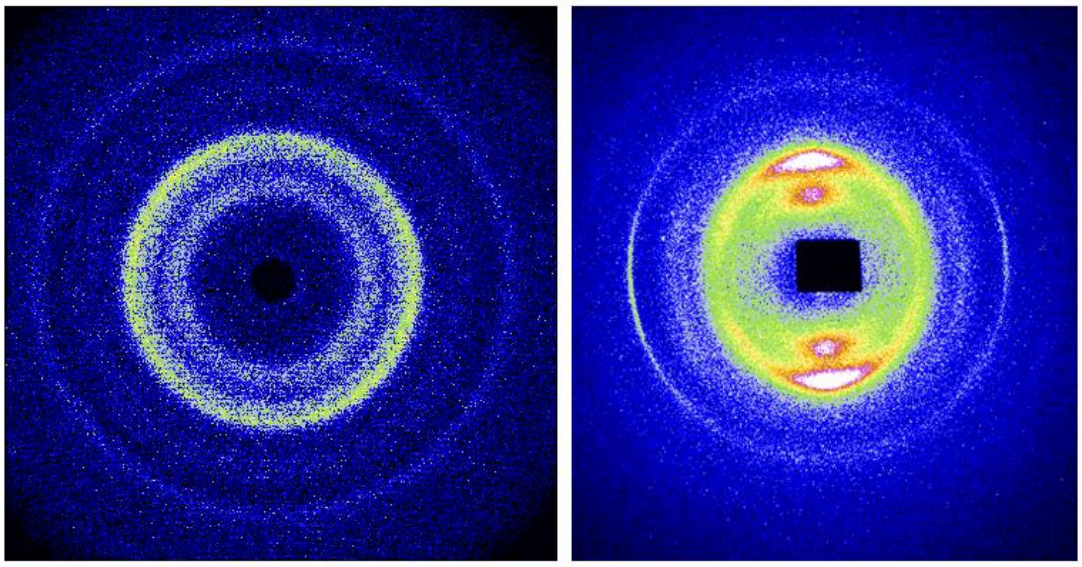

Figure 2-6 – The data that is typically obtained from an isotropic sample on the left (filter paper) and an anisotropic sample on the right (wood). In isotropic samples the data appears as symmetric rings while anisotropic data can produce streaks, partial rings or dots depending on the particular type of preferential orientation present.

2.3.1 Separating Instrumental Broadening

In an ideal experiment, the sample is a perfect single crystal and is exposed to monochromatic radiation with perfectly defined experimental parameters. The results of such an experiment were considered by many in the early days of XRD, including Darwin and Ewald (Klug and Alexander, 1974). The theoretical Darwin profiles proposed for perfect crystals are very closely approached for refined samples of highly crystalline materials such as diamond, however more coarse samples such as rock salts deviate to a much greater extent.

For a polycrystalline sample, such as cellulose, the broadening of Bragg peaks is a convolution of several different effects. The observed profile is considered to be defined as $h(\varepsilon)$, where $\varepsilon = 2\theta - 2\theta_B$ and $2\theta_B$ is a Bragg angle. The observed profile can thus be written as in equation (2.2).

$$h(\varepsilon) = \left(w(\varepsilon) \otimes g(\varepsilon)\right) \otimes f(\varepsilon) + b \qquad (2.2)$$

Here $w(\varepsilon)$ is the function related to the spectral effects of the incident radiation, $g(\varepsilon)$ is the instrumental function and $f(\varepsilon)$ is the specific specimen profile. This convolution is superimposed on the background, b (Snyder *et al.*, 1999).

Separation of the instrumental contribution to broadening from the specimen contribution is not a trivial task. The most straight forward approach to the problem requires extensive knowledge of the instrumental parameters, known as the fundamental parameters approach (Alexander, 1954). In the fundamental parameters approach, the instrumental function is a convolution of the emission profile and each component of the instrument. Although each of the instrumental components contribute varying amounts of broadening, each will broaden a given Bragg peak for the same reason, that is the dispersion of energy from the incident beam (Cullity, 1967).

The direct convolution method makes use of a standard material which contains ‘infinite’ crystallites with no internal strain. This material will therefore show broadening only from the instrument. Given that no real material contains infinite crystallites or zero strain, there will always be some broadening from the size and strain of the sample, small though it may be. This results in an overestimate of the instrumental function (Cheary and Coelho, 1998).

The third method for separating the instrumental broadening of a diffraction pattern is the Stokes Deconvolution. This makes use of the properties of the Fourier transform to simplify the convolution integral. If equation (2.2) is considered with the spectral and instrumental functions combined as $g(\varepsilon)$, then there is

$$h(\varepsilon) = g(\varepsilon) \otimes f(\varepsilon) \tag{2.3}$$

Here, *g(ε)* is the function related to the spectral effects of the incident radiation and the instrumental function, *f(ε)* is the sample specific profile and ε is defined as above in equation 2.2. Equation (2.3) can be rewritten as the convolution integral

$$h(\varepsilon) = \int_{-\infty}^{\infty} g(s) f(\varepsilon - s) ds \tag{2.4}$$

In equation (2.4), *s* is a dummy variable for convolution used to facilitate the operation. The Fourier transform of the convolution integral yields equation (2.5).

$$H(\xi) = G(\xi) \cdot F(\xi) \tag{2.5}$$

The use of capital letters in equation (2.5) for *H(ξ)*, *G(ξ)* and *F(ξ)* denotes the same functions as *h(ε)*, *g(ε)* and *f(ε)* but in the Fourier domain. In the Fourier domain equation (2.5) can thus be rewritten so that the pure specimen, *F(ξ)* is a quotient of the observed line profile, *H(ξ)* and the instrumental profile, *G(ξ)* with ξ being the inverse variable to ε (Klug and Alexander, 1974).

$$F(\xi) = \frac{H(\xi)}{G(\xi)} \tag{2.6}$$

And taking the inverse Fourier transform of equation (2.6)

$$f(\varepsilon) = \frac{1}{\sqrt{2\pi}} \int_{-\infty}^{\infty} \frac{H(\xi)}{G(\xi)} \exp(-2\pi \cdot i \cdot \varepsilon \cdot \xi) d\xi \tag{2.7}$$

The solution to such a Fourier integral is not trivial so substitutions and the expansion of the integral to a sum aid in simplifying the system. Importantly, the limits of integration can also be changed to a finite value to reflect the *2θ* range (Klug and Alexander, 1974).

2.3.2 The Warren-Averbach Method

The extraction of the instrumental broadening from the measured diffraction patterns needs to be performed before any analysis of the data can take place. The separation of size and strain contributions to peak broadening is a routine that is commonly undertaken when analysing one dimensional $I(2\theta)$ profiles. However the terms size and strain need to be used with care when used in the context of XRD experiments. Size broadening typically describes domain size which can be defined by any structure resulting in coherent diffraction (e.g. stacking, dislocation ordering, grain boundaries and lattice defects). Hence, the X-ray domain size does not necessarily correspond to particle or grain size, such as those measured by microscopic means (Snyder *et al.*, 1999).

Strain broadening is sometimes a difficult concept to visualise. It is easiest to imagine the phenomena in the context of a metallic sample. Deformation in the metal produces an array of dislocations, ordered such that the crystallites are divided into smaller domains which scatter incoherently. The ordered dislocations induce a strain within the domains and result in a broadening of the Bragg peak. For non-metallic samples, the source of the strain varies and in many instances the effects of this phenomena are so small compared to the effect of size broadening they can be ignored as negligible. However what can be considered 'negligible' is often not known until after analysis (Snyder *et al.*, 1999).

The Warren-Averbach method (Warren, 1969) was developed for investigation of distortions in metals using XRD results. It has since been applied to other strained materials with and without small crystallite effects (Klug and Alexander, 1974). Similar to the Stokes deconvolution for separating instrumental broadening, the Warren-Averbach method makes use of the unique properties of the Fourier transform. There are a number of assumptions about the method which are made. One is that the crystal (either above or below the size broadening limit) is composed of smaller domains, and these domains are made up of unit cells. For any given crystallographic plane (*hkl*), the size obtained (column height) is equivalent to the height of a column of cells perpendicular to the given plane (Snyder *et al.*, 1999).

The derivation of the Fourier series representation of an intensity profile for a diffraction experiment is based on the assumption that a large crystal has been broken down into smaller diffracting domains. The derivation of this Fourier transform is given in Appendix One. The major result obtained is given in equation (2.8) below

$$P'(2\theta) = \frac{KNF^2}{\sin^2\theta} \sum_{n=-\infty}^{\infty} \{A_n \cos(2\pi \cdot n \cdot h_3) + B_n \sin(2\pi \cdot n \cdot h_3)\} \qquad (2.8)$$

In this equation, K and N (defined in full in Appendix One) is a collection of constants and the number of cells in the sample respectively. However the important parts of this equation are the Fourier coefficients.

$$A_n = \frac{N_n}{N_3} \langle \cos(2\pi \cdot l \cdot Z_n) \rangle \quad ; \quad B_n = -\frac{N_n}{N_3} \langle \sin(2\pi \cdot l \cdot Z_n) \rangle \qquad (2.9)$$

Here, N_n is the average number of n pairs in the same column throughout the sample and N_3 is the average number of cells per column of unit cells (Klug and Alexander, 1974). Also, l is the order of reflection and Z_n is the distortion component. Within these Fourier coefficients are the size and strain components of the broadening due to the sample.

The coefficient A_n is a product of N_n/N_3, dependent on the column length and hence a size component, and $\langle \cos(2\pi.l.Z_n) \rangle$, which depends only on the distortion in the domain and hence a strain component.

$$A_n^S = \frac{N_n}{N_3} \quad ; \quad A_n^D = \langle \cos(2\pi \cdot l \cdot Z_n) \rangle \qquad (2.10)$$

Where A_n^S is the portion of the Fourier coefficient related to size and A_n^D is the portion related to the distortion (or strain).

$$A_n = A_n^S \cdot A_n^D \qquad (2.11)$$

As A_n contains the components for size and strain as a product, this is sufficient to perform the separation, and the coefficient B_n is not needed (Klug and Alexander, 1974). From equation (2.10) it can be seen that the size component of the coefficient is independent of l, the order of reflection, while the strain component is dependent on this variable. Also it should be noted that A_n^D approaches unity as l goes to zero, so setting l and n as sufficiently small that $l.Z_n$ is also small equation (2.12) is obtained.

$$\left\langle \cos(2\pi \cdot l \cdot Z_n \right\rangle \rightarrow 1 - 2\pi^2 \cdot l^2 \left\langle Z_n{}^2 \right\rangle \tag{2.12}$$

$$\ln\left\langle \cos(2\pi \cdot l \cdot Z_n \right\rangle = \ln(1 - 2\pi^2 \cdot l^2 \left\langle Z_n{}^2 \right\rangle) = -2\pi^2 \cdot l^2 \left\langle Z_n{}^2 \right\rangle \tag{2.13}$$

Equation (2.13) is obtained by taking natural logarithms of equation (2.12) for small values of l and n. Therefore taking the natural logarithm of equation (2.9) with the appropriate substitutions results in equation (2.14) (Klug and Alexander, 1974).

$$\ln\left|A_n(l)\right| = \ln\left|A_n{}^S\right| - 2\pi^2 \cdot l^2 \left\langle Z_n{}^2 \right\rangle \tag{2.14}$$

Part of the Warren-Averbach method relies on the set up of a crystallite as an array of unit cells as in Figure 2-7. In this figure, the length of ordered columns of cells along a given crystallographic direction (a_3) can be calculated as the addition of n number of cells.

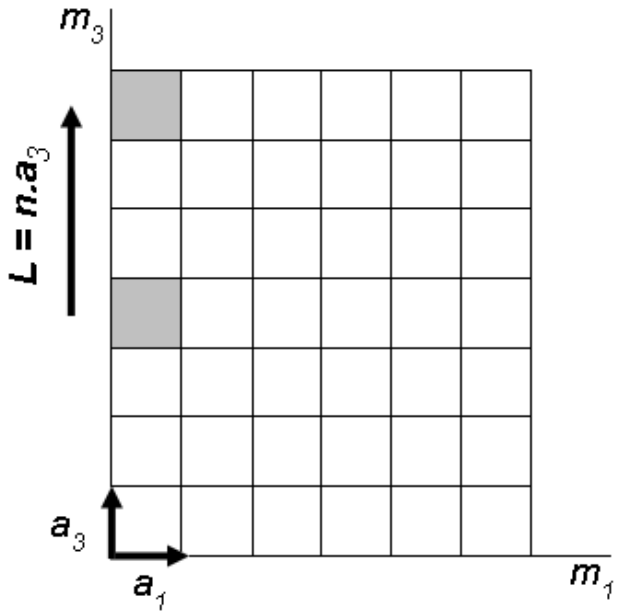

Figure 2-7 - The representation of a crystal as an array of cells as suggested by Warren (Warren, 1969)

If a strain is considered to be distorting this column, then that column length will change proportional to the strain (Klug and Alexander, 1974). So in this case it can be seen that

$$L = n \cdot a_3 \rightarrow \Delta L = a_3 \cdot Z_n \text{ given the distortion } \delta_m = Z_m \cdot \vec{a}_3 \qquad (2.15)$$

Now the fact that the strain in a_3 can be written as $\varepsilon_L = \frac{\Delta L}{L}$ allows the rewriting of equation (2.14) as

$$\ln A_L \frac{1}{d} = \ln A_L{}^S - \frac{2\pi^2 \left\langle \varepsilon_L{}^2 \right\rangle L^2}{d^2} \qquad (2.16)$$

Practically, the use of the Warren-Averbach method is accompanied by the use of Stokes deconvolution to determine the instrumental broadening. This is convenient as both methods involve a Fourier series; hence the coefficients found in the Stokes deconvolution for instrumental broadening equation (2.7) can be applied to equation (2.9).

2.3.3 The Integral Breadth Method

The integral breadth of a diffraction line is defined as the integrated intensity over the maximum intensity. This is best visualised as the width of a rectangle with the same height and area as the observed line (Cullity, 1967). The method of integral breadths depends on some assumptions regarding the profile shape of each broadening component. Once an appropriately shaped function has been fit to diffraction data using a best fit approach the parameters that define the said function are used to determine the size and strain components of the broadening (Klug and Alexander, 1974).

The definition of the integral breadth for a given diffraction peak is given in equation (2.17) (Klug and Alexander, 1974).

$$\beta = \frac{1}{I_P}\int I(2\theta)d(2\theta) \qquad (2.17)$$

Here I_P is the intensity of the given peak and $I(2\theta)$ is the intensity of the diffraction line as a function of 2θ. In a similar way to the diffraction profile being a convolution of the instrumental and sample profiles, the size component and strain component of the sample broadening can be convoluted together.

$$f(\varepsilon) = \int h_S(s)h_D(\varepsilon - s)ds \qquad (2.18)$$

The previously defined $f(\varepsilon)$, s and ε are reused here as for instrumental broadening ($f(\varepsilon)$ being the sample specific profile in equation (2.4). Now h_S and h_D are introduced as the functions of size and strain (or distortion) respectively.

Now that separate functions have been set up for the size and strain components to the peak width, the assumptions about the profile shape needs to be made. It is generally accepted that a purely size broadened peak will be strongly Lorentzian and a purely strain broadened peak will be strongly Gaussian (Klug and Alexander, 1974). However it needs to be remembered that diffraction peaks are very rarely ever

strictly Gaussian or strictly Lorentzian so a new function needs to be introduced which contains characteristics of both. The Voigt function is defined as a convolution of a Gauss function and a Lorentz function (Langford, 1978). The Langford development of the Voigt function starts with the familiar convolution integral

$$I(\varepsilon) = \int_{-\infty}^{\infty} I_L(s) I_G(\varepsilon - s) ds \tag{2.19}$$

With

$$I_L(\varepsilon) = I_L(0) \frac{{w_L}^2}{{w_L}^2 + \varepsilon^2} \quad ; \quad I_G(\varepsilon) = I_G(0) \exp\left(\frac{-\pi\varepsilon^2}{{\beta_G}^2} \right) \tag{2.20}$$

While Langford uses *x* and *u* for the convolution variables, the more familiar ε and *s* are used here with their usual meanings. The appearance of the terms β_G and w_L are most important as these are the width parameters for the Gaussian and Lorentzian components respectively, with $2w_L = \frac{2}{\pi} \cdot \beta_L$. As with other convolution integrals, the use of the Fourier transform can simplify the situation, so taking the transform of equation (2.20) gives

$$I'_L(s) = \beta_L \cdot I_L(0) \cdot \exp(-2\beta_L \cdot s) ; I'_G(s) = \beta_G \cdot I_G(0) \cdot \exp(-\pi \cdot {\beta_G}^2 \cdot s) \tag{2.21}$$

And using these as the basis of the transform of equation (2.19)

$$I'(s) = I'_L(s) I'_G(s) = \beta_L \beta_G I_L(0) I_G(0) \cdot \exp(-2\beta_L s - \pi {\beta_G}^2 s^2) \tag{2.22}$$

In this equation *I'(s)*, $I'_L(s)$ and $I'_G(s)$ represent the Fourier transformations of equations (3.19) and (3.20). Taking the inverse transform of equation (2.22)

$$I(\varepsilon) = \mathrm{Re}\{\beta_L I_L(0) I_G(0) \cdot \exp[k^2(1-iy)^2] \cdot erfc[k(1-iy)]\} \tag{2.23}$$

Where $k = \frac{\beta_L}{\pi^{1/2}\beta_G}$ and $y = \frac{\pi \cdot x}{\beta_L}$. The inclusion of the complementary error function (*erfc*) in equation (2.23) as a result of the inverse Fourier transform of equation (2.22) may seem to complicate matters. In fact the properties of this function, and its relationship to the complex error function (specifically $w(s) = e^{-s^2} erfc(-i \cdot s)$ where *w(s)* is the complex error function) allow for a reduced and explicit definition of the Voigt profile in terms of the Lorentz and Gauss parameters (Langford, 1978).

$$I(\varepsilon) = \mathrm{Re}\left(\beta_L I_L(0) I_G(0) \cdot w\left[\frac{\pi^{1/2} x}{\beta_G} + ik \right] \right) \tag{2.24}$$

There is an important result from this equation and from equation (2.22) for evaluating the breadth of the Voigt profile.

$$A = I'(0) = \beta_L \cdot \beta_G \cdot I_L(0) \cdot I_G(0) \tag{2.25}$$

$$I(0) = \beta_L \cdot I_L(0) \cdot I_G(0) \cdot w[ik] = \beta_L \cdot I(0) \cdot I(0) \cdot \exp(k^2) \cdot erfc(k) \tag{2.26}$$

Combining the results of equation (3.25) and (3.26) the form of the integral breadth is

$$\beta_V = \beta_G \cdot \frac{\exp\left(\frac{-1}{\pi} \left(\frac{\beta_L}{\beta_G} \right)^2 \right)}{1 - 2erfc\left(\frac{\beta_L}{\beta_G} \sqrt{\frac{2}{\pi}} \right)} \tag{2.27}$$

Here the parameter *k* from equation (2.23) has been substituted out so that the Lorentz and Gauss breadths can be observed (Langford, 1978) (Ruland, 1965). This result is rather unwieldy as a tool for analysis of diffraction data, so various approximations have been made (Halder and Wagner, 1966) (Schoening, 1965).

$$\frac{\beta_L}{\beta_V} = 1 - \left(\frac{\beta_G}{\beta_V} \right)^2 \tag{2.28}$$

Given these three unknowns, the Voigt breadth, the Lorentz breadth and the Gauss breadth, the contribution of size and strain can be obtained from the component Lorentz and Gauss functions. All that is required are relationships between size and strain and these breadth parameters.

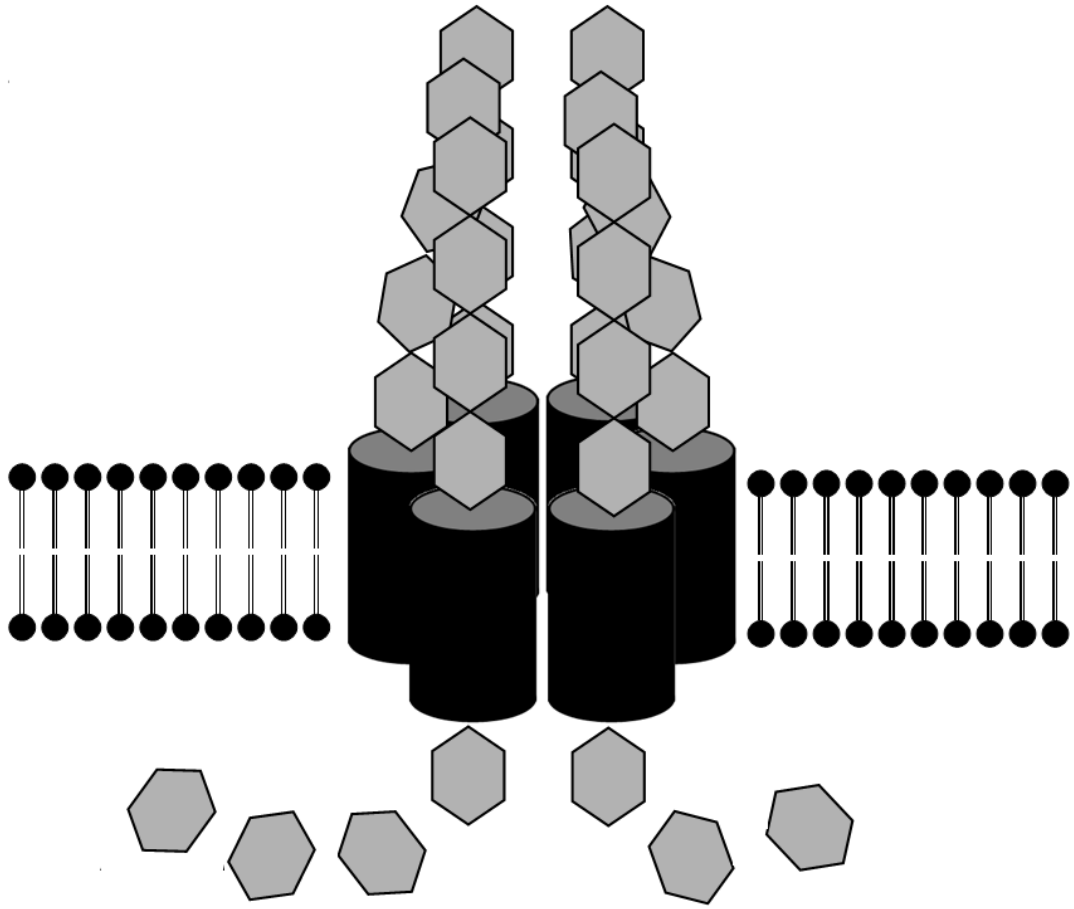

Figure 2-8 – A simplified schematic of free glucose rings (inside the cell) being polymerised into cellulose chains via the rosette complex.

In the synthesis of cellulose (Figure 2-8), many rosette complexes come together to polymerise many cellulose chains at once. As these chains are in close proximity a hydrogen bonding network can start to form almost immediately and as a result the synthesis of cellulose molecules also results in the synthesis of the cellulose microfibril (like those in Figure 2-3). This is an important point to consider when investigating the lateral dimensions of the crystallite from XRD data as the size of the microfibril is linked to the size of the rosette complexes formed (Delmer, 1987).

For a polycrystalline material, the grain size has an effect on the appearance of the diffraction pattern. If between 10 and 1 μm, the Debye rings can appear spotty, rather than continuous, and the level of 'spotty-ness' was used as a way to estimate the grain size (Cullity, 1967). Between 0.1 and 10 μm, there is no appreciable broadening of peaks due to size, so in this range XRD experiments are essentially insensitive to grain size. These boundaries are approximate and can be varied with the use of modern microbream experiments. The effects of crystal size are comparable to the phenomena of varying the size of diffraction gratings in optical diffraction (Guinier, 1963).

Individual crystals less than about 0.1 μm start to be labelled with the term 'particle', and so XRD experiments become concerned with determining particle size. Cellulose crystallites are an interesting case to consider as they are only a few nanometers in cross section (Garvey *et al.*, 2005a), well within the range to be considered a particle, but are up to 10 μm long.

The problem of determining particle size by XRD was approached by Scherrer who posed equation (2.29) (Cullity, 1967).

$$B = \frac{K\lambda}{t_{hkl} \cdot \cos(\theta)} \tag{2.29}$$

Here K is a shape factor, B is the full width half maximum in radians and t is the diameter of the crystal particle (Cullity, 1967). In the case of cellulose the (002) reflection (Figure 2-3) is well suited to the Scherrer equation as it has a single direction that corresponds to the lateral dimension of the microfibril. Other reflections, particularly those down the length of the microfibril and those which are heavily overlapped become harder to interpret.

The challenge when applying such an equation is to measure the breadth of the peak. This can often be simplified by the addition of a standard with a particle size greater than 0.1 μm and comparing the sample broadening to the standard broadening (Cullity, 1967).

Equation (2.29) was refined by Stokes and Wilson to be expressed in terms of the integral breadth rather than the FWHM (Klug and Alexander, 1974).

$$\beta_L(2\theta) = \frac{K\lambda}{t_{hkl} \cdot \cos(\theta)} \tag{2.30}$$

Here the integral breadth is used, $\beta_L(2\theta)$ (Stokes, 1948). Once the integral breadth from the Lorentzian component of the Voigt broadening has been determined it can be used in equation (2.30) to give the crystallite dimension. Similarly, an equation to relate the strain to the Gaussian component of the Voigt broadening has been developed. This equation was developed from the Bragg condition for diffraction, equation (2.1). If the maximum strain on a crystal is denoted *e*, then the lattice spacing will vary from $d(1+e)$ to $d(1-e)$ (Wilson, 1949). In addition to the varying of *d*, θ will vary over a numeric range equivalent to $2 \cdot e \cdot d \frac{\partial \theta}{\partial d} = 2e \cdot \tan(\theta)$. Wilson used these variations to define the maximum strain in terms of the integral breadth.

$$\beta_G(2\theta) = 4e \cdot \tan(\theta) \tag{2.31}$$

It is necessary to define an 'apparent strain', η.

$$\begin{aligned} \eta &= \beta_G(2\theta) \cdot \cot(\theta) \\ \beta_G(2\theta) &= \eta \cdot \tan(\theta) \end{aligned} \tag{2.32}$$

From equation (2.32) it should be clear that the apparent strain, η, is approximately four times the maximum strain. The problem of determining strain from broadening is not as satisfactory as the problem of crystallite size, but used in conjunction with each other the modelling of peak broadening by samples with sufficient contributions from size and strain broadening gives good results.

2.3.4 The Williamson-Hall Analysis

The Williamson-Hall analysis is based on the plots of Williamson and Hall in their investigation of aluminium and tungsten (Williamson and Hall, 1953). This form of analysis also makes use of the integral breadth, which is defined in Section 2.2.3. The contributions from crystallite size, strain and instrumentation can be separated if the peaks are Lorentzian or Gaussian in nature.

$$\begin{aligned} \beta &= \beta_S + \beta_D + \beta_I \\ \beta^2 &= \beta_S{}^2 + \beta_D{}^2 + \beta_I{}^2 \end{aligned} \qquad (2.33)$$

Where β is the experimentally observed peak breadth, β_S is the breadth due to size, β_D is the breadth due to strain and β_I is the breadth due to instrumentation. In equation (2.33) the top line shows the addidion of breadths for Lorentzian peaks while the second shows the addition of squares for Gaussian peaks (Klug and Alexander, 1974).

The Williamson-Hall analysis assumes a Lorentzian shape. Re-arranging the Scherrer equation (2.30) using the integral breadths form, equation (2.34) is obtained (Cullity, 1967).

$$\beta_L(2\theta)\cdot\cos(\theta) = \frac{\lambda}{d} \qquad (2.34)$$

Using equation (2.31) and the Bragg condition and the fact that strain can be defined as $\frac{\Delta d}{d}$ results in (Cullity, 1967).

$$\beta_L(2\theta)\cdot\cos(\theta) = -2\frac{\Delta d}{d}\sin(\theta) \qquad (2.35)$$

From this equation, the Williamson-Hall plot can be made with $\beta\cdot cos(\theta)$ plotted as a function of $sin(\theta)$, where β is the experimentally observed integral breadth with the

instrumental broadening removed and θ is the Bragg angle. From this graph it should become immediately obvious if there is significant strain broadening present as strain broadening is order of reflection dependent. If the Williamson-Hall plot is a horizontal line then only size broadening is significant.

The diffraction of x-rays by crystalline materials contains a great deal of information related to the microstructure of that material. To unlock this information it is clear that there are rather complicated procedures that have been developed over the last hundred years. Although almost every method discussed above was developed to aid in the analysis of metals, they can be applied generally to other materials undergoing analysis by XRD. While the theory of these methods has been developed here generally for application to any class of materials, the development of a model for the microfibril angle (MFA) is applied uniquely to cellulosics.

2.3.5 Measurement of the Microfibril Angle

Figure 1-3 is typical of softwoods (conifers). Hardwoods, while similar in the structure of the cell wall, have a more complex water and nutrient transport system occurring along the length of the fibre. This results in pores in the woody tissues of hardwoods. Although there are significant structural differences between hardwoods and softwoods, the model of a cell wall composed of layers of cellulose is adaptable to both hardwoods and softwoods for the purposes of considering microfibril orientation (Knox *et al.*, 2001).

In the model of the cell wall from a mature cell the thickest layer is the S2 layer (with the S2 thickness being a function of cell age), which is also the most highly orientated (Fengel and Wegener, 1989). The implications for such a model in a diffraction experiment are that the S2 layer influences the data to a greater extent than the others. However there will be contributions from the primary (isotropic), S1 (anisotropic) and S3 (anisotropic) layers to the diffraction (Knox *et al.*, 2001). These extra contributions are particularly noticeable in the transmission mode. The MFA is defined as the angle that S2 microfibrils make with the cell axis, as in Figure 2-9 (Meylan, 1967).

The anisotropic cell wall layers do not produce symmetric Debye-Scherrer rings for the 2θ values that satisfy the Bragg condition. In the case of cell wall materials the cellulose microfibrils are wound around the fibre axis. This results in Debye-Scherrer rings that are symmetric (Figure 2-6) as the microfibrils on one side of the cell are 180° out of phase.

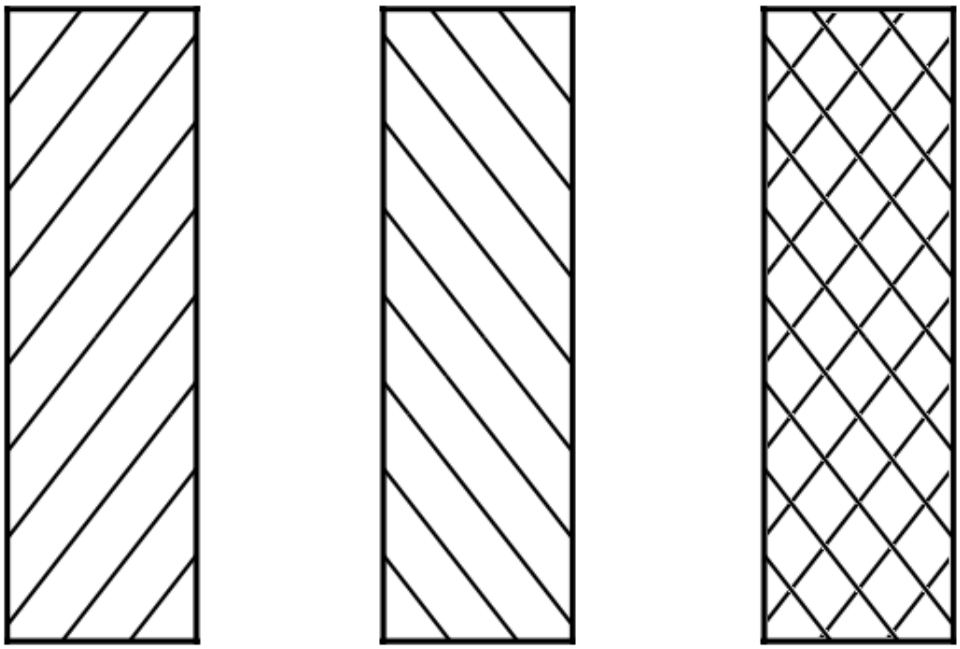

Figure 2-9 – A simplified view of the microfibrils in the S2 layer from the front (left) and back (centre) and with the two views superimposed on each other as when looking through the fibre (right).

XRD experiments require minimal sample preparation which makes it possible to collect a large amount of data in a short period of time. The theory of how to measure the MFA from X-ray data was developed in 1966 (Cave, 1966). In this paper a number of assumptions are made as to the geometry of the experimental set up and the shape of the cellular cross sections. This theory has undergone various forms of testing and revision with an experimental approach used to compare the results of the theory with more direct methods such as iodine stained microscopy (Meylan, 1967).

Some years later, Cave presented a substantial review of this theoretical work up and the revisions that have come since (Cave, 1997a, b). The x-ray beam in a typical diffraction experiment illuminates a number of tracheids in a single measurement. As

a result the calculation of mean MFA is used more often (except in specific experiments using microbeam x-ray diffraction) (Muller *et al.*, 2000a). The calculation of the mean MFA is considerably simpler than the solutions obtained from the rigorous tensor based approach of Cave (Cave, 1997a).

Typically when determining the MFA, the (040) reflection is desirable to use as this is the only reflection with components entirely in the direction of the microfibril axis. (Cave, 1966). However this is often poorly resolved, or not within the angular ranges of the experiment. The (002) is used more often to determine the MFA as it is the best resolved and most intense cellulosic peaks. If the intensity of (002) peak is observed as a function of the azimuthal angle (α) then two peaks will be observed (180° apart) in most cell wall materials, particularly those with an S2 layer (Figure 2-10). The width of these azimuthal peaks is denoted by the parameter *T*, which has been used to determine the mean MFA since the late 1960's (Meylan, 1967). It has been noted that there is a relationship between this parameter *T* and the MFA (equations 2.37 and 2.38).

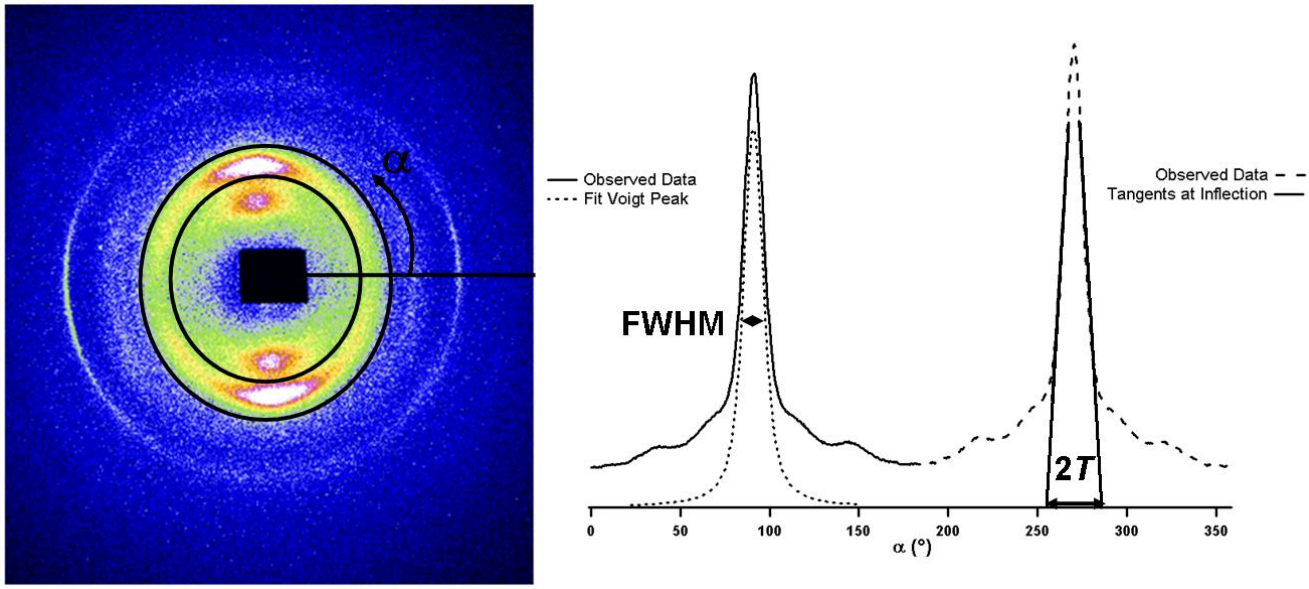

Figure 2-10 - Two dimensional data from a piece of *acacia* wood with data after azimuthal averaging. As noted the patterns are symmetric and have been used to show the two different ways to determine the width of the azimuthal peaks, FWHM and 2*T*.

The calculation of *T* would traditionally involve drawing a tangent to the point of inflection on each side of the peak. The distance between the resulting x-intercept of these two lines gives a value for 2*T*. This hand measured method is quite time

consuming and not particularly precise given the judgements that need to be made for the position of the inflection line. However the fitting of curves to the peak with computer packages makes the calculation of the full width half maximum (FWHM) quite simple, and this is easily related to the parameter *T* (equation 2.36) (Stuart and Evans, 1995).

$$T = \frac{FWHM}{\sqrt{2\ln(2)}} \tag{2.36}$$

$$MFA = 0.6 \cdot T \tag{2.37}$$

These equations can be used together to rapidly calculate the mean MFA from large volumes of data (Meylan, 1967). Stuart and Evans (1995) make use of equation 2.37 and also mention another equation that can be used for the rapid calculation of MFA from diffraction data. They report this other equation (2.38) to be a refinement by Yamamoto *et. al.* for MFA values from other wood species with small microfibril angles. Typically the 10° to 20° range shows good agreement between the two equations with Evans reporting differences of up to 2° in this range (Stuart and Evans, 1995).

$$MFA = 1.575 \times 10^{-3} T^3 - 1.431 \times 10^{-1} T^2 + 4.693T - 36.190 \tag{2.38}$$

The determination of the orientation of cellulose within the cell wall structure is an important part of any investigation into cellulosic microstructure. Together with the determination of crystallite sizes and strains, information from XRD experiments continue to give key structural information as input to the suite of analytical techniques currently available for cellulosic research.

2.4 The Theory of Small Angle Scattering

There is a reciprocal relationship between the size of a scattering centre and the scattering angle. That is to say, the smaller the scattering angle the larger the feature incident x-rays are scattered from. In order to better resolve the data obtained at small angles, the detector is placed some distance away from the scattering centre. This is because in the Debye-Scherrer geometry (Figure 3-4) the scattering angle that can be observed is determined by the distance of the detector from the sample (assuming the wavelength is constant). This idea can be best visualised if a Debye-Scherrer cone is considered with the same sized detector in various positions (Figure 2-11).

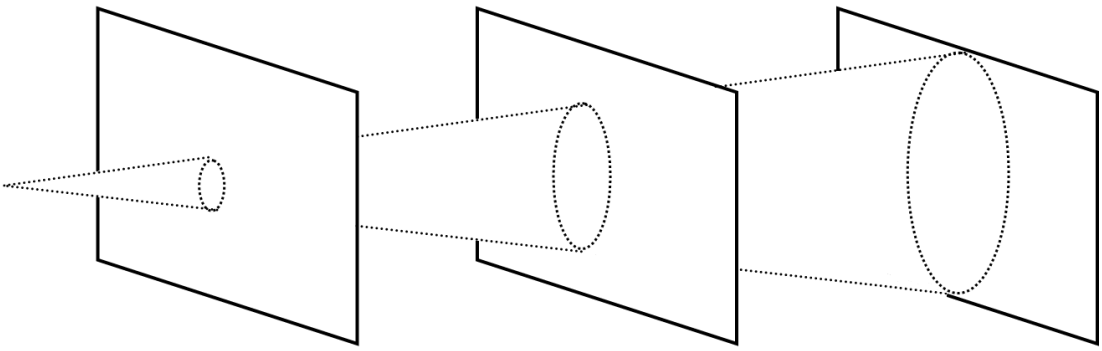

Figure 2-11 – A single Debye-Scherrer cone representing small scattering angle, where the detector size is kept constant and is moved further from the sample to show how the small angle becomes more prominent in the detector.

Small angle scattering data (from x-rays and neutrons) often needs to be compared even if the wavelength of the incident radiation is different. In order to do this a quantity related to the scattering angle needs to be introduced that will perform the same function as the scattering angle (2θ, as for XRD) but will not change if the wavelength is allowed to vary. The scattering vector is defined from the geometry of incident x-rays being scattered from a scattering body. The magnitude of this vector is determined from the scattering angle and the wavelength.

$$|\vec{q}| = q = \frac{4\pi \cdot \sin(\theta)}{\lambda} \qquad (2.38)$$

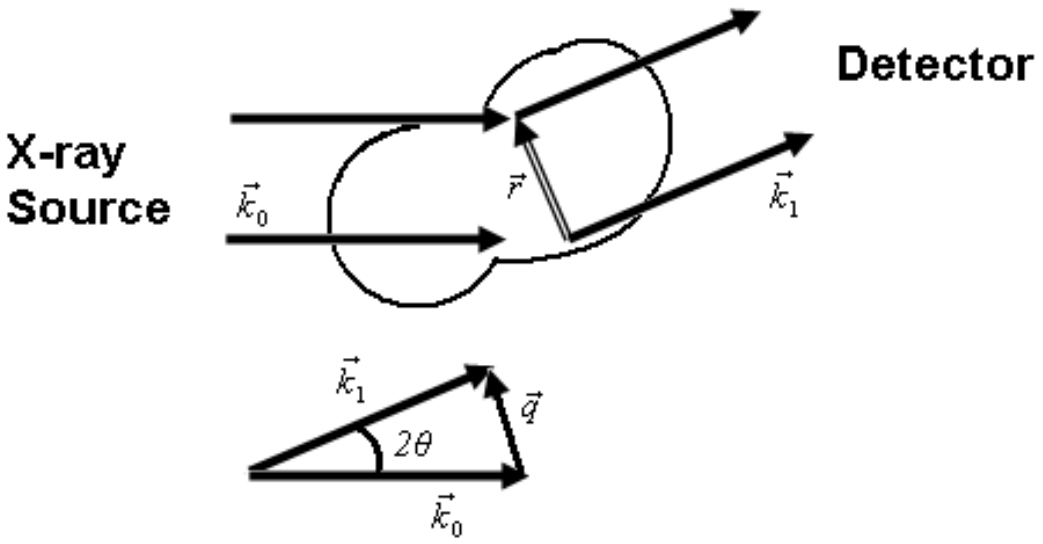

Figure 2-12 – An arbitrarily shaped scattering centre has incident x-rays ($\vec{k}_0$) scattered from it ($\vec{k}_1$). The angle between $\vec{k}_0$ and $\vec{k}_1$ is the scattering angle (2θ).

The geometric definition of the scattering vector, *q*, is therefore $\vec{q} = \vec{k}_1 - \vec{k}_0$. The interaction of interest in x-ray scattering is between the incident x-rays and the electrons (where as in neutron scattering it is between incident neutrons and the nucleus). In order to observe small angle scattering from x-rays there must therefore be an electron density difference in the region of 1 to 100 nanometres (in general). The challenge of small angle x-ray scattering is relating the observed scattering profile to the electron density distribution. The electron density distribution, $\rho(\vec{r})$, is related to the angle dependent scattering amplitude, $A(\vec{q})$, via a Fourier transform.

$$A(\vec{q}) = A_e \int_V \rho(\vec{r}) e^{-i\vec{q}\cdot\vec{r}}\, dV \qquad (2.39)$$

Here A_e is the scattering amplitude of a single electron and V is the volume irradiated by the incident beam. The scattering intensity of a single particle is the product of $A(\vec{q})$ and its complex conjugate $A(\vec{q})$*. Here, the Thomson formula for the electron scattering intensity, I_e, is required with I_O being the incident intensity of the beam (Guinier, 1963).

$$I_0(\vec{q}) = A(\vec{q}) \cdot A(\vec{q})^* = I_e \iint_{VV} \rho(\vec{r})\rho(\vec{r}')e^{-i\vec{q}(\vec{r}-\vec{r}')}dVdV' \quad (2.40)$$

$$I_e(\theta) = I_O \cdot 7.9\times10^{-30}\left(\frac{1+\cos^2(2\theta)}{2}\right) \quad (2.41)$$

Where the numerical factor is the square of the classical electron radius, $r_e = 2.818\times10^{-15}m$. Or else described as $r_e = \frac{1}{4\pi\varepsilon_0}\frac{e^2}{mc^2}$ where $\varepsilon_0 = 8.85\times10^{-12}Fm^{-1}$, $e = 1.602\times10^{-19}C$, $m = 9.11\times10^{-31}kg$ and $c = 3.0\times10^{8}ms^{-1}$.

These considerations of single particle scattering of an incident beam from a single electron are not very practical in light of the vast number of electrons present in a real sample. So assumptions about the system are used to make approximations for the scattering from real samples. In general it is assumed that there is no long range order between particles. That is to say that there is no correlation between particles over a large distance (large being relative to the size of the particles). The matrix in which the particles are embedded have a homogenous electron density ρ_0. The electron density difference between the matrix and the particles, $\Delta\rho = \rho - \rho_0$, is used to replace the electron density distribution used for a single particle in equations 2.39 and 2.40.

The structure of the cell wall discussed previously (Figure 1.6) is considered here in terms of the electron density of cell wall materials. The major cell wall components are cellulose, hemi-cellulose and lignin. The hemi-celluloses and lignins in a cell wall exists as the amorphous matrix in which cellulose microfibrils are arranged. There needs to be a contrast in electron density in the sample for scattering to be observed. This electron density difference term ($\Delta\rho$) appears in the intensity functions as a squared term (equation 2.48). The electron density of each phase in a material can be used to calculate a scattering length density (SLD) for these phases to determine what contrast, if any, is present.

$$SLD = \frac{\rho_M N_A}{M} \sum_i n_i b_i \qquad (2.42)$$

Where ρ_M is the macroscopic density, N_A is Avogadro's Number M the molecular weight, b_i is the scattering length of atom i and n_i is the number of atoms of type i (Guinier and Fournet, 1955). Using equation 2.42 the scattering length density of the major cell wall polymers can be approximated.

Cell Wall Component	Molecule for Calculation	C	H	O	Density (gcm^{-3})	SLD (cm^{-2})
Cellulose	Glucose	6	10	5	1.5	1.337E+11
Hemi-cellulose	Xylose	5	10	5	1.5	1.345E+11
Lignin	Paracoumaryl alcohol	9	10	2	1.5	1.343E+11
	Coniferyl alcohol	10	12	3	1.5	1.339E+11
	Sinapyl alcohol	11	14	4	1.5	1.334E+11

Table 2-1 – Calculated SLD density for the important cell wall components. The density of cell wall components from Fengel (1989).

The SLD values presented in Table 2-1 were calculated from the SASfit calculator (available at http://sasfit.ingobressler.net/manual/Overview under the creative commons licence). The cell wall components selected are all polymers with hemi-cellulose and lignin being chemically quite poorly defined. These materials contain a number of different monomer units in varying amounts. Xylose is always the most abundant monomer in hemi-cellulose although most other pentose rings are present. The three lignin monomers given in Table 2-1 are the most common monolignols but practically any phenolic compound can be incorporated into the structure. In general it would seem that the SLD is poorly sensitive to the range of cell wall chemistry.

The calculated SLD values for the different cell wall components show very little variation. This would suggest that there is limited contrast between these materials for the purposes of SAXS experiments. Not shown in the table is the SLD for another major component of cell walls, voids. The voids in the cell wall are areas where the SLD is essentially zero, gaps in between the cellulose microfibrils and the amorphous matrix. The SLD difference between the voids in the cell wall and any of the major cell wall components is significantly larger than even the largest difference between major components ($0.011 \times 10^{11} cm^{-1}$ between hemi-cellulose and one of the lignins). This would suggest that the scattering profile will be dominated by the

scattering from the voids in the cell wall rather than the cell wall materials themselves.

According to Guinier (1963) Dutch physicist Peter Debye stated that the average over all orientations leads to a fundamental formula.

$$\left\langle e^{-i\vec{q}\vec{r}} \right\rangle = \frac{\sin(qr)}{qr} \tag{2.43}$$

Using this relation, then equation 2.40 can be written as

$$I_0(q) = 4\pi V \int_0^\infty \gamma(r) \frac{\sin(qr)}{qr} r^2 dr \tag{2.44}$$

Here $\gamma(r)$ is the correlation function (also known as the characteristic function). This equation is the most general form of the scattering pattern that assumes no long range order and a homogenous electron density difference. The correlation function is routinely obtained from an inverse Fourier transform of the scattering intensity.

$$\gamma(r) = \frac{1}{2\pi^2 V} \int_0^\infty I_0(q) \cdot q^2 \frac{\sin(qr)}{qr} dq \tag{2.45}$$

2.4.1 The Guinier Approximation

For a region of low q ($q.r << 1$), equation 2.43 can be simplified with a Taylor expansion

$$\frac{\sin(qr)}{qr} \cong 1 - \frac{(qr)^2}{3!} + \frac{(qr)^4}{5!} - \frac{(qr)^6}{7!} + \ldots \tag{2.46}$$

So equation 2.44 reduces to

$$I_0(q) = 4\pi \int \gamma(r)\left(1 - \frac{(qr)^2}{6} + \ldots\right) r^2 dr \qquad (2.47)$$

Guinier was the first to propose a solution to this problem in 1939 (Guinier & Fournet, 1955). He proposed that

$$I_0(q) = (\Delta n_e)^2 e^{\frac{-q^2 R_g{}^2}{3}} \qquad (2.48)$$

Here $(\Delta n_e)^2 = \Delta\rho^2 V^2$ where V is the volume of the particle (Glatter and Kratky, 1982). The radius of gyration (R_g) is introduced in this solution and is defined as the mean square distance from the centre of gravity, with the role of mass being played by electrons. The radius of gyration can be related to the correlation function (and hence the electron density distribution) though these are not trivial to determine.

$$R_g{}^2 = \frac{\int \gamma(r) r^4 dr}{2\int \gamma(r) r^2 dr} = \frac{\int \rho(\vec{s}) s^2 d\vec{s}}{\int \rho(\vec{s}) d\vec{s}} \qquad (2.49)$$

In equation 2.49 the vector $\vec{s}$ is defined as being from the centre of gravity for $\rho(\vec{r})$. For a homogenous particle, the radius of gyration is only dependent on the geometry of the particle. The Guinier approximation (equation 4.10) is remarkably accurate in the majority of cases. Only for very anisometric particles should it be replaced by another approximation (Glatter and Kratky, 1982). The approximation is very important in small angle scattering experiments as it is possible to obtain a value for R_g without any *a priori* knowledge of the particle size, shape or internal structure. Two shapes commonly encountered in small angle scattering are spheres and cylinders. The geometry of these rigid bodies are related to the radius of gyration below.

$R_g = \sqrt{3/5}\, r$; For a sphere of radius *r*. (2.50)

$R_g = \sqrt{\frac{r^2}{2} + \frac{H^2}{12}}$; For a cylinder or radius *r* and length *H*. (2.51)

2.4.2 Scattering From Cylindrical Particles

The scattering from cylindrical particles is a special case of small angle scattering. Cellulosic materials are often described as being composed of crystalline microfirbils, which are approximated by cylinders or rod-like particles. If a cylindrical particle is considered to have a radius *R* and a length *H* (Figure 2-13) then the form factor for randomly orientated particles with any ratio of *R* to *H* will be

$$P(q) = 4\int_0^1 \frac{J_1{}^2[q \cdot R\sqrt{(1-x^2)}}{\left[q \cdot R\sqrt{(1-x^2)}\right]^2} \cdot \frac{\sin^2(qHx/2)}{\left(qHx/2\right)^2} dx \qquad (2.52)$$

Here J_1 is a first order Bessel function. As noted previously the microfibrils of cellulose are highly orientated in the S2 layer of the cell wall. This will result in anisotropic small angle scattering being observed. This orientation in the sample is able to be observed and quantified in small angle scattering experiments as detailed below in Chapter 2.4.3.

There are two special cases that can be considered. The first is when the length is much greater than the radius ($H >> R$) which is useful in the modelling of long-stretched particles. The second is the reverse ($H << R$) which approximates flat disc like particles (Feigin and Svergun, 1987). As microfibrils are best approximated by rod-like particles (having lateral dimensions on the order of nanometres and a fibre length of micrometers) only the special case of $H >> R$ will be considered.

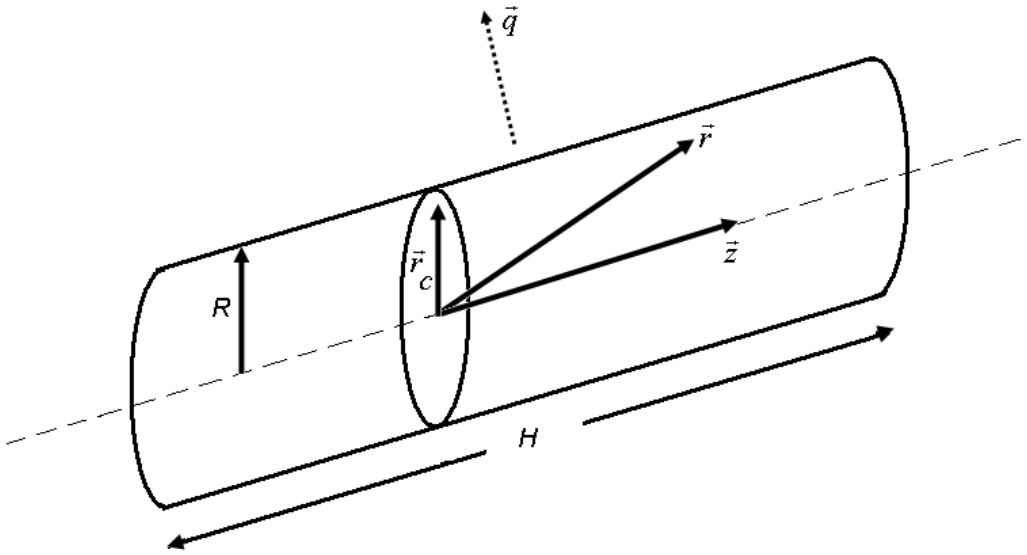

Figure 2-13 – The geometry of a cylinder radius *R* and length *H*. This case has *H* >> *R* although this geometry is consistent for any ration of *H* to *R*.

The use of cylinders for small angle scattering analysis is not restricted to rod-like crystallites, as for cellulose. Polymer chains, liquid crystals, materials with parallel stacking can all be modelled with cylinders (Feigin and Svergun, 1987). In such fluid systems, the use of a rigid bodied cylinder requires some special consideration. For the case of a cellular void, the crystallite is so stiff that such considerations often are not required.

The vector $\vec{r}$ in Figure 2-13 is made up of the component vectors in the radial and axial directions ($\vec{r} = \vec{r}_C + \vec{z}$). Splitting the vector into components allows the scattering amplitude derived from equation 2.52 to be written as a product of the two separate contributions.

$$F(q) = \Delta\rho \cdot \left[H \cdot \frac{\sin\left(qH\gamma/2\right)}{\left(qH\gamma/2\right)} \right] \cdot \left[\iint dA \cdot e^{-i \cdot q \cdot \vec{r}_C} \right] \tag{2.53}$$

In equation 2.53 the scattering contributions from the axial component vector and those from the radial component are in the first and second set of square brackets respectively. Here γ is used to denote the angle between the vectors $\vec{q}$ and the $\vec{z}$ in reciprocal space. Equation 2.53 can be rewritten as follows

$$F(q) = F_H(q) \cdot F_C(q)$$
$$F_H(q) = \frac{H \cdot \sin(q.H.\gamma/2)}{q.H.\gamma/2} \qquad (2.54)$$
$$F_C(q) = \iint dA \cdot e^{-i \cdot q \cdot \vec{r}_C}$$

The length factor can be given by

$$I_H(q) = \langle F_H(q) \rangle^2 = H^2 \int_0^1 \frac{\sin^2\left(q \cdot H \cdot \gamma/2\right)}{\left(q \cdot H \cdot \gamma/2\right)^2} d\gamma \cong H \cdot \frac{\pi}{q} \qquad (2.55)$$

The evaluation of equation 4.17 to $H \cdot \frac{\pi}{q}$ is only valid for situations in which $q \cdot H > 2\pi$ is satisfied. The remaining factor $F_C(q)$ is squared and averaged similar to $F_H(q)$.

$$I_C(q) = \langle F_C(q) \rangle^2 = (\Delta\rho)^2 \cdot \iint \iint dA_1 dA_2 \cdot e^{-i \cdot q \cdot \vec{r}_C} \qquad (2.56)$$

For the radial vector, the variation occurs in two dimensions, so the following substitution is applied

$$\left\langle e^{-i \cdot q \cdot \vec{r}_C} \right\rangle = J_0(qr_C); J_0(qr) = 1 - \frac{q^2 r^2}{4} + \ldots \qquad (2.57)$$

Substitution into equation 2.56 gives

$$I_C(q) = (\Delta\rho)^2 \cdot A^2 \cdot \left[1 - \frac{q^2 r^2}{4} + \ldots\right] \qquad (2.58)$$

Equation 2.58 is reminiscent of equation 2.47. In equation 2.47 the Guinier approximation was developed as a solution to the Taylor series expansion of

$\frac{\sin(qr)}{qr}$. By analogy, a similar result can be obtained from approximation of the power series expansion of the Bessel function in equation 2.57. This approximation is valid for small values of the scattering vector, *q*.

$$I_C(q) \cong (\Delta\rho)^2 \cdot A^2 \cdot e^{-\frac{1}{2}R_C^2 q^2} \qquad (2.59)$$

This is the Guinier approximation for cylinders that defines the radius of gyration in terms of the cross section R_C. In this case a circular rod will have an R_C defined as $R_C = \frac{1}{\sqrt{2}}R$. Having evaluated the two components individually they are now combined.

$$I_0(q) = I_H(q) \cdot I_C(q) \cong \frac{H \cdot \pi}{q} \cdot (\Delta\rho)^2 A^2 \cdot e^{-\frac{1}{2}R_C^2 q^2} \qquad (2.60)$$

The factor of $1/q$ is characteristic of rod-like particle. The plot of ln(*I(q).q*) vs q^2 then has no dependence on *q* in the high *q* region for the contribution from $I_H(q)$. The modelling of scattering profiles from cylindrical objects has many applications to small angle scattering experiments of real samples. Here they will be used for the modelling of cellulose microfibrils as long thin rod-like particles in a sample of woody tissue. The biosynthetic process that produces these particles is geared towards the production of crystallites with consistent lateral dimensions. These samples can therefore be considered monodisperse systems.

2.4.3 Orientation Investigation Using SAXS

Small angle scattering data can be used to investigate the occurrence of a preferred orientation in a sample in the much the same way that wide angle scattering experiments can. The observation of scattering from small angle scattering is often not as pronounced as is wide angle scattering. Orientation studies of cellulose are also performed with a related technique, microbeam small angle x-ray scattering (μ-

SAXS). In the μ-SAXS experiment a position resolved microbeam is used to scan a sample. The experiment performed at the European Synchrotron Radiation Facility used an x-ray beam 2 μm in diameter (Riekel *et al.*, 1997). This technique will not be discussed here as it is outside the scope of this project but it has been used on cellulosic materials specifically to look at orientation (Muller *et al.*, 1998).

Small angle scattering scans as a method for examining cellulose have been used since the 1950's (Heyn, 1950; Wardrop, 1952). Although the method requires less sample preparation than stained microscopy, the method requires much thinner samples than those for WAXS methods. The geometry of the SAXS experiment is very similar to the WAXS experiment for determining MFA with a few subtle variations.

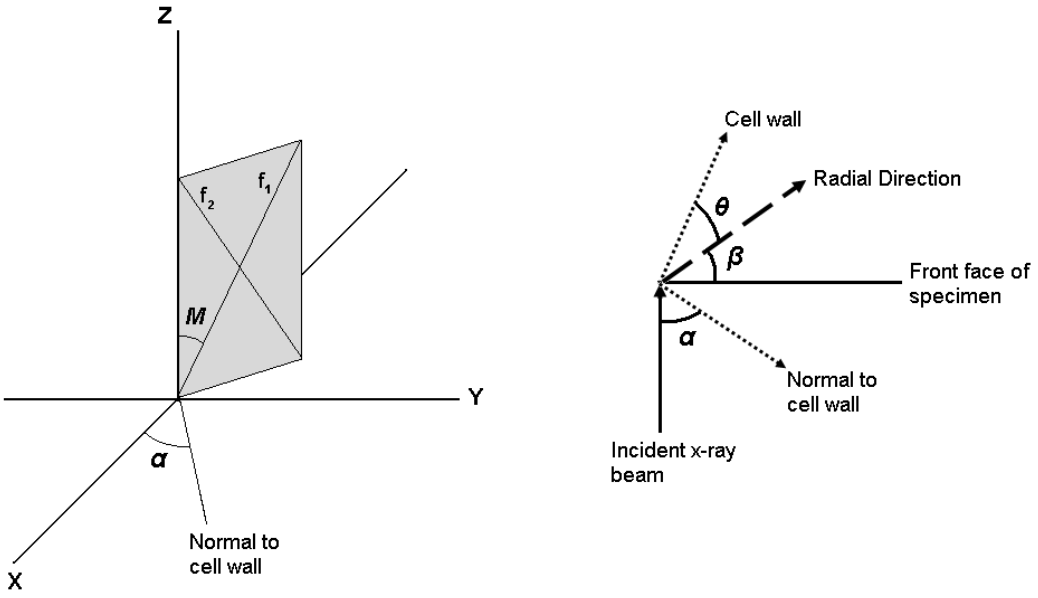

Figure 2-14 – The geometry of a small angle scattering experiment for the determination of MFA (Entwistle and Navaranjan, 2002; Entwistle and Terrill, 2000).

In Figure 2-14 the cell wall (grey) is positioned with the fibre axis being parallel to **Z**. The cell wall is made up of fibres (two shown) at an angle *M* to the fibre axis. This is the MFA for fibres parallel to f_1 with the fibres parallel to f_2 being identical to f. but 180° out of phase. The angle α is defined as the angle between the incident beam and the normal to the cell wall. The definition of α is better visualised in the diagram on the right. It shows that the value for α is related to the sectioning of the

sample. It is used to show that a specimen can be collected with the cell wall being at any angle to the incident beam, rather than perpendicular. In the case of a cell wall perpendicular to the incident beam, θ, β and α are all zero (Reiterer *et al.*, 1998).

In the case of a cell wall being normal to an incident beam SAXS measurements produce strong lobes of intensity in the equatorial region. These lobes originate from the scattering of an incident beam with the faces of the cell (with a square cross-section) that are parallel to the beam (Jakob *et al.*, 1994). Orientating the cell walls at some angle to the incident beam removes this large streak from the side walls and allows the MFA to be read from the data directly (Entwistle and Terrill, 2000). An incident beam directed at 45° to the face of the cell wall is a convenient angle to use. The major streaks in a small angle scattering pattern from cellulose can be seen below.

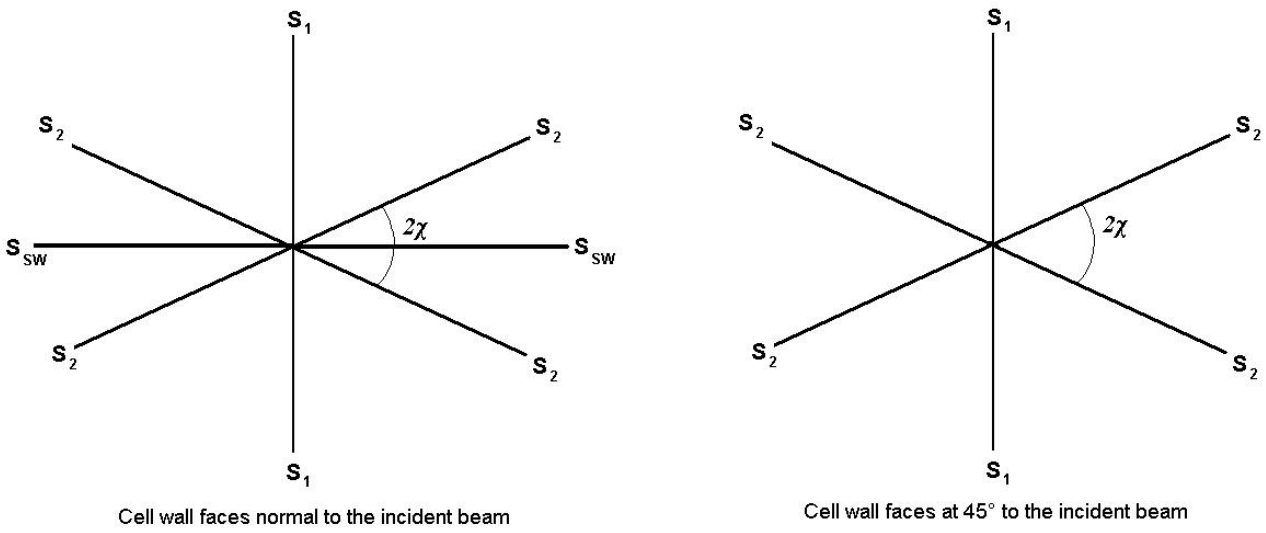

Figure 2-15 – The major streaks from a sample of wood with the cell wall layers corresponding to each streak labelled (S_1 cell wall layer, S_2 cell wall layer and the streak from the side walls of the cells). The azimuthal angle between the two S_2 streaks on the right of the S_1 streak is given as 2χ and is used to calculate the MFA (Entwistle and Terrill, 2000).

In a response to the article describing Figure 2-15 and the rotation of the sample to extract the MFA it was noted that experiments to determine the MFA did not require a sample rotation (Lichtenegger *et al.*, 2001). The three streaks observed in samples with a cell wall normal to the incident beam can be modelled by three Gaussian profiles and the distance between the two S_2 profiles gives the MFA. In Figure 2-15

the angle between the two S_2 streaks is given by 2χ. This is much easier to resolve in samples that are positioned at an angle to the incident beam. In this case

$$\tan(\chi) = \cos(\alpha)\tan(M) \qquad (2.61)$$

Here M is the microfibril angle and α is the angle between the cell wall face and the incident beam. In the case of the cell wall being normal to the incident beam $\alpha = 0$ and equation 4.23 reduces to $\chi = M$ (Reiterer *et al.*, 1998).

2.5 The Theory of Nuclear Magnetic Resonance Spectroscopy

Nuclear magnetic resonance spectroscopy (NMR) makes use of the fact that nuclear spin is quantised. Spin is an intrinsic property of the nucleus and is described by the nuclear spin quantum number, *l*. This spin quantum number defines the number of allowed spin states for a given nucleus. Any nucleus that contains an odd number of protons (and/or neutrons) will have a quantised spin angular moment and magnetic moment. Similarly the nuclei that contain an even number of protons will have a spin of zero due to the alignment of nucleons with opposite spin states. For this reason important nuclei that makes up organic and bio-molecules (specifically ^{12}C and ^{16}O) are not suited to NMR studies while the ^{1}H nucleus is a common target. The natural abundance and relative sensitivity of the ^{1}H and ^{13}C nuclei are presented in Table 2-2. Here the relative sensitivity is given for the same number of nuclei in a constant applied field (McBrierty and Packer, 1993). The CP-MAS technique has been used in this thesis as it is a way overcoming the difficulties described above in obtaining ^{13}C spectra of cell wall materials in their natural state.

Nucleus	Abundance (%)	Relative Sensitivity	Magnetogyric Ratio ($x10^{-8}$ rad s^{-1} T^{-1})
^{1}H	99.89	1	6.6752
^{13}C	1.1	0.0159	0.6762

Table 2-2 – The abundance and sensitivity of the hydrogen-1 and carbon-13 nucleus (McBrierty and Packer, 1993).

The NMR experiments of solids are quite different to those conducted on liquids and solutions. When carried out under the same conditions solid lines are often broad and featureless. Magic Angle Spinning (MAS) is a technique that has been developed to narrow spectral lines by spinning the sample rapidly (typically 1 to 70 kHz) at the magic angle. The technique involves spinning the sample at 54.74° (the so called magic angle) to the permanent magnetic field. The rate of the sample spinning needs to be sufficient to replicate the tumbling of molecules in solution or liquid form. For spectrometers used in this work the technique is restricted to reducing the broadening of ^{13}C lines as the rate of spinning required to narrow ^{1}H lines would be too great (Andrew, 1971).

Cross-polarisation, CP, techniques were developed in the 1960's as a way to increase the sensitivity of the experiment to dilute spins such at ^{13}C (Table 2-2). This technique may be used to enhance the signal of a dilute low-gyromagnetic nucleus such as ^{13}C. This is achieved by bringing the two nuclei populations into thermal contact by fulfilling the Hartmann-Hahn condition (Hartmann and Hahn, 1962). A thermal analogy where the temperature is defined by nuclear spin may be used to understand the experiment where polarisation is transferred in this case from ^{1}H to ^{13}C nuclei for enhancement of the ^{13}C signal (Fukushima and Roeder, 1993).

CP-MAS techniques have been utilised to improve the quality of data from ^{13}C spectra of solid cell wall materials. This technique improves the intensity of the observed resonance peaks (CP) as well as the resolution (MAS). The CP-MAS method has been used in the study of cell wall materials (in particular cellulose) to investigate nanostructure and chemistry (Atalla *et al.*, 1980). As x-ray scattering methods have been used for the purposes of nanostructure investigation the CP-MAS experiments are used to give some insight into the chemistry of the cell wall materials.

Chapter 3 Materials

Laboratory grade filter paper (Whatman, Grade 2; 8 μm) was used as a standard reference material for cellulose. The filter paper is a highly crystalline example of a cellulosic material having been processed chemically and mechanically during pulping. As a result Bragg peaks from filter paper tend to be better resolved than natural cellulose samples. The filter paper sample is a composite material with the cellulose microfibrils being embedded in an amorphous matrix of other polymers and calcite for binding. Microfibrils in filter paper are randomly orientated which results in isotropic diffraction patterns.

3.1 Palm Fibres

Samples of palm fibres were generously provided by Dr Rushdan Ibrahim of the Forest Research Institute Malaysia (Kuala Lumpur, Malaysia). The palm fibres used for these experiments are from the empty fruit bunches of the African oil palm, *Elaeis guineensis*. Initially they were used without any additional preparation than slow drying in air to prevent any cellular damage from the rapid movement of water (Barber and Meylan, 1964). Some fibres were boiled in 1.0 M NaOH for 24 hours to remove lignin. Fibre diameters were determined by analysing the cross sectional area at either end of a particular fibre with an optical microscope (Martinschitz *et al.*, 2007). Fibres provided had a width within the range of 0.08 – 0.5 mm. Fibres with a diameter of 200 μm were selected for measurement both as treated and untreated samples (summarised in Table 3-1). The fibres were mounted on a rotating frame for the WAXS and SAXS experiments conducted on a Nanostar SAXS instrument as in Figure 3-1.

Reference Number	Diameter	Treatment	Chapter
1	200	Untreated	5.1
2A	200	Untreated	5.2
2B	200	NaOH treatment	5.2

Table 3-1 – Summary of the palm fibres used in Chapter 5.1 and 5.2 courtesy of Dr Ibrahim.

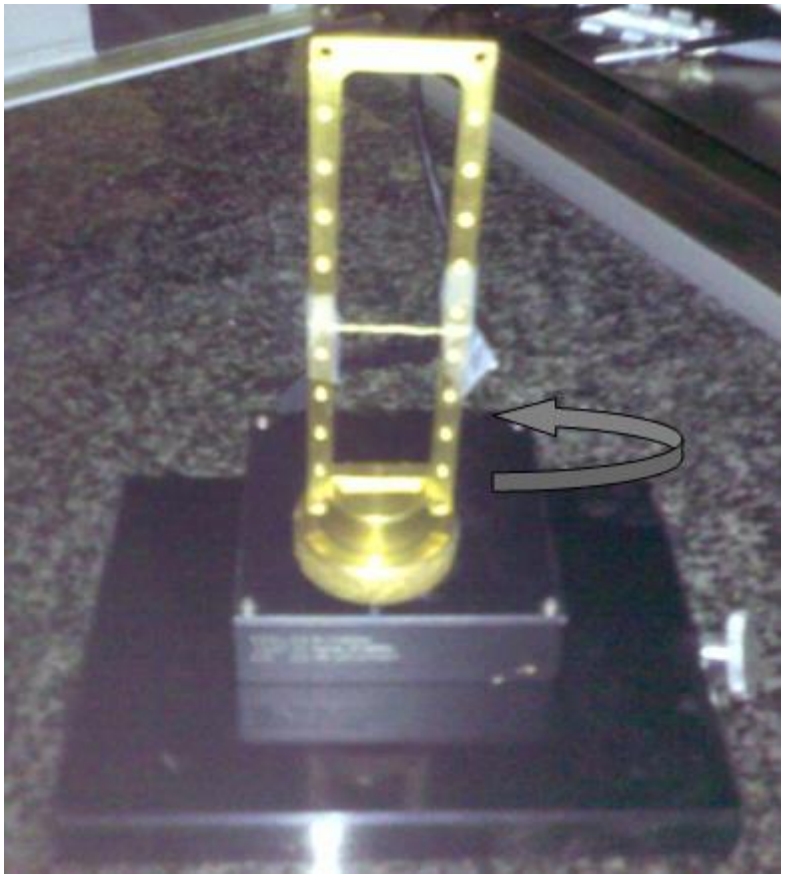

Figure 3-1 – Rotating sample stage with a single palm fibre mounted.

3.2 Maturing Native Tree Stems

Samples of maturing woody stems were collected from four sites in New South Wales (NSW), Australia. The four sites represent a variety of soil and rainfall conditions. A summary of the species (all hardwoods) collected and the location characteristics is presented in Table 3-2 (Wright *et al.*, 2002).

	Site 1	Site 2	Site 3	Site 4
Lattitude (S)	33°34	33°41	35°32	32°58
Longitude (E)	151°17	151°08	146°08	146°08
Vegetation	Closed forest	Open woodland	Open woodland	Open shrub mallee
Rainfall (mm/yr)	1220	1220	387	387
Total P (ppm)	442.3	93.6	250.4	132.4
Species	*A. floribunda*	*A. suaveolens*	*A. doratoxylon* *B. populneus*	*A. havilandiorum* *B. cunninghamii*

Table 3-2 – Rainfall and soil information for the four sites species were collected from Sites 1 and 2, in the Ku-ring-gai Chase National Park, NSW, and sites 3 and 4, in the Round Hill Nature Reserve, NSW. Total P is the total phosphorous present in the soil.

Stems were collected on site and debarked for measurements of the mechanical properties. The samples had a sapwood diameter of 4 – 6 mm from the outer canopy and were selected from the terminal axis of the main branch (Onoda *et. al.*, 2010). The maturing stems contained between 2 and 4 faint rings that could be identified as annual rings although this was not confirmed. In order to preserve the structure of the wood, the samples were dried slowly at 60°C. Rapid drying can disrupt the fibrils in the cell wall as the water in between them is displaced (Barber and Meylan, 1964). The intact stems were rehydrated and stored in water until required for preparation.

The samples for this set of measurements were prepared minutes before being mounted in the path of the beam. Samples were not always mounted vertically; some had the fibre axis at an angle to the vertical. This was done to preserve the structure of the cells as much as possible by keeping them wet. The cylindrical stems were sectioned with a sharp scalpel down the length of the sample. The samples were approximately 5 mm wide and between 2 – 3 mm thick.

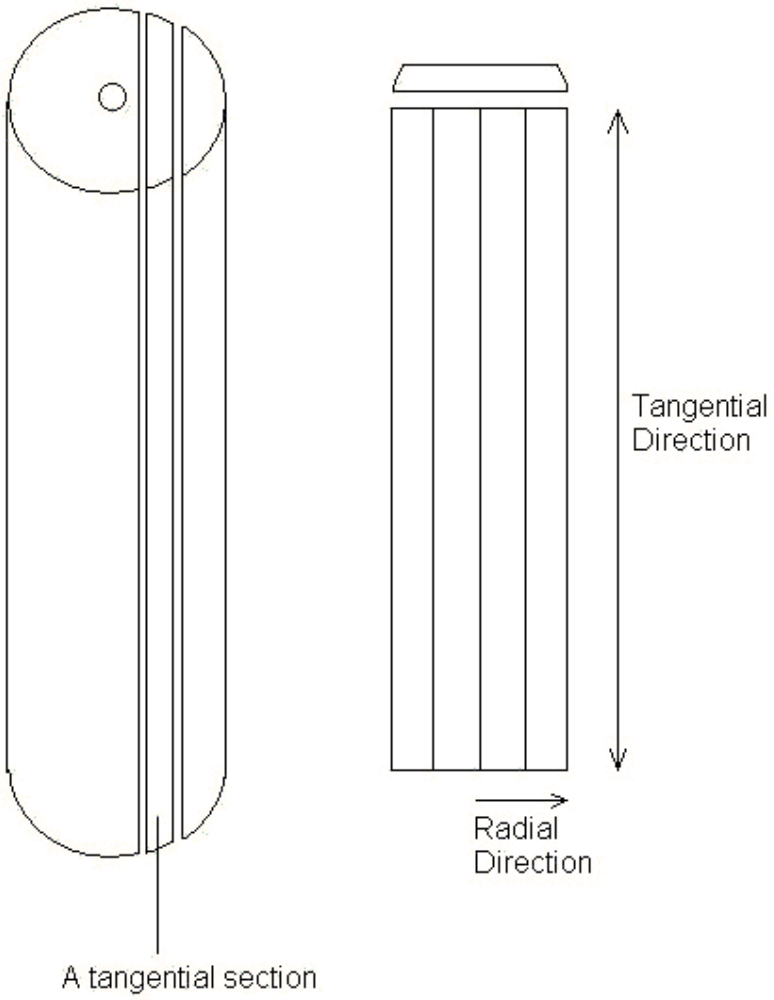

Figure 3-2 – The samples were sectioned to obtain a spread of tissue maturity. The wood in the centre of the sectioned sample is the oldest and decreases in maturity moving out in the radial direction.

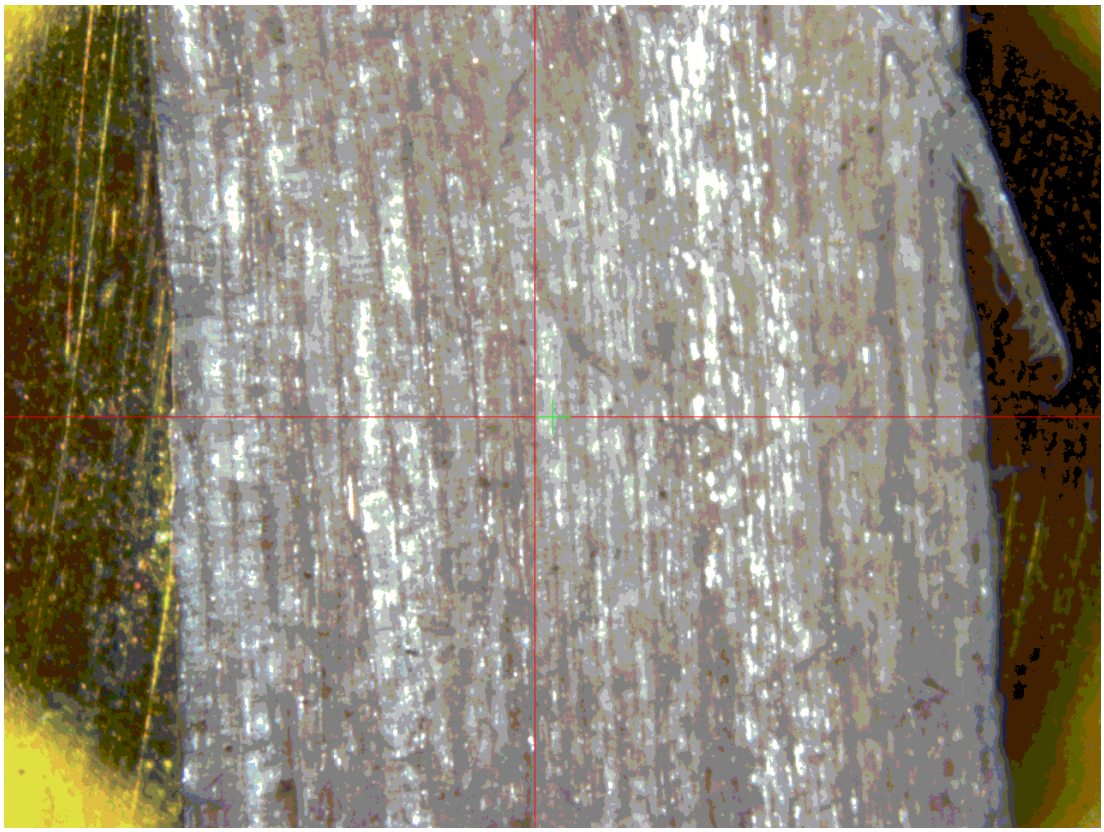

Figure 3-3 – The on-axis digital image of *B. cunninghamii*. Note the fibres are almost parallel to the vertical, and the engle with the vertical is well defined..

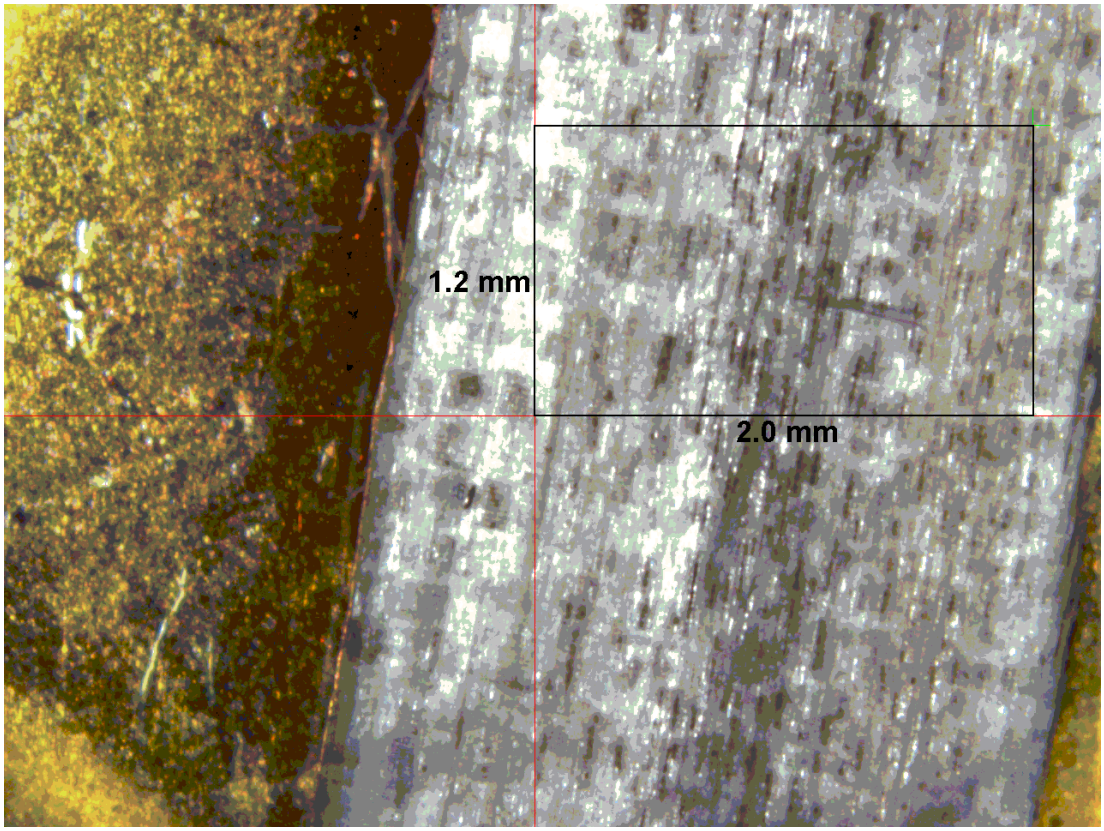

Figure 3-4 – The on-axis image of *A. suaveolens* with the outline of the collection grid (to scale). Note the fibres are at an angle to the vertical.

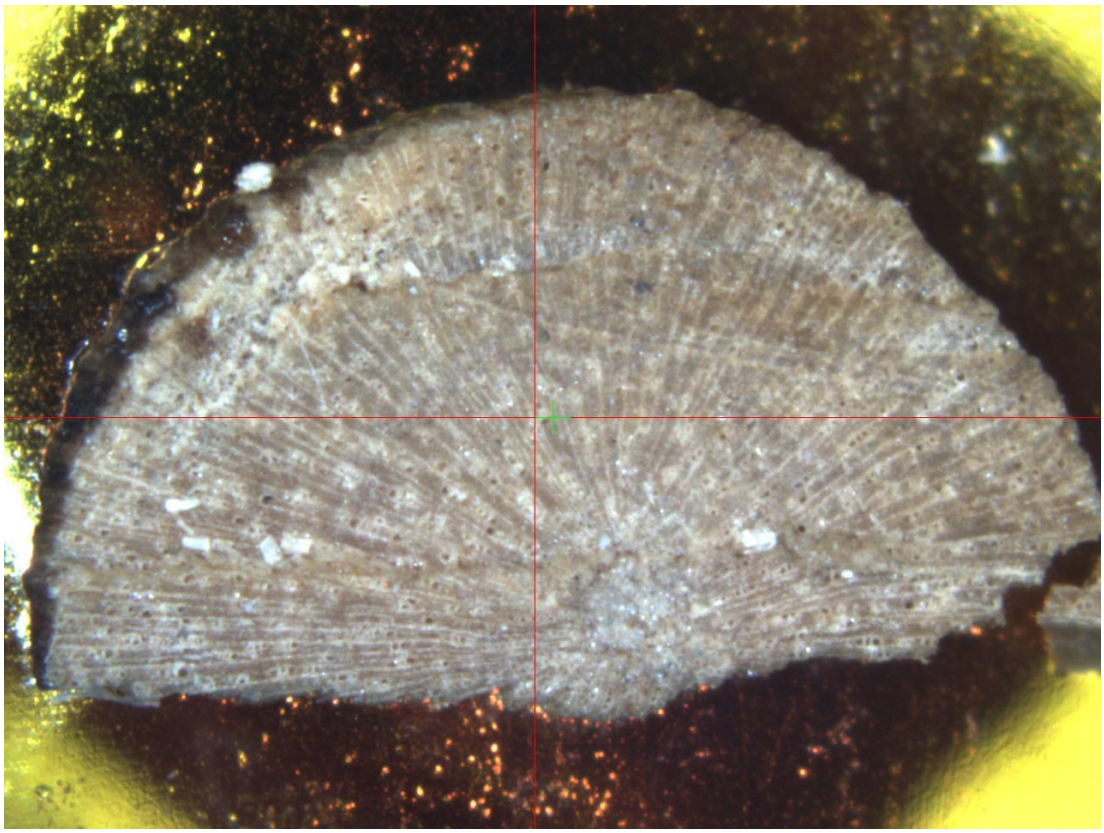

Figure 3-5 – A cross sectional image of *B. cunninghamii*.

3.3 An Acacia Species

A sample of *acacia* wood was generously provided by Dr. Rob Evans of the Commonwealth Scientific and Industrial Research Organisation (CSIRO). The sample of *acacia* wood shows an unusual formation of reaction wood (Hillis *et al.*, 2004). This sample was chosen for x-ray scattering investigation to look at the structure and arrangement of cellulose in the cell wall of different types of wood within the sample (early wood, late wood and reaction wood). Reaction wood usually refers to any wood that is formed in response to an external or internal force acting on the developing tissue (Scurfield, 1973). A typical situation under which reaction wood will form is the formation of a branch on the main trunk. The mass of wood in a tree results in the trunk being under compression, which is dealt with by the tree with the alignment of cellulose microfibrils in the main trunk being aligned in the direction of this compressive force. The growth of a branch complicates this method of coping with pressures due to the mass of the wood.

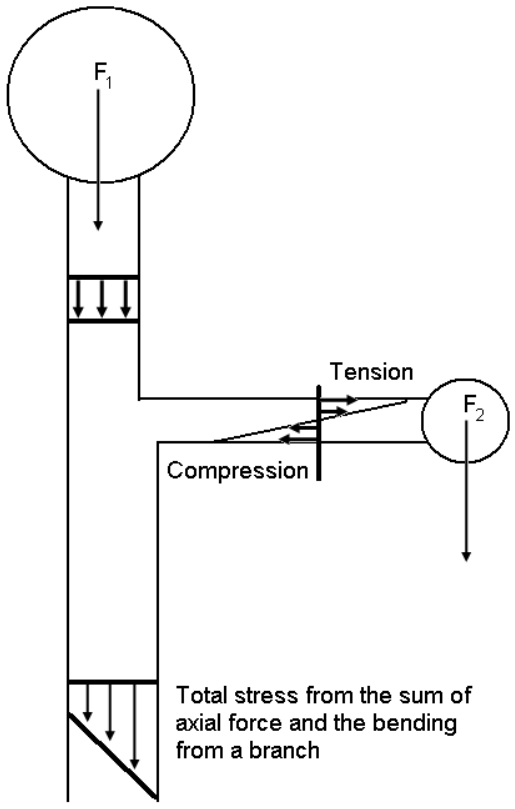

Figure 3-6 – The internal stresses in a tree which can cause the formation of reaction wood in the trunk and/or branch (Mattheck and Kubler, 1995). Reaction wood formed in response to tension is called tension wood, and in response to compression it is named compression wood.

Reaction wood in a hardwood will generally form as a response to an external force rather than an internal one (e.g. the presence of high winds) (Scurfield, 1973). This sample is unique in that it has grown vertically upwards, suggesting no significant or sustained windy periods, and yet there is a 5 mm band of reaction wood, in this case associated with tension, observed in the heartwood. The tree that the straight log sample came from was estimated to be 20 years of age, closely resembling *Acacia melanoxylon*, though a definitive identification was not made. For the purposes of the experiment, the sample had to be thinly sectioned, while still retaining the integrity of the fibre structure. This was achieved by carefully using a chisel to lever a thin layer of wood from the main sample (Hillis *et al.*, 2004; Mattheck and Kubler, 1995).

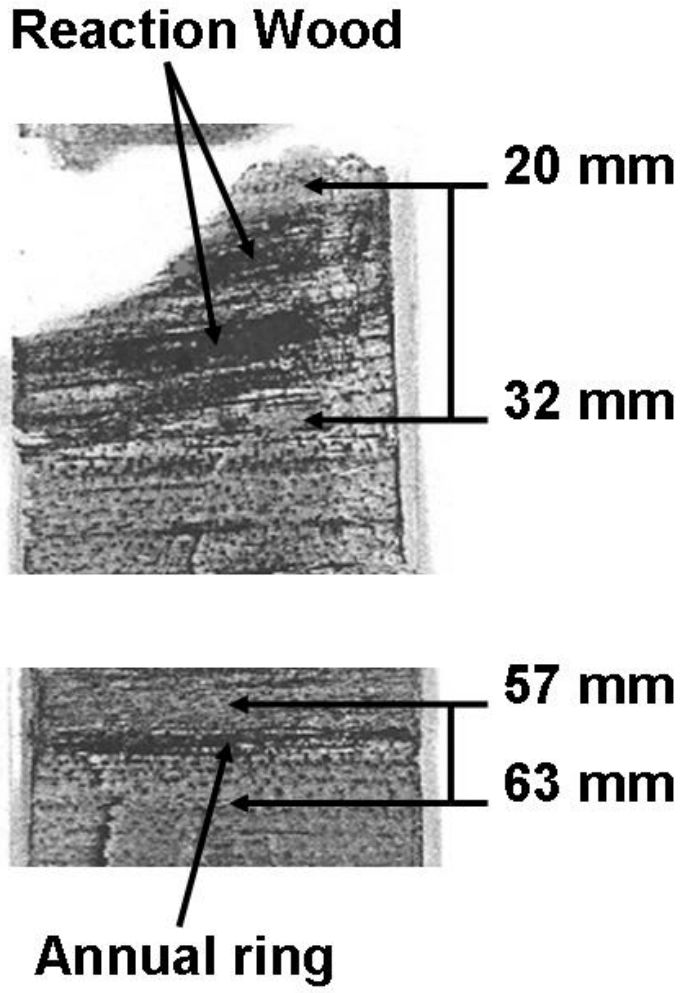

Figure 3-7 – This thin section is an example of the samples prepared for transmission x-ray diffraction studies. The band of reaction wood was located between 20 mm and 32 mm while the annual ring was located between 57 mm and 63 mm.

3.4 Domestic Timbers

Samples of native timbers were selected to investigate the effect of grain direction on reflection mode XRD experiments. Four samples of Australian timber were obtained from a timber wholesaler. These samples consisted of one gymnosperm (*Pinus radiata*) and three angiosperms (*Eucalyptus marginata*, commonly Jarrah, *Eucalyptus patens*, commonly Blackbutt and *Eucalyptus regnans*, commonly Australian Oak). These samples were sectioned and mounted in circular sample holders for measurement by an incident beam parallel and perpendicular to the grain.

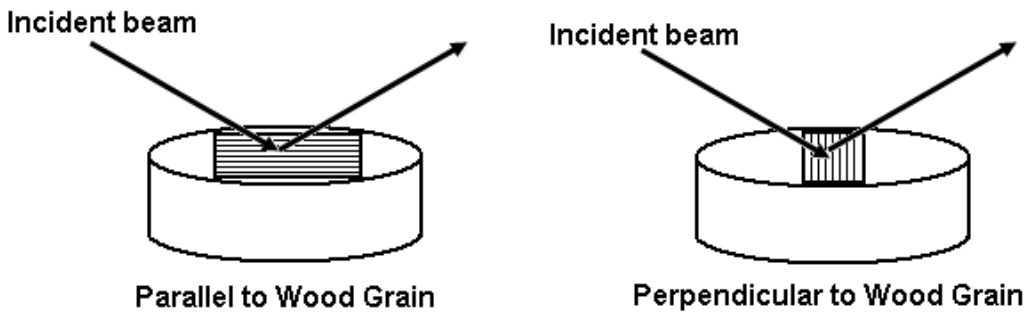

Figure 3-8 – The orientation of timber samples in the Bruker D8 Diffractometer.

Chapter 4 Experimental Methods

4.1 Wide Angle X-ray Scattering & X-Ray Diffraction

WAXS and/or XRD measurements were made for each sample in this study. As indicated previously in this thesis WAXS will refer specifically to an incident x-ray beam transmitting through a sample while XRD will refer to an incident x-ray beam reflecting from a sample. Both lab based x-ray generators and synchrotron light sources have been used to conduct experiments.

4.1.1 Palm Fibres

WAXS experiments were performed on a Bruker AXS Nanostar at the Australian Nuclear Science and Technology Organisation (ANSTO) small angle x-ray scattering facility and at the Australian Synchrotron on the SAXS/WAXS beamline using samples of palm fibres (Chapter 3.1). Image plates were used to record data from the ANSTO Nanostar with a sample to detector distance of 76.0 mm. The image plates have a resolution of 4096 by 5120 with 40 pixels per mm. The fibres were mounted on a rotating frame for the WAXS experiments conducted on the Nanostar (Figure 3.1). Measurements at the Australian Synchrotron were made on a Pilatus 1M detector.

The Nanostar operates with a rotating anode x-ray generator producing CuK_{α} radiation (λ = 0.1541 nm). The beam is passed through cross-couple Gobel mirrors and a three pinhole collimation system. Average collection times varied between 5 mins and 5 hours however these were normalised for ease of comparison. The x-ray optics, short camera length and resolution of the image plates can contribute significant instrumental broadening to the data. This was investigated by collecting scattering data from the National Institute of Standards and Technology (NIST) standard reference material (SRM) 660a, or lanthanum hexaboride (LaB_6). This sample was selected as it contained no sample related broadening in the observed

diffraction patterns (micrometer sized crystallites and no strain). This data is presented below (Figure 4-1).

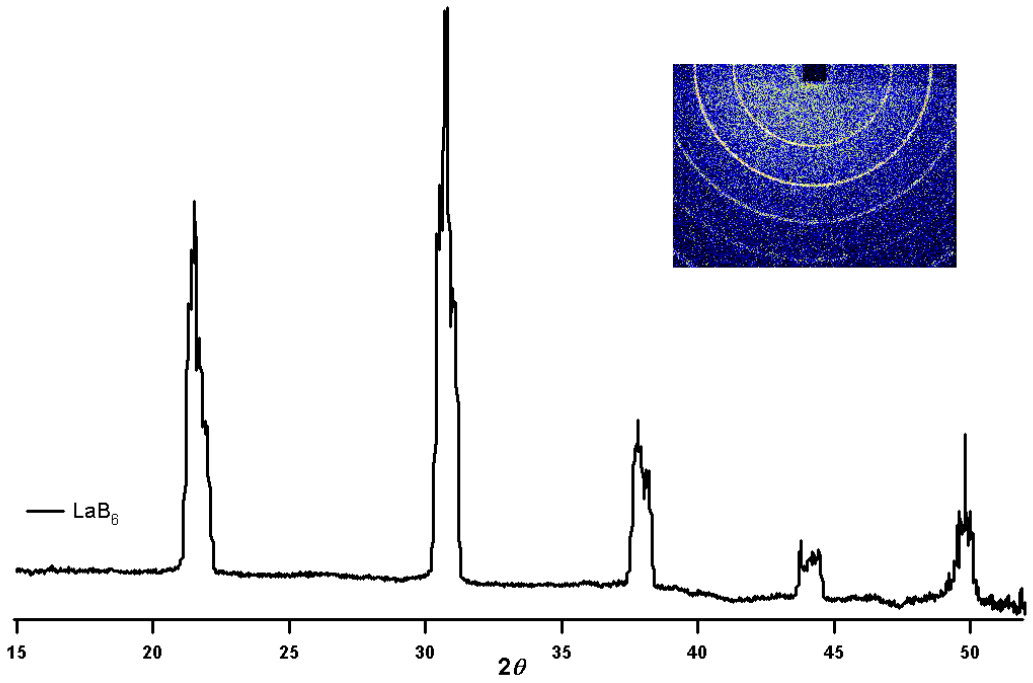

Figure 4-1 – SRM 660a scattering data collected on the ANSTO Nanostar (2D data shown inset).

The first three reflections in Figure 4-1 ((100), (110) and (111) at 21.5°, 30.7° and 37.8° respectively) were fit to determine the FWHM of these peaks.

Reflection	2θ (°)	FWHM (°)
(100)	21.50	0.57
(110)	30.70	0.54
(111)	37.80	0.58

Table 4-1 – FWHM values for the data in Figure 4-1.

These values indicate a significant instrumental broadening in the data obtained from the ANSTO Nanostar in the short camera (wide angle) configuration. If a cellulose peak had an observed FWHM of 2.3° then it was considered that at least 0.5° of this was from instrumental sources, or over 20%. The data was corrected for the instrumental broadening as a result of this observation prior to processing.

The image plate was removed and replaced in between each measurement using a line in the sample chamber as a guide. Due to the difficulties in removing and

replacing the image plates in the same position after each measurement there was some drift in the distance from the sample to the image plate for the measurements. The detector distance was calibrated using the 002 peak (2θ = 23° for λ = 1.541 Å). Data was collected from two positions on the palm fibre for the wide angle configuration approximately 5 mm apart. At one of the positions data was collected with varying angles of rotation on the sample stage. Rotations of 0°, 10°, 20°, 25° and 45° were applied to the mounted sample and wide angle scattering data collected for each point (Figure 4-2).

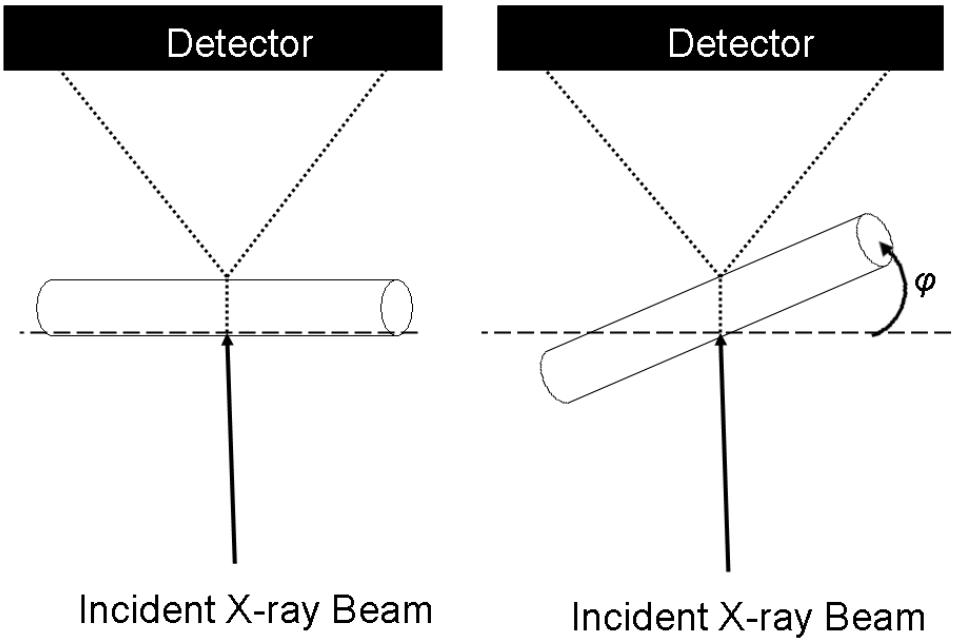

Figure 4-2 – The geometry for transmission measurement x-ray scattering on a palm fibre. Data is collected scanning the length of the fibre (perpendicular to the incident x-ray beam. A set of data was generated by making measurements of a point as the fibre is rotated through an angle, φ, as in the set up shown to the right.

Measurements made at the Australian Synchrotron on the SAXS/WAXS beamline were optimised for cell wall materials so that the (040) cellulose reflection could be observed (λ = 0.06199 nm; Cameral length = 355.2 mm). The Dectris – Pilatus 1M detector was composed of 10 modules in a 2 × 5 array. There is a 7 × 17 pixel gap between each module. Pixel sizes are 172 × 172 μm and the readout time of the detector is 30 ms.

Two dimensional WAXS patterns collected on the Nanostar were reduced to one dimensional patterns in Fit2D, http://www.esrf.eu/computing/scientific/FIT2D/ (Hammersley, 2004).

4.1.2 Maturing Native Tree Stems

The maturing native tree stems (Chapter 3.2) were sectioned tangentially (i.e. Figures 3.2 and 3.3) for WAXS measurements conducted at the Australian Synchrotron. The SAXS WAXS beamline was configured for wide angle measurements and optimised for cell wall materials so that the (002) cellulose reflection could be observed (λ = 0.0688 nm; Camera length = 329.9 mm). The combination of low wavelength and short sample to detector distance allowed observation of q-values up to 23 nm^{-1}. The detector used was the MAR-165 CCD camera. The detector was 165 mm in diameter with 80 μm x 80 μm pixels. The resolution of the detector was 2048 by 2048 with a 1 Hz frame rate. An on-axis digital camera was mounted along the path of the incident beam so that images of the sample could be taken prior to measurement.

The instrumental broadening associated with synchrotron measurements is typically small enough to be considered negligible due to the high intensities achieved. However the low resolution set up of the beamline at the time can result in some instrumental broadening, therefore scattering data of NIST SRM 640c was collected for examination.

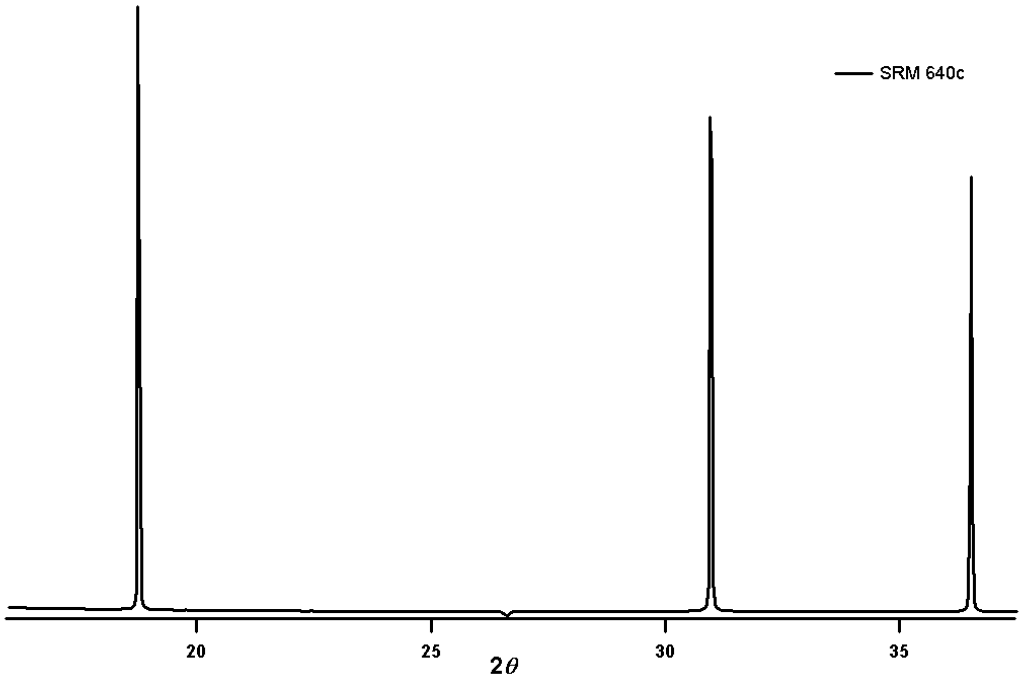

Figure 4-3 – SRM 640c scattering from the WAXS/SAXS beamline at the Australian synchrotron.

Peak fitting of the scattering data from SRM 640c gave FWHM values of up to 0.01°. The material has been certified to contain no sample broadening so this was all attributed to instrumental broadening. The broadening associated with instrumental effects (camera length and resolution) is much smaller than those observed from scattering data from the samples (as much as 1°). As a result the instrumental broadening from the synchrotron was considered negligible for this experiment and the data was not corrected prior to processing (instrumental broadening being less than 1% of the observed broadening).

In the experiment, grids of diffraction patterns were collected to observe spatial variations in the stems. Structurally the grid related columns to the direction along a single fibre while the rows spanned across multiple fibres (Figure 4-4). The grids collected varied in area based on the size of the sample. The grids were 2 – 3 mm wide by 1 – 2 mm high and contained between nine and twenty four data points. The species *A. doratoxylon* and *B. cunninghamii* had grids four rows by six columns. The *B. populneus* grid was three rows by six columns. The *A. floribunda* grid was four rows by four columns. The *A. suaveolens* grid was four rows by five columns. The *A. havilandiorum* grid was four rows by three columns.

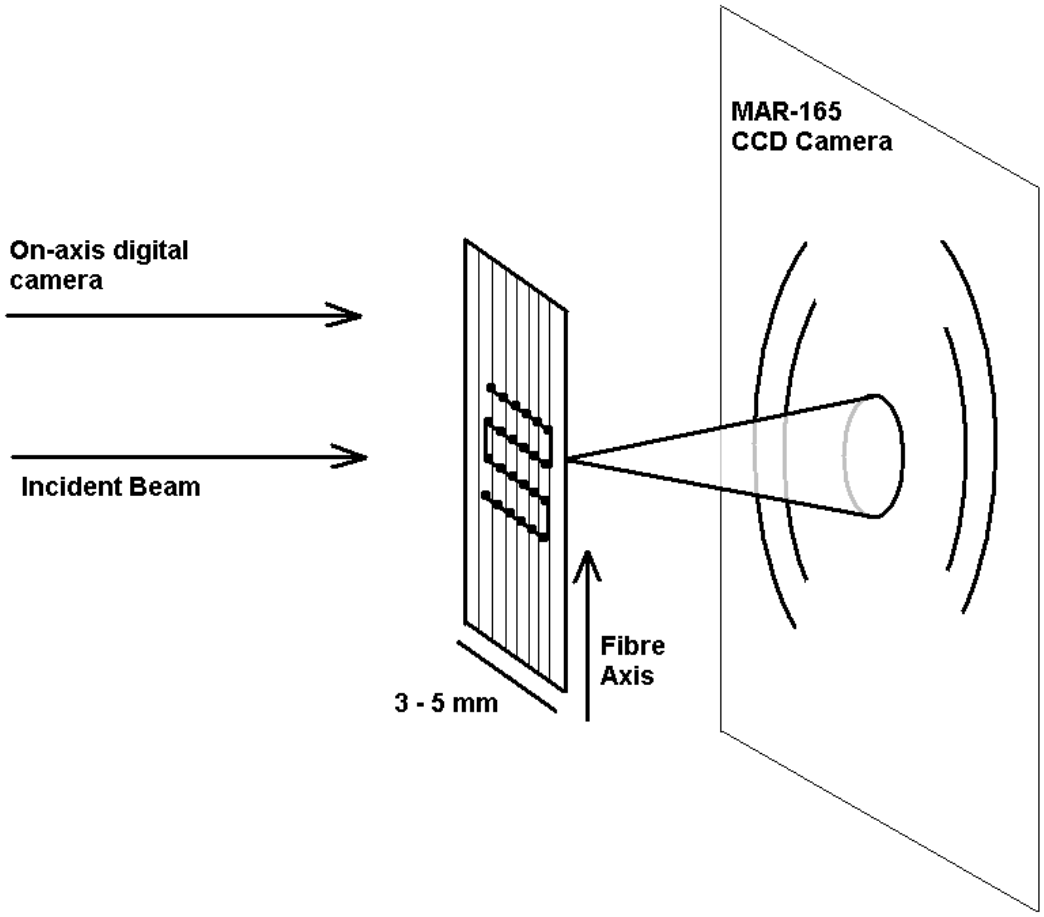

Figure 4-4 – Schematic diagram of the WAXS experiment. The samples were positioned with the fibre axis perpendicular to the incident beam and an on-axis digital camera positioned to collect optical images of the samples in position.

The incident x-ray beam can be collimated to focus on an individual fibre using modern optical systems (Muller *et al.*, 1998). However rather than focussing on individual fibres the beam foot print sampled multiple fibres in a single measurement. The use of multiple fibres in the irradiated sample volume results resulted in a measurement containing the average MFA over the sample volume. The fibre dimensions were estimated based on the high resolution optical images of the on-axis digital camera. The fibre diameter was estimated to be ~20 μm. This estimate suggests that there are a minimum of 10 fibres per measurement with the illuminated volume being composed of multiple layers even in the thinnest of samples.

Samples were not always mounted perfectly perpendicular to the incident beam. Some samples had the fibre axis at an angle to the vertical. These angles were 9.2°, -

8.0° and -8.8° to the vertical for the samples *A. floribunda*, *A. suaveolens* and *A. havilandiorum* respectively.

For samples that are aligned at an angle to the vertical the grid co-ordinates were rotated so that the axes of the grid are parallel and perpendicular to the grain respectively. The rotational transformations are shown below,

$$x' = x \cdot \cos\theta - y \cdot \sin\theta \tag{4.1}$$

$$y' = x \cdot \sin\theta + y \cdot \cos\theta \tag{4.2}$$

where x and y are the horizontal and vertical co-ordinates and θ is the angle the grain makes with the vertical. It should be clear that for samples with the grain parallel to the vertical $\theta = 0°$ and in this case $x' = x$ and $y' = y$.

Raw data obtained from the synchrotron contained a scattering signal from the tape used to mount the samples. This tape signal was subtracted from the raw data prior to processing. Due to a technical fault with the photodiode on the beamstop at the synchrotron actual collection times varied slightly from what was recorded. As a result of this the background subtraction was sometimes over or under applied to the data

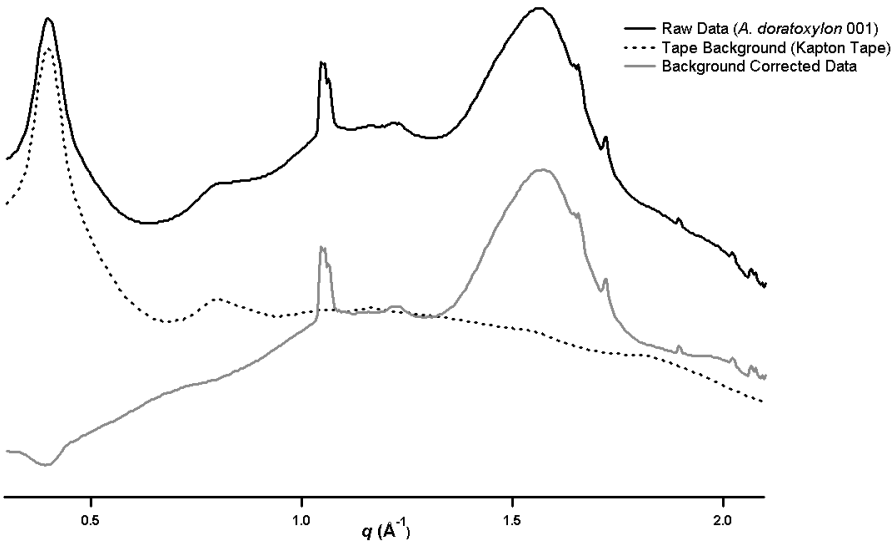

Figure 4-5 – Raw data with an over-subtraction of the tape background resulting in a noticeable drop in intensity at ~0.4Å^{-1}.

In Figure 4-5 the over-subtraction was observed as a drop in intensity at approximately 0.4 $Å^{-1}$ while other samples showed an under-subtraction of the background resulting in the tape peak still being present around this region. To properly subtract the background a scalar factor was applied to the tape background prior to subtraction so that the intensity was a smooth increase around the 0.4 $Å^{-1}$ region. The scale factor ranged from 0.8 to 1.1 depending on the data.

4.1.3 An Acacia Sample

A sample of an acacia wood (most likely *A. melanoxylon*, Chapter 3.3) was prepared for WAXS measurements at the (ANSTO) small angle x-ray scattering facility. The instrument used was the Bruker AXS Nanostar described in Chapter 4.1.1. The Nanostar was operated using images plates, 4096 × 5120 with 40 pixels per mm, positioned 76 mm from the mounted samples. The beam is generated on a rotating anode emitting from a CuK_{α} source (λ = 1.541 Å).

As observed in the standard data collected previously significant instrumental broadening was present. This was confirmed by measuring scattering data from NIST SRM 676 (alumina, or corundum). As in the previous standard data it was assumed there was no sample related broadening present so all broadening observed in Figure 4-6 was attributed to the instrument. However given that NIST SRM 676 is not a line profile standard, rather an internal quantitative standard this data was not used to determine the amount of instrumental broadening present. Instead for this set of data the instrumental corrections were based on the observations made in Chapter 4.1.1 prior to processing.

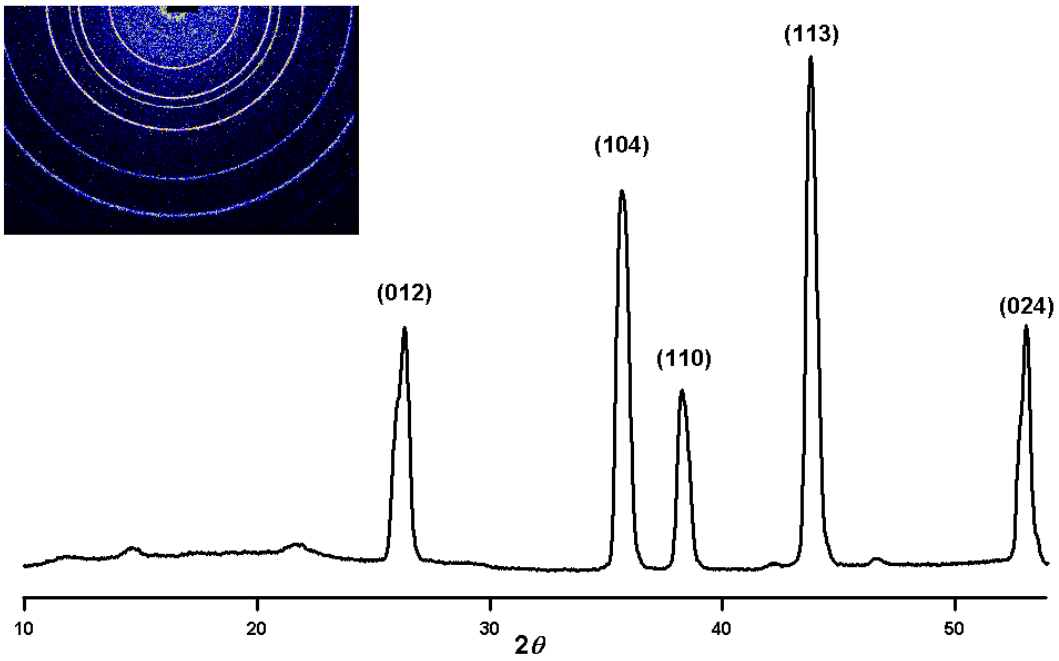

Figure 4-6 – The two dimensional and radially averaged one dimensional diffraction patters of NIST standard material, NBS-676.

Two dimensional WAXS patterns collected on the Nanostar were reduced to one dimensional patterns in Fit2D, http://www.esrf.eu/computing/scientific/FIT2D/ (Hammersley, 2004).

4.1.4 Domestic Timbers

The native timber samples (Chapter 3.4) were investigated by XRD on a Bruker AXS D8 Advance at Curtin University. Although powder samples are often spun continuously in the Bragg-Brentano geometry, the timber samples were stationary throughout the measurement and the same sample subjected to an incident beam parallel to the grain and perpendicular to the grain, as in Figure 3.8. The D8 advance uses a CuK_{α} x-ray source providing x-rays with a wavelength of $\lambda = 0.1541$ nm.

The instrument collected diffraction data over a period of 15 minutes, scanning a 2θ range of 4° to 60°. No standard was measured for this set of experiments as the fundamental parameters approach was used to determine instrumental broadening from the D8. The fundamental parameters approach is the preferred method here as the D8 has an extensively characterised instrumental broadening.

4.2 Small Angle X-Ray Scattering

4.2.1 Palm Fibres

SAXS experiments were performed on palm fibre samples (Chapter 3.1) at ANSTO on a Bruker AXS Nanostar instrument. Small angle scattering data was collected from the same point used to collect the WAXS data (Chapter 4.1.1). A Vantec 2000 two dimensional detector (55 μm resolution) was used to record the data. The CCD was positioned 1.2 m from the mounted palm fibre. The x-ray generator is described above in Chapter 4.1.1 and provides a wavelength of λ = 0.1541 nm.

Again small angle scattering data was collected from various points along the fibre. In one position there was a rotation of the fibre to collect data as the cells in the bundle are moved through a rotation angle φ (Figure 4-2).

4.2.2 Maturing Native Tree Stems

SAXS measurements were made of the maturing native tree stems (Chapter 4.2) at the Western Australian Small Angle X-Ray Scattering Facility within Curtin University. The measurements were made on the facility's Bruker AXS Nanostar SAXS instrument. This instrument is similar to that described previously in chapter 4.1.1. The main difference is in the x-ray generator; ANSTO having a rotating anode source and Curtin having a sealed tube. The Curtin Nanostar contains a CuK_{α} x-ray source resulting in an operational wavelength of 0.1541 nm. Samples are mounted in a vacuum chamber and positioned 654 mm from the detector (the detector is a 2-D gas (Xe) wire detector 1024 × 1024 pixels).

The spatial resolution of the beam on the Nanostar is limited by the fact the sample holder only has one degree of freedom in the chamber and hence can only move in one dimension. The variations along the direction of the fibre axis are quite small relative to the variations lateral to this. So the lateral direction is where the variations would ideally be observed. However the movement of the sample in the path of the

beam is restricted to the fibre axis and so one measurement was made for each sample on the Nanostar as opposed to the grids of WAXS patterns collected on the synchrotron for these samples.

Each species was sectioned twice for measurement on the Curtin Nanostar. One section was a cross section of the stem, as in Figure 3.5. The other was a tangential section, as in Figures 3.3 and 3.4. The cross-sectional and tangential sections of the maturing stems were positioned in the path of the incident mean so that the beam samples mature wood rather than the pith of the stem. The tangential sections were also prepared and mounted so that the beam on the Nanostar was incident on the mature regions of the stem.

The sections prepared were air dried over a period of a few hours before being mounted for measurement in the Nanostar. As the measurements on the Nanostar were performed in a vacuum the samples needed to be dry to prevent the possibly disruptive rapid transfer of water out of the sample. Measurements were made for three hours to ensure that the measurement statistics were sufficient for the patterns obtained.

4.3 Nuclear Magnetic Resonance Spectroscopy

4.3.1 Palm Fibres

In addition to WAXS and SAXS measurements NMR experiments were performed on the palm fibres (Chapter 3.1). Samples of palm fibre were dried in air so that the rapid movement of water from oven drying didn't damage the cellular structure. Some fibres were treated overnight in a 1M NaOH solution. The aim of this chemical treatment was to remove lignin in the samples while leaving the structure and arrangement of the cellulose microfibrils in the cell wall in tact.

Untreated palm fibres were packed uniformly into 7.5 mm zirconium oxide rotors spinning at 5 kHz. Spectra for these samples were collected on a Varian Inova 300 spectrometer operating with a resonant frequency of 75 MHz for ^{13}C and 300 MHz for ^{1}H. Measurements were conducted at 23° C. A 90^{o}_{x} ^{1}H pulse was applied for approximately 4 μs. Cross polarisation was achieved with a contact time of 2 ms and high-powered decoupling was switched on at the start of each ^{13}C acquisition, with the sequence being repeated after a delay of 3 s. More than 4000 transients were collected and added before the spectrum was transformed in the Fourier domain. The spectrum of hexamethylbenzene, and peaks at 17.36 ± 0.25 and 132.18 ± 0.25 ppm were used as a chemical shift reference (Earl and Van der Hart, 1982). For comparison with a well characterised cellulose sample (Newman and Hemmingson, 1994), the spectrum of Whatman filter paper was recorded.

Chapter 5 Results and Discussion

5.1 WAXS & SAXS Measurements of Rotated Palm Fibres

5.1.1 Radial Vs Sector Averaging

Wide angle X-ray scattering (WAXS) measurements have been made on a sample of palm fibre (See Chapters 3.1 and 4.1 for details). The measurements were made on points along the length of the fibre to investigate any changes in structure or orientation of cellulose in the cell wall. Measurements were also made at a single point on the fibre with rotation around the axis ϕ (Figure 3-1). These measurements were made to investigate the effect of cell orientation on the scattering data obtained.

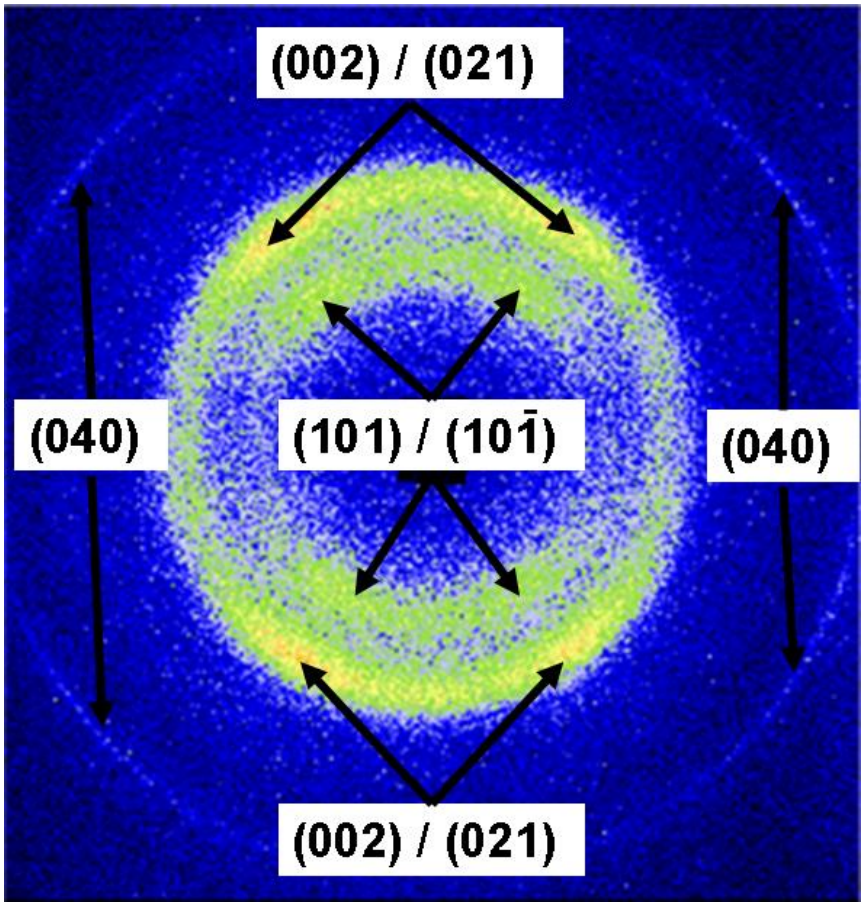

Figure 5-1 – Typical WAXS pattern from the palm fibre sample. The major crystallographic reflections have been labelled.

Figure 5-1 is a typical WAXS pattern from the palm fibre sample showing that the sample contains both isotropic data and anisotropy in the cellulose diffraction peaks. The position and broadened nature of the reflections is typical of cellulosic materials in general. Calculation of the lateral dimensions of the cellulose crystallites from patterns such as Figure 5-1 requires averaging the data to transform it into a one dimensional form.

For a totally isotropic WAXS pattern, such as that from Al_2O_3 (Figure 4.3), radial averaging is used to obtain a one dimensional pattern. This process involves taking the average intensity around the beam stop for each 2θ value. This averaging results in what is effectively a powder diffraction pattern (as the data is what would be expected from the sample in powder form placed in a reflection mode diffractometer).

In the case of anisotropic patterns there needs to be a decision if the average for each 2θ value will be around the whole circle (radial averaging) or only part of it (sector averaging). Sector averaging is a more computationally intensive process so radial averages are preferred where possible. However the use of a radial average can distort the observed WAXS patterns in some highly anisotropic materials. The WAXS data from the palm fibre sample in Figure 5-1 was averaged with both a radial method and a sector method for comparison.

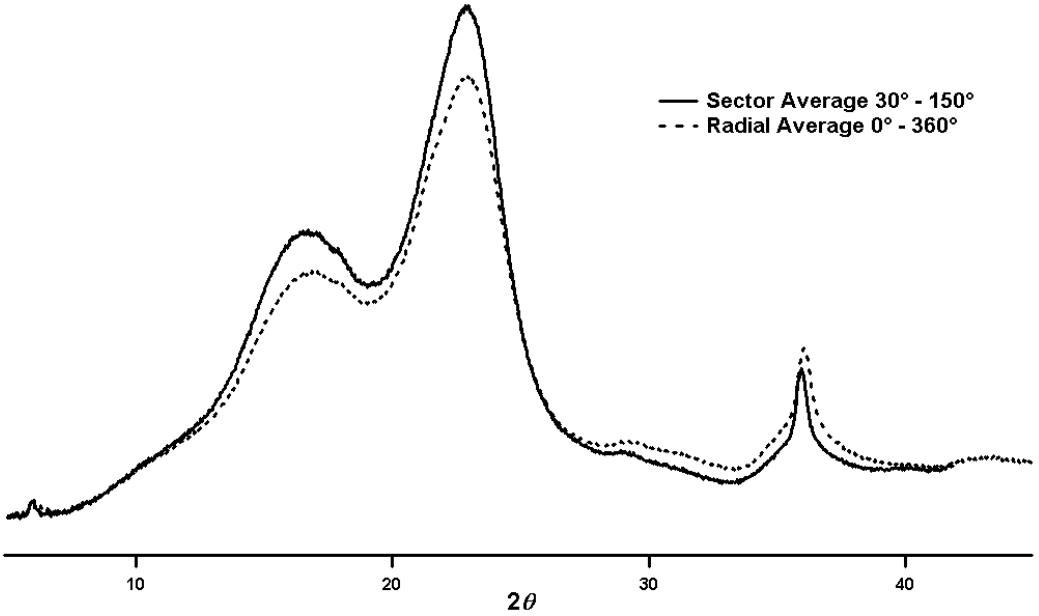

Figure 5-2 – Sector and radial averaged WAXS pattern from a sample of palm fibres.

In Figure 5-2 the sector was taken between the azimuthal angles χ = 30° to 150° as this region contains the (002) reflection (as does the sector from χ = 210° to χ = 330° due to the symmetric nature of cell wall WAXS data). It was observed that the WAXS patterns obtained are very similar with the sector averaged data showing slightly more intensity than the radial averaged data. To allow comparison of the two patterns the intensity was normalised with respect to the (002) reflection. The intensity of the one pattern is of course fixed and what is observed is an increase in the apparent intensity when the data is reduced to one dimension. The reason for this increase is that the sector average has been focussed on the region of the pattern with greater intensity while the areas with low intensity are not included to bring the averages down.

As the sector is focussed on the more intense portion of the WAXS pattern there will be a greater contribution from crystalline material. The amorphous signal is isotropic since it is evenly distributed around the beam centre and the sector average will show an increase in the ratio between crystalline signals and amorphous signals.

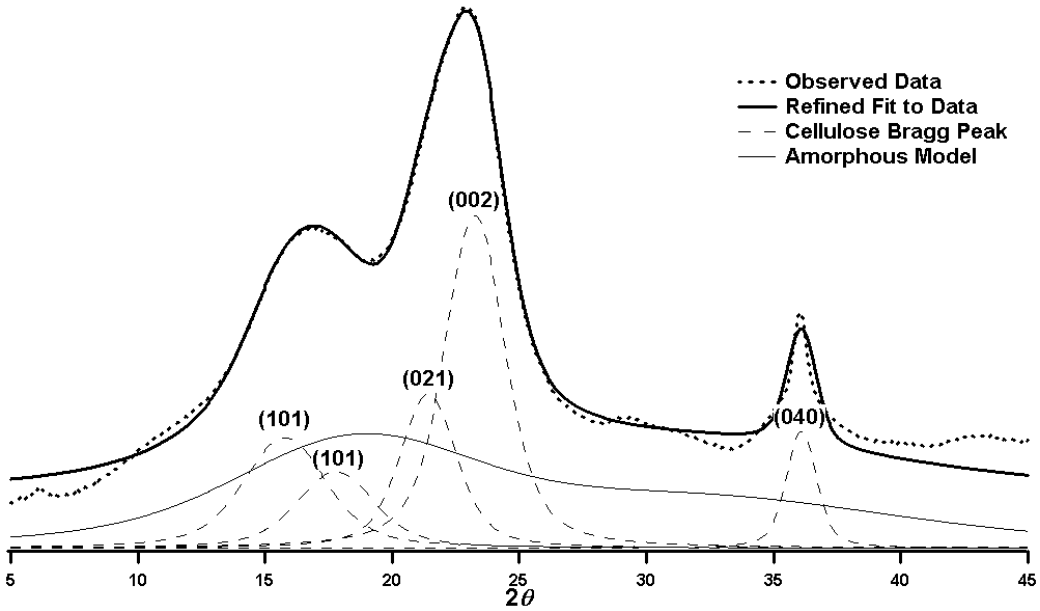

Figure 5-3 – Deconvoluted WAXS pattern for radially averaged palm fibre data.

The intensity of Bragg peaks from cellulose patterns are often described in terms of how they relate to the (002) peak. This is because the (002) peak is significantly more intense than the others. Because of this the intensity of the (002) peak in the different diffraction patterns has been normalised. In addition to the greater intensity of the (002) it is representative of a very significant crystallographic direction in the cellulose crystallite (Figure 2.3). Convention is to label the **b**-axis as running down the length of the crystallite and therefore it is always the long axis in cellulose crystallography.

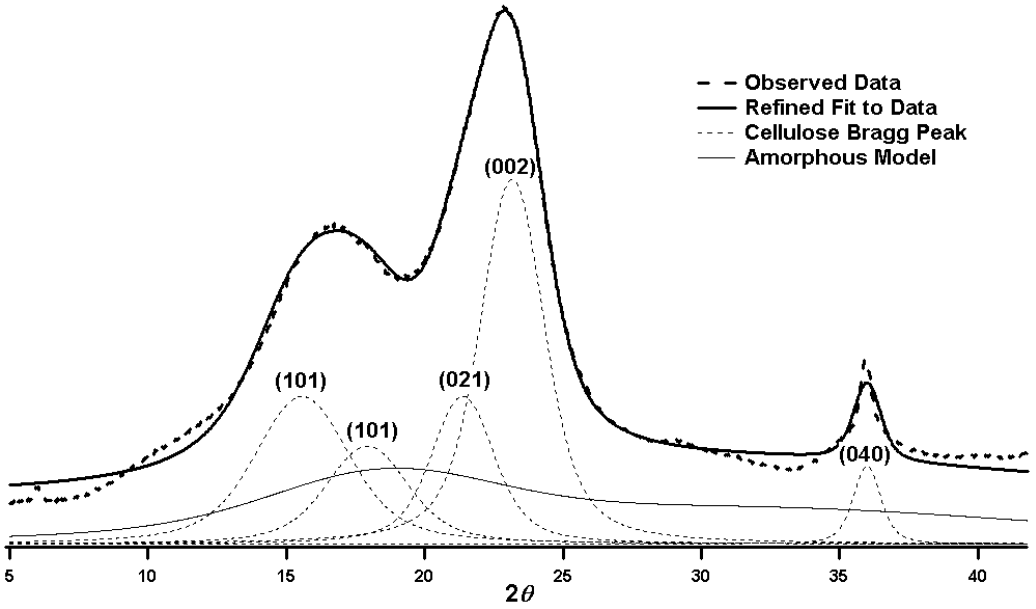

Figure 5-4 – Deconvoluted WAXS pattern for sector averaged palm fibre data.

Five peaks were used to fit the cellulose reflections in the patterns between 10° and 40° in 2θ (For a Cu K_α x-ray source, λ = 1.541 Å). A Voigt profile was placed in the approximate position of the five reflections based on literature values (Nishiyama et al., 2002; Nishiyama et al., 2003). These profiles were allowed to refine on the basis of peak position (within 1% of initial value), width (within 10% of initial value) and intensity (within 25% of initial value) to provide good fits to the experimental diffraction data.

The amorphous model used in the peak fitting is based on the literature findings related to the diffraction of amorphous materials (Hermans and Weidinger, 1950). Two Voigt profiles were used to build up this model with fixed 2θ values (18° and 32°). These peaks were allowed to refine in intensity by 25 % and in width by 10 %. The amorphous model is built up on the assumption that the resulting diffraction pattern of non-crystalline material is dominated by the correlations between C-C bonds and the will not be sensitive to specific chemistry (Hermans and Weidinger, 1950). Hence the scattering from lignin will be much the same as the scattering from any other organic polymer.

In Figure 5-3 and Figure 5-4 the Bragg peaks from cellulose have been labelled. From observation of the patterns there appears to be little difference in these peaks.

The amorphous model on the other hand seems to be less intense in Figure 5-4. This was quantified in the ratio of the (002) intensity to the amorphous intensity. The ratio of intensities in the radial pattern was 3.32 while the sector average was 6.03. This suggests much less amorphous material in the sector averaged scattering pattern. However as these patterns are from the same scattering data it was assumed that the change in amorphous content was due to the sector averaging.

While the amorphous content could be accounted for it was important that the width of the crystalline peaks were not altered as a result of the averaging procedure. Because the crystallites present are so small it results in a very large sample based broadening of the peaks. The Scherrer equation (equation 2.2) was used to make a calculation of the approximate lateral dimensions of the microfibril from the two patterns. The FWHM values were corrected for instrumental broadening as discussed in Chapter 4.1.1.

	2θ	FWHM	Crystallite Width (nm)
Radial	23.25	2.28 ± 0.1	4.0 ± 0.2
Sector	23.16	2.22 ± 0.1	4.1 ± 0.2

Table 5-1 – Results of the Scherrer analysis of the (002) reflection from Figure 5-3 and Figure 5-4.

The peak parameters from the two data sets were used to calculate the lateral dimensions of the microfibril. In Table 5-1 it can be seen that calculated values agree with each other within the uncertainty of the calculation. From this it was assumed that the radial and sector averaged data would produce the same value for the lateral dimensions of the microfibril. Radial averages were used due to the extra computation required of sector averaging.

5.1.2 Results from Radial Averaging

Radial averages were made for all WAXS patterns collected from the palm fibre samples at the ANSTO facility (Figure 5-5).

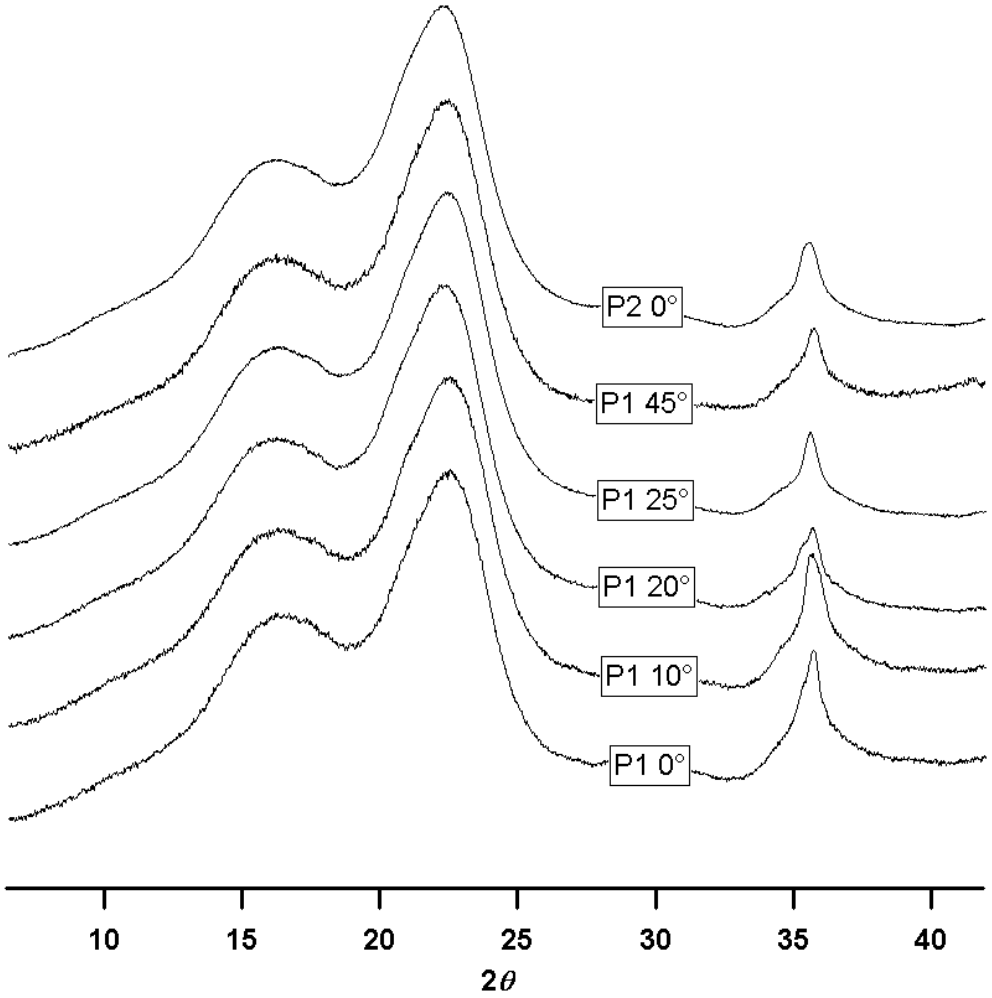

Figure 5-5 – Patterns from the two dimensional WAXS measurements from a single palm fibre.

All patterns collected were deconvolved using the same set of cellulosic peaks and amorphous model described previously. From these peak fitting routines the parameters for 2θ and the full width at half maximum (FWHM) were used to calculate the lateral dimensions of the microfibril based on the Scherrer equation as applied to the (002) reflection (Figure 2.3). The FWHM values were corrected for instrumental broadening as described in Chapter 4.1.1.

Point	Rotation (°)	2θ (°)	FWHM (°)	Crystallite Width (nm)
1	0	22.85	2.38 ± 0.1	3.8 ± 0.2
1	10	23.01	2.62 ± 0.1	3.4 ± 0.2
1	20	22.88	2.35 ± 0.1	3.8 ± 0.2
1	25	22.92	2.48 ± 0.1	3.6 ± 0.2
1	45	23.06	2.54 ± 0.1	3.5 ± 0.2
2	0	22.78	2.57 ± 0.1	3.5 ± 0.2

Table 5-2 – The average crystallite width in the (002) plane measured for WAXS patterns collected from the palm fibre sample on a Bruker Nanostar.

The calculated values from the radial averaging of the palm fibre data are presented in Table 5-2. In this table it can be seen that scattering patterns were collected from two points. The measured FWHM value for the (002) peaks in these two scattering patterns agreed with each within the uncertainties of the fitting routines. The uncertainties given in Table 5-2 have been estimated from the 95% confidence intervals of the peak fitting routines (Appendix Two). The FWHM was compared for the five peaks on position 1 at different rotation angles. Similarly there was good agreement between the FWHM values obtained for these patterns.

The WAXS patterns collected from position 1 were noticeably different at the (040) reflection (Figure 2.3). The intensity of this reflection seemed to vary as a function of the rotation angle. This result highlights the difficulties in using a radial average to reduce anisotropic data as the result is not strictly a powder pattern. However the varience observed in the (040) is not observed in the (002) reflection which is often of more use in cell wall polymer investigations.. For comparison the WAXS patterns were normalised with respect to the (002) reflection and compared to the (040) intensity.

Point	Rotation (°)	(002) Intensity	(040) Intensity	(002) : (040)
1	0	54.06	22.65	2.4
1	10	58.02	22.88	2.5
1	20	58.05	15.30	3.8
1	25	60.17	12.49	4.8
1	45	54.24	26.79	2.0

Table 5-3 – The ratio of the (002) intensity to the (040) intensity from WAXS patterns at different rotations.

The values for the ratio of the (002) intensity to the (040) intensity presented in Table 5-3 showed variations between rotation angle. The greater (002):(040) ratio the smaller the relative intensity of the (040) reflection in the deconvoluted WAXS pattern. In general the relative intensity of the (040) reflection decreased as a function of the rotation angle up to a rotation of 25°. The (040) reflection for the data at 45° rotation angle had a higher relative intensity.

5.1.3 Meylan's Equation Vs Yamamoto's Equation

The measurements were averaged in the azimuthal direction around the (002) crystallographic plane. The width of the two prominent peaks from this average was used to determine the *T* parameter as described in section 2.3.5 (Figure 2-10). In Stuart and Evans paper (1995) two equations were identified that use the *T* parameter to calculate the MFA; the Meylan equation (equation 2.37) and the Yamamoto equation (equation 2.38). To compare these equations consider the hypothetical *T* values in Table 5-4.

T (°)	Meylan MFA (°)	Yamamoto MFA (°)
5	3.0	-16.1
10	6.0	-2.0
15	9.0	7.3
20	12.0	13.0
25	15.0	16.3
30	18.0	18.3
35	21.0	20.3
40	24.0	23.4
45	27.0	28.7
50	30.0	37.6
55	33.0	51.1
60	36.0	70.4
65	39.0	96.8
70	42.0	131.4
75	45.0	175.3

Table 5-4 – A comparison of the results from equation 2.37 (Meylan) and equation 2.38 (Yamamoto) for a hypothetical *T* value.

In the table above there is good agreement between the two equations calculated MFA between a *T* value of 25° (MFA ≈ 15°) and 45° (MFA ≈ 27°). In general outside this range the values obtained from the Yamamoto equation fall outside the expected values from the model of the cell wall adopted for defining the microfibril angle (Figure 1-3 and 2-9); i.e. a value between 0° and 90° was expected.

Stuart and Evans (1995) note that the Yamamoto equation was put forth as a revision on the Meylan equation to more accurately determine the MFA. This might suggest that in the specified range equation (2.38) gives a better value for the MFA than equation (2.37). However as noted above this difference is at most 2°. The paper

highlights the need for a secondary technique for comparison in order to calibrate the magnitude of the MFA. There is an absence of such a secondary technique here however this was considered acceptable given that the absolute values were not considered as important as the comparison between measurements.

In the analysis that follows equation 2.37 has been used exclusively to calculate the MFA from azimuthally averaged x-ray data. This was done because equation 2.38 appears to be valid over a limited range of values for the parameter *T*. Although perhaps a better option for a certain range equation 2.38 was not applied selectively to some regions as the comparison between data points was of most concern and so a single equation was selected with the aim being to keep any uncertainties related to the calculation consistent.

5.1.4 Results from Azimuthal Averaging

The calculation of an orientational parameter (i.e. MFA) was made from the two dimensional diffraction data. To calculate the average MFA in the illuminated volume the azimuthal average is taken of the two dimensional data as described previously in Chapter 2.2. The azimuthal average of the 002 reflection collected from the position 2 scattering pattern of the palm fibre sample during sample rotation is shown in Figure 5-6. The five WAXS patterns for the series of rotations at position 1 have been presented on a single axis for better comparison (Figure 5-7).

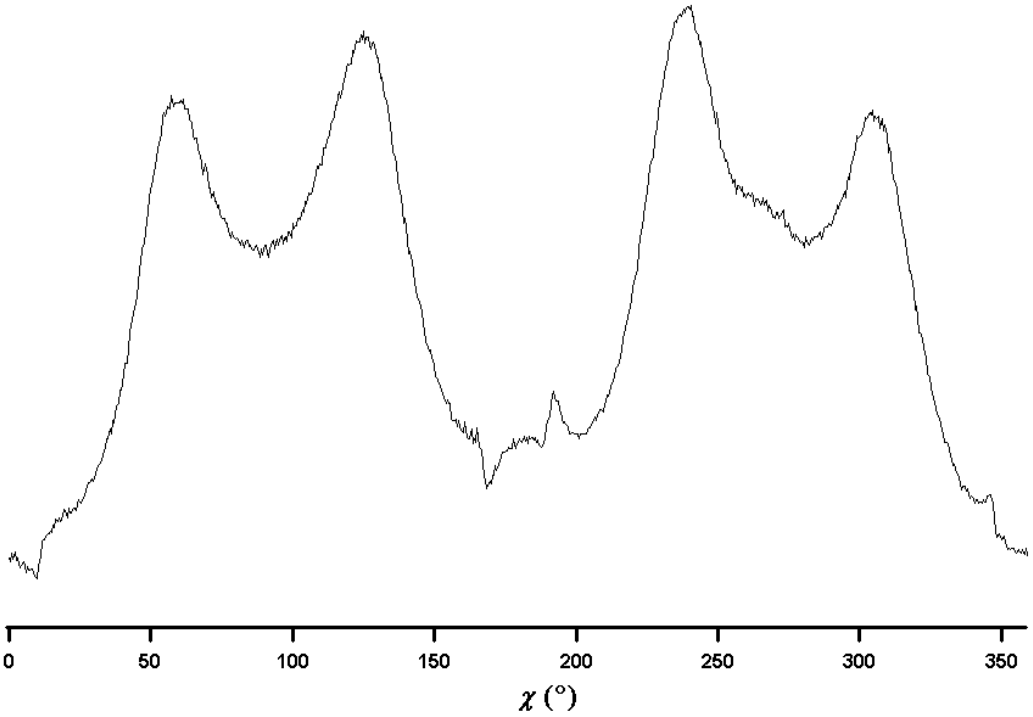

Figure 5-6 – The azimuthal average of the WAXS pattern from position 2 of the palm fibre samples (graph showing an arbitrary intensity on the *y*-axis).

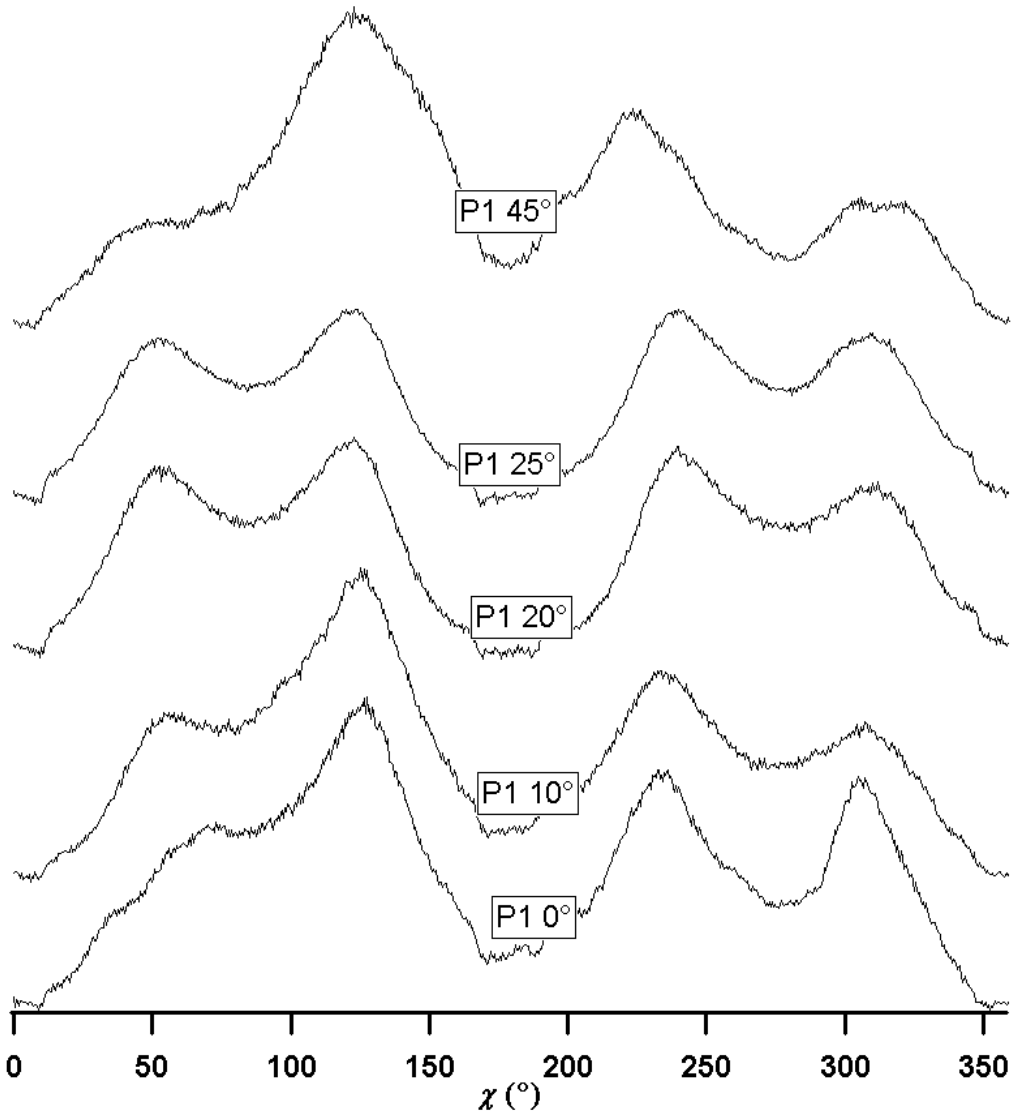

Figure 5-7 – The azimuthal average of the WAXS patterns collected from position 1 of the palm fibre samples with different rotations (graph showing an arbitrary intensity on the *y*-axis).

The appearance of the azimuthal profiles from palm fibre data were characteristic of the profiles obtained from cellulose samples with a small rectangular cellular cross section. In general the effects of cell size become more apparent with larger cell sizes (Meylan, 1967). It was observed that as the sample was rotated the intensity of some of peaks change, in particular the peak at ~50° azimuthal angle. As the patterns are symmetric the MFA was calculated from the peaks greater than 180° in the azimuthal profiles. These peaks were located at approximately 230° and 305°. The breadth of these peaks resulted in a significant overlap between them. The two peaks were imagined as the component parts of a single peak and the width of this peak used for the measurement of MFA from the palm fibre. The method involved measuring tangents on the outer sides of the two peaks and extrapolating them to the x-axis. The

distance between these two intercepts gave the value of 2*T*, *T* being directly related to the MFA (Martinschitz *et al.*, 2006).

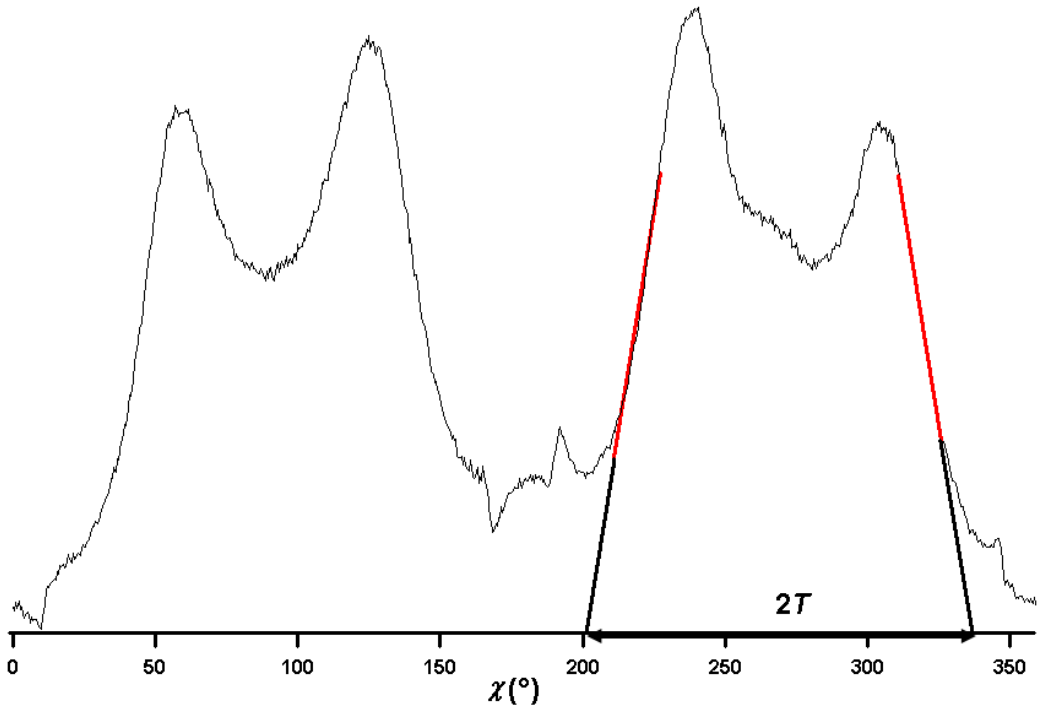

Figure 5-8 – The definition of the parameter 2*T* used to calculate the MFA in palm fibre data. 2*T* is calculated from the fitting of linear regions on the outer slopes of the peaks (graph showing an arbitrary intensity on the *y*-axis).

After the parameter *T* was calculated for each data set the average MFA could be calculated. The relationship between *T* and MFA is given by equation 2.37. The results from this analysis are summarised in Table 5-5.

Point	Rotation (°)	2T (°)	MFA (°)
1	0	190.4	57.1
1	10	194.6	58.4
1	20	196.2	58.9
1	25	195.7	58.7
1	45	198.8	59.6
2	0	182.4	54.7

Table 5-5 – Summary of the average MFA values for the data collected from a sample of palm fibre.

This method was used to calculate an average of a distribution of MFA values. The uncertainty of this value is often given in the literature as the standard deviation of the distribution (Cave, 1966). The standard deviation is also related to the *T* parameter and can be as much as 15°. Given this level of uncertainty the

measurements were in good agreement. The agreement between point one and two was within the upper bounds of uncertainty. This would suggest that there is no measurable change in the MFA over this region of the palm.

5.1.5 Discussion of WAXS Results

One of the challenges of investigating cellulose crystallite widths using a peak broadening approach is that the peaks are so broad they overlap and must be deconvoluted to properly determine their width. The approximate positions of the prominent cellulose reflections have previously been identified and this *a priori* information is crucial in the peak fitting procedures employed.

The (002) reflection (Figure 2.3) was used as a way of measuring the width of the crystallites. This was because the (002) reflection is normal to the crystallite and is more clearly resolved. Using this property of the (002) reflection, it was possible to calculate a first approximation for the width of cellulose mircofibril in the palm fibre based on the scattering data. The refinement of scattering data described above resulted in a calculated 2θ value and FWHM value for the (002) reflection. The average width of the microfibrils illuminated by the beam was calculated from these observed parameters.

The results summarised in Table 5-1 showed little difference between the lateral dimensions of the microfibrils from two different points (separated by an order of magnitude relative to the beam footprint). The lateral dimensions of the crystallite are linked to the synthetic processes that produce cellulose microfibrils for the cell wall (Hotchkis and Brown, 1987). In a particular sample it was assumed that the synthetic process at one end of the fibre would be the same along all points of the fibre (i.e. the rosette complexe is the same for the whole sample). Hence the agreement of the data between two different points of the fibre was the expected outcome.

There was some difference observed in the scattering patterns obtained from rotation of the palm fibre. When the rotated data was observed together the (040) reflection (Figure 2.3) seemed to be decreasing in intensity as the angle of rotation increased.

This reflection is the most sensitive to orientational effects as the planes are normal to the microfibril axis (Cave, 1966). It is also the only plane in the cellulose crystal that is purely normal to the long axis. The rotation of the palm fibre in the path of the x-ray beam alters the orientation of the crystallite planes as they are illuminated. This rotation of the sample modulates the intensity of the (040) peak and this is observed as a decrease in the intensity of the peak relative to the (002) peak.

The measurements made on the palm fibre sample were used to measure the MFA. These results were consistent when different positions on the fibre were compared and when a single position was compared with varying rotation angles. The spread of MFA values at position 1 with a varying rotation angle was from 57.1° to 59.6° with the average being 58.5° and having a standard deviation of 1.8°. This difference in measured MFA values is well within experimental uncertainty. The difference between position 1 and position 2 (57.1° and 54.7° respectively) at 0° rotation are also in good agreement.

The measurements of MFA for the palm fibre are quite large compared to the literature values of MFA for wood samples as summarised in Reiterer (1998) and Barnett and Bonham (2004). This larger MFA observed in the palm fibre samples is most likely a result of the fibres not requiring high compressive strength. The MFA values observed here are compared to those measured by SAXS below. However the results are not in good agreement as discussed in detail in section 5.1.7

5.1.6 Small Angle X-Ray Scattering Results

SAXS measurements are a good complementary structural probe for the wide angle scattering experiment. The details of the experiment that produced these results can be found in Chapters 3.1 and 4.2. The SAXS data was analysed to obtain information on the arrangement of the polymers in the cell wall (Chapter 2.3.3). As discussed in Chapter 2.3.1 (Table 2.1) the contrast in SLD between the cell wall polymers is significantly smaller than the contrast between cell wall polymers and voids in the sample. It was assumed that the scattering observed was due to the voids present in the palm fibre sample.

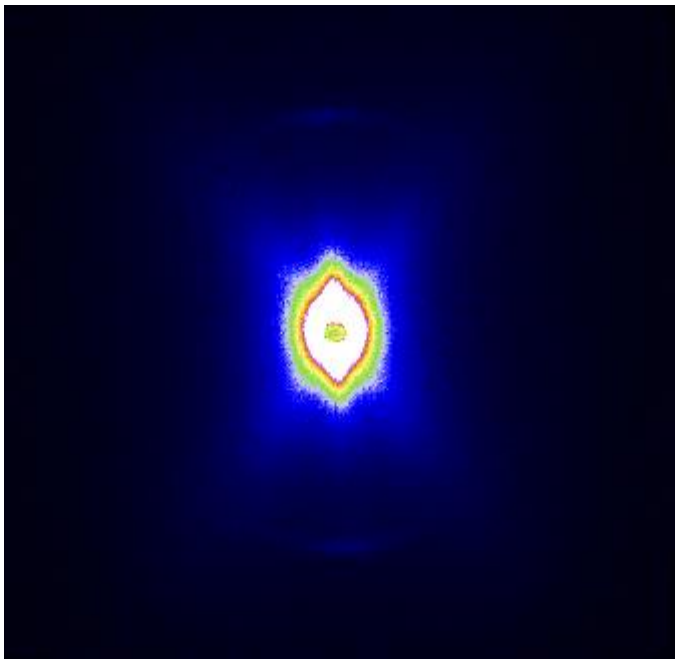

Figure 5-9 – Two dimensional SAXS pattern from 34.6 mm along the the palm fibre with 0° rotation.

The SAXS pattern in Figure 5-9 was typical of the patterns collected from the palm fibre sample. Several measurements were made along the length of the fibre and were labelled with a distance from an arbitrary origin within the sample chamber. The measurements started at one side of the fibre (labelled 34.6 mm) and moved along the length of the fibre to include the points 35.0 mm, 35.5 mm, 36.0 mm, 36.5 mm and 37.0 mm. Of these points the one labelled 34.6 mm was the site of several measurements that involved rotation of the palm fibre in the path of the x-ray beam (0°, 25° and 45°). In total eight small angle scattering measurements were conducted on the palm fibre with three comparing the patterns for a rotated sample and five comparing the patterns along the length of the sample.

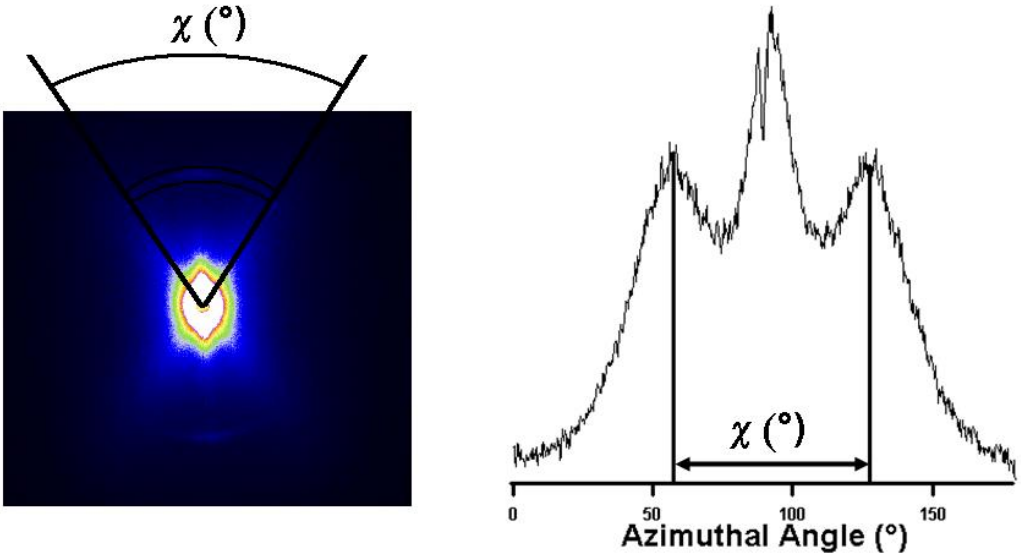

Figure 5-10 – Calculating the angle between the two streaks corresponding to the S2 layer in the palm fibre cell involves the azimuthal averaging of the SAXS pattern. The azimuthal average was taken with the inner and outer radius displayed on the 2D pattern (left).

The azimuthal average was used to obtain the angle between the two streaks corresponding to the S_2 layer. In Chapter 2.3.3 the angle between the two S_2 streaks was used to calculate the MFA (equation 2.61). The calculated MFA value is an average of the values for the cells within the illuminated volume (upwards of 200 cells). A summary of the calculated MFA is presented below.

Position (mm)	Rotation Angle(°)	Collection time	χ (°)	MFA (°)
34.6	0	15 hours	69.54 ± 2.5	34.8 ± 5
34.6	25	3 hours	77.64 ± 2.5	38.8 ± 5
34.6	45	15 hours	82.00 ± 2.5	41.0 ± 5
35.0	0	30 mins	69.48 ± 2.5	34.7 ± 5
35.5	0	30 mins	68.86 ± 2.5	34.4 ± 5
36.0	0	30 mins	74.66 ± 2.5	37.3 ± 5
36.0	0	5 mins	77.04 ± 2.5	38.5 ± 5
36.5	0	5 mins	73.18 ± 2.5	36.6 ± 5
37.0	0	5 mins	74.42 ± 2.5	37.2 ± 5

Table 5-6 – The calculated MFA values from SAXS measurements of a palm.

There was good agreement between those points with a 0° rotation angle (varying between 34.4° and 38.5° over the seven measurements with the same rotation angle). There was slightly more variation between the measurements comparing a single point on the fibre with a varying rotation angle. These three measurements at 34.6 mm range from 34.8° to 41.0°.

The uncertainties associated with these measurements are related to the width of the streaks. As the calculated MFA is an average of all the cells in the volume there will be a distribution of values in the sample and the more variation in the distribution (i.e. the wider the streak) the greater the associated uncertainty (Reiterer *et al.*, 1998). Uncertainties were estimated to be ~5° based on the width of the peak, the 95% confidence intervals for fitting and literature reports (Lichtenegger *et al.*, 2001). Exact uncertainties were not calculated for the MFA as the comparison of the values between points was of more interest than the individual values. It was assumed that peak fitting uncertainties were the major components to the MFA uncertainty and hence consistent across all measurements.

5.1.7 Discussion of SAXS Results

The MFA was observed along the length of the palm fibre. This was based on the assumption that the mechanical properties of a cell wall material are linked to the spiral angle of the microfibrils in the S2 cell wall layer. From the minimal variation in the MFA along the length of the palm fibre it is predicted that there are no significant difference in the mechanical properties in this range.

The palm fibre was rotated in the path of the beam to investigate the effect of a non-orthogonal beam on the measured MFA in both SAXS and WAXS experiments. The MFA is defined with respect to the cell axis and it would be expected that this shouldn't change as a result of the angle of the incident beam. It was observed that the calculated MFA increased as the rotation angle increased.

Although SAXS and WAXS are related techniques there is a fundamental difference in what is being measured. While WAXS patterns measure the scattering of x-rays based on the crystallinity of the sample SAXS patterns are formed due to fluctuations in the electron density of the sample (Glatter and Kratky, 1982). This distinction is particularly significant for cell wall materials as the electron density difference between the polymers in the cell wall is small relative to the difference between polymer and voids (air).

The literature suggests there are three regions of notably different electron density; the cellulose microfibril ($\rho_C \approx 5 \times 10^{23}$ cm^{-3}), a lignin-hemicellulose matrix ($\rho_M \approx 4.6 \times 10^{23}$ cm^{-3}) and voids in the sample (electron density equal to zero) (Jakob *et al.*, 1994). In general there are two length-scales for voids in cell wall materials; those of the cell lumen (which are too large to be observed by SAXS) and the nanoscale pores that are present in the cell wall for nutrient and water transportation (Garvey *et al.*, 2006; Jakob *et al.*, 1994) .

Given that pores in the cell wall can have a diameter in the nm range then the electron density contrast between the cell wall polymers and the voids will dominate the SAXS profile. Given the degree of anisotropy observed in the SAXS patterns it is reasonable to assume that these pores have a preferred orientation much like the S2 microfibrils. The values for the MFA calculated in Chapter 5.1.5 were based on the assumptions and work of Jakob *et. al.* (1994). However these studies correlate the mechanical properties to the MFA observed in wood. Given the differences in cell structure between the palm fibre and wood it does not seem likely that this orientational parameter can be called the MFA. It is more likely that the orientational parameter is related to the preferred orientation of the pores in the sample and while this could be related to the orientation of microfibrils in the S2 layer it is not the same parameter. This could also explain why the MFA calculated from WAXS data in Chapter 5.1.4 do not agree with SAXS calculations.

5.2 WAXS & NMR Measurements of NaOH Treated Palm Fibres

5.2.1 Results from Radial Averaging of WAXS Patterns

WAXS measurements (Chapter 4.1) were made on a sample of palm fibre before and after treatment with NaOH solution (Chapter 3.1). These measurements were made to investigate the effect of the treatment on the sample with a focus on delignification. WAXS was used as a way to observe the crystallinity of the sample before and after treatment. These measurements were conducted at the Australian Synchrotron and the two dimensional data typically produced is shown in Figure 5-11.

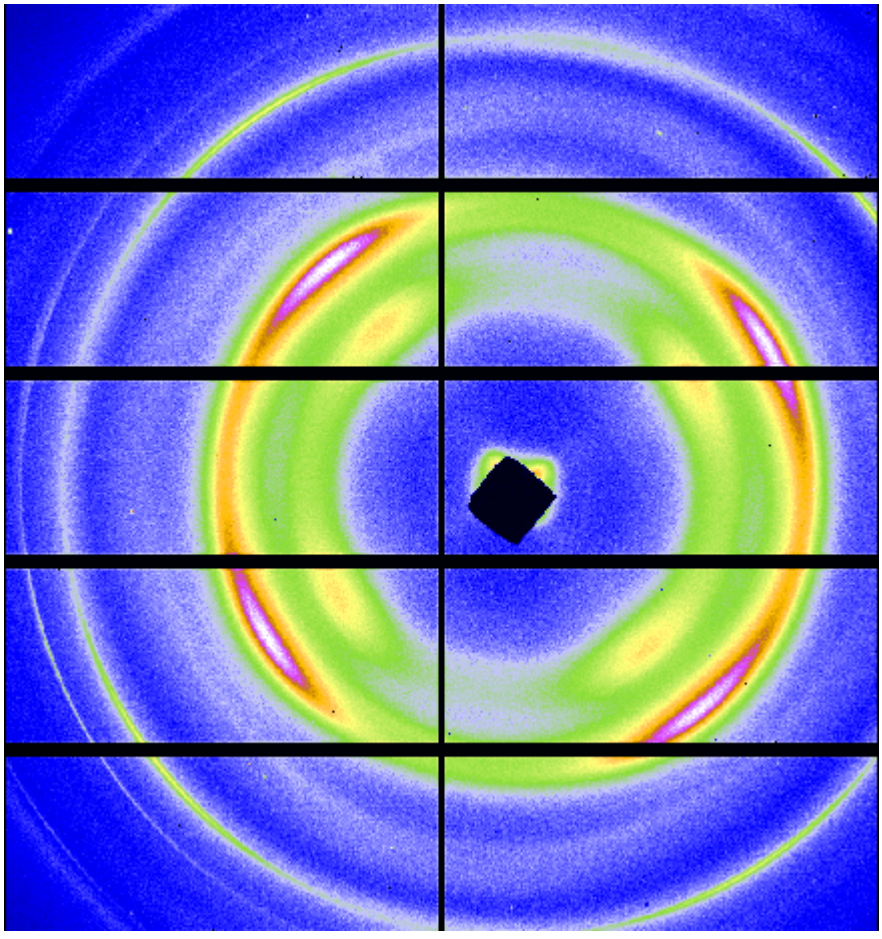

Figure 5-11 – Two dimensional data of the palm fibre sample recorded at the Australian Synchrotron.

The data presented in Figure 5-11 is from the Dectris – Pilatus on the SAXS/WAXS beam line. Although the diffraction patterns looked different to those collected from

image plates in Chapter 5.1 features such as the (002) and (040) reflection were still observable. This set of two dimensional data proved to be difficult to analyse in terms of the orientation of cellulose microfibrils. The azimuthal averaging normally performed is based on radially symmetric diffraction rings and hence was not used here due to difficulties in processing the gaps in the detector. Instead the analysis of this data focused on the radial averages of the diffraction patterns, corrected for the distortion of the peaks.

The WAXS patterns before and after NaOH treatment were radially averaged to produce one dimensional data.

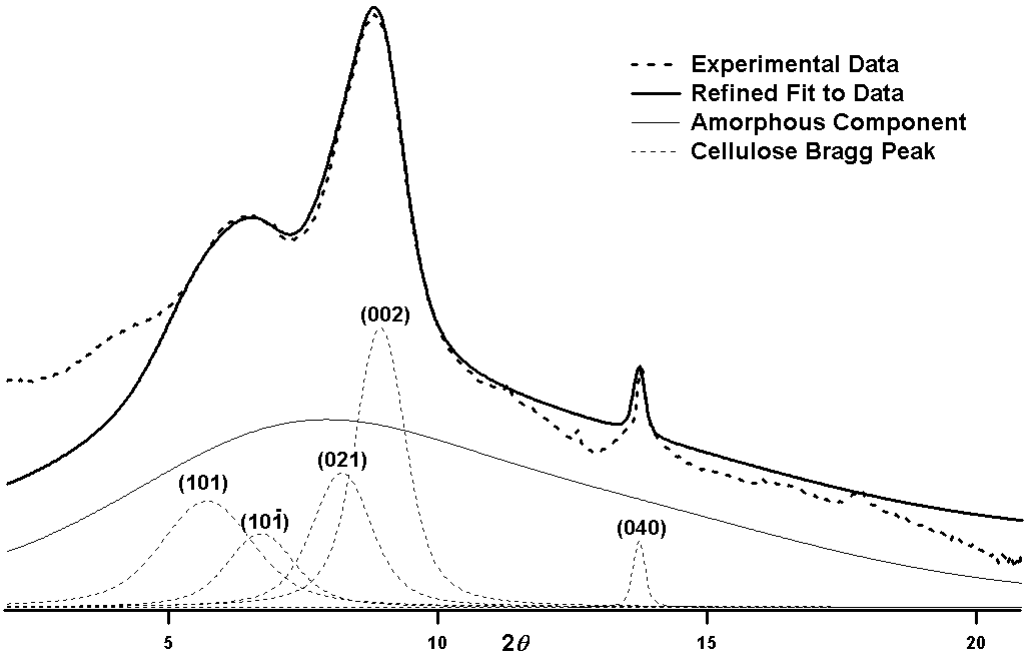

Figure 5-12 – Deconvoluted WAXS pattern of untreated palm fibres.

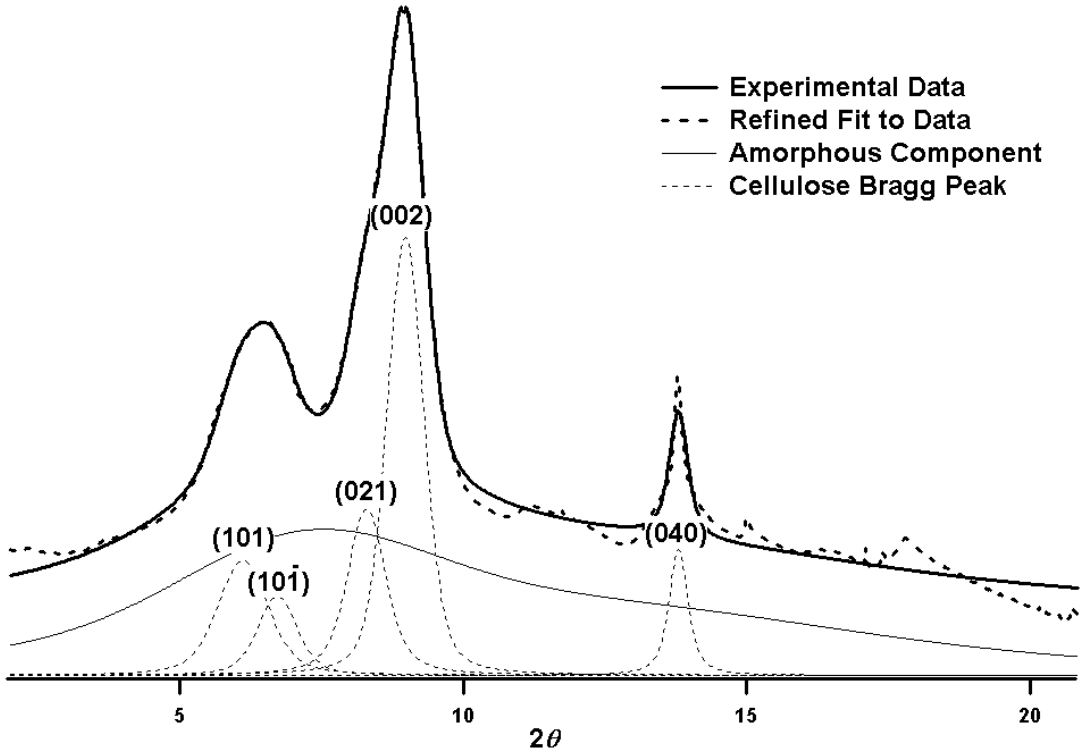

Figure 5-13 – Deconvolved WAXS pattern of treated palm fibres.

Figure 5-12 and Figure 5-13 were observed to have the component with the characteristic shape of the WAXS patterns from cellulose in an amorphous matrix. However it was noted that the positions of the peaks in 2θ were not the same as those previously encountered. This was attributed to the wavelength of the synchrotron radiation being much lower than the CuK_{α} x-ray sources of lab based instruments previously described. To obtain a pattern independent of the wavelength the *q*-scale can be used (units $Å^{-1}$) (equation 2.38).

Estimates for the initial 2θ values for the cellulose Bragg peaks were found in the literature to begin the peak fitting procedure (Garvey *et al.*, 2005b). These initial estimates for the peak centres in 2θ were allowed to refine to within 1% of their initial value. The other parameters were adjusted manually to give the best "eyeballed" fit to the data and then allowed to refine (within 5% for width and within 10% for intensity).

The scattering data from the untreated and treated fibres were deconvoluted to separate the crystalline Bragg peaks and amorphous signal. The parameters from these peak fitting routines were used to calculate the lateral dimensions of the

microfibrils based on the Scherrer equation (equation 2.2). In addition to the microfibril dimensions the ratio between the crystalline intensity and amorphous intensiy were also compared.

Sample	2θ (°)	FWHM	Crystallite Width (nm)	(002) : Amorphous
Untreated	8.93	1.11 ± 0.1	3.2 ± 0.2	2.6
Treated	8.98	0.77 ± 0.1	4.6 ± 0.2	19.1

Table 5-7 – A comparison of the results from WAXS scattering for untreated and treated palm fibres. The (002) : Amorphous data is a ratio of the intensities of the (002) Bragg peak to the amorphous signal.

The calculated crystallite dimensions in Table 5-7 do not agree with each other in the range of uncertainty, suggesting that the NaOH treatment altered the crystallite structure of the cellulose. However this does not agree with what is known about cellulose crystallites, i.e. they are not weak acid/base reactive (Fengel and Wegener, 1989). A possible explanation is that the width measured for the treated sample is due to the aggregation of cellulose crystallites after the amorphous content has been removed. This could only be possible if the material between crystallites (the amorphous polymers) is no longer occupying space between adjacent microfibrils. The ratio of intensities between crystalline and amorphous signals was calculated. The higher the number the more crystalline material is present as a proportion of the sample. As extra crystalline material cannot be created by the treatment it strongly suggests a decrease in the amount of amorphous material after treatment.

5.2.2 Discussion of WAXS Results

The scattering data from the untreated palm fibre (Figure 5-12) showed a strong amorphous profile relative to the crystalline (002) reflection. As with other scattering data from cellulose the Bragg peaks that were observed are quite broad and prone to overlapping. The large amorphous component to the diffraction pattern compounded the problem giving the appearance of a very poorly resolved piece of data. Deconvolution of the data allowed the crystalline peaks to be separated from the amorphous signal. After separating the crystalline and amorphous components of the scattering pattern the results before and after treatment were compared.

From observation of the WAXS data before and after NaOH treatment it was seen that the treated sample contains less of an amorphous signal than the untreated sample. The reduction in amorphous background can be attributed to the NaOH treatment removing much of the non-crystalline material present (specifically lignin). In order to quantify this observation the intensity of the (002) Bragg peak was compared to the intensity of the amorphous signal for the two sets of data (Table 5-7). The increase in the ratio between the (002) intensity and the amorphous signal in the treated fibre was believed to be evidence of the removal of lignin as a result of the treatment.

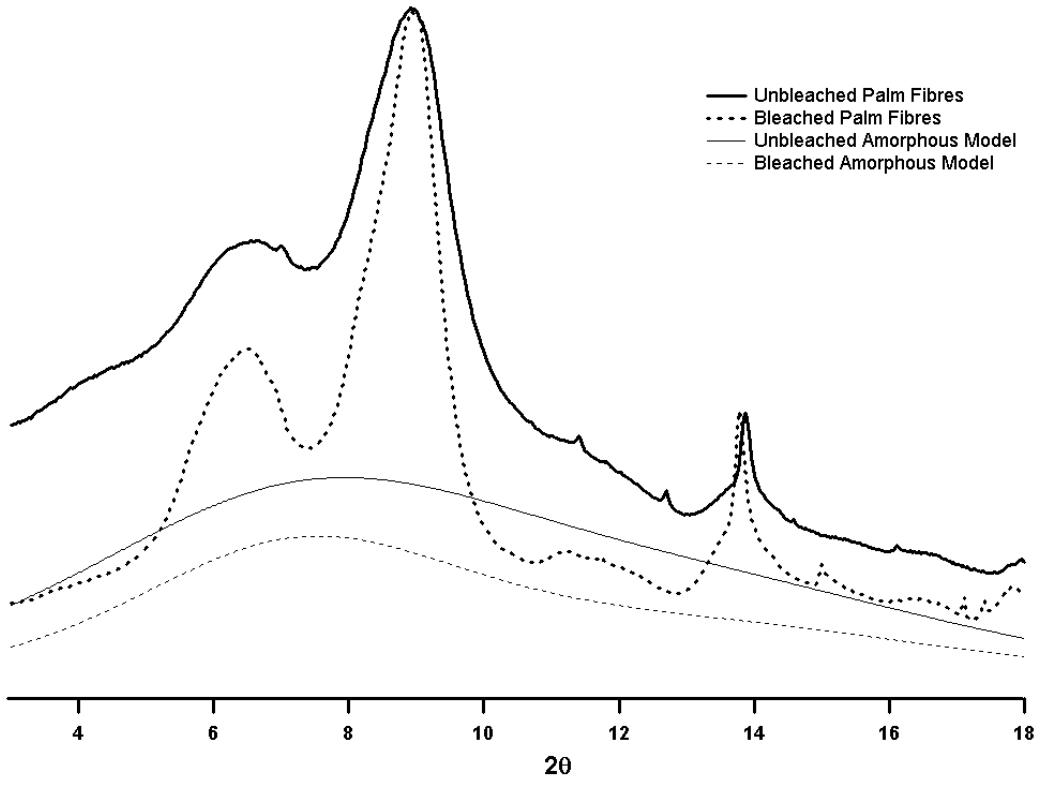

Figure 5-14 – WAXS patterns for the palm fibre before and after NaOH treatment with associated amorphous component to the scattering pattern.

The effect of NaOH treatment on the palm fibres can be better observed by plotting the before and after scattering patterns on a single axis. In Figure 5-14 the amorphous component of the scattering has been added to the before and after patterns. The decrease in amorphous scattering in the treated sample has corresponded to sharper looking Bragg peaks (i.e. more crystalline).

While the WAXS data for the treated and untreated palm fibre samples indicates a loss in the amorphous component due to the treatment it cannot distinguish specific polymer(s) on the basis of chemistry. In order to examine the chemical changes that might be occurring as a result of the treatment NMR spectra were recorded of the samples.

5.2.3 Results from CP-MAS NMR Spectroscopy

A spectra of filter paper was recorded to act as a cellulose standard against which the palm fibre samples could be compared.

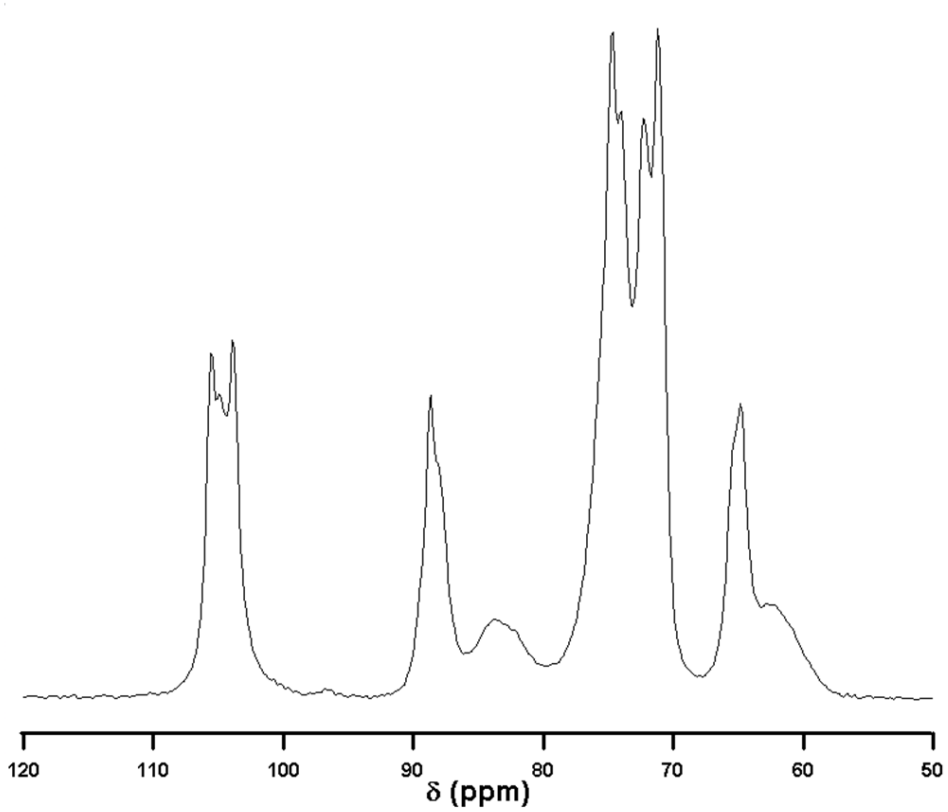

Figure 5-15 – NMR spectra collected from a filter paper sample.

δ (ppm)	Assignment
105.6 - 103.9	Cellulose C1
88.7 - 83.9	Cellulose C4
74.7 - 71.2	Cellulose C2/C3/C5
64.8 - 62.6	Cellulose C6

Table 5-8 – Assignment of the four spectral regions as described by R.H. Atalla and D.L. Van der Hart for the filter paper data given in Figure 5-16.

The spectrum of filter paper (Figure 5-15) showed peaks characteristic of cellulose. Being a very pure form of cellulose, a simplified assignment procedure was used for this data as in the papers by R.H. Atalla and D.L. Van der Hart (Atalla and Van der Hart, 1984) (Van der Hart and Atalla, 1984). In this scheme four distinct regions of the spectra were identified, and assigned to non-equivalent carbon nuclei in the cellobiose monomeric unit (two glucose rings bonded via a β 1→4 linkage). These four regions are described above in Table 5-8. The spectra recorded for palm fibres were more complicated with additional signals due to lignin and other cell wall polymers being present.

The observed signals in an NMR spectrum come from non-equivalent carbon nuclei. The position of these signals varies depending on the specific chemical, physical (e.g. the interior versus exterior of the cellulose crystallite) and dynamic environments that the nuclei exist in (Van der Hart and Atalla, 1984). In the case of cellulosic materials, the prominence of cellulose based signals compared to other materials (due to the amount of cellulose present) such as hemi-cellulose and lignin aids in the assignment.

The carbons in one glucose ring are chemically equivalent to those in another glucose chain in the cellobiose unit or along the length of a cellulose chain. However with the proper application of cross polarisation (signal boosting) and magic angle spinning (signal resolution) techniques the resolution of the spectra can be so improved that it is possible to distinguish between chemically equivalent carbons with non-equivalent symmetries. This was first observed in the early NMR experiments of the 1980's and the spectral regions were identified at this time (Earl and Van der Hart, 1981).

The multiple resonances of the four main spectral regions described can be used to make inferences regarding the crystallography of cellulose. This method typically involves the identification of regions of the spectra for internal cellulose and surface cellulose in the microfibril. This method was not utilised in this study as the data was collected to present a comparison between treated and untreated fibres however an overview of the method is presented in Appendix Three.

The filter paper sample was a well behaved example of cellulosic materials and has been used to establish a methodology for studying the NMR spectra of natural cell wall materials. The sample for which the NMR methodology was established, the palm fibres, had spectra recorded before and after NaOH treatment.

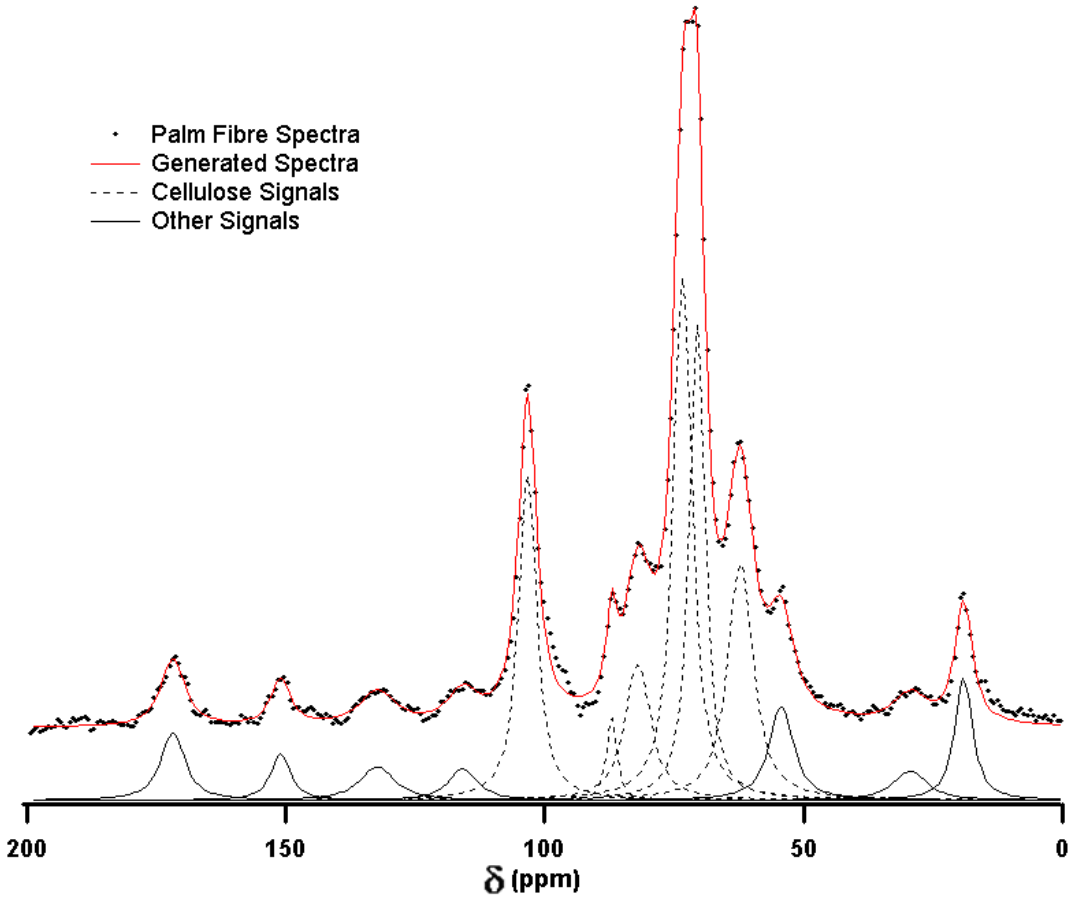

Figure 5-16 – Palm fibre spectra recorded before treatment with NaOH.

Chemical Shift (ppm)	Assignment
171.85	Carbon bonded to a carboxyl group
151.05	Non-ether C3/C5 from Guaiacol & Syringol
132.36	Lignin
115.88	Aromatic Carbon from Guaniacol & Syringol
103.33	Cellulose C1
87.09	Cellulose C4 Interior (Ordered Chains)
82.01	Cellulose C4 Exterior (Disordered Chains)
73.38	Cellulose C2/C3/C5
70.56	Cellulose C2/C3/C5
62.22	Cellulose C6 Interior
54.32	Cellulose C6 Exterior
29.45	Ether linked methyl (-O-CH_3)
19.10	Acetyl CH_3

Table 5-9 – Signal assignment for the palm fibre spectra in Figure 5-19 (Fabbri *et al.*, 1998; Jarvis and Apperley, 1990).

The spectra in Figure 5-16 contained a lot of information regarding the different components of cell wall materials. In particular there were many cellulose peaks observed as well as lignin and some of the products of pyrolysis of cell wall polymers, guaiacol and syringol (Chew and Bhatia, 2008). The signals are summarised in Table 5-9. As with the filter paper spectra the main signals were grouped together into smaller sub-spectra (Table 5-8) (Atalla and Van der Hart, 1984; Van der Hart and Atalla, 1984).

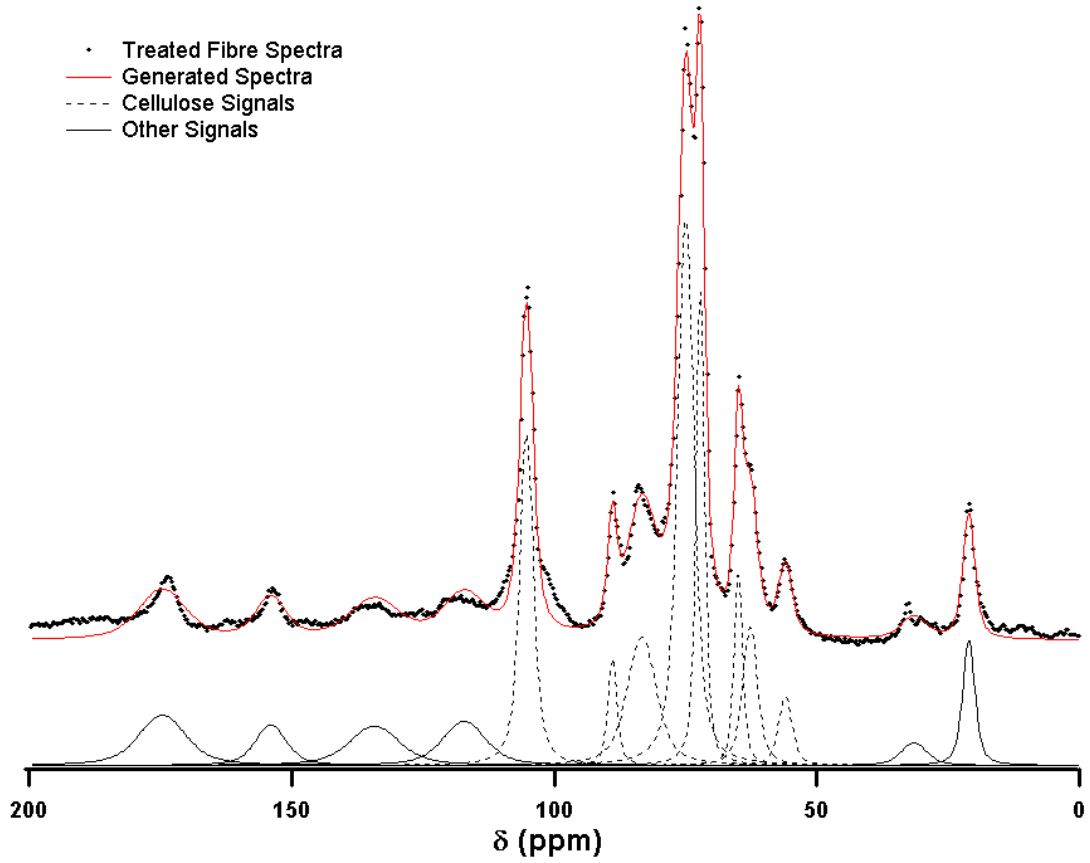

Figure 5-17 – NMR spectra for the palm fibre recorded after treatment with NaOH.

The spectral assignments in Table 5-9 were used for the spectra collected after treatment (Figure 5-17). For ease of comparison the spectra have been plotted on a single axis without the fitted peaks.

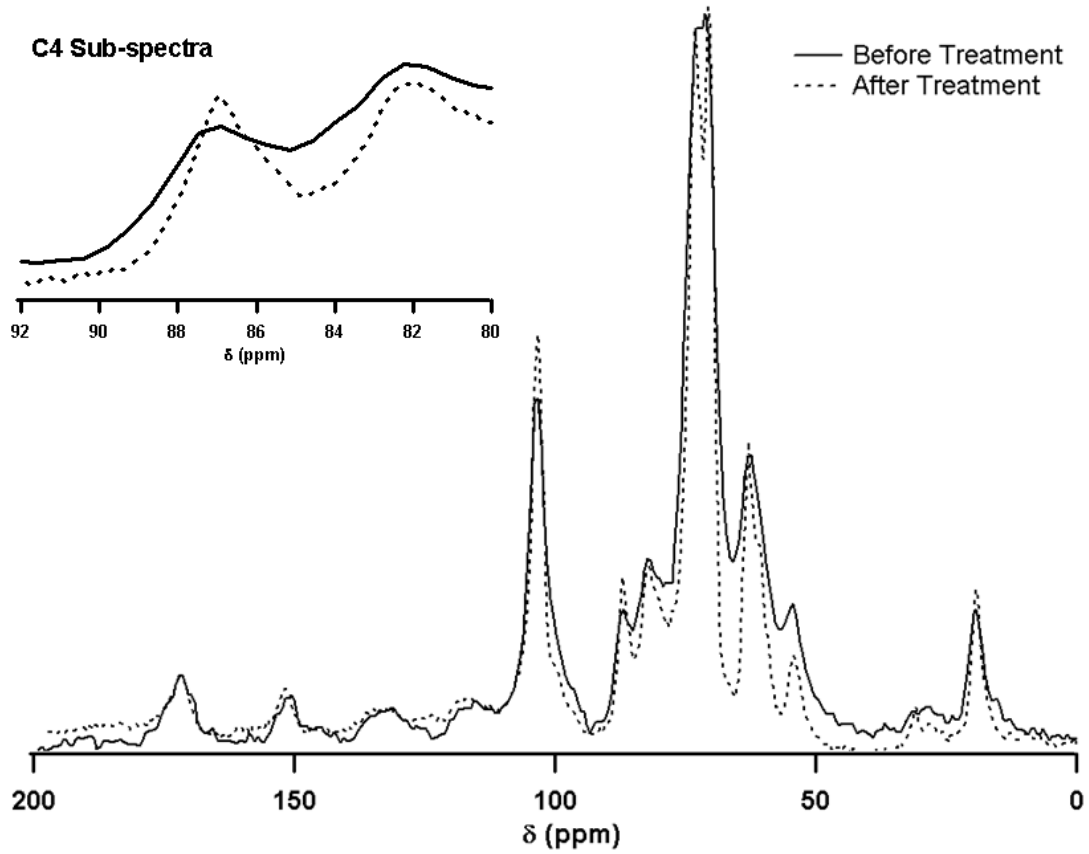

Figure 5-18 – Palm Fibre spectra before and after NaOH treatment. C4 sub-spectra displayed inset.

The spectrum in Figure 5-18 compares the palm fibre sample before and after NaOH treatment. As the C4 region is shown to be particularly important in calculating the lateral dimensions of the microfibril (Appendix Three) this has been expanded and shown inset. It was observed that the C4 region of the spectra had a different appearance than expected based on the filter paper sample. Due to the difficulties in deconvoluting the resonances in the spectra the lateral dimensions of the microfibril were not calculated from NMR data.

5.2.4 Discussion of CP-MAS NMR Results

The CP-MAS technique was used to investigate palm fibre samples to boost the ^{13}C NMR signal and improve the resolution of the observed resonances. The technique was used to measure a sample of filter paper in order to compare with a standard cellulose sample. The measurements from the filter paper sample were successfully analysed based on literature methods, in particular those of Newman (Newman, 1999). The measurement identified key spectral regions from cellulose that were

used in the identification of resonances from palm fibre samples based on the assignments in the literature (Atalla and Van der Hart, 1984; Van der Hart and Atalla, 1984).

The measurement of NMR spectra from palm fibre samples gave resonances attributed to cellulose and other polymers and compounds. In particular the cellulose signals show good agreement in terms of resonance position before and after the treatment. This would suggest that treatment has not had a measureable effect on the cellulose present in the sample. Attempts to confirm this with the measurement of lateral microfibril dimensions before and after treatment were unsuccessful. This was attributed to the difficulty in deconvoluting the complex spectra obtained from palm fibres. It was also observed that the spectra obtained from palm fibre samples before and after treatment did not contain the expected surface and interior resonances for C4 and C6 based on the filter paper analysis.

The calculation of the lateral dimensions of the microfibril was unsuccessful using NMR data however this information has been obtained from WAXS measurements. This highlights the importance of using complimentary experimental techniques. The focus of the analysis therefore shifted to what information could be obtained from the available NMR data. The NaOH treatment of palm fibres had a more measureable impact on the WAXS data than it did the NMR data. It was observed in the WAXS data that a significant portion of the amorphous content of the palm fibre had been removed by NaOH treatment. This observation was expected in the NMR data as well but was more ambiguous.

Figure 5-18 shows good agreement between the resonances attributed to lignin and cellulose before and after treatment. This observation was combined with observation from WAXS measurements that were indicative of a substantial reduction in the amorphous content in the palm fibres. This would suggest that a significant amount of non-cellulosic polysachharides is removed by the NaOH treatment. Although the NMR signals indicated that lignin was still present after the treatment it was not possible to determine how much lignin was present relative to before treatment. Integration of the resonances is a usual method by which the amount of a particular nucleus present can be determined. However the differential

spin-lattice relaxation rates for ^{13}C in different parts of cellulose crystallite nuclei during CP and measurement would make this a prohibitively detailed study (Hill *et al.*, 1994).

The WAXS measurements suggested some amorphous component to the sample was present, which had been decreased by NaOH treatment, but could give no indication what this was. NMR measurements indicated the presence of lignin and cellulose as well as some compounds typically associated as by-products of pyrolysis of cell wall materials (guaiacol and syringol) (Fabbri *et al.*, 1998). It is possible that these compounds were formed during the extraction of oil from the palm trees that produced the palm fibre by-product.

5.3 WAXS & SAXS Measurements from Maturing Native Tree Stems

5.3.1 Results from Radial Averaging of WAXS Measurements

WAXS measurements (Chapter 4.1) were made on samples of maturing native tree stems (Chapter 3.2) and radially averaged as described previously (Chapter 5.1.1). These radially averaged sets of data were used to calculate the lateral dimensions of the cellulose microfibrils in the cell wall (as described in Chapter 5.1.1). With over a hundred diffraction measurements made from the six samples the Scherrer analysis provided rapid results that could be compared within a sample and across samples.

A typical radial average of the two dimensional data collected from the synchrotron is presented below. The (002) reflection was used to calculate the lateral dimensions of cellulose microfibrils in the cell wall of these samples.

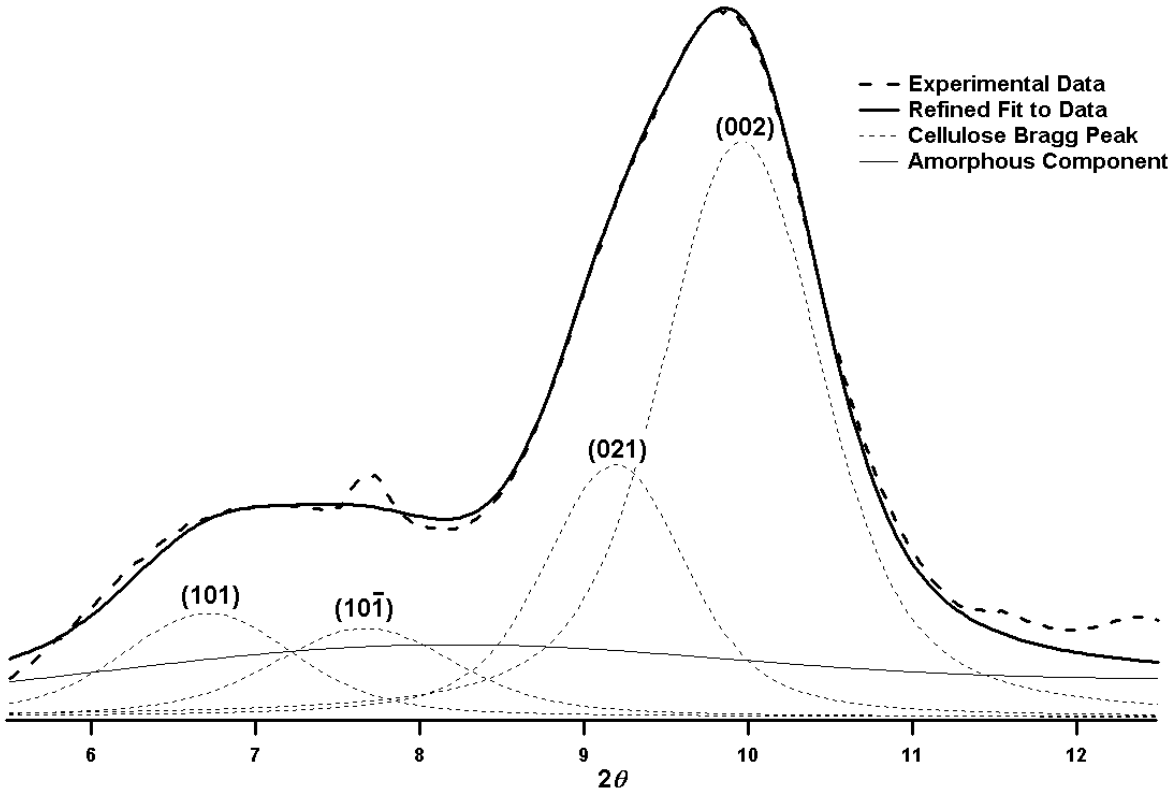

Figure 5-19 – A diffraction pattern from *A. suaveolens* modelled with an amorphous component and Bragg peaks for cellulose.

The WAXS data obtained from the synchrotron is given in terms of the scattering vector *q*. The patterns were converted to be given in terms of the scattering angle, 2θ. The scattering angle is dependent on wavelength and as a result the scale of 2θ in Figure 5-19 will be different to the scale observed in patterns from lab based x-ray generators.

Plots of the crystallite widths obtained from these calculations and using the (002) reflection are presented below in Figure 5-20 and Figure 5-21 (tabulated results in Appendix Four). The error bars associated with these graphs are used to show the standard deviation in the measurements.

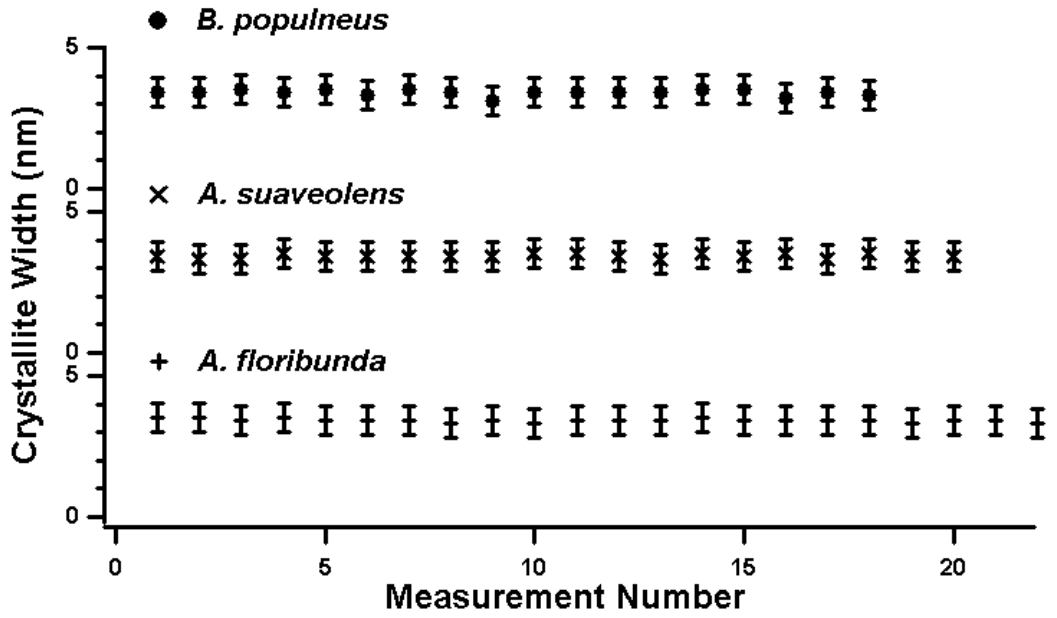

Figure 5-20 – Results of the Scherrer calculations for *B. populneus*, *A. suaveolens* and *A. floribunda*.

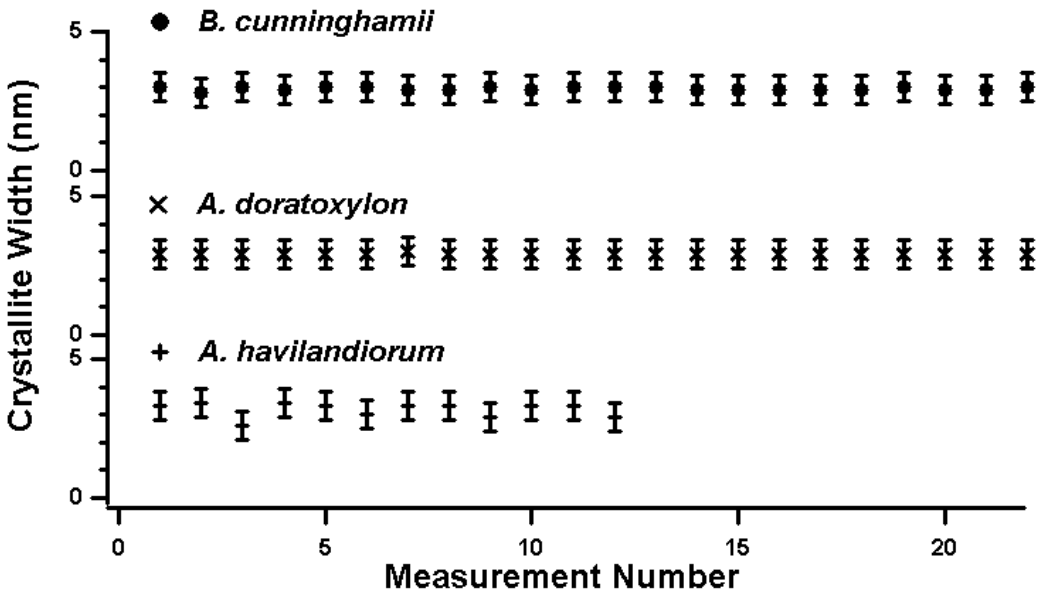

Figure 5-21 – Results from the Scherrer calculations for *B. cunninghamii*, *A. doratoxylon* and *A. havilandiorum*.

The graphs in Figure 5-20 and Figure 5-21 indicated very little variation in the calculated crystallite width within a particular sample. There was also little variation observed between samples and hence the graphs needed to be presented on their own axes to avoid overlapping. Within an individual stem the most variation was observed in the *A. havilandiorum* with a 0.3 nm standard deviation for the measured microfibril widths. The sample with the least variation is *B. populneus*, having a standard deviation of 0.1 nm. There is no observable trend in the measured crystallite size with the measurement position.

5.3.2 Results from Azimuthal Averaging of WAXS Measurements

The WAXS measurements from the maturing stems were used to investigate the orientation of the crystallites. Using the method described in Chapter 5.1.3 the MFA was calculated for the diffraction patterns measured from the maturing stems. The grids of scattering patterns were used to investigate variations in the MFA in two directions; down wood grain and across the wood grain.

	A. floribuna		*A. suaveolens*		*A. doratoxylon*	
Column	**Mean**	**SD**	**Mean**	**SD**	**Mean**	**SD**
1	8.6	0.1	13.9	2.0	8.0	0.3
2	8.3	0.6	13.9	0.8	32.5	1.4
3	8.3	0.3	11.7	0.3	32.5	3.4
4	9.0	0.8	10.9	0.1	32.3	4.7
5			10.3	0.4	32.2	1.5
6					16.0	2.9
	B. populneus		***A. havilandiorum***		***B. cunninghamii***	
Column	**Mean**	**SD**	**Mean**	**SD**	**Mean**	**SD**
1	22.6	0.9	16.6	1.2	23.6	0.5
2	21.1	0.8	8.1	0.5	11.3	1.4
3	20.5	1.3	8	0.7	8.9	0.7
4	23.0	0.9			10.9	1.3
5	25.5	2.5			10.1	0.6
6	23.1	3.1			21.8	1.4

Table 5-10 – The average MFA down each column for the maturing stems. The averages along the grid columns correspond to averages down the wood grain (see Figure 4.3).

	A. floribuna		*A. suaveolens*		*A. doratoxylon*	
Row	**Mean**	**SD**	**Mean**	**SD**	**Mean**	**SD**
1	9.0	0.7	12.4	2.4	27.5	12.1
2	8.7	0.2	12.4	2.1	24.2	10.7
3	8.5	0.2	11.9	1.3	24.4	10.6
4	8.0	0.5	11.9	1.8	26.3	10.7
	B. populneus		***A. havilandiorum***		***B. cunninghamii***	
Row	**Mean**	**SD**	**Mean**	**SD**	**Mean**	**SD**
1	21.9	3.2	10.8	4	14.5	6.1
2	22.6	1.6	10.9	4.2	14.0	6.2
3	23.3	1.8	10.7	5.8	14.3	7.4
4			11.0	5.9	15.0	6.3

Table 5-11 – The average MFA across each row for the maturing stems. The averages across the grid rows correspond to averages across the wood grain (see Figure 4.3).

It was observed that the variation in MFA is significantly less down the grain than across the grain. The average MFA down each column of the grid is shown for each sample in Table 5-10 with the associated standard deviation (individual tables in Appendix Two). The average MFA across each row with the standard deviations is shown in Table 5-11.

The experimental uncertainty is based on the fact that this recipe calculates an average MFA for a distribution of microfibril orientations within the illuminated volume. The average MFA is calculated from the width of the azimuthal peaks observed as described in Chapter 2.2.5. The use of the parameter *T* (a measure of this width) is used in the calculation of the standard deviation for the distribution.

Each diffraction pattern will give a different width and hence a different standard deviation for the MFA distribution of the crystallites illuminated in the volume. These values generally fall between approximately 3° and 10°, however some of the samples showing a larger MFA have an associated standard deviation as much as 18°. The standard deviation associated with each measurement is significantly greater than the standard deviation of the average down each column.

There were three specific results observed for the measurement of MFA across the grain. The first result showed limited and randomly ordered variation in MFA across the wood grain. The samples from which this result was observed were *A. floribunda* (high rain and soil nutrient), *A. Suaveolens* (high rainfall and low soil nutrient) and *B. populneus* (low rainfall and high soil nutrient). Of these samples the variation across the grain in *A. floribunda* was by far the smallest. *A. floribunda* and *A. suaveolens* are rotated by 9.2° and -8.0° with respect to the vertical axis. The grain of *B. populneus* is parallel to the vertical axis. In Figure 5-22 the measurements and error bars shown for *B. populuneus* are calculated values and standard deviations from Table 5-9 down the grain. Single points from the rotated co-ordinate system are shown for the samples with the grain at an angle to the vertical.

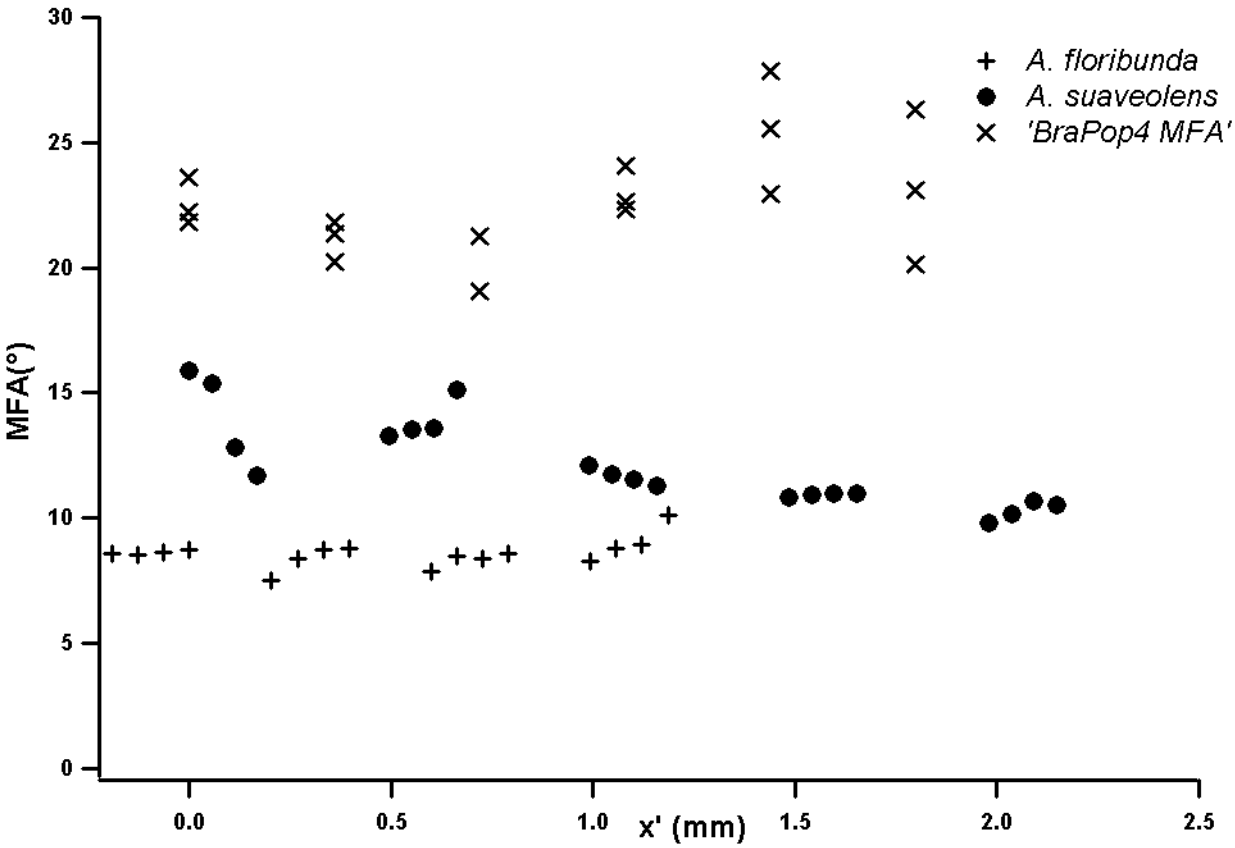

Figure 5-22 – The MFA measured across the grain for *A. floribunda*, *A. suaveolens* and *B. populneus*. The bars on *B. populneus* indicate a range of values for that particular *x'* position rather than an uncertainty value.

In Figure 5-22 the variations in MFA that were observed for the three samples do not show any periodicity which would suggest that there is no ordering of the woody tissue. These samples were considered to be made up of woody tissue with a single value for the MFA as the greatest variation was observed in *B. populneus* which had a standard deviation of 3.2° across the grain (Row 1, Table 5-11). The relationship between the MFA and the mechanical properties previously reported (Onoda *et al.*, 2010) are presented in Figure 5-23.

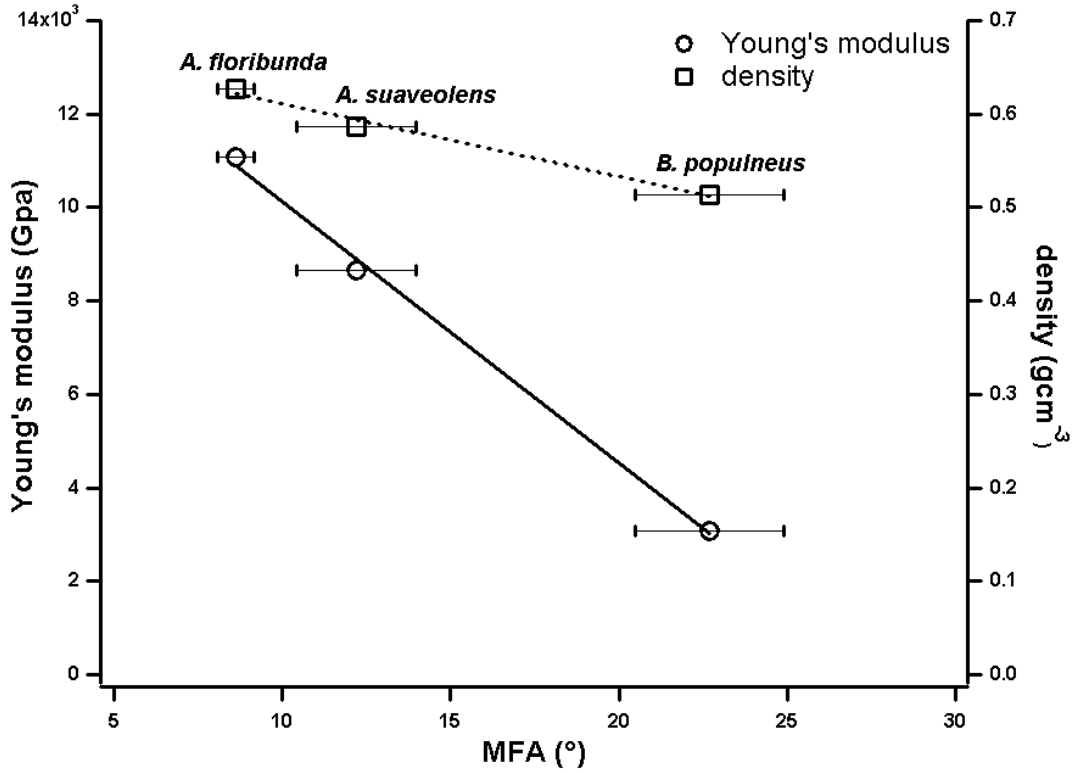

Figure 5-23 – The relationship between the MFA and the measured mechanical properties of those samples with no significant variation in MFA across the grain. Mechanical properties measured by Onoda *et. al.* (2010).

The samples from low rainfall and soil nutrient environments (*A. havilandiorum* and *B. cunninghamii*) showed regions of wood on the edges of the sample with a different MFA to the wood in the centre. In the sample of *A. havilandiorum* the sectioned sample showed one edge of wood on the left side of the stem. The sample of *B. cunninghamii* showed two regions of wood with the left and right side of the stem having a significantly higher MFA than the central region. The sample from the low rainfall and high soil nutrient site in Table 3.1 was *A. doratoxylon*. This sample was similar to *B. cunninghamii* in that there were two distinct regions of MFA value; one on the left and right sides of the stem and one in the centre.

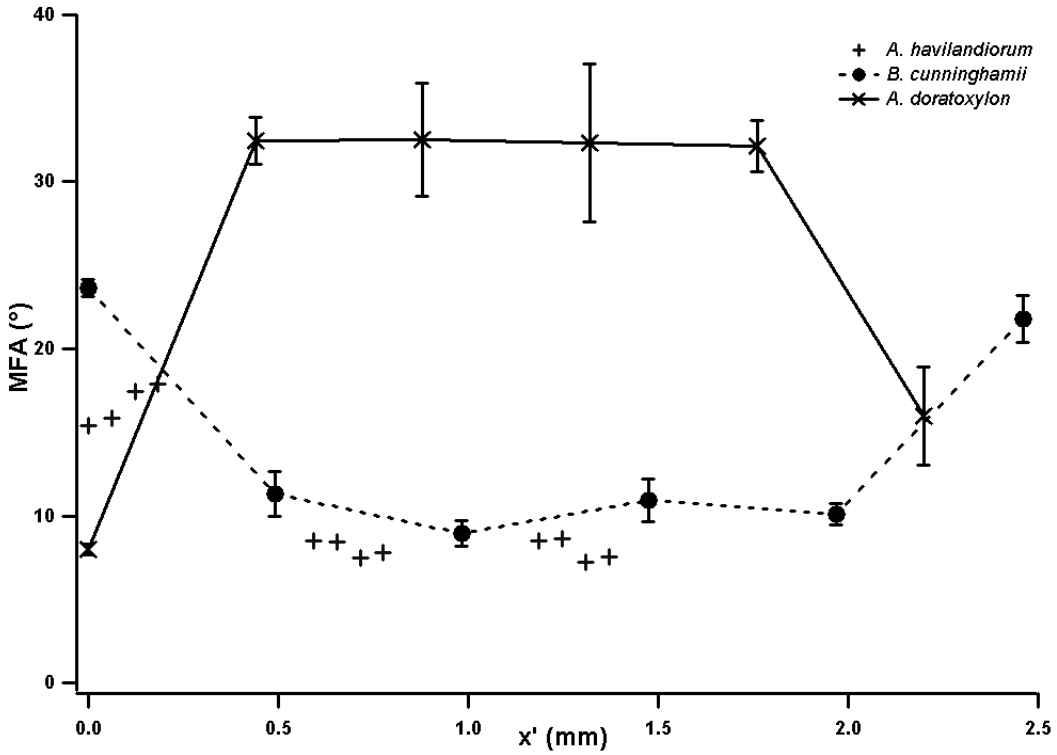

Figure 5-24 – The MFA measured across the grain for *A. havilandiorum*, *A. doratoxylon* and *B. cunninghamii*. The samples *B. cunninghamii* and *A. doratoxylon* have fibres parallel to the vertical and so the points in *x'* are the averages down the grain and the bars indicate the range of these values down the grain.

In Figure 5-24 the error bars associated with *A. doratoxylon* and *B. cunninghamii* come from the standard deviation of the average MFA measured down the grain. The regions of wood on the edges of these samples (*x'* = 0.0 mm and *x'* = 2.2 mm and 2.46 mm respectively) have MFA values that were observed to be outside the standard deviation range of the central regions. The results of *A. havilandiorum* showed the calculated MFA near the left edge of the sample was greater than the rest of the sample. The difference between the region of high MFA and low MFA is significantly large to be outside the range of normal experimental uncertainties.

The comparison of the measured bulk mechanical properties of these samples to the measured MFA was problematic. The average MFA of the main portion of the stem (i.e. the central portion) was considered to contribute to the mechanical properties of the stem to a greater extent than the edges. These values were then used as an approximate base for comparison. The average MFA values are used for plotting in Figure 5-24.

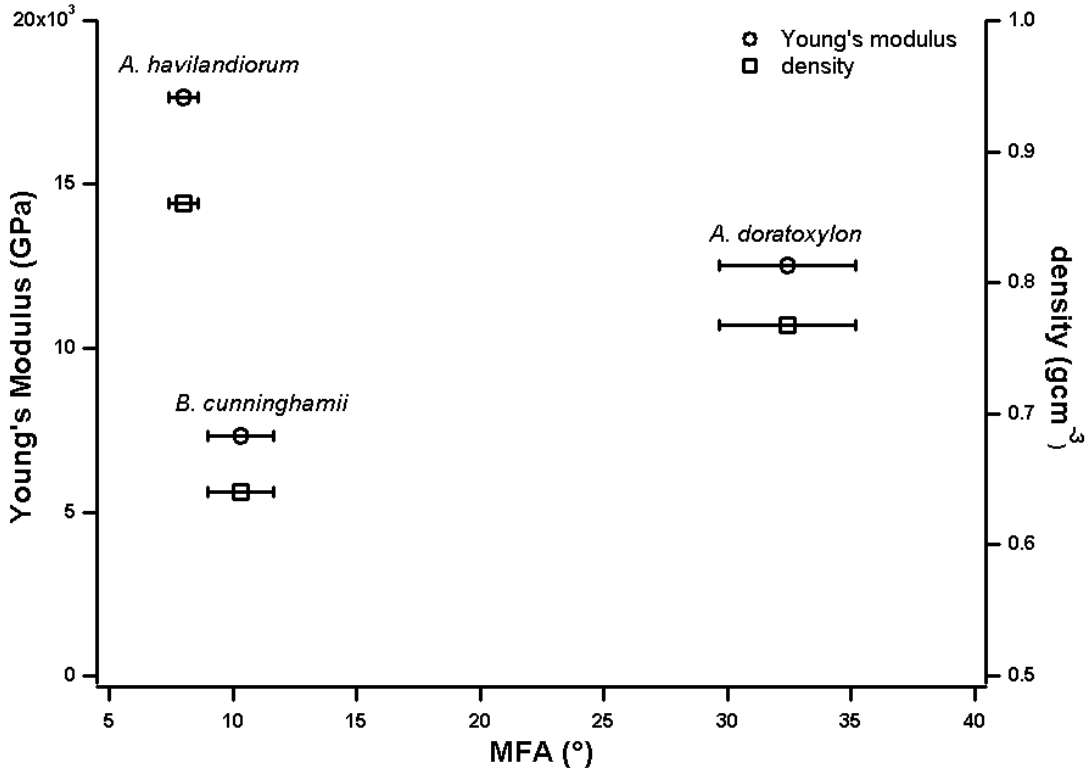

Figure 5-25 – The mechanical properties of the samples in Figure 5-24. Mechanical properties measured by Onoda *et. al.* (2010).

5.3.3 Discussion of WAXS Results

The plots of lateral microfibril dimensions (Figure 5-20 & Figure 5-21) showed little variation as a function of measurement number. This would suggest that there is no significant variation in the calculated lateral microfibril dimensions within a particular sample. Previously the microfibril width was linked to the size of the rosette complex that synthesises cellulose (Chapter 5.1.4) (Hotchkis and Brown, 1987). The variation in lateral dimensions of the microfibril does not appear to be sufficient to suggest that there is a different synthetic process being used by different regions of the stem.

Given that no significant variation was observed in the lateral dimensions of the cellulose microfibril within a sample the average values were used to compare different species.

Sample	Average Microfibril Width (nm)	Standard Deviation (nm)	95% Confidence Interval
B. populneus	3.4	0.1	3.381 – 3.384
A. suaveolens	3.4	0.06	3.403 – 3.405
A. floribunda	3.4	0.06	3.396 – 3.398
B. cunninghamii	2.9	0.05	2.935 – 2.396
A. doratoxylon	2.9	0.03	2.905 – 2.906
A. havilandiorum	3.2	0.3	3.152 – 3.162
Average	3.2	0.2	

Table 5-12 – Summary of the calculated microfibril widths for each species.

The variation between species in lateral dimensions of the microfibril was within experimental uncertainties. From this observation it was inferred that the synthetic process can be considered to be the same for all species under investigation. The different samples exhibited a spread of bulk mechanical properties as shown in Figure 5-23 and Figure 5-25 (Onoda *et al.*, 2010). Given the similarities between the microfibril widths of the different species it appears that this is not correlated to the bulk mechanical properties.

The measurement of the MFA from WAXS data was used to try and explain why the samples with similar microfibril widths had different mechanical properties. The link between MFA and mechanical properties had previously been established in the literature (Cave and Walker, 1994; Meylan and Probine, 1969). This has resulted in an extensive literature base of the various techniques for measuring MFA from different species (Barnett and Bonham, 2004). These samples are all angiosperms and fairly typical of Australian hardwoods. The measured MFA for such species ranges from the very low, 0.3° from confocal microscopy (French *et al.*, 2000), to the highest values observed, 34° from XRD (Abasolo *et al.*, 1999).

The range of MFA measurements observed from XRD studies is summarised by Barnett and Bonham (2004). The range covered by such measurements (for angiosperms and gymnosperms) is 5.5° (Watson and Dadswell, 1964) to a maximum value of 40° (Matsumura and Butterfield, 2001). As *acacia* species are two-thirds of the samples represented in the maturing stems they form an important group to consider in the literature. MFA measurements have been made on acacia samples ranging from upwards of 28° in typical woody tissues to 10° in reaction wood and annual rings (Hillis *et al.*, 2004).

There appears to be a correlation between the bulk mechanical properties of these samples measured by Onoda *et al.* (2010) and the MFA (Figure 5-23). Although this only represents half of the species in the study these are the samples that presented no significant variation in the MFA within the sample. The variation of MFA in a tree is associated with specific mechanical property modulation such as in the formation of reaction wood (Burgert *et al.*, 2004) (Farber *et al.*, 2001). This is of particular interest for those samples that showed variation in MFA across the wood grain (Figure 5-24 and Figure 5-25).

The linear relationship between MFA and mechanical properties (Figure 5-25) breaks down when these samples are included as there are distinctly different regions of woody tissue within the stem. Samples from low rainfall and soil nutrient level environments show a large variation in the MFA across the grain. As the wood across the grain varies in age, the variation can be considered to be a function of the woods maturity. As these stems are maturing the timescale across which these variations are observed is much smaller than those across annual rings (Wimmer *et al.*, 2002).

Taking the mechanical properties determined by Onoda et. al. (2010) the specific modulus can be calculated and compared to MFA. This allows for a comparison of mechanical properties that have been normalised for density (specific modulus is the Young's modulus divided by density).

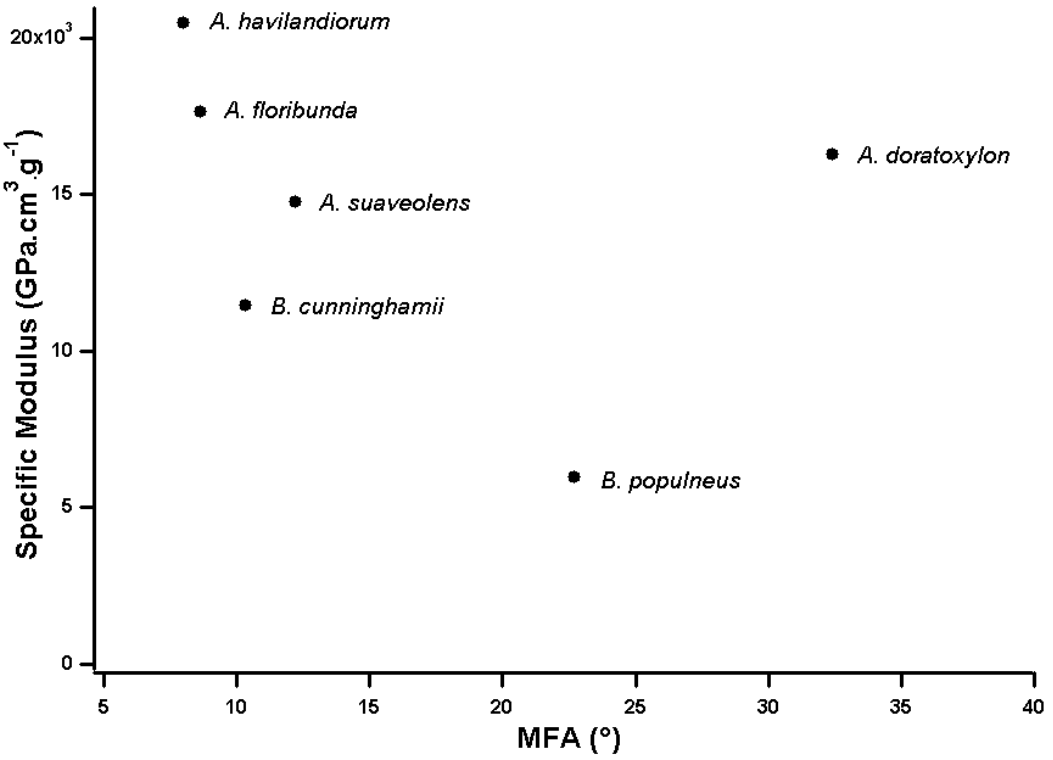

Figure 5-26 – The relationship betweenMFA and the specific modulus as calculated from Onoda's mechanical properties.

In Figure 5-26 it can be seen that there is a stronger correlation between the mechanical properties and the MFA when normalised for density. This relationship also includes more samples than the previously discussed Young's modulus relationship with only *A. doratoxylon* being an outlier in this case.

5.3.4 Results of SAXS Measurements

A single SAXS measurement was made on each of the maturing stems described in Table 3-1 in both a cross sectional and a tangential preparation of each sample. The tangential sections showed a higher degree of anisotropy than the corresponding cross-sectional measurements. One dimensional data was obtained from a sector average unlike the radial average used for WAXS data. The sector averaged data is compared to the radially averaged data for *A. doratoxylon* below.

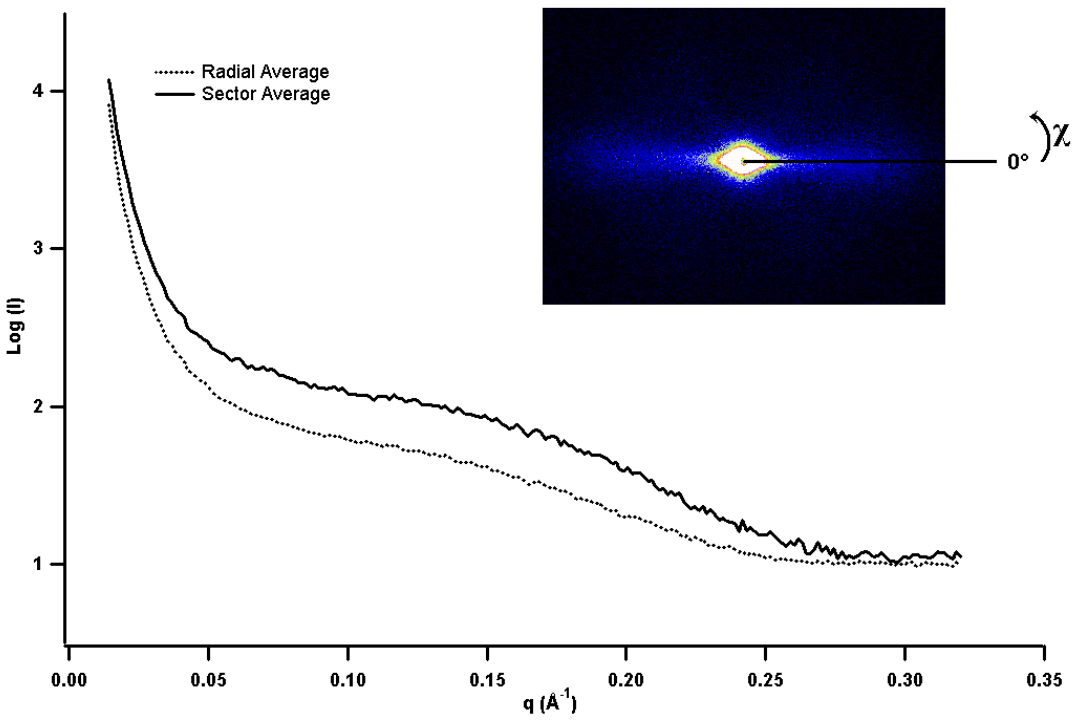

Figure 5-27 – A comparison of the radial and sector averaged one dimensional profiles of *A. doratoxylon*. The sector average was taken from χ = -25° to 25°.

Figure 5-27 shows the differences in the scattering curve of *A. doratoxylon* for a sector and a radial averaging of the two dimensional data. As $q \to 0\,\text{Å}^{-1}$ the scattering curves became more alike. Similarly the scattering profile of the samples became similar for scattering vectors greater than about 0.27 Å^{-1}. The middle region of the scattering profile shows the most significant difference. In this region the intensity is greater in the sector averaged data as there are fewer pixels with very low intensity contributing to the average. The shape of the graph is also different with the shoulder from the scattering of cylindrical particles being more prominent. The sector average was preferred for analysis and the smaller sample size was not as much of an issue in terms of computation requirements.

Analysis of small angle scattering data began with the application of the Guinier approximation (equation 2.48). The Guinier analysis assumes that; q is much smaller than $1/R_g$ and that the particles scatter independently of each other. Practically this is often reduced to the following condition for using the approximation, $R_G \cdot q_{\max} < 1.2$ (Konarev *et al.*, 2003). Typically a Guinier approximation is only valid over a small range of the scattering profile. The ranges that are typically associated with Guinier regions are the regions of the scattering profile with a low gradient. Observation of

the scattering curves of the maturing stems (Appendix Two Figure A4-1 and A4-2) indicated low gradient regions were between 0.15 $Å^{-1}$ and 0.25 $Å^{-1}$.

In the usual Guinier approximation a plot of $\ln(I)$ vs q^2 is used and a linear line of best fit applied to the data points. The gradient of this line is related to the radius of gyration. For cylindrical particles, the Guinier approximation is modified so that the plot is of $\ln(I.q)$ vs q^2. Again the gradient of the line of best fit for this plot is used to determine the radius of gyration. In this case the radius of gyration is in the radial direction.

PRIMUS, from the ATSAS software suite developed by Dmitri Svergun, was used to scan through the portion of the scattering profiles deemed to be suitable from observation of the gradient to find suitable Guinier regions (Konarev *et al.*, 2003). Suitable Guinier regions were determined if they met of the $R_G \cdot q_{\max} < 1.2$ condition and contained a minimum of ten data points. All samples were found to contain a Guinier region.

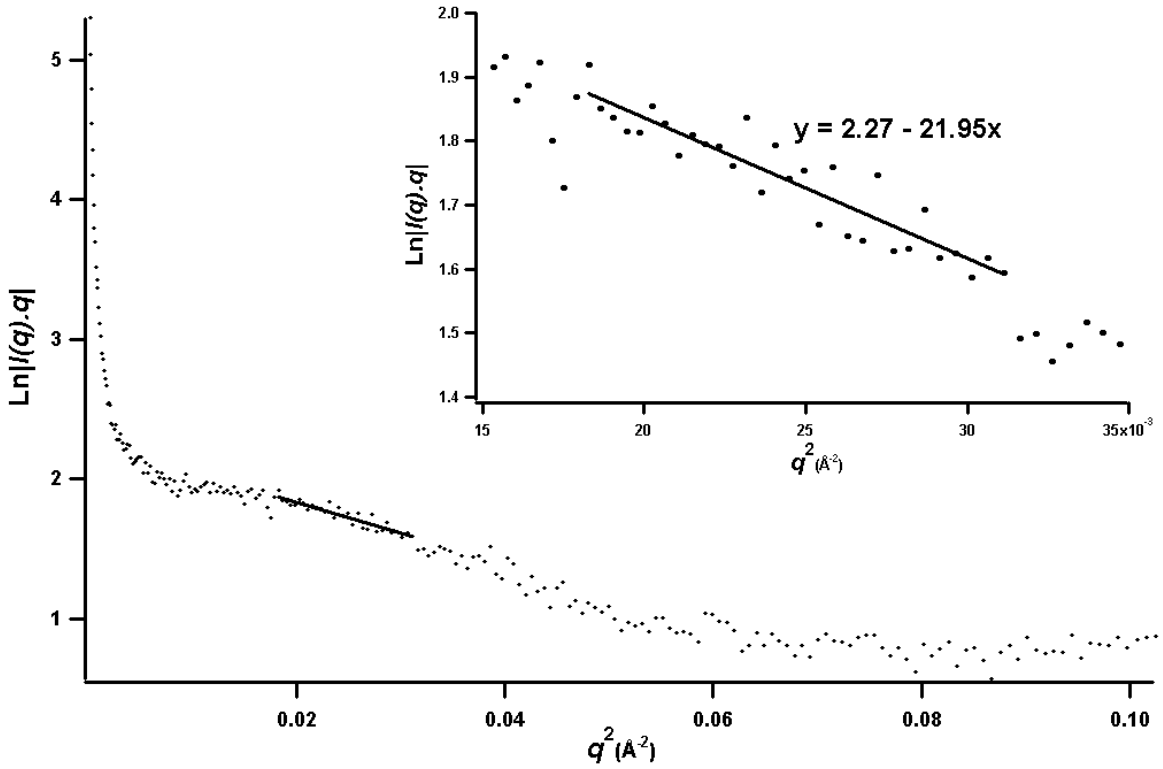

Figure 5-28 – *A. floribunda* ln|*I(q).q*| vs q^2 plot. The inset graph is zoomed in on the Guinier region along with the linear line of best fit.

The PRIMUS software automatically calculated the R_g value for the scattering profiles over a given range along with the $R_g.q_{max}$ values. The calculation was confirmed from the line of best fit obtained (as in Figure 5-28) and equation 2.59. Using the notation from these equations, the cross sectional radius of gyration was calculated (R_C). PRIMUS automatically corrected for the use of cylinders in the Guinier model by selecting rod-like particles.

Sample	R_C (Å)	q_{max} (Å^{-1})	$R_C.q_{max}$
B. populneus	6.33 ± 0.29	0.1792	1.134
A. suaveolens	6.67 ± 0.26	0.1777	1.185
A. floribunda	6.63 ± 0.22	0.1764	1.170
B. cunninghamii	6.62 ± 0.12	0.1792	1.186
A. doratoxylon	6.53 ± 0.31	0.1821	1.189
A. havilandiorum	6.45 ± 0.11	0.1721	1.110

Table 5-13 – Summary of the R_C values calculated from the Guinier approximation for tangentially sectioned samples.

In Table 5-13 the R_C values calculated from PRIMUS showed good agreement between species. PRIMUS also calculated the uncertainty given from a least squares algorithm. Each value was obtained from a valid Guinier region as the q_{max} condition was satisfied in each case. As discussed in Chapter 2.3 the SAXS profile will originate from structures in which the electron density difference is greatest. In the case of cell wall materials this will mean the void-polymer boundaries. Because the scattering originates from the electron density fluctuations it is very difficult to determine if the scattering object is the void in the sample or the polymer.

In addition to the tangential sections, cross sections were prepared from the maturing stems. In these samples the beam is effectively looking down the length of the cellulose fibre axis. In the cross sections the voids in the stem that are typical of hardwood species were more prominent. While the voids that were visible are extreme examples, smaller voids were present throughout the sample across all size scales (Maloney and Paulapuro, 1999). The samples were positioned so that the incident beam passed through an area of wood without any of the pith being included.

The measurements made on the cross sectioned samples showed a small degree of anisotropy located very near the beamstop. It was not clear if this anisotropic scattering was sample related or an artefact of the measurement. The anisotropy observed in the scattering patterns was not attributed to the sample based on the experimental geometry. This portion of the scattering was therefore removed from the averaging of the two dimensional data. The remainder of the data was isotropic and so a radial average was deemed appropriate for the calculation of one-dimensional scattering profiles.

In these scattering profiles there was little difference observed between the samples in terms of intensity and the shape of the scattering profile (Appendix Two). A distinguishing feature of the scattering profiles was a flat linear region between q = 0.10 Å^{-1} and q = 0.20 Å^{-1}. In this region a valid Guinier approximation was made. The cylindrical form of the Guinier approximation was to be applied (i.e. plotting $\ln|q.I(q)|$ vs q^2). The result of this form of the Guinier approximation was the determination of the cross sectional radius of gyration.

Sample	R_c (Å)	q_{max} (Å^{-1})	$R_c.q_{max}$
A. doratoxylon	4.10 ± 0.19	0.20908	0.86
A. floribunda	4.48 ± 0.27	0.19771	0.89
A. havilandiorum	4.27 ± 0.26	0.19344	0.83
A. suaveolens	4.42 ± 0.21	0.21050	0.93
B. cunninghamii	4.26 ± 0.57	0.17780	0.76
B. populneus	4.52 ± 0.29	0.23326	1.05

Table 5-14 – Summary of the R_C values calculated from the Guinier approximation for cross sectioned samples.

The PRIMUS software was used to calculate R_C for the six samples. Again good agreement was found between the samples with the uncertainties associated with each value being determined by PRIMUS based on the goodness of fit. While there was good agreement within the data set there was no agreement between the R_C values calculated for the tangentially sectioned samples (Table 5-13) and the cross sectioned samples (Table 5-14).

Orientational parameters were not investigated in the cross sectioned samples due to the lack of anisotropic scattering. The orientation of structures in the tangential

sections was investigated by analysing the significant anisotropic scattering in these patterns. The horizontal streaks from the scattering of side cell walls were so prominent the streaks from the S_2 microfibrils were not easily observed in the data. The azimuthal averages from the tangential sections were deconvoluted and the position of the peaks from the S_2 layer was identified. The distance between the two S2 peaks is a measure of 2χ from equation 2.61.

Sample	2φ (°)	MFA (°)
B. populneus	46.91	23.5
A. suaveolens	18.69	9.3
A. floribunda	22.76	11.4
B. cunninghamii	29.17	14.6
A. doratoxylon	17.16	8.6
A. havilandiorum	23.58	11.8

Table 5-15 – Calculated MFA values for the scattering patterns from tangentially sectioned stems.

5.3.5 Discussion of SAXS Results

The results in Table 5-14 indicate that a MFA value has been calculated from SAXS measurements. Given the ambiguity surrounding the source of small angle scattering in cell wall materials this is perhaps a slightly misleading name for the orientational parameter obtained from SAXS. However the literature reports this to be the MFA in the sample and the same nomenclature is used here (Jakob *et al.*, 1994). There is some orientational parameter obtained from SAXS and these values presented in Table 5-14 agree with the MFA values obtained by WAXS measurements (Figure 5-22 and Figure 5-24). For those samples where there is a variation across the wood grain the values in the central region are used to compare to the SAXS measurements.

As noted previously the SAXS measurements are likely to be obtained from the pore structure in the material while the WAXS measurements relate to the cellulose microfibril structure. In the palm fibre sample (Chapter 5.1) there was a notable difference between these measurements and it was attributed to the pore structure not being aligned to the microfibrils. In this sample there seems to be better agreement in the data suggesting an alignment of the pores to the S2 microfibrils.

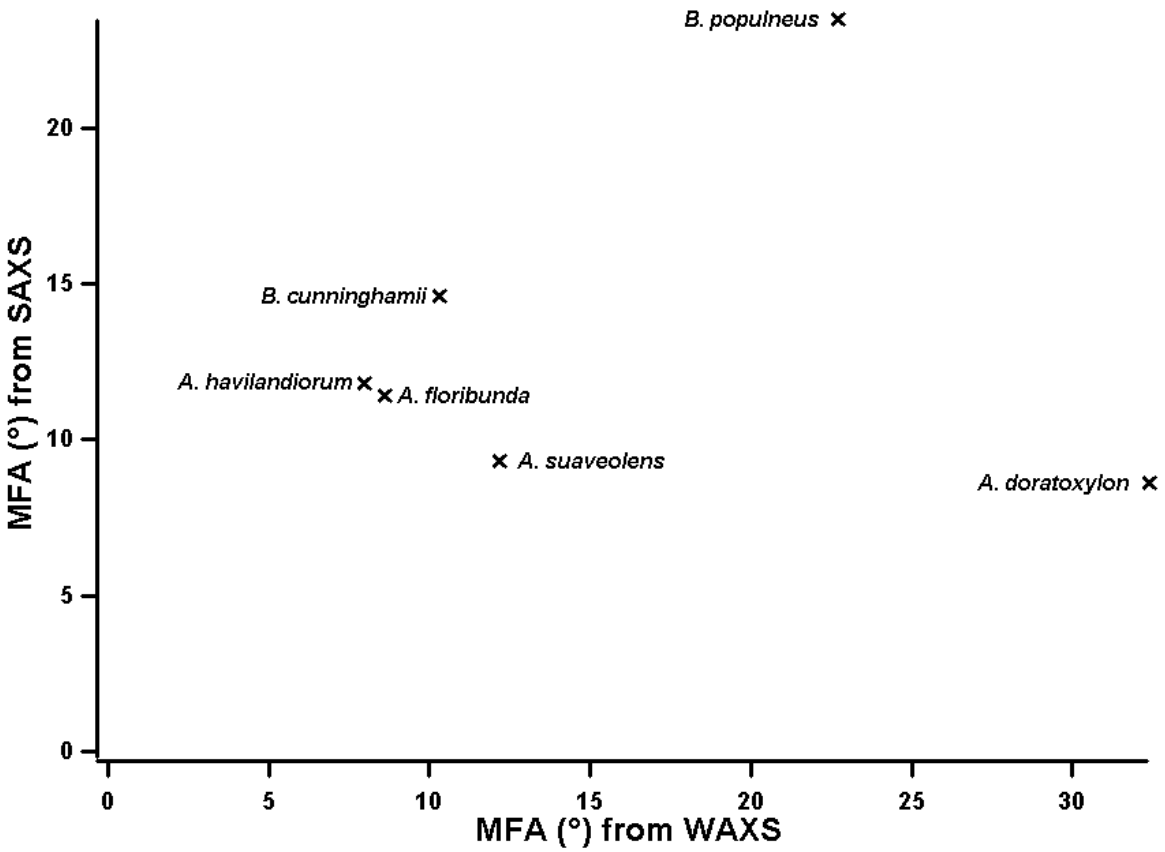

Figure 5-29 – Scatter plot of the MFA measurements made on the six samples from WAXS and SAXS methods.

In Figure 5-29 there is a good agreement between the MFA from WAXS measurements and the orientational parameter measured by SAXS for four of the six samples. These samples are *A. havilandiorum, A. floribunda, B. Cunninghamii and B. populneus*. It has previously been suggested that the most likely source of scattering in these materials is from the voids in the sample. This would indicate that the voids within these samples are aligned almost parallel to the cellulose microfibrils in the cell wall. The *A. suaveolens* and *A. doratoxylon* samples show some deviation between the SAXS and WAXS measurements. However the A. doratoxylon sample shows a SAXS MFA (8.6°) that is comparable to that measured on the edge of the sample by WAXS (11.9°)

The interpretation of SAXS results from cell wall materials is complicated by the ambiguity of the source of the observed scattering. Because of this ambiguity the parameters obtained from SAXS measurements of cell wall materials cannot be related to specific features (such as the cellulose microfibril) as they are in WAXS

measurements. Although this leaves the R_C values calculated in Table 5-12 and Table 5-13 lacking some physical context the results are internally consistent. The good agreement between the different species would suggest that the sources of small angle scattering in the maturing stems are of similar size in the different samples.

There is a good agreement between the species within Table 5-12 and within Table 5-13 however the results do not agree with each other when comparing the two data sets. The difference between the R_C values in tangential samples compared to cross sectional samples are most likely due to the different orientation of the sample with respect to the incident beam. The different orientation presented to the incident beam will illuminate different dimensions of the crystallite.

The analysis of SAXS data to obtain information about the size of polymer structures in the cell wall has been problematic. There is an ambiguity regarding the nature of the observed scattering. Also the analysis yields a radius of gyration parameter rather than, for example, a crystallite width as in WAXS. These factors make comparison between SAXS and WAXS data difficult with regards to the size of polymer structures in the cell wall. What can be said is that the WAXS data indicates no significant difference in the lateral microfibril dimensions between species and the SAXS data agrees to an extent suggesting there is some structure present that appears not to be varying in size across the different species. Although the comparison of the size of polymer arrangements in the cell wall has proven difficult the comparison of orientational parameters is clearer.

The use of WAXS and SAXS techniques can give comparable information about a sample however the nature of the scattering experiments makes it likely that the information obtained comes from different sources in the cell wall. WAXS measurements have given information here about the cellulose microfibril while the SAXS measurements appear to be linked to the voids in the sample. WAXS measurements are also more sensitive to the amorphous matrix of the cell wall than SAXS measurements. Hence the observation of scattering from the amorphous matrix was esaier using WAXS techniques.

5.4 Position Resolved WAXS Measurements of an Acacia

5.4.1 Results from Radial Averaging

Position resolved WAXS measurements (Chapter 4.1) were made from a piece of an *acacia* tree (Chapter 3.3) in order to investigate the different types of wood present; early wood, late wood and reaction wood. A typical two dimensional scattering pattern for the *acacia* sample is shown in Figure 5-30.

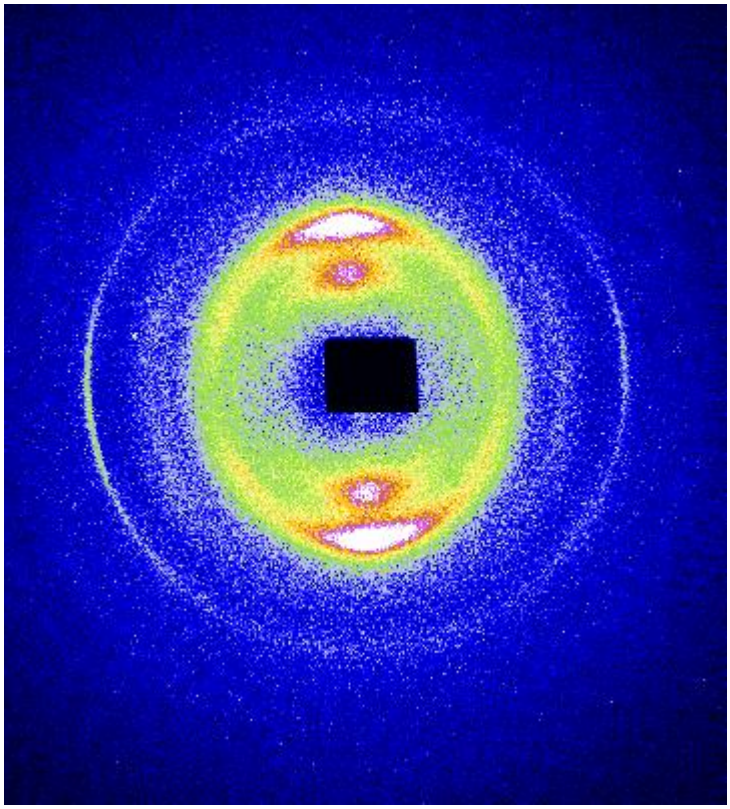

Figure 5-30 – Two dimensional WAXS pattern of an *acacia* from the Nanostar at ANSTO.

As for previous samples the instrumental broadening in the WAXS pattern is considered to be negligible compared to the size broadening of the sample. Also the radial average was preferred over the sector averaging for the reasons stated in Chapter 5.1.1. An empty sample holder was used to subtract a background from the raw data. After background subtraction the data was fit with Voigt profiles for the cellulose Bragg peaks and a model of the amorphous matrix.

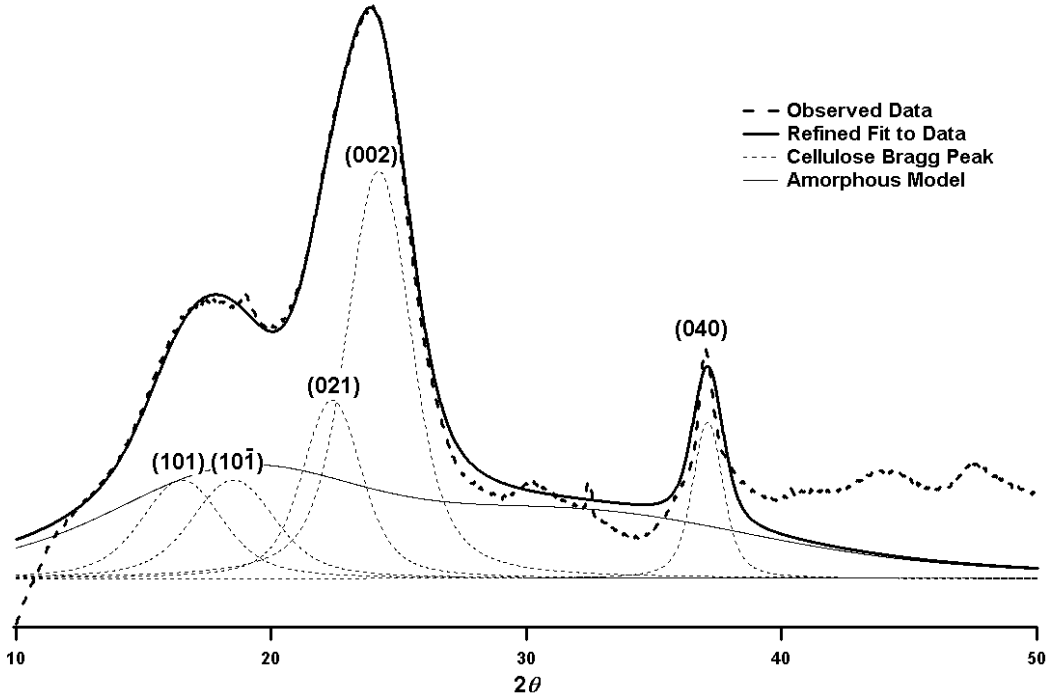

Figure 5-31 – Deconvolved WAXS pattern for the 20mm position of the *acacia* sample.

The deconvolution of the WAXS patterns was used to obtain the parameters related to the (002) reflection. These parameters were used to make use of the Scherrer equation previously described (equation 2.2). The Scherrer equation was used to calculate the crystallite width in the (002) direction which was used as a measurement of the lateral dimensions of the cellulose microfibril.

Position (mm)	2θ (°)	FWHM (°)	Crystallite Width (nm)
20	24.21	2.44 ± 0.1	3.7 ± 0.2
21	24.32	2.56 ± 0.1	3.5 ± 0.2
22	24.10	2.45 ± 0.1	3.7 ± 0.2
23	24.07	2.51 ± 0.1	3.6 ± 0.2
24	23.99	2.39 ± 0.1	3.8 ± 0.2
25	23.95	2.41 ± 0.1	3.7 ± 0.2
26	24.12	2.45 ± 0.1	3.7 ± 0.2
27	23.99	2.31 ± 0.1	3.9 ± 0.2
28	23.70	2.36 ± 0.1	3.8 ± 0.2
29	24.11	2.43 ± 0.1	3.7 ± 0.2
30	23.83	2.36 ± 0.1	3.8 ± 0.2
31	24.00	2.44 ± 0.1	3.7 ± 0.2
32	23.88	2.40 ± 0.1	3.8 ± 0.2
Average			3.7 ± 0.2
St Dev			0.1
57	23.99	2.40 ± 0.1	3.8 ± 0.2
58	24.12	2.43 ± 0.1	3.7 ± 0.2
59	24.25	2.45 ± 0.1	3.7 ± 0.2
60	24.17	2.43 ± 0.1	3.7 ± 0.2
61	23.99	2.39 ± 0.1	3.8 ± 0.2
62	24.16	2.43 ± 0.1	3.7 ± 0.2
63	24.34	2.50 ± 0.1	3.6 ± 0.2
Average			3.7 ± 0.2
St Dev			0.1
Filter Paper	24.04	0.93 ± 0.1	9.7 ± 0.2

Table 5-16 – Summary of the Scherrer analysis of the (002) reflection from the deconvolved WAXS patterns from an *acacia* sample.

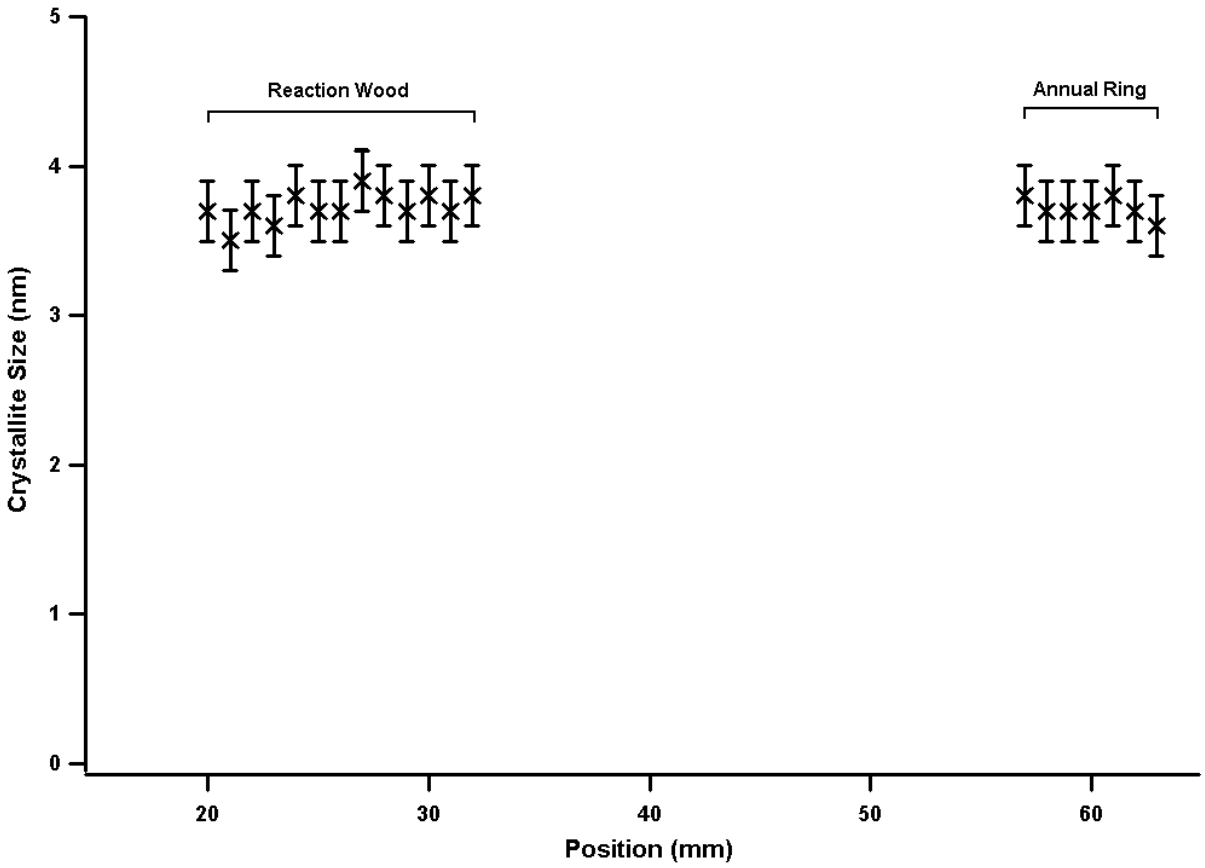

Figure 5-32 – The calculated crystallite size from the Scherrer analysis as a function of the position along the *acacia* sample.

The experimental uncertainties in Table 5-16 and Figure 5-32 were estimated from the confidence intervals of the deconvolution of the WAXS patterns. The measurements along the length of the *acacia* sample showed little variation in the width of the (002) reflection after deconvolution (Table 5-16). The width of this reflection was used to determine the lateral dimensions of the cellulose microfibrils and hence there was little variation observed in the width of the microfibrils along the length of the sample (Figure 5-32).

5.4.2 Results from Azimuthal Averaging

The WAXS measurements of an acacia sample were also analysed after azimuthal averaging. The azimuthal averaging of the data (Figure 5-33) allowed for the calculation of the MFA along the length of the sample.

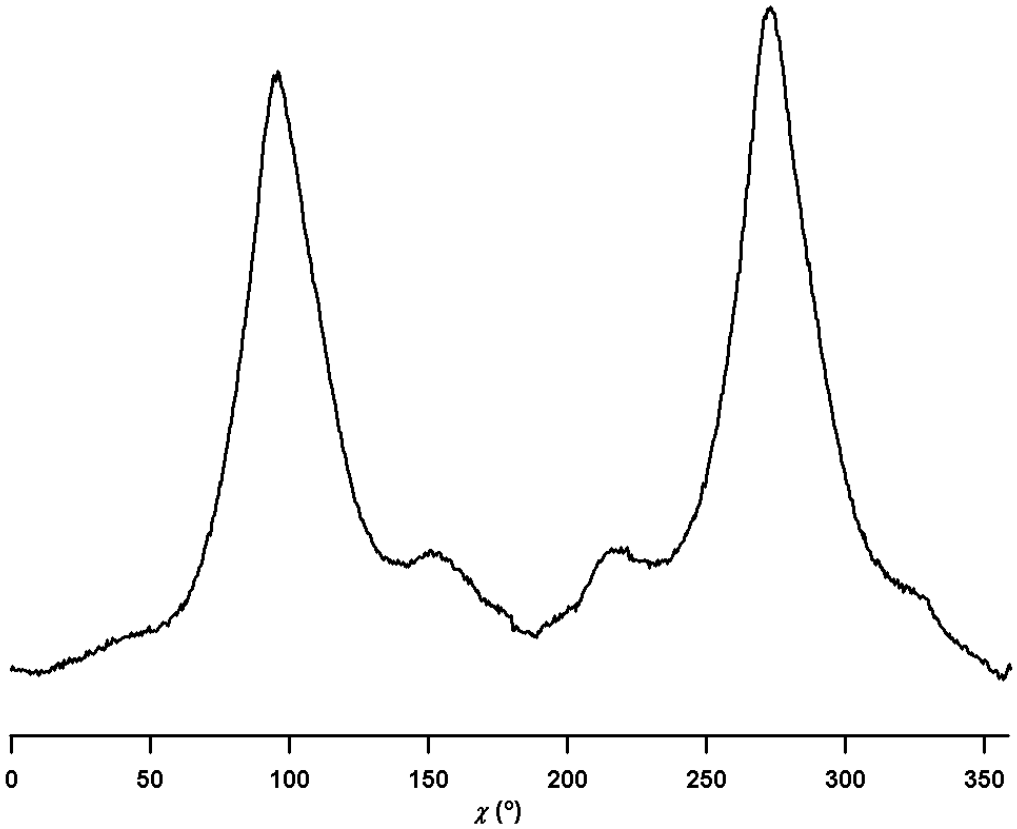

Figure 5-33 – The azimuthal average of the WAXS pattern at 20 mm on the *acacia* sample.

The MFA was calculated from measuring the width of the peaks in the azimuthal profile (such as those at ~100° and ~280° in Figure 5-33). The width of the azimuthal peaks was measured from fitting Voigt profiles to the data and using the FWHM parameter as in Figure 2-10. The FWHM was related to the *T* parameter (equation 2.36) and then *T* was used to calculate the MFA (equation 2.37).

Position	FWHM Peak 1 (°)	*T* (°)	MFA (°)	FWHM Peak 2 (°)	*T* (°)	MFA (°)
20	27.80	23.61	14.17	26.91	22.86	13.71
21	41.94	35.62	21.37	41.85	35.54	21.33
22	16.95	14.40	8.64	18.44	15.66	9.40
23	13.94	11.84	7.10	13.80	11.72	7.03
24	12.47	10.59	6.35	12.08	10.26	6.16
25	12.04	10.23	6.14	11.86	10.07	6.04
26	13.51	11.47	6.88	13.14	11.16	6.70
27	12.46	10.58	6.35	12.33	10.47	6.28
28	11.97	10.17	6.10	12.18	10.34	6.21
29	15.40	13.08	7.85	15.52	13.18	7.91
30	15.49	13.16	7.89	14.92	12.67	7.60
31	14.56	12.37	7.42	13.80	11.72	7.03
32	15.48	13.15	7.89	14.97	12.71	7.63
Average			7.15			7.09
St Dev			0.86			1.01
57	11.88	10.09	6.05	11.80	10.02	6.01
58	15.00	12.74	7.64	14.45	12.27	7.36
59	16.63	14.12	8.47	15.94	13.54	8.12
60	12.97	11.02	6.61	13.02	11.06	6.63
61	12.98	11.02	6.61	13.06	11.09	6.66
62	12.10	10.28	6.17	12.13	10.30	6.18
63	16.85	14.31	8.59	16.74	14.22	8.53
Average			7.16			7.07
St Dev			1.07			0.97

Table 5-17 – MFA values along the length of the *acacia* sample calculated from the width of the azimuthal peaks.

In general there was good agreement between MFA values along the length of the *acacia* sample. The first two values were found to lie outside three standard deviations of the mean MFA and hence were not included in the calculation of the mean. The MFA in woody samples has been shown to vary by such amounts in the literature (Hillis *et al.*, 2004). It was not clear if this observation was a product of the sample preparation or a property of the sample. There is good agreement between the reaction wood values (20 mm – 32 mm) and the annual ring values (57 mm – 63 mm). Each data set also shows comparable variances as measured by standard deviation.

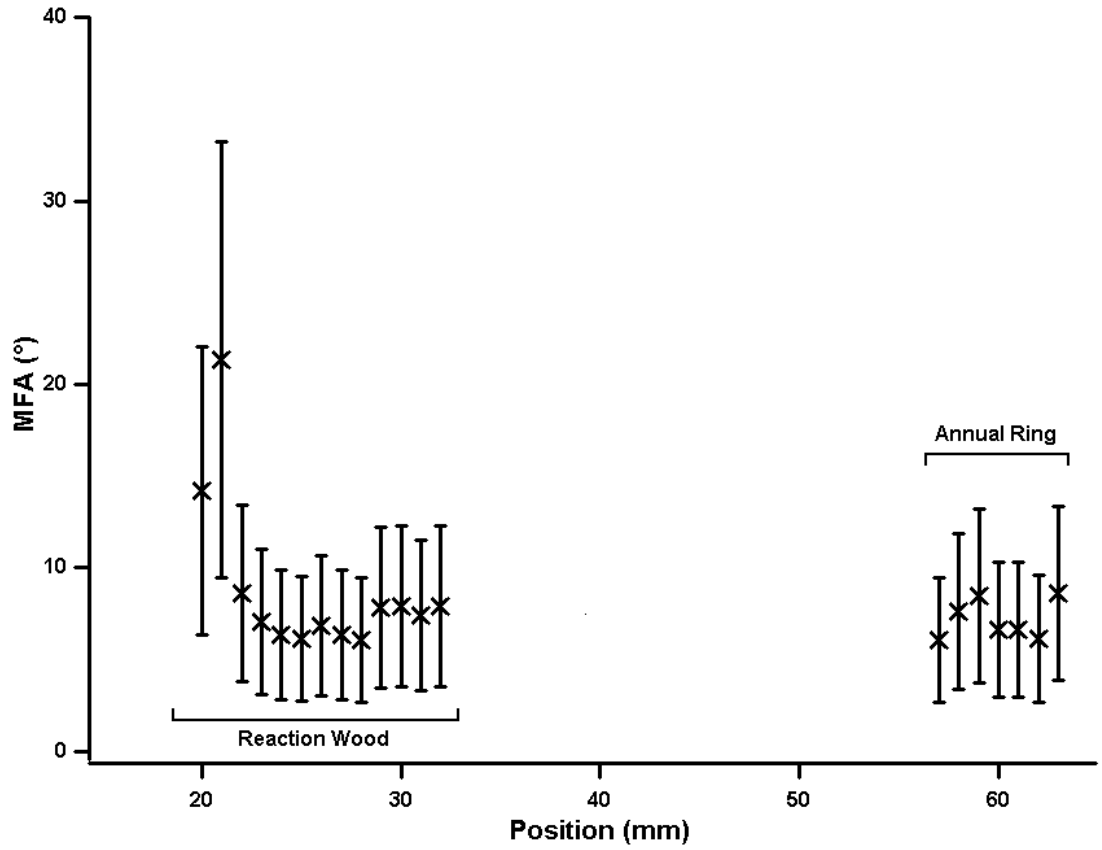

Figure 5-34 – MFA as a function of the position on the acacia sample.

The uncertainties in Figure 5-34 were estimated from the standard deviation of the MFA distribution. The parameter *T* was used for this estimate as Cave (1966) states that

$$\sigma = T/3 \qquad (5.1)$$

5.4.3 Discussion of WAXS Results

Deconvolution of the radially averaged WAXS data indicated there was no significant variation observed in the width of the (002) reflection. This reflection was used as a way to measure the lateral dimensions of the microfibril in cell wall materials from scattering and diffraction experiments. The Scherrer analysis of the (002) reflection was used to calculate these lateral dimensions along the length of the *acacia* sample. There was little variation observed in these values and they agreed with each other within experimental uncertainties.

While little variation was observed within the sample there was a significant difference between the lateral dimensions of the sample and the filter paper standard. This difference can be attributed to the filter paper being produced from a species with significantly greater lateral dimensions than the acacia sample and/or swelling of the microfibrils as a result of the pulping process to make the filter paper.

The lack of variation in the lateral dimensions of the microfibril is indicative of similar sized rosette complexes being used to synthesis the cellulose microfibril along the length of the sample (Hotchkis and Brown, 1987). This observation was made in previous samples (Chapter 5.1 and Chapter 5.2) which suggest that within a specimen the lateral dimensions of cellulose microfibrils are highly conserved parameters of the cell wall.

The Scherrer analysis was used to rapidly compare the different WAXS patterns collected along the sample. The other parameter used for such rapid comparisons is the MFA. This was also found to not vary significantly along the length of the *acacia* sample. The MFA measured at 20 mm and 21 mm were observed to be significantly higher than the rest of the measurements, although these were in the range of experimental uncertainties. These larger measurements came from the part of the wood that would be considered early-wood. The measurements were made to scan through the band of reaction wood, starting and ending in early-wood. It was expected that any observations related to the early wood would appear before and after the band of reaction wood (as well as before and after the annual ring). Four regions of early-wood were identified that were expected to agree with each other (~20 – 23 mm, 30 – 32 mm, 57 – 58 mm and 62 – 63 mm). Three out of these four regions showed good agreement in the measured MFA. The lesser degree of agreement in the 20 – 23 mm region was considered to be an aberration in the data, most likely attributed to the disruption of the cellulose microfibrils in the cell wall as a result of the preparation of the sample.

The nature of the MFA measurements (i.e. an average over all the cells in the illuminated volume) from WAXS resulted in significant uncertainties attached to the values. Taking multiple measurements along the length of the sample seemed to indicate that the MFA was essentially the same for all types of wood present. This

indicated that the error bars included in Figure 5-33 were an overestimate of the experimental uncertainty. The average value of the MFA for a given scattering pattern is strongly correlated with mechanical properties so minimising the range of possible values is important in the estimation of uncertainties in the mean MFA.

Reaction wood has been a particularly important system for the relation of MFA to mechanical properties as the formation is a result of the application of a force (internal or external). In general it is found that the MFA measured in reaction wood is greater than in normal wood. These trends are summarised in tables of literature values in the papers by Reiterer *et. al.* (1998) and Barnett and Bonham (2004). The tables report numerous values for the MFA from different species and experimental techniques. The values for compression wood show values as high as 45°.

Bulk mechanical properties were not measured for the sample of *acacia* wood. However the lack of variation in the MFA along the length of the sample would suggest that the mechanical properties of the sample show a similar lack of variation. The measurement of mechanical properties at points along the length of the sample is experimentally difficult and often destructive so the use of MFA as a parameter for timber quality was investigated. The use of WAXS to study a sample of timber resulted in the rapid generation of two parameters along the length of the sample; the width of cellulose microfibrils and the MFA. Of these two parameters the MFA has been linked to mechanical properties while the width of the cellulose microfibril has been linked to the synthetic processes that generate cellulose.

5.5 XRD of Domestic Timbers

5.5.1 Results of XRD

X-ray Diffraction (XRD) measurements (Chapter 4.1) were made on samples of native commercial timbers (Chapter 3.4). These samples were measured on a lab based x-ray diffractometer in the reflection mode. The samples were aligned with the wood grain parallel and perpendicular to the incident x-ray beam.

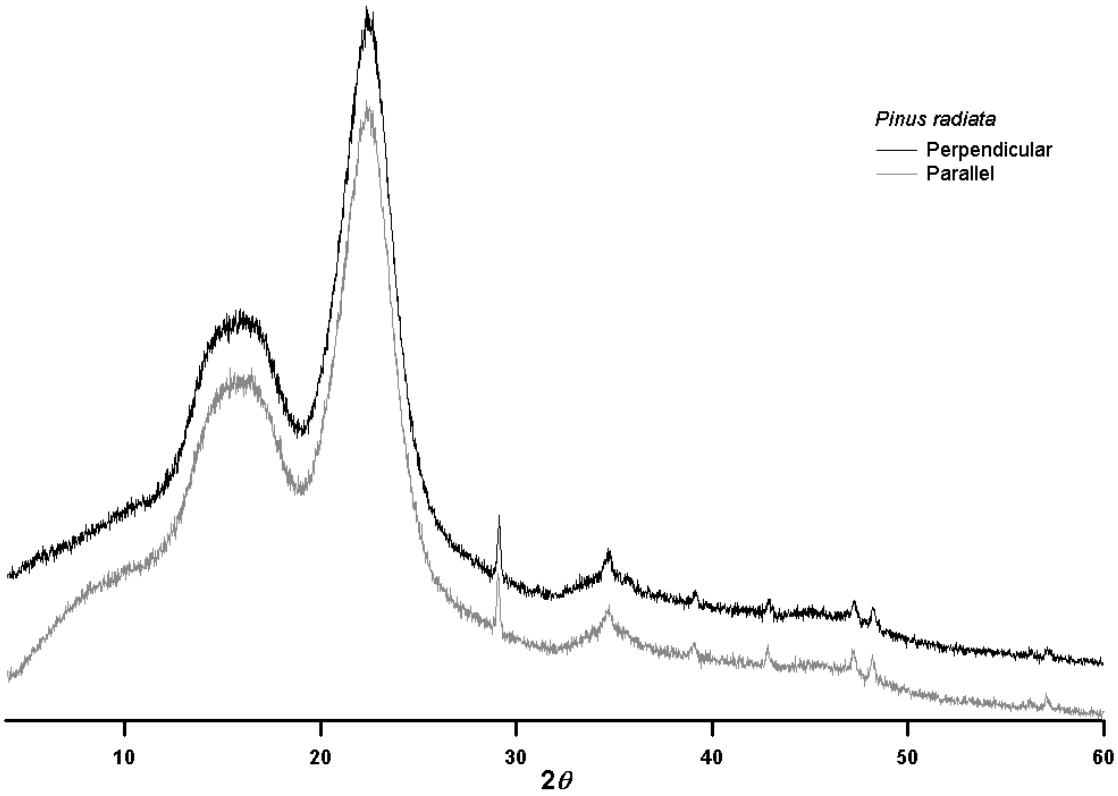

Figure 5-35 – XRD patterns collected from a sample of *P. radiata*.

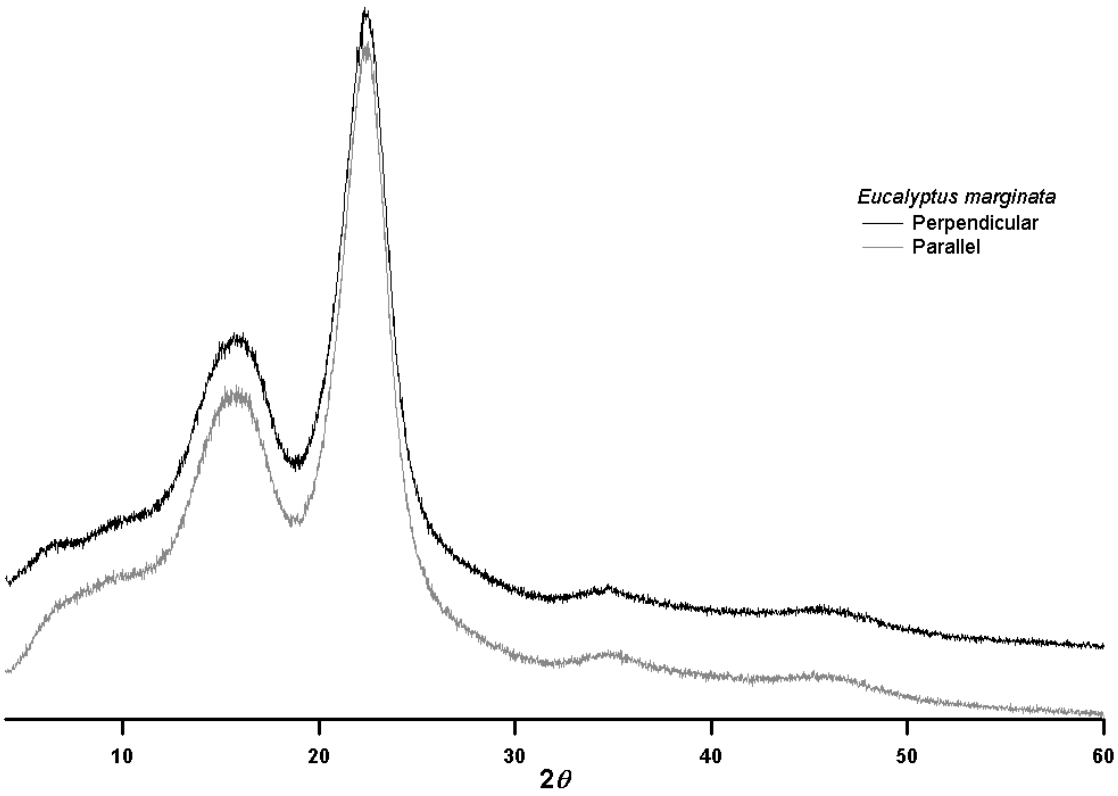

Figure 5-36 – XRD patterns collected from a sample of *E. marginata*.

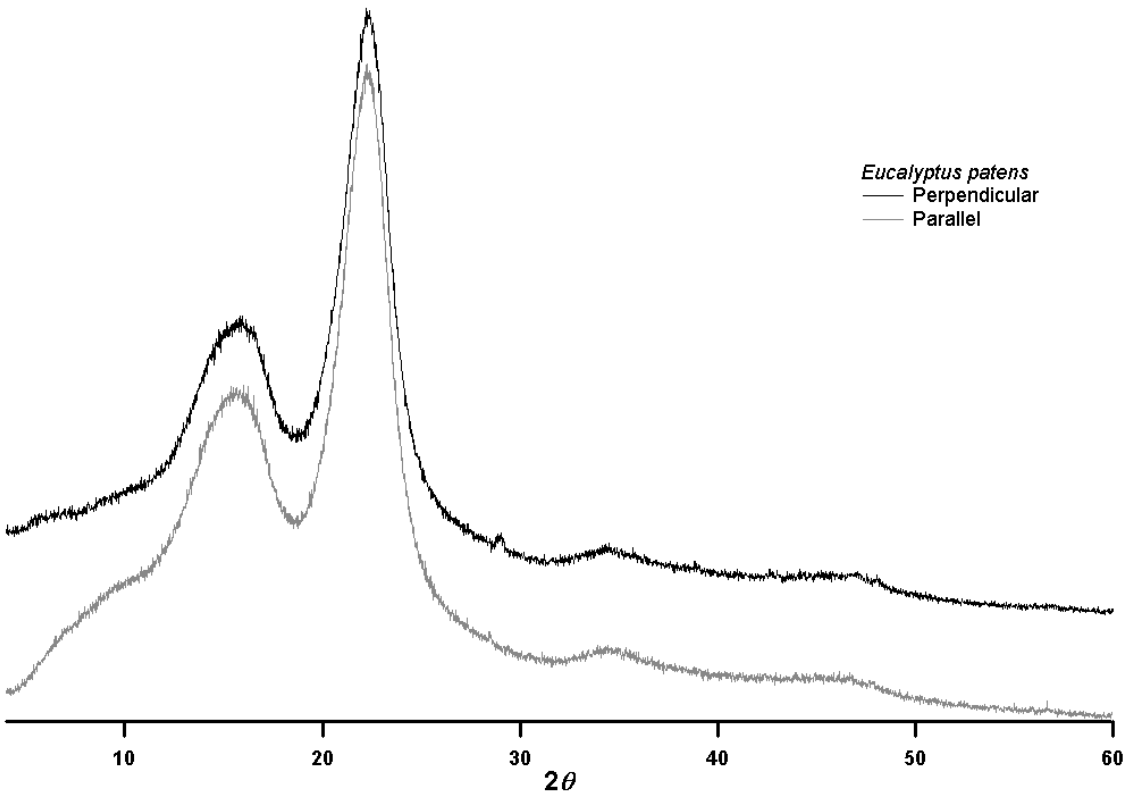

Figure 5-37 – XRD patterns collected from a sample of *E. patens*.

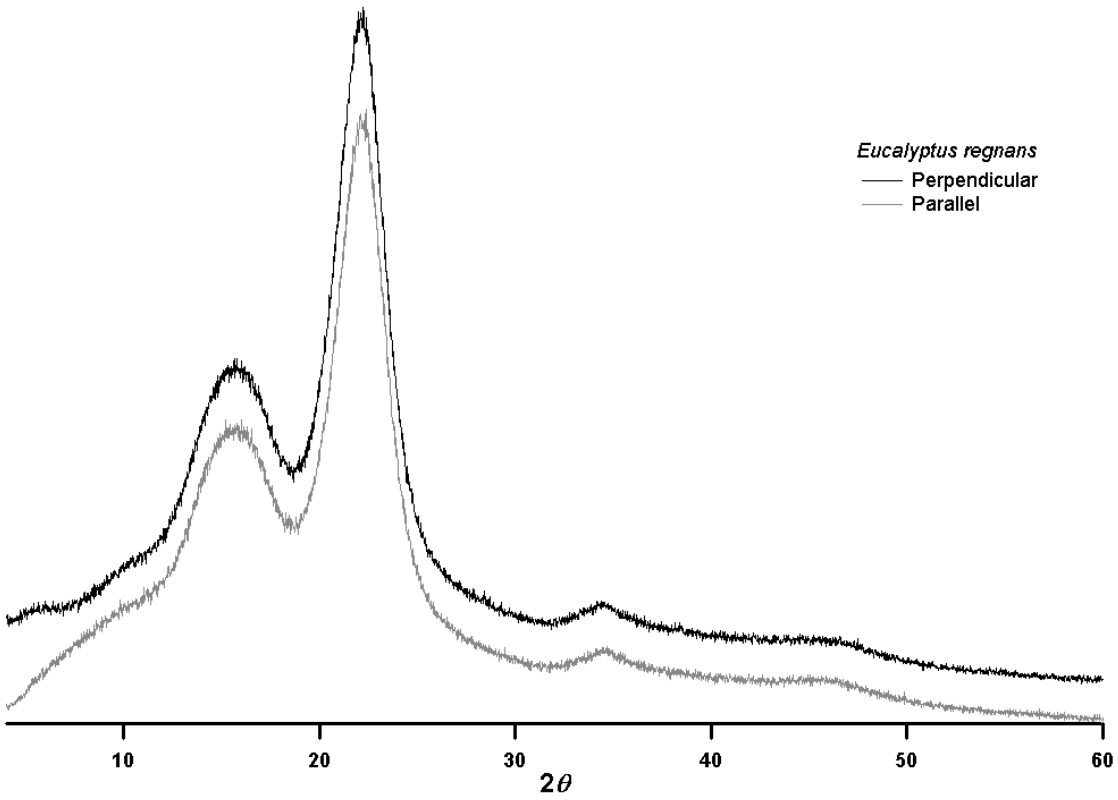

Figure 5-38 – XRD patterns collected from a sample of *E. regnans*.

The diffraction patterns presented above were collected on the Bruker D8 Advance and so the outputted data was suited to analysis in the TOPAS suite (Bruker proprietry software). The fitting routines identical to those previously discussed (i.e. five Voigt profiles used to model the cellulose Bragg peaks over an amorphous signal). The TOPAS software refined these data fits and evaluated the parameters that are output into size and strain values for the sample (Chapter 2.2)

	Crystallite Size (nm)		Strain(e^0)	
	Parallel	**Perpendicular**	**Parallel**	**Perpendicular**
P. radiata	2.1	2.1	0.0001	0.00003
E. marginata	2.4	2.4	0.0005	0.0001
E. regnans	2.3	2.3	0.00002	0.0005
E. patens	2.2	2.2	0.00003	0.00002

Table 5-18 – The size and strain data obtained from the timber samples from measurement on the D8.

5.5.2 Discussion of XRD Results

The diffraction patterns shown above present the data in a way that is easy to compare the orientation perpendicular to the grain and parallel to it. In each graph, the parallel data set trailed to zero at low angles much quicker than in the perpendicular data. This was seen as a better distinguishing feature of the orientation than the intensity of the Bragg peaks as two data sets had a higher intensity for parallel orientation (*E. marginata* and *E. patens*), whereas the other two had a higher intensity for perpendicular orientations (*P. radiata* and *E. regnans*). The data collected from the D8 was analysed using the fundamental parameters approach to correct for the instrumental broadening. The integral breadth method was used to perform a size-strain analysis on the samples (results in Table 5-18).

The fundamental parameters approach to correct for instrumental broadening in the data before analysis. It was expected that the crystallite size measured for each sample would be the same in the parallel and perpendicular orientations. The crystallite size is approximately 2 nm for each sample. Although these values were in the lower region of literature values they were not unrealistic for timber samples. Such a small crystallite size resulted in very large peak broadening resulting in significant overlapping. The overlapping of peaks complicated the fitting of data in the TOPAS software but *ab initio* information regarding the cellulose peaks was used to overcome these difficulties.

There was very little strain measured in the samples. Such small values for the strain make it difficult to evaluate the TOPAS output as it would suggest such a small amount of strain based broadening in the samples compared to the very significant size based broadening. While it might be possible for these samples to contain some lattice strain it does not appear to be a detectable amount from the data obtained.

Chapter 6 Conclusions

Highly ordered examples of cellulose tend to be from the tissues of complex vascular plants. The adaptation of cellulose in vascular plants to deal with the large compressive forces associated with a tree trunk was a major step in the evolution of plants. Although the orientation of cellulose in the trunk of the palm was not investigated here, the development of orientated cellulose was observed in other tissues of the palm. The palm fibres, a by product of the extraction of palm oil for the burgeoning bio-diesel industry in South-East Asia, were investigated as a potentially important commercial resource.

Of the current applications for such a material pulp for the paper industry is one of the most enticing. The cellulose required for paper making can be highly orientated but ends up being an isotropic phase in the binding matrix. Breaking down the texture of the starting material is a process that involves physical and chemical treatments. Wide angle x-ray scattering techniques are perfectly suited for investigating this aspect of palm fibre structure as it reveals crystallite orientation in a rapid manner.

Wide angle scattering experiments on palm fibres revealed a significantly higher MFA than is observed in most other examples of native cellulosics. This would imply that the compressive strength of the palm fibres is significantly less than the samples with cellulose aligned almost parallel to the cell axis. It may be expected that this makes for a more flexible material, able to bend and contort to a greater degree than a sample of woody tissue.

The treatment of palm fibres with a dilute alkaline solution was also investigated by wide angle x-ray scattering. In this instance the amorphous content of the sample decreased significantly after treatment. It was assumed that the majority of the amorphous signal came from the lignin present as there is no hemi-cellulose in the palm fibres. However subsequent NMR measurements showed a prominent lignin signal that was virtually unchanged before and after treatment. While this might suggest that the amorphous signal is composed of materials other than lignin, it could

also highlight the lack of sensitivity in these NMR measurements to quantitative studies.

The palm fibre samples were measured with a variety of techniques. Each technique is capable of producing unique measurements and the collection of data was used to characterise the sample. The complexity and variety of naturally occurring cellulosics makes this type of analysis essential in determining their structure.

While palm fibres represent a more primitive plant tissue the methods used for investigation of cellulose microfibrils in the samples have been applied to more advanced tissues. The development of stems composed primarily of woody tissue is problematic to a plants continued growth. While there are a limited number of compounds available to the plant for building these structures there are very different mechanical properties required at different stages of the stems development. To investigate this development of maturing stems wide and small angle scattering techniques were employed. Presented in this chapter is a selection of maturing stems from different species that are typical of Australian hardwood varieties. The stems were selected from a variety of environments to encompass a range of rainfall and soil nutrient levels.

The wide angle scattering experiments were performed at the Australian synchrotron on the SAXS/WAXS beamline. The measurements were made on a two dimensional detector with the wavelength and sample-detector distances optimised to observe the (002) Bragg reflection. The (002) reflection is important in cellulosic studies as this is used to give an indication of lateral dimensions of the crystallites and the orientation of the microfibrils in the cell wall. The MFA is an important orientation parameter for cellulose and a quality indicator of the timber industry. Measurements of the MFA on the maturing stems were spatially resolved with multiple patterns collected on each sample. The grids of patterns were made along the grain and across the grain to observe variations in these two directions.

The variations in the MFA down the grain were observed to be significantly smaller than those across the grain in maturing stems. The measurement of diffraction patterns across the grain in the stems highlights the changes in the wood as a function

of the maturity of the tissue. The growth mechanism of the stems produces layers of freshly synthesised tissue on the stem next to bark layer. From this method of growth the wood furthest from the pith is the youngest tissue synthesised with the maturity of the tissue increasingly moving towards the centre.

Variations in the MFA are an important parameter in determining the mechanical properties of woody tissue. Three results were obtained observing variations in the MFA across the grain. These results were interpreted in terms of the growth mechanism described above. The first result was observed in three of the six species. In these samples there was no significant or ordered variation observed in the MFA as a function of the wood's maturity. In these samples the MFA maps very well to the mechanical properties measured for the stems in the bulk. In particular there is a linear trend observed between Young's modulus and the MFA (Figure 5-23). Such a relationship has previously been reported in the literature (Burgert *et al.*, 2004). Such studies have investigated the changes in woody tissue over specific anatomic features (reaction wood or annual rings). The observation of a relationship between MFA and the maturing tree stems has not previously been reported.

The second result was obtained from samples collected from a low rainfall and soil nutrient environment (*A. havilandiorum* and *B. cuninghamii*). In these samples the microfibril angle measured from diffraction patterns on the edges of the stems (the younger woody tissue) was significantly smaller than those measured from the central portion of the stem. From this result it is suggested that the microfibril angle changes during the lifetime of the stem. The orientation of the cellulose crystallites is modulated within the stem suggesting that the mechanical properties within the stem are also modulated. The immature wood on the edges of the stem, having a larger MFA than the wood in the centre, would be expected to have lower mechanical properties than the mature wood. The mechanical properties measured on these stems were bulk measurements so spatially resolved mechanical property measurements, using indentation techniques (Zhu *et al.*, 2006), would be required to confirm such a hypothesis.

Similar to the second result was a layered structure observed in the final sample. The trend in the MFA across the grain in the A. doratoxylon stem is the inverse of the

trends observed in the samples from *A. havilandiorum* and *B. cunninghamii*. In this case the tissue on the outer portion of the stem has a lower microfibril angle than the wood in the central portions. This would imply that the more mechanically strong tissue is the younger tissue on the outer regions of the stem. This observation requires follow up investigations in order to confirm such a model of the growing stem, including spatially resolved mechanical properties measurements and stems from different species showing this particular layered structure.

The layering of woody tissue in terms of the MFA has not previously been reported and is proposed here to be a method by which the maturing tree stem modulates the mechanical properties in the woody tissue. Six samples were selected as being representative of Australian hardwoods from a range of different environments. The role that microfibril angle plays in the development of woody stems is only suggested by the data collected here. More measurements are required on a wider range of species to make a definitive link between the microfibril angle and the stems growth. While there appears to be some dependency on the samples environment more measurements are required.

In addition to the orientation of the cellulose crystallites the size of the microfibrils can be investigated with wide angle scattering measurements. In this case the widths of the microfibrils were calculated from the Scherrer equation. The large degree of broadening observed in the stems indicates a very small lateral dimension for the microfibrils. The width of the (002) reflection is the reflection typically associated with the lateral dimensions of microfibril. For a given stem there was little variation observed in calculated microfibril width. The production of consistently sized crystallites suggests that there is no modification in the synthetic process over the lifetime of the stem. The size of the crystallite was not expected to vary within a sample based on literature findings (Delmer, 1987).

In addition to wide angle scattering measurements small angle scattering measurements were made on the maturing stem samples. The samples prepared for small angle scattering measurements were sectioned along the length of the stem to produce a tangential section and through the stem to produce a cross section. These samples were measured on a lab based instrument. A single measurement was made

on each section of the different stems from the wood nearest the middle of the stem without containing any pith.

From the small angle scattering measurements the cross sectional radius of gyration, R_C, was calculated. In the case of the tangential sections a sector average was employed to obtain the scattering profile from the two dimensional data. The anisotropy observed in the cross sectional data was not definitively attributed to the sample owing to considerations of the samples geometry. For these samples a radial average was used to obtain the scattering profile and excluded the scattering around the beam-stop.

In the tangential sections the crystallites are aligned perpendicular to the incident beam. These profiles were modelled with the cylindrical form of the Guinier approximation (equation 4.21). The R_C values calculated in these models were found to agree with each other within experimental uncertainty. The R_C values are the same length-scale as the lateral dimensions of the microfibrils. However the ambiguity around the scattering centre in SAXS experiments using cellulosic materials prevents any conclusions being made regarding polymer arrangements in the cell wall. This form of the radius of gyration can be applied to the cross section of the rod-like particle. The measured values for R_C between samples with the cross sectional preparation is in good agreement with each other. However these values do not agree with those obtained from the tangentially sectioned samples. It is assumed that the structures would not be different in the two sections so the change in orientation of the samples with respect to the incident beam is the most likely cause for the this discrepancy.

In addition to the size of cellulose crystallites the orientation of the microfibrils is an important consideration in the structure of the cell wall. Small angle scattering data has been reported in the literature as suitable for measuring the MFA in woody samples. In this case the scattering from the side walls of the cell dominates the scattering profiles. The result is that the scattering of interest (the S_2 scattering) for the calculation of MFA is buried in the side wall streak. Deconvolution of the scattering profiles yields the position of the peaks of interest and the MFA can be calculated. The results obtained in (Table 5-15) are in good agreement with the MFA

values calculated from the WAXS data. While the data shows good agreement in this regards the directness with which WAXS can calculate both orientation and microfibril size makes it a powerful technique in the field of cellulose research with SAXS capable of providing complimentary results.

WAXS is a powerful tool for the study of cellulosic materials. The advantage of scattering studies often lies in the sample preparation and the analysis of the measurements. Mounting samples for a scattering experiment is often as simple as holding the sample in place and beginning the experiment. The analysis is also rapid, and produces results that are averaged over the irradiated volume, giving good statistics on the measurement. These advantages of WAXS methods were exploited in the analysis of a sample of *acacia* wood.

A data set was obtained from the measurement of scattering patterns from an *acacia* species on the Bruker Nanostar at ANSTO. This experiment was performed in transmission geometry to obtain two dimensional data allowing for the analysis of crystallite size and orientation. The measurements made on the *Acacia* sample scanned through interesting features of the wood, namely a band of reaction wood and an annual ring. The experiment was performed in order to examine what changes, if any, would occur through these regions with regard to crystallite size and orientation.

Variations observed in the crystallite orientation and size through the features of interest was not of sufficient size, or with any sort of order, to say that these regions were fundamentally different to the ‘normal’ wood in the sample. The lack of variation in the crystallite size is rationalised by the fact that the synthesis of cellulose is presently not believed to change for regions of early wood, late wood or reaction wood.

The most useful reflection in cellulose diffraction patterns is the (002). From this reflection, the Scherrer analysis can yield a crystallite size in the direction of the fibre width. For the *acacia* sample this was particularly stable with an average microfibril width of 3.4 nm being measured across the twenty measurements made along the length of the sample. The standard deviation of these measurements was calculated

to be 0.4 nm. Similar to the microfibril width, the MFA was observed to not vary according to position when scanning through the wood. The average MFA was measured to be 8.17° with a standard deviation of 3.57°. These calculations have been skewed by the first two data points which were significantly larger than those of the remaining eighteen. If these two points are removed the average becomes 7.12° with a standard deviation of 0.94°. As these two points are at the start and near the edge of the sample, it is likely that the considerably larger MFA measured here is due to a defect in the sample. This can occur when sectioning the wood if clean planes are not removed and the fibre structure is disturbed.

The use of size and strain analysis is not common for cellulosic materials. This is due to the large degree of size broadening present in diffraction patterns as a result of the microfibril widths only being a few nanometres. However a rigorous analysis of woody materials is presented here to demonstrate the difference between size broadening and strain broadening in a typical timber. The timber samples *P. radiata*, *E. marginata*, *E. regnans* and *E. patens* were obtained from a timber wholesaler as examples of ready to use timber products. These samples were sectioned and mounted in the reflection geometry on a Bruker D8 Advance diffractometer.

The measurements obtained from these samples were analysed in TOPAS, an analysis suite developed by Bruker specifically for data collected on their reflection mode instruments. The fitting of instrumental parameters and background was critical to ensuring a rigorous analysis of the sample broadening. The analysis in TOPAS resulted in calculations of microfibril width of between 2.1 nm and 2.4 nm. These values are reasonable in terms of the available literature. The strain however was at most 0.0005 (strain being unitless as a ratio of the change in length over length). Such low values for strain become unreliable as crystallite size cannot be measured at these levels. From the analysis of the timber materials using a rigorous integral breadths method, the samples were considered to be free of any measurable lattice strain.

The results from this study were fairly typical of woody tissue. The examination of cellulose in timbers is often hindered by numerous factors related to the sample. The challenges associated with diffraction experiments of cellulose can be overcome to

provide good quality results. Sample preparation, experimental design and analysis are all stages where different methods can be used to examine different aspects of the crystalline cellulose phase.

Chapter 7 Further Studies

The scope of this project can be widened greatly to open many lines of additional investigation. In general the cell wall polymers can be observed in terms of polymer arrangements and sizes in the different layers of the cell wall or in terms of the quantities and composition of polymer involved.

The palm fibre samples in particular are a candidate for 'before and after' studies with measurements being made on the sample before and after treatment. NaOH treatment of palm fibres was presented previously in this thesis as a 'before and after' study utilising both WAXS and NMR measurements. The same experiment can be performed using any chemical treatment to investigate how this alters the structure and arrangement of cell wall polymers. In addition to chemical treatments physical treatments can be applied to the samples. An example of such an experiment might be the measurement of NMR and WAXS patterns from the palm fibre before gently annealing the sample under vacuum. Such an experiment could give an insight into the nature of the cellulose microfibril crystal structure in the palm fibre and how this might be altered.

The measurement of spatially resolved WAXS patterns from maturing stems gave important results earlier in this thesis. However these results were in the preliminary phase as evidenced by the relatively small number of samples and scattering patterns collected. There is great potential in this experiment to expand the number of samples investigated. This could open up the statistically significant outputs of the study and establish new models for the growth of woody tissue as it relates to the orientation of cellulose crystallites in the cell wall.

Synchrotron measurements were used for this study and are likely to be the most suitable method for any additional investigations into maturing tree stems. This is because of the spatial resolution of the synchrotron beam and the large volume of data generated from making upwards of 25 measurements per sample. The rapid processing of data is also suited to further studies related to the addition of more samples to the collection of maturing stems. As well as adding more samples to the

investigation, sample preparation could be improved upon. The sectioning of samples through the maturing stems can be improved as can the mounting of the samples. Careful sectioning and mounting will be essential to providing even grids of scattering patterns with over 20 patterns per sample. The more patterns collected across the grain the better as this is the direction most likely to show variations within a sample. Scattering patterns collected down the grain would be expected to be similar.

While generally considered quite straightforward relative to other experimental methods, the preparation of samples of cell wall materials for scattering experiments still requires careful consideration. This is due to the possibility of altering the arrangement of cell wall structures due to the section of samples thin enough for experiments in the transmission geometry. A sample of mature wood (such as the piece of wood the *acacia* sample came from) would be an ideal starting material to prepare several samples from using different methods. The different methods for sectioning the sample could then be measured by WAXS to compare the orientational parameters.

The focus of the further studies suggested thus far has been on expanding the experiments presented in this thesis. Although there is great potential to develop these experiments further there are also other avenues of study that relate to the investigation of cell wall polymers in general. In particular the suite of experimental methods can be expanded to include other structural probes such as microscopic methods and *in situ* scattering studies.

While other structural probes can be deployed to aid in the examination of some of the cell wall materials discussed here other fruitful avenues of study could include the examination of different samples using these experimental methods. In particular bacterial cellulose is an important cellulosic material and can be grown in a laboratory under a variety of conditions. These samples can be examined using scattering methods in the same way natural samples are examined. The potential for study of cell wall polymers are almost limitless and WAXS studies are an attractive method for such studies, often offering significant advantages over other structural probes.

Appendices

Appendix One

The Warren-Averbach method is a popular way of separating the size and strain components of broadening in a diffraction pattern. Equation (3.8) is a convenient starting place for the method as it is a Fourier series. The use of a Fourier series for this structural analysis is particularly useful if used in conjunction with the Stokes deconvolution for the modelling of instrumental broadening. This method also makes use of the Fourier transform and when the two methods are used in conjunction the Fourier constants for one can be applied to the other. The method was laid out by Warren in 1969 but has since been reviewed and summarised in more modern contexts (Snyder *et al.*, 1999) (Warren, 1969). The revision by Klug and Alexander in 1974 is also particularly comprehensive (Klug and Alexander, 1974). These important texts will form the basis of the derivation of equation (3.8).

Klug and Alexander showed that using a (00*l*) reflection from an orthorhombic crystal is equivalent to the general treatment. Considering a crystal to be made up of smaller coherently diffracting domains and each domain to be an array of unit cells, the position of any given cell (m_1, m_2, m_3) is

$$\boldsymbol{R}_m = m_1\boldsymbol{a_1} + m_2\boldsymbol{a_2} + m_3\boldsymbol{a_3} + \boldsymbol{\delta}(m_1, m_2, m_3) \qquad \text{(A1.1)}$$

Here $\boldsymbol{\delta}(m_1, m_2, m_3)$ denotes a small distortion in the domain with the $\boldsymbol{a}_1$, $\boldsymbol{a}_2$, $\boldsymbol{a}_3$ as the unit cell axes. Assuming the distortion within some cell to be negligible then the structure factor for cells within a domain doesn't vary. The intensity of the reflection from this structure factor is

$$I = F^2 \sum_{m} \sum_{m'} \exp\left[\frac{2\pi \cdot i}{\lambda}(\boldsymbol{s} - \boldsymbol{s}_0)(\boldsymbol{R}_{m'} - \boldsymbol{R}_m)\right] \qquad \text{(A1.2)}$$

F is the structure factor, λ is the wavelength, $(\boldsymbol{s} - \boldsymbol{s}_0)$ is the vector representing the diffracted x-ray and *m/m'* are a pair of unit cells. The intensity here is given in terms

of electron units but multiplying the RHS of equation (A1.2) by I_e (the classical scattering of a free electron) gives intensity in arbitrary units (Klug and Alexander, 1974) (Guinier, 1963). Accounting for the peak broadening in a powder diffraction pattern requires the scattering vector from equation (A1.2) to be defined in terms of continuous variables (h_1, h_2, h_3). These are analogous to the indices (h, k, l) usually used for single crystal diffraction. Using $\mathbf{a}_1$*, $\mathbf{a}_2$* and $\mathbf{a}_3$* as the reciprocal lattice transforms of the unit cell axis, $\mathbf{a}_1$, $\mathbf{a}_2$ and $\mathbf{a}_3$ from above then

$$(\boldsymbol{s}-\boldsymbol{s}_0)/\lambda = h_1\boldsymbol{a}_1^* + h_2\boldsymbol{a}_2^* + h_3\boldsymbol{a}_3^* \tag{A1.3}$$

Using this new definition for the diffraction vector equation (A1.2) can be transformed into

$$I = F^2 \sum \sum \exp\{2\pi \cdot i[(m_1'-m_1)h_1 + (m_2'-m_2)h_2 + (m_3'-m_3)h_3] + \frac{\boldsymbol{s}-\boldsymbol{s}_0}{\lambda}(\boldsymbol{\delta}_{m'} - \boldsymbol{\delta}_m)\} \tag{A1.4}$$

The distortion vector in equation (A1.4) can be replaced with

$$\boldsymbol{\delta}_m = X_m\boldsymbol{a}_1 + Y_m\boldsymbol{a}_2 + Z_m\boldsymbol{a}_3 \tag{A1.5}$$

Only the (00l) reflection is considered here which can be used to make an approximation for the diffraction vector. This approximation is based on the visualisation of the reflection in a two dimensional section of the orthorhombic crystal (Warren, 1969). From this diagram it should be clear that

$$\frac{\boldsymbol{s}-\boldsymbol{s}_0}{\lambda} \cong l \cdot \boldsymbol{a}_3^* \tag{A1.6}$$

And so the scalar product of equations (A1.5) and (A1.6) is

$$\frac{\boldsymbol{s}-\boldsymbol{s}_0}{\lambda}\delta_m = l\boldsymbol{a}_3^*(X_m\boldsymbol{a}_1 + Y_m\boldsymbol{a}_2 + Z_m\boldsymbol{a}_3) = lZ_m \tag{A1.7}$$

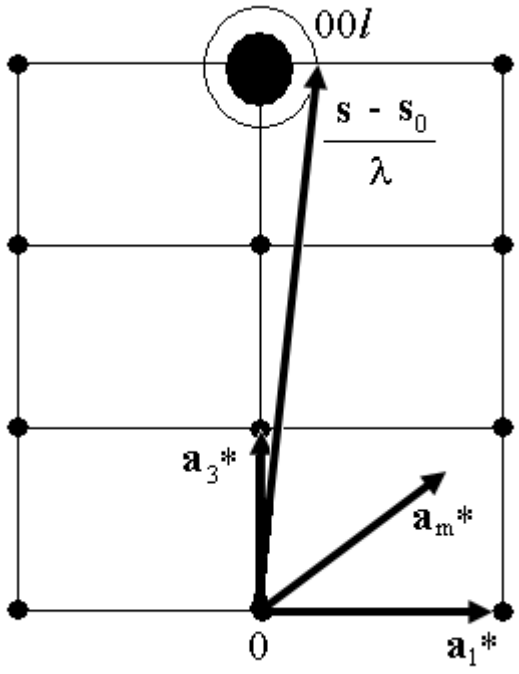

Figure A1-1 – Recreation of Warrens representation of the (00*l*) reflection (Klug and Alexander, 1974).

Equation (A1.7) can be used to substitute into equation (A1.4) to obtain

$$I(h_1h_2h_3) = F^2 \sum \sum \exp\{2\pi \cdot i[(m_1'-m_1)h_1 + (m_2'-m_2)h + (m_3'-m_3)h_3] + l(Z_{m'} - Z_m)\} \quad \text{(A1.8)}$$

The total power in a given reflection is expressed as the integral of the power distribution $P(2\theta)$ which can be calculated from equation (A1.8). It is important again to note that equation (A1.8) is in electron units and the classical scattering of a free electron is used to correct the dimensions for Warrens powder patter power theorem (Klug and Alexander, 1974).

$$P = \int P(2\theta)d\theta = \frac{I_e M R^2 \lambda^3 p(hkl)}{4v_a} \iiint \frac{I(h_1h_2h_3)}{\sin\theta} dh_1 dh_2 dh_3 \quad \text{(A1.9)}$$

Here I_e is the classical scattering from a free electron as defined by Thomson (Guinier, 1963). M is the number of domains in the sample, R is the distance from the sample to the diffraction circle, λ is the wavelength, $p(hkl)$ is a multiplicity factor

confining the integration in reciprocal space and v_a is the volume of the unit cell (Klug and Alexander, 1974). In the case of a 00*l* reflection the intensity is non-zero if h_1 and h_2 are very small. As noted above in Figure A1- 1 the scattering vector can be approximated for this reflection type.

$$s = \frac{|\boldsymbol{s} - \boldsymbol{s}_0|}{\lambda} = \frac{2\sin\theta}{\lambda} = |h_1\boldsymbol{a}_1^* + h_2\boldsymbol{a}_2^* + h_3\boldsymbol{a}_3^*| \cong h_3|\boldsymbol{a}_3^*| \tag{A1.10}$$

This allows an expression to be made for the continuous variable h_3 in terms of θ and taking the derivative of this expression can simplify equation (A1.9)

$$dh_3 = \frac{\cos\theta}{\lambda|\boldsymbol{a}_3^*|} d(2\theta) \tag{A1.11}$$

Substitution of equation (A1.11) into (A1.9)

$$P(2\theta) = \frac{I_e M R^2 \lambda^2 p(hkl)\cos\theta}{4v_a|a_3^*|\sin\theta} \iint I(h_1 h_2 h_3) dh_1 dh_2 \tag{A1.12}$$

The power of the reflection that is measured by experiment, $P'(2\theta)$, is proportional to the power per unit length.

$$P'(2\theta) = \frac{P(2\theta)}{2\pi R\sin(2\theta)} \tag{A1.13}$$

The constant *K* is defined as a singular value for the large number of constants used in previous equations.

$$K = \frac{I_e R\lambda^2 p(hkl)}{6\pi v_a|\boldsymbol{a}_3^*|} \tag{A1.14}$$

Using this expression for the collected constants and substituting equation (A1.8) into equation (A1.13) the observable power function becomes

$$P'(2\theta) = \frac{KMF^2}{\sin^2\theta} \iint \sum_m \sum_{m'} \exp\{2\pi \cdot i[(m'_1 - m_1)h_1 + (m'_2 - m_2)h_2 + (m'_3 - m_3)h_3 + l(Z_{m'} - Z_m)]\} dh_1 dh_2 \quad \text{(A1.15)}$$

Considering only 00*l* reflections the values of h_1 and h_2 are considered small so integration of equation (A1.15) is taken over - $\frac{1}{2}$ and + $\frac{1}{2}$.

$$P'(2\theta) = \frac{KMF^2}{\sin^2\theta} \sum_m \sum_{m'} \frac{\sin \pi(m'_1 - m_1)}{\pi(m'_1 - m_1)} \frac{\sin \pi(m'_2 - m_2)}{\pi(m'_2 - m_2)} \times \exp\{2\pi \cdot i[(m'_3 - m_3)h_3 + l(Z_{m'} - Z_m)]\} \quad \text{(A1.16)}$$

The values for the sine functions in equation (A1.16) goes to unity when $m'_1 = m_1$ and $m'_2 = m_2$.Equation (A1.16) can be simplified to

$$P'(2\theta) = \frac{KMF^2}{\sin^2\theta} \sum_{m_1} \sum_{m_2} \sum_{m_3} \sum_{m_4} \left[\exp\{2\pi \cdot il[Z(m'_3) - Z(m_3)]\} \times \exp\{2\pi \cdot i(m'_3 - m_3)h_3\}\right]_{m_1 m_2} \quad \text{(A1.17)}$$

Given the restrictions on the direction of the reflections in reciprocal space diffracting domains can be considered as columns of unit cells in the $\boldsymbol{a}_3$ direction. This is perpendicular to the 00*l* reflecting plane. This can be visualised as in (Figure A1-1). Using the substitutions $n = m'_3 - m_3$ and $Z_n = Z(m'_3) - Z(m_3)$ equation (A1.17) can be simplified further.

$$P'(2\theta) = \frac{KF^2}{\sin^2\theta} \sum_{n=-\infty}^{\infty} N_n \left\langle \exp 2\pi \cdot ilZ_n \right\rangle \exp\{2\pi \cdot inh_3\} \quad \text{(A1.18)}$$

Here N_n is the number of cells in the whole sample and $\left\langle \exp 2\pi \cdot ilZ_n \right\rangle$ is the average overall pairs of neighbors in any given column throughout the sample. This replaces the factor *M* and the necessity of a four-fold summation as in equation (A1.17). Now *N* can be set to the number of cells in the sample with N_3 the average number of cells

per column and N_n the average number of n pairs in each column (Klug and Alexander, 1974).

$$P'(2\theta) = \frac{KNF^2}{\sin^2\theta} \sum_{\substack{-\infty \\ n}}^{\infty} \frac{N_n}{N_3} \langle \exp 2\pi \cdot ilZ_n \rangle \exp\{2\pi \cdot inh_3\} \tag{A1.19}$$

The complex exponentials in equation (A1.19) can be expanded to give

$$P'(2\theta) = \frac{KNF^2}{\sin^2\theta} \sum_{\substack{-\infty \\ n}}^{\infty} \frac{N_n}{N_3} \left[\langle \cos 2\pi lZ \rangle \cos 2\pi nh_3 - \langle \sin 2\pi lZ_n \rangle \sin 2\pi nh_3 \right. \tag{A1.20}$$

$$\left. + i\left(\langle \cos 2\pi lZ_n \rangle \sin 2\pi nh_3 + \langle \sin 2\pi lZ_n \rangle \cos 2\pi nh_3 \right) \right]$$

As noted above the substitutions $n = m'_3 - m_3$ and $Z_n = Z(m'_3) - Z(m_3)$ are used in equation (A1.20). From these it should be noted that $-n = m_3 - m'_3$ and also that $Z_{-n} = Z(m_3) - Z(m'_3)$ or $Z_{-n} = -Z_n$. From these properties of the substitutions n and Z_n it should be clear that the imaginary components of equation (A1.20) cancel out. This leaves the trigonometric Fourier series

$$P'(2\theta) = \frac{KNF^2}{\sin^2\theta} \sum_{\substack{-\infty \\ n}}^{\infty} (A_n \cos 2\pi nh_3 + B_n \sin 2\pi nh_3) \tag{A1.21}$$

With the Fourier constants being

$$A_n = \frac{N_n}{N_3} \langle \cos 2\pi \cdot lZ_n \rangle \;\; ; \;\; B_n = -\frac{N_n}{N_3} \langle \sin 2\pi \cdot lZ_n \rangle \tag{A1.22}$$

Equations (A1.21) and (A1.22) are the starting points for the Warren-Avrebach method to separate the size and strain components of a broadened diffraction line.

Appendix Two

The uncertainty attributed to the lateral dimensions of the microfibril is based on the 95% confidence interval of the peak fitting routine. After the two dimensional data has been reduced to a one dimensional data set of intensity as a function of 2θ it was used to fit a number of profiles to model the various components of the sample and how these scatter an incident x-ray beam. The peak fitting routines used in the main document also return a 95% confidence interval for the fitted data.

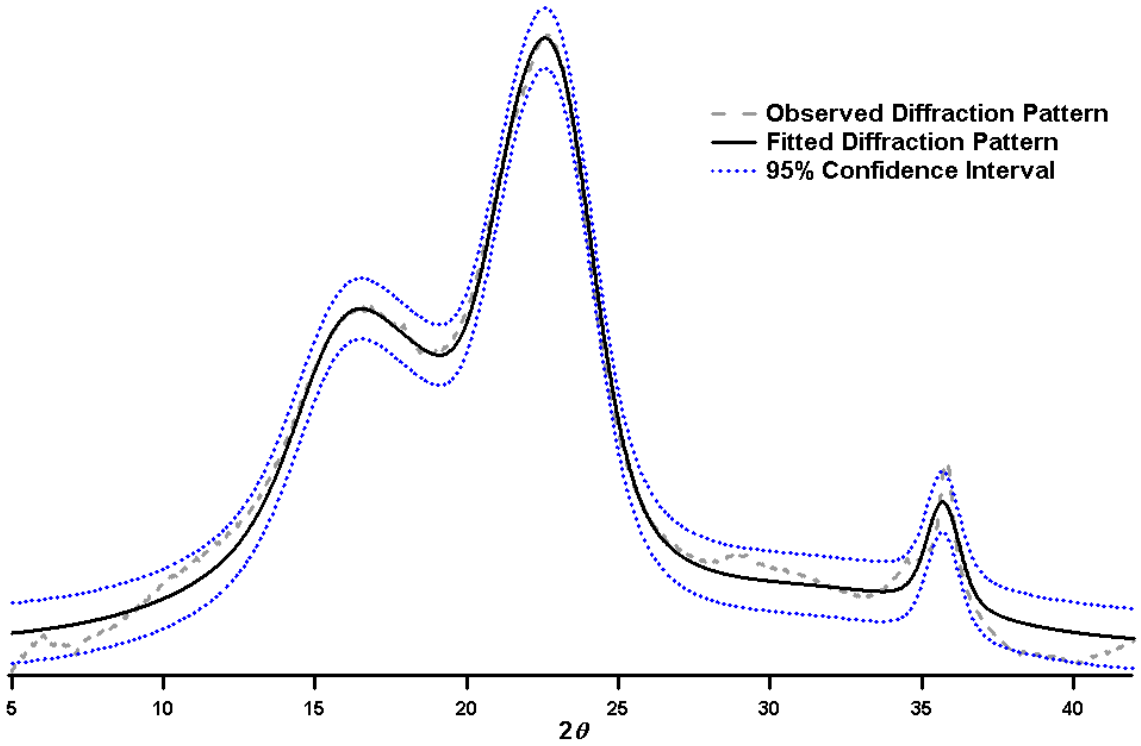

Figure A2-1 – The 95% confidence interval for the fitted diffraction pattern from a palm fibre sample.

It can be observed that the most confident regions are on the sides of the (002) reflection suggesting this is the best fitted area. This allows a better uncertainty to be attributed to the FWHM value of the (002) peak that is deconvolved from the main spectra. This smaller uncertainty in FWHM is propagated to the uncertainty in the lateral dimension of the microfibril and the upper and lower bounds of values forms the uncertainty in the observed crystallite width.

Appendix Three

The multiple resonances of the four main spectral regions described can be used to make inferences regarding the crystallography of cellulose. In the case of the C1 region, the shape of the signal can be used to identify the particular crystal form of cellulose present (i.e. I_α, I_β or a combination of the two). In the case of the filter paper shown above, the splitting of this C1 signal into a doublet is characteristic of the I_β form of cellulose. However the presence of a sharp singlet followed by a broad hump in the C6 region of the spectra is characteristic of the I_α form of cellulose. This would suggest that the filter paper sample is composed of a combination of the two crystalline forms of cellulose.

In addition to the crystal structure(s) present in the sample, there is information present regarding the dimensions of the crystallites embedded within the four spectral regions. The C4 and C6 regions of the spectra are notable for the sharp peak located directly next to a broad hump. The two different resonances were assigned to carbon atoms in two different environments with the sharp peak originating from the surfaces of cellulose microfibrils and the broader peak being from internal chains (Earl and Van der Hart, 1981).

The C4 region was focused on and the region between 92 and 86 ppm was attributed to the interior cellulose chains while the spectra between 86 and 80 ppm was from the surface cellulose chains (Newman, 1999). The ratio of surface chains to interior chains is used to calculate the crystallite lateral dimensions. This ratio can be determined from NMR spectroscopy by measuring the areas under the surface and interior signals (Newman, 1999).

$$X = \frac{\textit{Area Under Interior Signal}}{\textit{Total Area of C4 Sub-spectra}} \qquad \text{(A3.1)}$$

The parameter *X* is equivalent to the fraction of cellulose chains inside the crystallite. To make use of this value for calculating the lateral dimensions a model of the crystallite was established. Diffraction experiments in the literature suggest a square cross section for the crystallites can be defined(GARVEY *et al.*, 2005a). This

crystallite is monoclinic with 0.54 nm between chains on one face and 0.60 nm between chains on the other. The characteristic angle, γ, for the $P2_1$ space group was determined to be 97.3° with the other two angles being square (Sugiyama *et al.*, 1991a). This model was simplified so that all angles were 90° and the distance between cellulose chains was 0.57 nm on each face (Newman, 1999). The lateral dimension of a crystallite, *L*, is related to the number of chains present by $L = 0.57n$. The ratio of internal chains in the crystallite can be put in terms of the lateral dimension, *L*.

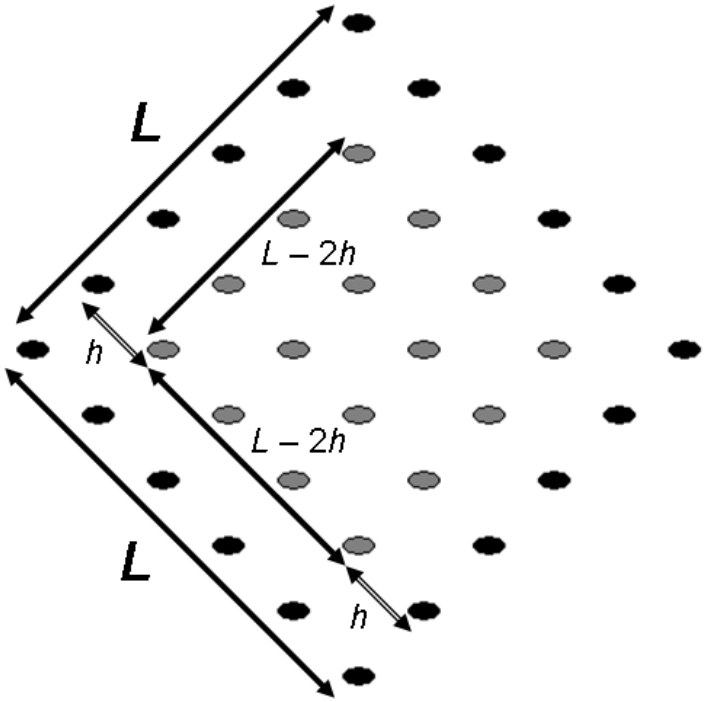

Figure A3-1 – The cellulose crystallite with the internal cellulose chains determined as a fraction of the whole from the lateral dimension, *L* (Newman, 1999).

$$X = \left(L - 2h\right)^2 \Big/ L^2 \qquad \text{(A3.2)}$$

In equation (5.2) the parameter *X* is the same as for equation (5.1) and the parameter *h* is the spacing between cellulose chains *h* = 0.57 nm. Rearranging equation (5.2) gave an expression for the lateral dimension in terms of *X*, which was determined from the NMR data.

$$L = 2h \Big/ \left(1 - \sqrt{X}\right) \qquad \text{(A3.3)}$$

The parameter *X* was determined for the filter paper spectra from the fitting of a few starting profiles. Although there were many more signals present in the data the aim of this fitting routine was to determine the area under the spectra for specific regions.

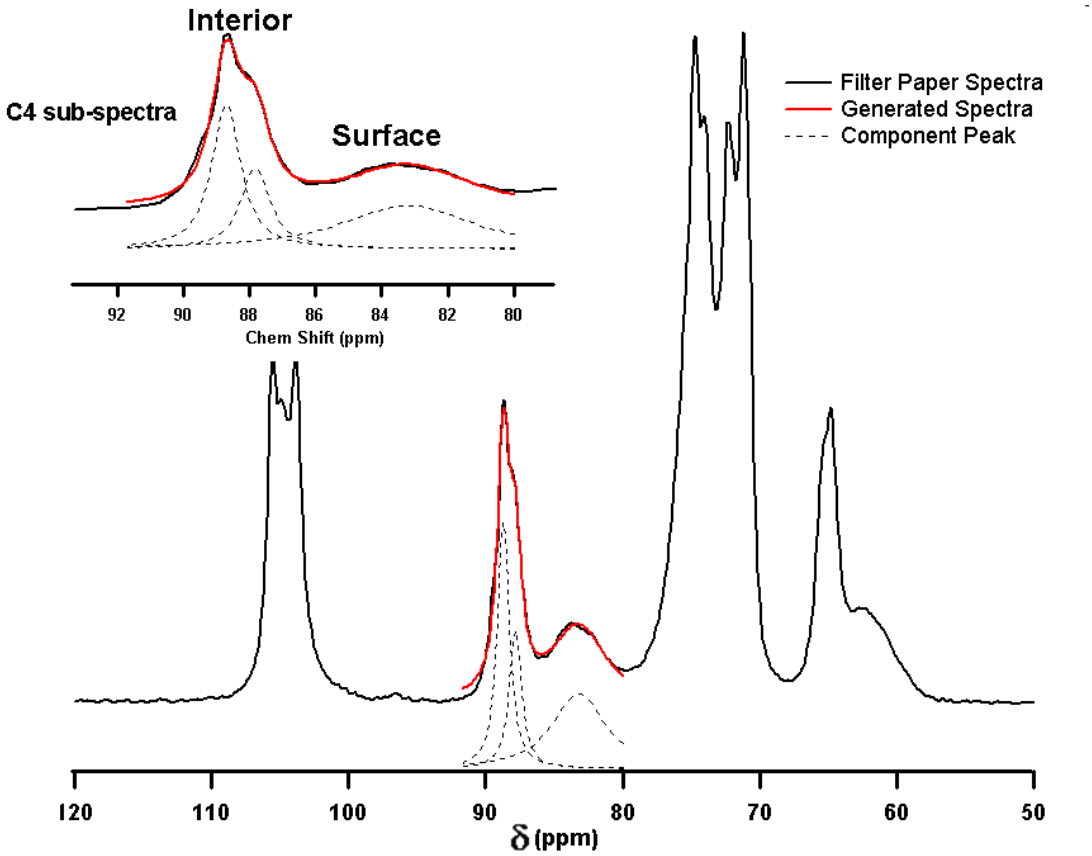

Figure A3-2 – Filter paper NMR spectra with C4 sub-spectra inset. The fitting of the C4 region was used to determine the parameter *X* and hence calculate the lateral dimensions of the crystallites in the filter paper.

From the fitting of initial profiles to the experimental data the parameter *X* was determined from the measured areas under the internal signal and surface signal. From equation (5.5) $X = 0.38$ and hence using equation (5.7) L = 2.97 nm. This value for the crystallite dimensions within a sample of filter paper was the weight averaged lateral dimensions as there will be some individual deviations from the very simplified model used for the analysis. The calculated value for the average lateral dimensions of the crystallites in the filter paper sample fell within the expected range (Newman, 1999).

Appendix Four

Crystallite Width Based on (002) Reflection (nm)						
	A. dor	***B. Cun***	***A. Flo***	***A. Sua***	***B. Pop***	***A. Hav***
001	2.95	2.97	3.54	3.39	3.41	3.33
002	2.89	2.83	3.47	3.33	3.44	3.36
003	2.92	3.01	3.37	3.35	3.46	2.55
004	2.93	2.93	3.53	3.45	3.38	3.37
005	2.93	2.99	3.38	3.40	3.46	3.34
006	2.87	2.99	3.39	3.39	3.29	2.99
007	2.95	2.85	3.43	3.35	3.47	3.32
008	2.88	2.90	3.31	3.41	3.39	3.28
009	2.94	3.00	3.36	3.39	3.07	2.87
010	2.88	2.93	3.33	3.49	3.40	3.33
011	2.88	2.99	3.36	3.53	3.43	3.30
012	2.92	2.95	3.36	3.39	3.40	2.85
013	2.94	2.98	3.39	3.33	3.40	
014	2.86	2.93	3.45	3.46	3.45	
015	2.89	2.88	3.37	3.41	3.46	
016	2.93	2.87	3.37	3.45	3.24	
017	2.89	2.91	3.44	3.32	3.44	
018	2.93	2.91	3.38	3.47	3.30	
019	2.94	2.96	3.35	3.42		
020	2.88	2.92	3.37	3.36		
021	2.88	2.91				
022	2.90	2.96				
023	2.90	2.97				
024	2.87	2.93				

Table A4-1 – The width of the cellulose microfibril as calculated from WAXS patterns and the Scherrer equation. The samples are from left to right; A. doratoxylon, B. cunninghamii, A. floribunda, A.suaveolens, B. populneus and A. havilandiorum.

(°)	1	2	3	4	5	6
1	19.6	11.3	7.4	8.9	8.7	17.9
2	19.9	8.8	7.4	10.1	8.2	17.2
3	20.6	9.1	7.1	7.9	8.2	19.8
4	20.2	9.3	8.5	10.3	9.3	19

Table A4-2 – Measured MFA for *B. cunninghamii*.

(°)	1	2	3	4	5	6
1	6.5	27.7	30.6	32.8	27.3	15.1
2	6.9	27.5	26.9	23.1	27.4	11.3
3	7.1	29	23.9	26.8	25.7	11.6
4	6.6	26.1	29	27.3	28.8	16.2

Table A4-3 – Measured MFA for *A. doratoxylon*.

(°)	1	2	3	4	5	6
1	18.5	17.2	16.2	19.3	24.6	17.1
2	18.9	18.1	18.1	18.9	21.7	19.6
3	20.1	18.5	18.1	20.4	19.5	22.4

Table A4-4 – Measured MFA for *B. populneus*.

(°)	1	2	3	4	5
1	7.4	7.5	7.3	8.6	7.3
2	7.4	7.1	7.6	7.3	7.1
3	7.2	7.5	7.3	6.4	6.7
4	7	7.1	7.2	7.2	7.6

Table A4-5 – Measured MFA for *A. floribunda*.

(°)	1	2	3	4	5
1	13.5	11.3	10.3	9.2	8.3
2	13.1	11.5	9.9	9.3	8.6
3	10.9	11.6	9.8	9.3	9.1
4	9.9	12.8	9.6	9.3	8.9

Table A4-6 – Measured MFA for *A. suaveolens*.

(°)	1	2	3
1	13.1	7.3	7.2
2	13.4	7.2	7.3
3	14.8	6.3	6.1
4	15.2	6.6	6.4

Table A4-7 – Measured MFA for *A. havilandiorum*.

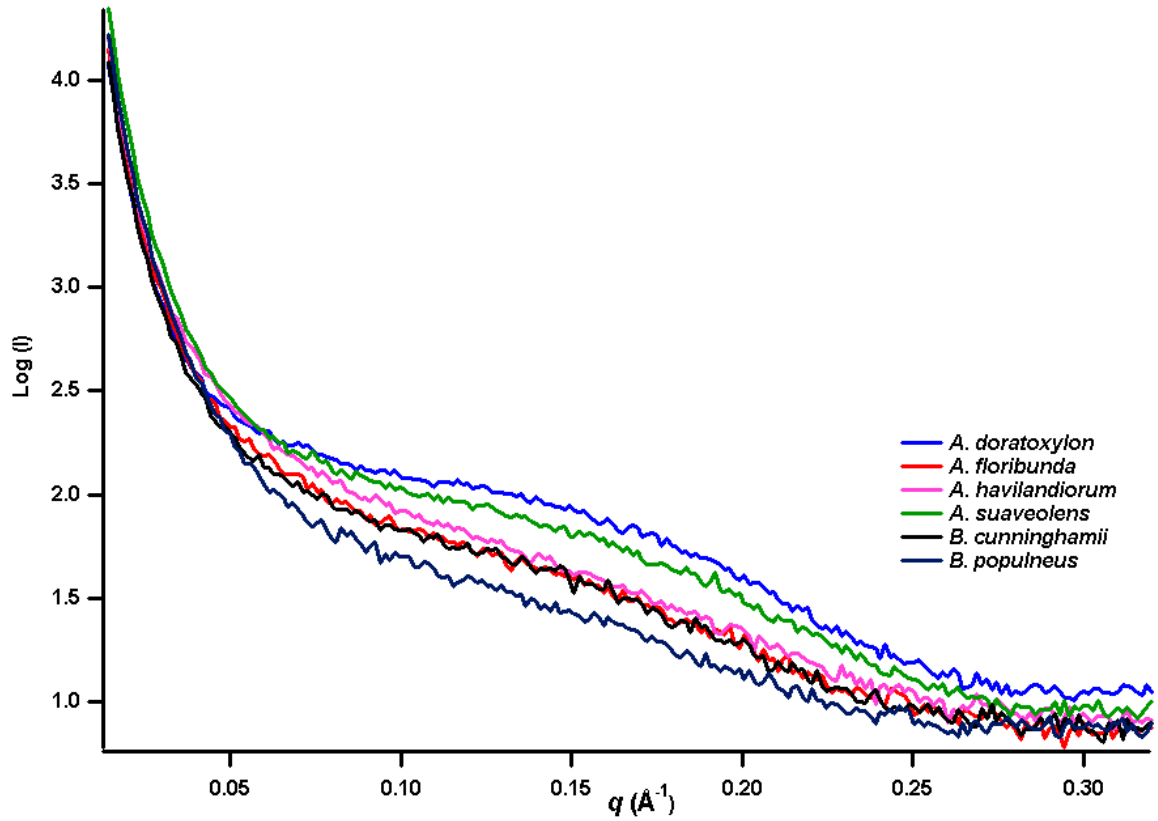

Figure A4-1 – SAXS profiles for the tangential sections of the maturing stems measured on a Bruker Nanostar at Curtin University.

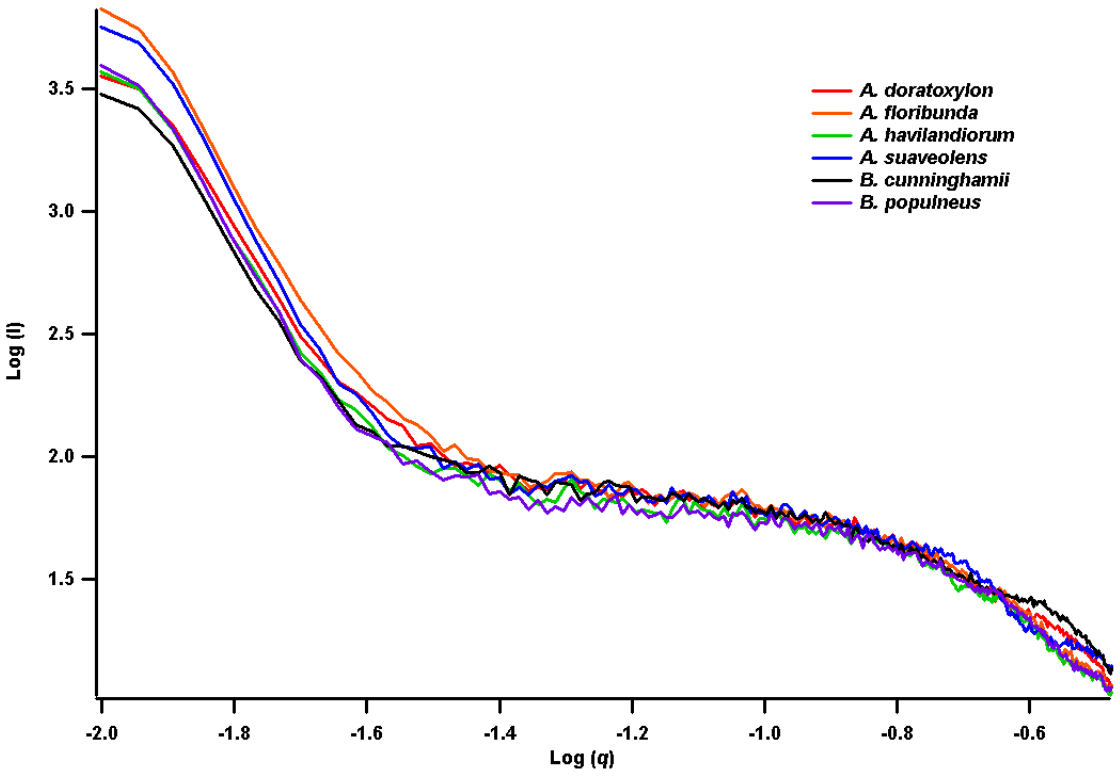

Figure A4-2 - SAXS profiles for the cross sectional samples of the maturing stems measured on a Bruker Nanostar at Curtin University.

References

Abasolo W, Yoshida M, Yamamoto H, Okuyama T. 1999. Internal Stress Generation in Rattan Canes. *IAWA Journal* **20**, 45 - 58.

Alexander LE. 1954. The Synthesis of X-Ray Spectrometer Line Profiles with Application to Crystallite Size Measurements. *Journal of Applied Physics* **25**, 155 - 161.

Aloni Y, Delmer DP, Benziman M. 1982. Achievement of high rates of in vitro synthesis of 1,4-beta-glucan: activation by cooperative interaction of the Acetobacter xylinum enzyme system with GTP, polyethylene glycol and a protein factor. *Proceedings of the National Academy of Sciences of the United States of America* **171,** 6448 – 6452**.**

Andrew ER. 1971. The narrowing of NMR spectra of solids by high speed specimen rotation and the resolution of chemical shift and spin multiplet structure for solids. *Prog. NMR Spectroscopy* **8**, 1-39.

Arioli T, Peng L, Betzner AS, Burn J, Wittke W, Herth W, Camilleri C, Hofte H, Palazinski J, Birch R, Cork A, Glover J, Redmond J, Williamson RE. 1998. Molecular analysis of cellulose biosynthesis in arabidopsis. *Science* **279**, 717 – 720.

Atalla RH, Gast JC, Sindorf DW, Bartuska VJ, Maciel GE. 1980. Carbon-13 NMR spectra of cellulose polymorphs. *J. Am. Chem. Soc.* **102**, 3249 – 3251.

Atalla RH, Van der Hart DL. 1984. Native cellulose: A composite of two distinct crystalline forms. *Science* **223**, 283 – 285.

Barber NF, Meylan BA. 1964. The anisotropic shrinkage of wood - a theoretical model. *Holzforschung* **18**, 146 - 156.

Barnett JR, Bonham VA. 2004. Cellulose microfibril angle in the cell wall of wood fibres. *Biol. rev.* **79**, 462 - 472.

Baskin TI. 2001. On the alignment of cellulose microfibrils by cortical microtubules: a review and a model. *Protoplasma* **215**, 150 – 171.

Baucher M, Monties B, Van Montagu M, Boerjan W. 1998. Biosynthesis and genetic engineering of lignin. *Crit. Rev. Plant Sci.* **17**, 125 - 197.

Beg MM, Aslam J, Khan QH, Butt NM, Rolandson S, Ahmed AU. 1974. Neutron diffraction studies of the unit cell of cellulose I. *Polymer Letters Edition* **12**, 311 – 318.

Boerjan W, Ralph J, Baucher M. 2003. Lignin Biosynthesis. *Annu. Rev. Plant Biol.* **54**, 519 - 546.

Brown RM, Montezinos D. 1976. Cellulose microfibrils: visualization of biosynthetic and orienting complexes in association with the plasma membrane. *Proceedings of the National Academy of Sciences of the United States of America* **73**, 4098 – 4103.

Burgert I, Fruhmann K, Keckes J, Fratzl P, Stanzl-Tschegg S. 2004. Structure-function relationships of four compression wood types: micromechanical properties at the tissue and fibre level. *Trees* **18**, 480 - 485.

Campbell MM, Sederoff RR. 1996. Variation in lignin content and composition - Mechanisms of control and implications for the genetic improvement of plants. *Plant Physiol.* **110**, 3 - 13.

Cave ID. 1997a. Theory of x-ray measuremen of microfibril angle in wood. Part 1, The condition for reflection. *Wood Science and Technology* **31**, 143 - 152.

Cave ID. 1997b. Theory of x-ray measurement of microfibril angle in wood. Part2, The diffraction diagram. *Wood Science and Technology* **31**, 225 - 234.

Cave ID. 1966. X-ray measurement of the microfibril angle in wood. *Forest Products Journal* **16**, 37 - 42.

Cave ID, Walker JCF. 1994. Stiffness of wood in fast-growing plantation softwoods: The influence of microfibril angle. *Forest Products Journal* **44**, 43 - 48.

Cheary RW, Coelho AA. 1998. Axial Divergence in a Conventional X-ray Powder Diffractometer. II. Realization and Evaluation in a Fundamental-Parameter Profile Fitting Procedure. *J. Appl. Cryst.* **31**, 862 - 868.

Chew TL, Bhatia S. 2008. Catalytic processes towards the production of biofuels in a palm oil and oil palm biomass-based biorefinery. *Bioresources Technology* **99**, 7911 - 7922.

Claffey W, Blackwell J. 1976. Electron diffraction of valonia cellulose. A quantitative interpretation. *Biopolymers* **15**, 1903 – 1915.

Cousins SK, Brown M. 1995. Cellulose I microfibril assembly: computational molecular mechanics energy analysis favours bonding by van der Waals forces as the initial step in crystallization. *Polymer* **36**, 3885 - 3888.

Cullity BD. 1978. *Elements of X-Ray Diffraction*. London: Addison-Wesley Publishing Company.

Delmer DP. 1987. Cellulose Biosynthesis. *Ann. Rev. Plant Physiol.* **38**, 259 – 290.

Delmer DP, Amor Y. 1995. Cellulose Biosynthesis. *The Plant Cell* **7**, 987 - 1000.

Delmer PP. 1999. Cellulose biosynthesis: Exciting times for a difficult field of study. *Annu. Rev. Plant Physiol. Mol. Biol.* **50**, 245 - 276.

Desprez T, Juraniec M, Crowell EF, Jouy H, Pochylova Z, Parcy F, Hofte H, Gonneau M, Vernhettes S. 2007. Organization of cellulose synthase complexes involved in primary cell wall synthesis in Arabidopsis thaliana. *Proceedings of the National Academy of Sciences of the United States of America* **104**, 15572 – 15577.

Earl WL, Van der Hart DL. 1982. Measurement of 13C chemical shifts in solids. *Journal of Magnetic Resonance* **48**, 35 - 54.

Earl WL, Van der Hart DL. 1981. Observations by high-resolution carbon-13 nuclear magnetic resonance of cellulose I related to morphology and crystal structure. *Macromolecules* **14**, 570 – 574.

Entwistle KM, Navaranjan N. 2002. Small-angle X-ray scattering from cellulose micro-fibrils in the S2 layers of structurally characterised softwood specimens. *Journal of Materials Science* **37**, 539 - 545.

Entwistle KM, Terrill NJ. 2000. The measurement of the micro-fibril angle in softwood. *Journal of Materials Science* **35**, 1675 - 1684.

Evans R, Stuart S-A, van der Touw J. 1996. Microfibril angle scanning of increment cores by X-ray diffractometry. *Appita Journal* **49**, 411-414.

Evans R. 1999. A variance approach to the x-ray diffractometric estimation of microfibril angle in wood. *Appita.* **52**, 283 - 289.

Fabbri D, Mongardi M, Mantanari L, Galletti GC, Chiavari G, Scotti R. 1998. Comparison between CP/MAS 13C-NMR and pyrolysis-GC/MS in the structural characterization of humins and humic acids of soil and sediments. *Fresenius J Anal Chem* **362**, 299 - 306.

Farber J, Lichteneggar HC, Reiterer A, Stanzl-Tschegg S, Fratzl P. 2001. Cellulose microfibril angles in a spruce branch and mechanical implications. *Journal of Materials Science* **36**, 5087-5092.

Feigin LA, Svergun DI. 1987. *Structure Analysis of Small-Angle X-ray and Neutron Scattering*. New York: Plenum Press.

Fengel D, Wegener G. 1989. *Wood: Chemistry, Ultrastructure, Reactions*. Berlin: Walter de Gruyter & Co.

Fischer DG, Mann J. 1960. Crystalline modifications of cellulose. Part IV unit cell and molecular symmetry of cellulose I. *Journal of Polymer Science* **62**, 189 – 194.

French AD. 2000. Structure and biosynthesis of cellulose. Part I: Structure. In: Yang SF, Kung SD, eds. *Discoveries in Plant Biology*, Vol. 3. Singapore: World Scientific.

French J, Conn AB, Batchelor WJ, Parker IH. 2000. The Effect of Fibre Fibril Angle on Some Handsheet Mechanical Properties. *Appita.* **53**, 210 - 226.

Frey-Wyssling A. 1954. The Fine Structure of Cellulose Microfibrils. *Science* **119**, 80 - 82.

Frey-Wyssling A, Muhlethaler K. 1963. The elementary fibrils of cellulose. *Makromol. Chem.* **62**, 25 – 30.

Fukushima E, Roeder SBW. 1993. *Experimental Pulse NMR - A Nuts and Bolts Approach*. London: Addison-Wesley Publishing.

Gardiner JC, Taylor NG, Turner SR. 2003. Control of Cellulose Synthase Complex Localization in Developing Xylem. *The Plant Cell* **15**, 1740 – 1748.

Gardner KH, Blackwell J. 1974a. The hydrogen bonding in native cellulose. *Biochim. et Biophys. Acta* **343**, 232 - 237.

Gardner KH, Blackwell J. 1974b. The structure of native cellulose. *Biopolymers* **13,** 1975 – 2001**.**

Garvey CJ, Parker IH, Simon GP. 2005a. On the interpretation of X-ray diffraction powder patterns in terms of the nanostructure of cellulose I fibres. *Macromolecular Chemistry and Physics* **206**, 1568-1575.

Garvey CJ, Knott RB, Searson M, Conroy JP. 2006. USANS Study of Wood Structure. *Physica B* **385-386**, 877-879.

Garvey CJ, Parker IH, Simon GP. 2005b. On the interpretation of x-ray distraction powder patterns in terms of the nanostructure of of cellulose I fibres. *Macromol. Chem. Phys.* **206**, 1568 - 1575.

Giddings TH, Brower DL. 1980. Visualization of particle complexes in the plasma membrane of Micrasterias Denticula associated with the formation of cellulose fibrils in primary and secondary cell walls. *Journal of Cell biology* **84**, 327 - 339.

Giddings TH, Staehelin LA. 1991. Microtubule-mediated control of microfibril deposition: a re-examination of the hypothesis. In: Lloyd CW, ed. *The Cytoskeletal Basis of Plant Growth and form*. London: Academic.

Glaser L. 1957a. The enzymic synthesis of cellulose by Acetobacter xylinum. *Biochim. et Biophys. Acta* **25**, 436.

Glaser L. 1957b. The Synthesis of Cellulose in Cell-Free Extracts of Acetobacter Xylinum. *The Journal of Biological Chemistry* **232**, 627 – 636.

Glatter O, Kratky O. 1982. *Small-angle X-ray Scattering*. London: Academic Press.

Gromet Z, Schramm M, Hestrin S. 1957. Synthesis of Cellulose by Acetobacter xylinum. 4. Enzyme systems present in a crude extract of glucose-grown cells. *The Biochemical Journal* **67**, 679 – 689.

Gross ST, Clark GL. 1938. A Test of the Alternate Structures Proposed for Cellulose. *Textile Research Journal* **9**, 7 – 15.

Guinier A. 1963. *X-Ray Diffraction in Crystals, Imperfect Crystals and Amorphous Bodies*. San Francisco: W.H. Freeman and Company.

Guinier A, Fournet G. 1955. *Small Angle Scattering of X-rays*. New York: Wiley.

Haigler CH, Brown RM. 1983. Transport of rosettes from the Golgi apparatus to the plasma membrane in isolated mesophyll cells of Zinnia elegans during differentiation to tacheary elements in suspension culture. *Protoplasma* **134**, 111 – 120.

Halder NC, Wagner CNJ. 1966. Separation of particle size and lattice strain in integral breadth measurements. *Acta Cryst.* **20**, 312 - 313.

Hammersley A. 2004. The Fit2D Home Page.

Hartmann SR, Hahn EL. 1962. Nuclear Double Resonance in the Rotating Frame. *Phys. Rev.* **128**, 2042-2053.

Haworth WN. 1929. *The Constitution of Sugars*: London. E. Arnold & Co.

Heath IB. 1974. A Unified Hypothesis for the Role of Membrane Bound Enzyme Complexes and Microtubules in Plant Cell Wall Synthesis. *Journal of Theoretical Biology* **48**, 445 – 449.

Hermans PH, Weidinger A. 1950. Quantitative Investigation of X-Ray Diffraction by "Amorphous" Polymers and Some Other Noncrystalline Substances. *1950* **5**, 269 - 281.

Hestrin S, Schramm M. 1954. Synthesis of Cellulose by Acetobacter xylinum. 2. Preparation of freeze-dried cells capable of polymerizing glucose to cellulose. *The Biochemical Journal* **58,** 345 – 352.

Heyn ANJ. 1950. Small Angle Scattering by Cellulose Fibres: Experimental Study on the Orientation Factor in Model Filaments and Rayons. *J. Am. Chem. Soc.* **72**, 2284 - 2285.

Hill DJT, Le TT, Whittaker AK. 1994. A technique for the quantitative measurements of signal intensities in cellulose-based transformer insulators by 13C CPMAS NMR. *Cellulose* **1**, 237 - 247.

Hillis WE, Evans R, Washusen R. 2004. An unusual formation of tension in a natural forest Acacia sp. *Holzforschung* **58**, 241 - 245.

Hirai A, Horii F, Kitamaru R. 1987. Transformation of native cellulose crystals from Ib to Ia through solid state chemical reactions. *Macromolecules* **20**, 1440 – 1442.

Hon DN-S. 1994. Cellulose: a random walk along its historical path. *Cellulose* **1**, 1 – 25.

Honjo G, Watanabe M. 1958. Examinatin of cellulosefibre by the low-temperature specimen method of electron diffraction and electron microscopy. *Nature* **181**, 326 – 328.

Horii F, Yamamoto H, Kitamaru R, Tanahashi M, Higuchi T. 1987. Transformation of native cellulose crystals induced by saturated steam at high temperatures. *Macromolecules* **20**, 2946 – 2949.

Hotchkis AT, Brown RM. 1987. The association of rosette and globule terminal complexes with cellulose microfibril assembl in Nitella translucens Var. Axillaris (CHAROPHYCEAE). *Journal of Phycology* **23**, 228 - 237.

Hotchkiss AT. 1989. Cellulose Biosynthesis - the terminal complex hypothesis and its relationship to other comtemporary research topics. *Plant Cell Wall Polymers*, **399**, 232-247.

Jakob HF, Fratzl P, Stanzl-Tschegg S. 1994. Size and arrangement of elementary cellulose fibrils in wood cells: A small angle x-ray scattering study of picea abies. *Journal of Structural Biology* **113**, 13 - 22.

Jarvis MC. 2000. Interconversion of the I-alpha and I-beta crystalline forms of cellulose by bending. *Carbohydrate Research* **325**, 150 – 154.

Jarvis MC, Apperley DC. 1990. Direct observation of cell wall structure in living plant tissues by solid-state 13C NMR spectroscopy. *Plant Physiol.* **92**, 61 - 65.

Kang MS, Elango N, Mattie E, Young J, Robbins P, Cabib E. 1984. Isolation of chitin synthetase from Saccharomyces cerevisae. Purification of an enzyme by entrapment in the reaction product. *The Journal of Biological Chemistry* **259**, 14966 – 14972.

Kimura S, Laosinchai W, Itoh T, Cui X, Linder CR, Brown RM. 1999. Immunogold labeling of rosette terminal cellulose-synthesising complexes in the vascular plant vigna angularis. *The Plant Cell* **11**, 2075 – 2085.

Klemm D, Heublein B, Fink HP, Bohn A. 2005. Cellulose: Fascinating Biopolymer and Sustainable Raw Material. *Angewandte Chemie International Edition* **44**, 3358 - 3393.

Klug HP, Alexander LE. 1974. *X-Ray Diffraction Procedures For Polycrystalline and Amorphous Materials*. New York: John Wiley & Sons.

Knox B, Ladiges P, Evans B, Saint I. 2001. *Biology*. Sydney: McGraw-Hill Book Company Australia.

Kobayashi H, Fukuda H, Shibaoka H. 1988. Interrelation between the spatial disposition of actin filaments and microtubules during the differentiation of tracheary elements in cultured Zinnia cells. *Protoplasma* **143**, 29 – 37.

Konarev PV, Volkov VV, Sokolova AV, Koch MHJ, Svergun DI. 2003. PRIMUS: a Windows PC-based system for small-angle scattering data analysis. *Journal of Applied Crystallography* **36**, 1277-1282.

Kudlicka K, Brown RM. 1997. Cellulose and Callose Biosynthesis in Higher Plants: 1. Solubilization and Separation of (1-3)-beta and (1-4)-beta-Glucan Synthase Activities from Mung Bean. *Plant Physiology* **115**, 643 – 656.

Kudlicka K, Brown RM, Li L, Lee JH, Shin H, Kuga S. 1995. Beta-glucan snthesis in cotton fiber: IV. In vitro assembly of the cellulose I allomorph. *Plant Physiology* **107**, 111 – 123.

Kurek I, Kawagoe Y, Jacob-Wilk D, Doblin MS, Delmer D. 2002. Dimerizatoin of Cotton Fiber Cellulose Synthase Catalytic Subunits Occurs via Oxidation of the Zinc-Binding Domains. *Proceedings of the National Academy of Sciences of the United States of America* **99**, 11109 – 11114.

Langford JI. 1978. A Rapid Method for Analysing the Breadths of Diffraction and Spectral Lines using the Voigt Function. *J. Appl. Cryst.* **11**, 10-14.

Ledbetter MC, Porter KR. 1963. A "Microtubule" in Plant Cell Fine Structure. *The Journal of Cell Biology* **19**, 239 – 250.

Leloir LF. 1971. Two Decades of Research on the Biosynthesis of Saccharides. *Science* **172**, 1299 – 1303.

Lichteneggar H, Reiterer A, Stanzl-Tschegg S, Fratzl P. 1999. Variation of cellulose microfibril angles in softwood and hardwoods - a possible strategy of mechanical optimization. *Journal of Structural Biology* **128**, 257 - 269.

Lichtenegger HC, Reiterer A, Stanzl-Tschegg S, Fratzl P. 2001. Comment about "The measurement of the micro-fibril angle in soft-wood" by K.M. Entwistle and N.J. Terrill. *Journal of Materials Science Letters* **20**, 2245 - 2247.

Lin FC, Brown RM. 1989. Purification of cellulose synthase from Acetobacter xylinum. In: Scheurch C, ed. *Cellulose and Wood - Chemistry and technology*. New york: Wiley.

Lin FC, Brown RM, Drake RR, Haley BE. 1990. Identification of the uridine-5'-diphosphoglucose (UDP-gluc) binding subunit of cellulose synthase in Acetobacter xylinum using the photoaffinity probe 5-azido-UDP-glc. *The Journal of Biological Chemistry* **265**, 4782 – 4784.

Liss K-D, Bartels A, Schreyer A, Clemens H. 2003. High-Energy X-Rays: A tool for Advanced Bulk Investigations in Materials Science and Physics. *Textures and Microstructures* **35**, 219-252.

Lloyd CW. 1984. Toward a Dynamic Helical Model for the Influence of Microtubules on Wall Patterns in Plants. *International Review of Cytology* **86**, 1 – 51.

Maloney TC, Paulapuro H. 1999. The formation of pores in the cell wall. *Journal of Pulp and Paper Science* **25**, 430 - 436.

Martinschitz KJ, Boesecke P, Garvey CJ, Gindl W, Keckes J. 2006. Changes in microfibril angle in cyclically deformed dry coir fibers studied by in situ synchrotron x-ray diffraction. *J Mater Sci* **43**, 350 - 356.

Matsumura J, Butterfield BG. 2001. Microfibril angles in the root wood of Pinus radiata and Pinus nigra. *IAWA Journal* **22**, 57-62.

Mattheck C, Kubler H. 1995. *Wood - The Internal Optimization of Trees*. Berlin: Springer.

Mayer R, Ross P, Weinhouse H, Amikam D, Volman G, Ohana P, Calhoon RD, Wong HC, Emerick AW, Benziman M. 1991. Polypeptide composition of bacterial cyclic diguanylic acid-dependent cellulose synthase and the occurence of immunologically crossreacting proteins in higher plants. *Proceedings of the National Academy of Sciences of the United States of America* **88**, 5472 – 5476.

McBrierty VJ, Packer KJ. 1993. *Nuclear Magnetic Resonance in Solid Polymers*. Cambridge: Cambridge University Press.

McNeil M, Darvill AG, Fry SC, Albersheim P. 1984. Structure and function of the primary cell walls of plants. *Ann. Rev. Biochem.* **53**, 625 - 663.

McMillan JD. 1994. Pretreatment of Lignocellulosic Biomass. *Enzymatic Conversion of Biomass for Fuels Production*, Vol. 566. Wasington DC: American Chemical Society, 292-324.

Meylan BA. 1967. Measurement of microfibril angle by x-ray diffraction. *Forest Products Journal* **17**, 51 - 58.

Meylan BA, Probine MC. 1969. Microfibril angle as a parameter in timber quality assessment. *Forest Products Journal* **19**, 30 - 34.

Mitsuda N, Iwase A, Yamamoto H, Yoshida M, Seki M, Shinozaki K, Ohme-Takagi M. 2007. NAC Transcription Factors, NST1 and NST3, Are Key Regulators of the Formation of Secondary Walls in Woody Tissues of Arabidopsis. *The Plant Cell* **19**, 270 – 280.

Mueller SC, Brown RM. 1980. Evidence for an intramembrane component associated with a cellulose microfibril synthesizing complex in higher plants. *Journal of Cell biology* **84**, 315 - 326.

Muhlethaler K. 1969. Fine structure of natural polysaccharide systems. *Journal of Polymer Science Part C: Polymer Symposia* **28**, 305 – 316.

Mukherjee SM, Woods HJ. 1953. X-ray and electron microscope studies of the degradation of cellulose by sulphuric acid. *Biochim. et Biophys. Acta* **10**., 499 – 511.

Muller M, Czihak C, Burghammer M, Riekel C. 2000a. Combined X-ray microbeam small-angle scattering and fibre diffraction experiments on single native cellulose fibres. *J. Appl. Cryst.* **33**, 817 - 819.

Muller M, Czihak C, Schober H, Nishiyama Y, Vogl G. 2000b. All disordered regions of native cellulose show common low-frequency dynamics. *Macromolecules* **33**, 1834 - 1840.

Muller M, Czihak C, Vogl G, Fratzl P, Schober H, Riekel C. 1998. Direct Observation of Microfibril Arrangement in a Single Native Cellulose Fiber by Microbeam Small Angle X-ray Scattering. *Macromolecules* **31**, 3953 - 3957.

Newman RH. 1999. Estimation of the lateral dimentions of cellulose crystallites using C-13 NMR signal strengths. *Solid State Nuclear Magnetic Resonance* **15**, 21 - 29.

Newman RH, Hemmingson JA. 1994. Carbon-13 NMR distinction between categories of molecular order and disorder in cellulose. *Cellulose* **2**, 95 - 110.

Nishiyama Y, Langan P, Chanzy H. 2002. Crystal structure and hydrogen bonding system in cellulose I-beta from synchrotron x-ray and neutron fiber diffraction. *J. Am. Chem. Soc.* **124**, 9074 – 9082.

Nishiyama Y, Sugiyama J, Chanzy H, Langan P. 2003. Crystal structure and hydrogen bonding system in cellulose I-alpha from synchrotron x-ray and neutron fibre diffraction. *J. Am. Chem. Soc.* **125**, 14300 – 14306.

Nuhse TS, Stensballe A, Jensen ON, Peck SC. 2004. Phosphoproteomics of the Arabidopsis Plasma Membrane and a New Phosphorylation Site Database. *The Plant Cell* **16**, 2394 – 2405.

Onoda Y, Richards AE, Westoby M. 2010. The relationship between stem biomechanics and wood density is modified by rainfall in 32 Australian woody plant species. *New Phytologist* **185**, 493-501.

Paradez A, Wright A, Ehrhardt DW. 2006. Microtubule Cortical Array Organization and Plant Cell Morphogenesis. *Current Opinion in Plant Biology* **9**, 571 – 578.

Preston RD. 1964. *The Formation of Wood in Forest Trees*. New York: Academic.

Preston RD. 1975. X-ray analysis and the structure of the components of plant cell walls. *Physics Reports (Section C of Physics Letters)* **21**, 183 - 226.

Quader H. 1991. Role of linear terminal complexes in cellulose synthesis. In: Haigler CH, Weimer PJ, eds. *Biosynthesis and Biodegradation of Cellulose*. New York: Marcel Dekker.

Reid JD, Dryden EC. 1940. Anselme Payen-discoverer of cellulose. *Textile Colorist*, 43 – 45.

Reiterer A, Jakob HF, Stanzl-Tschegg SE, Fratzl P. 1998. Spiral angle of elementary cellulose fibrils in cell walls of Picea abies determined by small-angle X-ray scattering. *Wood Science and Technology* **32**, 335 - 345.

Riekel C, Cedola A, Heidelbach F, Wagner K. 1997. Microdiffraction experiments on single polymeric fibers by synchrotron radiation. *Macromolecules* **30**, 1033 - 1037.

Robinson DG, Quader H. 1981. Structure, synthesis and orientation of microfibrils. IX. A freeze-fracture investigation of the Oocystis plasma membrane after inhibitor treatments. *European Journal of Cell Biology* **25**, 278 – 288.

Ross P, Mayer R, Benziman M. 1991. Cellulose biosynthesis and function in bacteria. *Microbiological reviews* **55**, 35 - 58.

Ross P, Weinhouse H, Aloni Y, Michaeli D, Weinberger-Ohana P, Mayer R, Braun S, De Vroom E, Van der Marel GA, Van Boom JH, Benziman M. 1987. Regulation of cellulose synthesis in Acetobacter xylinum by cyclic diguanylic acid. *Nature* **325**, 279 – 281.

Ruland W. 1965. The integral width of the convolution of a Gaussian and a Cauchy distribution. *Acta Cryst.* **18**, 581.

Saha BC. 2003. Hemicellulose bioconversion. *J Ind Microbiol Biotechnol* **30**, 279 - 291.

Sarko A. 1976. Crystalline polymorphs of cellulose: prediction of structure and properties. *Appl. Polym. Symp.* **28**, 729 – 749.

Sarko A, Muggli R. 1974. Packing analysis of carbohydrates and polysaccharides. III. Valonia cellulose and cellulose II. *Macromolecules* **486**, 486 – 494.

Saxena IM, Brown RM, Dandekar T. 2001. Structure-function characterization of cellulose synthase: relationship to other glycosyltransferases. *Phytochemistry* **57**, 1135 – 1148.

Saxena IM, Brown RM, Fevre M, Geremia RA, Henrissat B. 1995. Multidomain Architecture of beta-Glycosyl Transferases: Implications for Mechanism of Action. *Journal of Bacteriology* **177**, 1419 – 1424.

Saxena IM, Lin FC, Brown RM. 1990. Cloning and sequencing of the cellulose synthase catalytic subunit gene of Acetobacter xylinum. *Plant Molecular Biology* **15**, 673 – 683.

Schaefer J, Stejskal EO. 1976. Carbon-13 Nuclear Magnetic Resonance of polymers spinning at the magic angle. *Journal of the American Chemical Society* **98**, 1031 – 1032.

Schaefer J, Stejskal EO, Buchdahl R. 1977. Macig-angle 13C NMR analysis of motion in solid glassy polymers. *Macromolecules* **10**, 384 - 405.

Scherrer P. 1918. Estimation of the Size and Internal Structure of Colloidal Particles by Means of Roentgen Rays. *Nachr. Ges. Wiss*, 98 - 100.

Schoening FRL. 1965. Strain and particle size values from X-ray line breadths. *Acta Cryst.* **18**, 975-976.

Schramm M, Gromet Z, Hestrin S. 1957. Synthesis of Cellulose by Acetobacter xylinum. 3. Substrates and inhibitors. *The Biochemical Journal* **67**, 669 – 679.

Schramm M, Hestrin S. 1953. Synthesis of Cellulose by Acetobacter xylinum. 1. Micromethod for the determination of celluloses. *The Biochemical Journal* **56**, 163 – 166.

Scurfield G. 1973. Reaction Wood: Its structure and function. *Science* **179**, 647 - 655.

Sjöström E. 1993. *Wood Chemistry Fundamentals and Applications*. San Diego: Academic Press.

Snyder RL, Fiala J, Bunge HJ. 1999. *Defect and Microstructure Analysis by Diffraction*. Oxford: Oxford University Press.

Spencer FS, Maclachlan GA. 1972. Changes in Molecular Weight of Cellulose in the Pea Epicotyl during Growth. *Plant Physiol.* **49**, 58-63.

Sponsler OL. 1928. The Molecular Structure of the Cell Wall of Fibers. A Summary of X-Ray Investigations. *American Journal of Botany* **15**, 525 – 536.

Sponsler OL. 1925. X-ray diffraction patterns from plant materials. *Science* **62**, 221 – 233.

Stewart OC. 1955. Fire as the first great force employed by man. *International Symposium on Man's Role in Changing the Face of the Earth*. Princeton, New Jersey: The University of Chicago Press.

Stokes AR. 1948. A Numerical Fourier-analysis Method for the Correction of Widths and Shapes of Lines on X-ray Powder Photographs. *Proceedings of the Physical Society* **61**, 382-391.

Stuart S-A, Evans R. 1995. X-ray diffraction estimation of the microfibril angle variation in eucalypt wood. *Appita.* **48**, 197 - 200.

Sugimoto K, Himmelspach R, Williamson RE, Wasteneys GO. 2003. Mutation or Drug-Dependent Microtubule Disruption Causes Radial Swelling without Altering Parallel Cellulose Microfibril Deposition in Arabidopsis Root Cells. *The Plant Cell* **15**, 1414 – 1429.

Sugiyama J, Persson J, Chanzy H. 1991. Combined infrared and electron diffraction study of the polymorphism of native cellulose. *Macromolecules* **24**, 2461 – 2466.

Sugiyama J, Vuong R, Chanzy H. 1991b. Electron difraction study on the two crystalline phases occurring in native cellulose and from an algal cell wall. *Macromolecules* **24**, 4168 – 4175.

Taylor NG. 2008. Cellulose biosynthesis and deposition in higher plants. *New Phytologist* **178**, 239 – 252.

Taylor NG, Gardiner JC, Whiteman R, Turner SR. 2004. Cellulose synthesis in the Arabidopsis secondary cell wall. *Cellulose* **11**, 49 – 61.

Taylor NG, Howells RM, Huttly AK, Vickers K, Turner SR. 2003. Interactions among three distinct CesA proteins essential for cellulose synthesis. *Plant Biology* **100**, 1450 – 1455.

Van der Hart DL, Atalla RH. 1987. Further Carbon-13 NMR Evidence for the Coexistence of Two Crystalline Forms in Native Celluloses. *The Structures of Cellulose*, Vol. 340: American Chemical Society, 88-118.

Van der Hart DL, Atalla RH. 1984. Studies of the microstructure in native cellulose using solid state C13-NMR. *Macromolecules* **17**, 1465 – 1472.

Vergara CE, Carpita NC. 2001. Beta-D-Glycan synthases and the CesA gene family: lessons to be learned from the mixed-linkage (1-3), (1-4) beta-D-glucan synthase. *Plant Molecular Biology* **47**, 145 – 160.

Viswanathan A, Shenouda SG. 1971. The helical structure of cellulose I. *Journal of Applied Polymer Science* **15,** 519 – 535.

Wada M, Nishiyama Y, Chanzy H, Forsyth T, Langan P. 2008. The structure of celluloses. *Powder Diffraction* **23**, 92 – 95.

Wardrop AB. 1952. The Low-Angle Scattering of X-Rays by Conifer Tracheids. *Textile Research Journal* **22**, 288 - 291.

Wardrop AB, Preston RD. 1947. Organisation of the cell walls of tracheids and wood fibres. *Nature* **160**, 911-913.

Warren BE. 1969. *X-ray Diffraction*. Massachusetts Addison-Wesley Publishing.

Watson AJ, Dadswell HE. 1964. Influence of Fibre Morphology on Paper Properties, 4. Micellar Spiral Angle. *Appita.* **17**, 151 - 156.

Williamson GK, Hall WH. 1953. X-ray Line Broadening From Filed Aluminium and Wolfram. *Acta Metallurgica* **1**, 22-31.

Wilson AJC. 1949. *Xray Optics - The Diffraction of X-rays by Finite and Imperfect Crystals*. London: Methuen & Co Ltd.

Wimmer R, Downes GM, Evans R. 2002. Temporal variation of microfibril angle in Eucalyptus nitens grown in different irrigation regimes. *Tree Physiology* **22**, 449-457.

Wong HC, Fear AL, Calhoon RD, Eichinger GH, Mayer R. 1990. Genetic organization of the cellulose synthase operon in acetobacter xylinum. *Proceedings of the National Academy of Sciences of the United States of America* **87**, 8130 – 8134.

Wright IJ, Westoby M, Reich PB. 2002. Convergence Towards Higher Leaf Mass per Area in Dry and Nutrient-Poor Habitats Has Different Consequences for Leaf Life Span. *Journal of Ecology* **90**, 534 - 543.

Yamamoto H, Horii F, Odani H. 1989. Structural changes of native cellulose crystals induced by annealing in aqueous alkaline and acidic solutions at high temperatures. *Macromolecules* **22**, 4130 - 4132.

Zhong R, Richardson EA, Ye Z-H. 2007. Two NAC domain transcription factors, SND1 and NST1, function redundantly in regulation of secondary wall synthesis in fibers of arabidopsis. *Planta* **225**, 1603 – 1611.

Zhu S-H, Chan C-M, Mai Y-W. 2006. Micromechanical Properties on the Surface of PVC/SBR Blends Speacially Resolved by a Nanoindentation Technique. *Polymer Engineering and Science* **44**, 609 - 614.